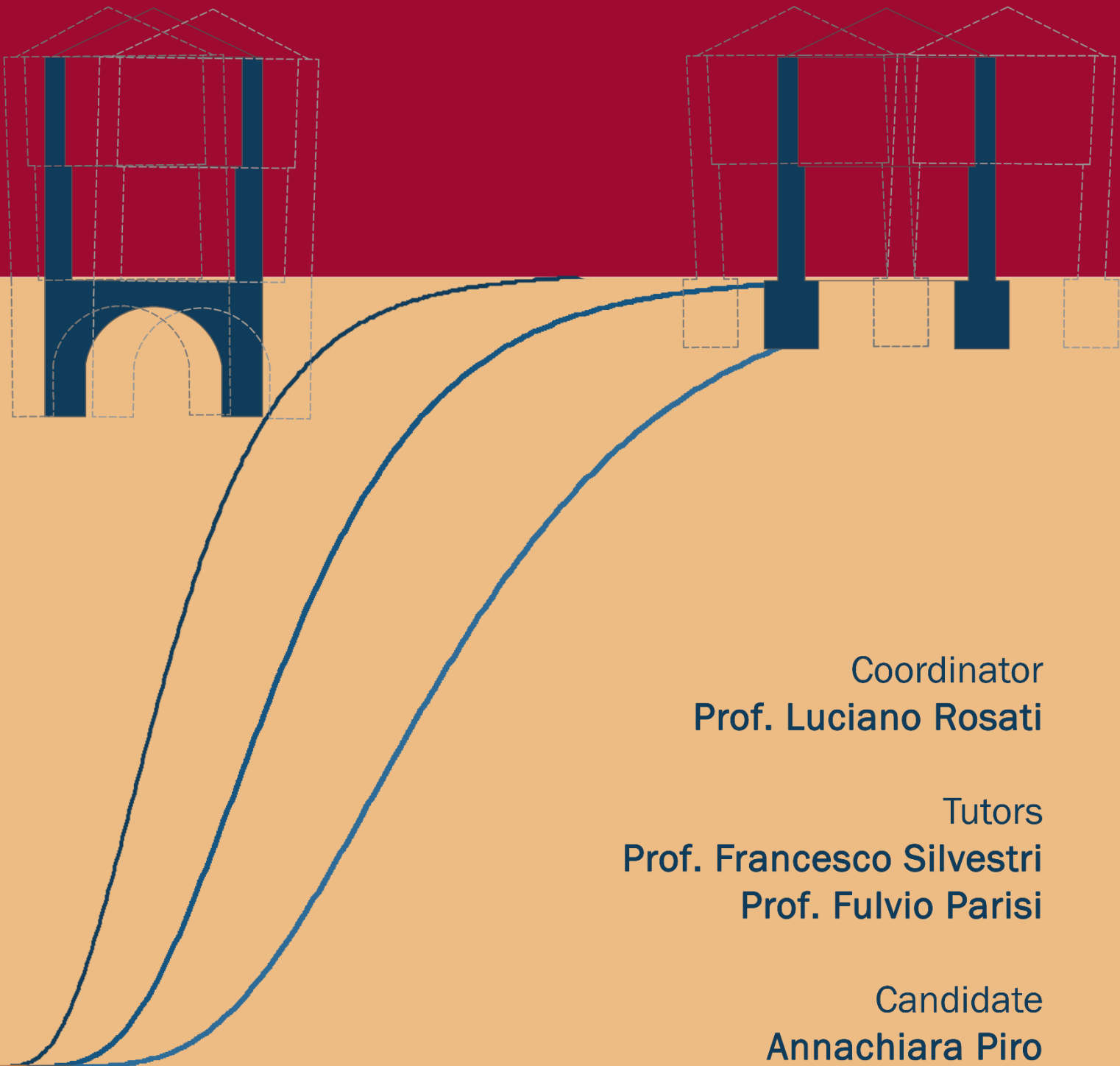




University of Naples Federico II

Department of Structures for Engineering and Architecture
&
Department of Civil, Architectural, Environmental
and Engineering

SOIL-STRUCTURE INTERACTION EFFECTS ON SEISMIC RESPONSE OF MASONRY BUILDINGS



Coordinator
Prof. Luciano Rosati

Tutors
Prof. Francesco Silvestri
Prof. Fulvio Parisi

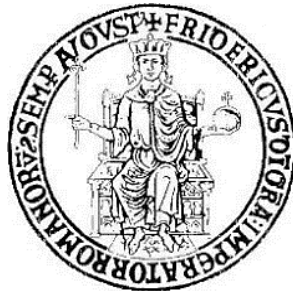
Candidate
Annachiara Piro

UNIVERSITY OF NAPLES FEDERICO II

DEPARTMENT OF STRUCTURES FOR ENGINEERING AND
ARCHITECTURE

and

DEPARTMENT OF CIVIL, ARCHITECTURAL, ENVIRONMENTAL
AND ENGINEERING



PH.D. PROGRAMME IN
STRUCTURAL AND GEOTECHNICAL ENGINEERING AND
SEISMIC RISK
XXXIII CYCLE

COORDINATOR PROF. ENG. LUCIANO ROSATI

ANNACHIARA PIRO

PH.D. THESIS
SOIL-STRUCTURE INTERACTION EFFECTS ON SEISMIC RESPONSE
OF MASONRY BUILDINGS

TUTORS

PROF. FRANCESCO SILVESTRI
PROF. FULVIO PARISI

2021

To my beloved family

To me

ACKNOWLEDGEMENTS

Like a famous movie mentions "It is not the destination so much as the journey", I could not use better words to describe this adventure. A three-year journey that allowed me to grow not only professionally, but above all personally. A journey that allowed me to live unique experiences and meet wonderful persons.

I state that I am not very good with "thank you notes", but I will try to say thanks in the best possible way to all those who have been close to me during this journey. I would like to start with my tutors, Prof. Francesco Silvestri and prof. Fulvio Parisi, who have guided and supported me (I would emphasize with a lot of patience) during these years. I thank them for the exchange of ideas and for the useful suggestions to improve the work, but especially for encouraging me to overcome my limits and help me grow.

Thanks also to prof. Carmine Galasso for valuable advice during the fantastic experience at the University College of London.

Thanks also to Emmanouil Rovithis for his fruitful suggestions to improve this work.

A huge thank you goes to Filomena, not only you are one of my closest friends but above all you are, for more than ten years now, a precious guide, who encouraged me and who has always believed in me, it was wonderful to be able to work with one of the brightest and best people I have ever met.

Thanks to my colleagues at DICEA, with whom I shared countless days, making them more enjoyable, thanks for our travels and laughter. Thanks to Domenico and Gianluca for the wise advice in moments of discouragement and the chats during the coffee breaks.

Thanks, to the new friends I met at DICEA, Stefania, Valeria and Gabriella, for the wonderful moments we spent together, for the many laughs and the evenings together. Special thanks go to Roberta, you have become one of my closest friends, and confidants, I thank you for the support, the daily chats, and the constant patience in putting up with me.

A huge thank you also to Sabrina, travel companion in the London experience, thanks to you for encouraging me and putting up with me during those three months.

Thanks to my friends Giovanna, Eleonora and Serena for their continued support.

Finally, thanks to my father Antonio, my mother Assunta and my sister Valeria, for encouraging me, and always believing in me even on those occasions when discouragement prevailed! I love you!

Annachiara

This study was carried out within the framework of the 2017-2018 and 2019–2021 ReLUIS-DPC research programmes funded by the Italian Civil Protection Department, as part of the geotechnical Task 16.3 ‘Soil-Foundation-Structure Interaction’.

RINGRAZIAMENTI

Come dice un famoso film “Non è la destinazione, ma il viaggio che conta”, non potevo usare parole migliori per descrivere quest’avventura. Un viaggio durato tre anni che mi ha permesso di crescere non solo professionalmente, ma anche personalmente. Un viaggio durante il quale ho avuto la fortuna di vivere esperienze uniche, e di incontrare persone stupende.

Premetto non sono molto brava con i ringraziamenti ma cercherò di dire grazie nel miglior modo possibile a tutti coloro che mi sono stati vicini durante questo viaggio.

Vorrei iniziare con i miei tutors, il Prof. Francesco Silvestri e il prof. Fulvio Parisi, che mi hanno guidato, supportato (sottolineerei con tanta pazienza) durante questi anni. Li ringrazio per lo scambio di idee e per i suggerimenti utili a migliorare il lavoro, ma li ringrazio soprattutto per avermi spronato a superare i miei limiti e avermi aiutato a crescere.

Un grazie anche al prof. Carmine Galasso per i preziosi consigli durante la fantastica esperienza presso la University College of London.

Un grazie anche a Emmanouil Rovithis per i suoi suggerimenti utili a migliorare questo lavoro.

Un immenso grazie va a Filomena, non solo sei una delle mie più care amiche ma soprattutto sei, da ormai più di dieci anni a questa parte, una preziosa guida, che mi ha incoraggiato e che ha sempre creduto in me, è stato bellissimo poter lavorare con una delle persone più brillanti e buone che abbia mai conosciuto.

Grazie ai miei colleghi del DICEA, con cui ho diviso innumerevoli giornate, rendendole più piacevoli, grazie per i nostri viaggi, le risate e molto altro ancora. In particolare, grazie a Domenico e Gianluca per i saggi consigli nei momenti di sconforto e le chiacchierate al caffè.

Grazie soprattutto alle nuove amiche conosciute al DICEA, Stefania, Valeria e Gabriella, grazie per i bellissimi momenti che abbiamo passato insieme, per le tantissime risate e le serate insieme.

Un ringraziamento speciale va a Roberta, sei diventata una delle mie più care amiche, e confidenti, ti ringrazio per il supporto, le chiacchierate giornaliere e la costante pazienza nel sopportarmi.

Un enorme grazie anche a Sabrina, compagna di viaggio nell’esperienza londinese, grazie a te per avermi spronato e sopportato in quei tre mesi.

Un grazie alle mie amiche Giovanna, Eleonora e Serena per il loro continuo sostegno. Infine, non per importanza grazie a mio padre Antonio, mia mamma Assunta e mia sorella Valeria, per avermi incoraggiato, ed aver sempre creduto in me anche in quelle occasioni in cui lo sconforto ha avuto il sopravvento!

Annachiara

Il progetto di ricerca è stato realizzato nell'ambito del WorkPackage 16.3 “Interazione Terreno-Fondazione-Struttura” della linea di ricerca Geotecnica finanziata dal Dipartimento di Protezione Civile attraverso il consorzio ReLUIS (Rete di Laboratori Universitari di Ingegneria Sismica) 2017-2018 e 2019-2021.

TABLE OF CONTENTS

LIST OF TABLES.....	11
LIST OF FIGURES	13
LIST OF SYMBOLS.....	22
LIST OF ABBREVIATION	27
ABSTRACT.....	29
I. INTRODUCTION.....	30
I.1. Framework and objectives of the study	30
I.2. Outline of the thesis	33
II. SOIL-FOUNDATION-STRUCTURE INTERACTION AND BEHAVIOUR OF MASONRY BUILDINGS UNDER EARTHQUAKES	35
II.1. Soil-Structure Interaction: theoretical basis and modelling approaches	35
II.2. Seismic response and damage of masonry buildings	45
II.3. Methods for seismic fragility analysis	50
III. EFFECTS OF SFS INTERACTION ON LINEAR DYNAMIC RESPONSE OF MASONRY BUILDINGS.....	54
III.1. Selected case studies and capacity models	55

III.2. Full time history analysis of SFS interaction model	61
<i>III.2.1. Fundamental frequency variation</i>	61
<i>III.2.2. Evaluation of radiation damping</i>	69
III.3. Simplified analysis: the replacement oscillator model	72
III.4. Comparison between full dynamic and simplified analyses	77
IV. EFFECTS OF SFS INTERACTION ON NONLINEAR DYNAMIC RESPONSE AND SEISMIC FRAGILITY OF MASONRY BUILDINGS	84
IV.1. Nonlinear SFS interaction models	85
<i>IV.1.1. Model description</i>	86
<i>IV.1.2. Numerical dynamic identification</i>	95
IV.2. Cloud analysis	103
<i>IV.2.1. Selection of strong ground motion records</i>	103
<i>IV.2.2. Intensity measures</i>	108
<i>IV.2.3. Engineering demand parameter and performance limit states for out-of-plane failure mechanisms</i>	112
<i>IV.2.4. Setting of the Rayleigh damping ratio</i>	114
<i>IV.2.5. Performance assessment of SFS components</i>	116
IV.3. Seismic fragility	127
<i>IV.3.1. Demand analysis</i>	127
<i>IV.3.2. Derivation of fragility curves</i>	133
V. APPLICATIONS TO CASE STUDIES	147

V.1. The proposed analytical approach	149
V.2. The case study of Matera buildings	151
V.3. The case study of a school building at Visso	159
<i>V.3.1. Geotechnical characterization</i>	160
<i>V.3.2. Calibration and assessment of the simplified model</i>	161
V.4. The case study of Sant’Agata de’ Goti historical centre	164
<i>V.4.1. Subsoil characterization</i>	166
<i>V.4.2. Numerical hill model</i>	176
<i>V.4.3. Dynamic response of the hill</i>	178
<i>V.4.4. Nonlinear dynamic analysis of the hill</i>	181
<i>V.4.5. SFS capacity models</i>	188
VI. CONCLUSIONS AND FUTURE PERSPECTIVES	200
REFERENCES	205
APPENDIX A	214
APPENDIX B	225

LIST OF TABLES

Table III.1. Physical and mechanical properties of materials.	59
Table III.2. Fundamental frequencies of soil and SFS systems with embedded foundation ($b/D = 3.2$)*.	65
Table III.3 Fundamental frequencies of soil and SFS systems with underground storey ($b/D=1.6$) *.	65
Table III.4. Inter-story drift ratio of the SFS systems with embedded foundation	67
Table III.5 Interstory drift ratio of the SFS systems with underground storey.....	68
Table III.6. Comparison between EC8-conforming and numerical estimates of fundamental frequency.	69
Table III.7 Radiation damping ratios of SFS systems with embedded foundation.	71
Table III.8 Radiation damping ratios of SFS systems with underground storey.	71
Table III.9. Regression coefficients and coefficient of determination of regression models for estimation of fundamental frequency and radiation damping ratio.....	76
Table III.10. Weighting coefficients for definition of σ_{eq}	80
Table IV.1 SFS models acronyms.....	86
Table IV.2 Physical and mechanical properties of the soil types.....	88
Table IV.3 Sigmoidal function parameters	90
Table IV.4 Physical and mechanical properties of the selected masonry types	92
Table IV.5 Physical and mechanical properties of the floor beam materials.....	94
Table IV.6 Rayleigh damping parameters for different materials.....	95
Table IV.7 Fundamental frequencies of soil and SFS systems	100
Table IV.8 Inter-story drift ratio of the SFS systems	101
Table IV.9 Properties of the selected records.	104
Table IV.10 Peak and integral IM values of selected records.....	109
Table IV.11 Spectral IMs of selected records for two-storey rubble stone masonry buildings ($h/b = 1$).	110
Table IV.12 Spectral IMs of selected records for four-storey rubble stone masonry buildings ($h/b = 2$).	110
Table IV.13 Spectral IMs of selected records for two-storey clay brick masonry buildings ($h/b = 1$).	111
Table IV.14 Spectral IMs of selected records for two-storey clay brick masonry buildings ($h/b = 2$).	111

Table IV.15 IDR thresholds associated with different DLs	113
Table IV.16 Rayleigh damping parameters adopted for the soil in the analyses.....	114
Table IV.17 Rayleigh damping parameters adopted for the structures in the analyses.	115
Table IV.18 Standard deviation, $\beta_{EDP IM}$ and probabilistic seismic demand (regression) models	128
Table IV.19 Fragility functions parameters of two-storey rubble stone masonry structures.....	141
Table IV.20 Fragility functions parameters of four-storey rubble stone masonry structures.....	141
Table IV.21 Fragility functions parameters of two-storey clay brick masonry structures	142
Table IV.22 Fragility functions parameters of four-storey clay brick masonry structures	142
Table IV.23 Reduction factor for the fixed base fragility functions ($R_{F_Dhe}=IM_{50Dhe}/IM_{50A}$ and $R_{F_Dho}=IM_{50Dho}/IM_{50A}$).....	143
Table IV.24 Reduction factor for the fixed base fragility functions ($R_{F_Dhe}=IM_{84Dhe}/IM_{84A}$ and $R_{F_Dho}=IM_{84Dho}/IM_{84A}$).....	144
Table V.1 Buildings characteristics	155
Table V.2 Mechanical properties of soil and masonry.....	156
Table V.3 SSI parameters (σ_{eq} and corresponding f^*/f_0 values)	158
Table V.4 Soil mechanical properties for soil (<i>ReLUIS 2018b</i>).....	161
Table V.5 Equivalent values of soil compliance for the different embedment	162
Table V.6 Small strain properties	169
Table V.7 Sigmoidal function parameters	172
Table V.8 Strength parameters	176
Table V.9 Properties of the selected records	181
Table V.10 Physical and mechanical properties of NYT masonry adopted in the analyses (<i>Vuoto et al 2018</i>).	188
Table V.11 Physical and mechanical properties of the floor beam materials adopted in the analyses.	188
Table V.12 Control points maximum and residual: displacements and drifts; RMDR.	192
Table V.13 IM values.....	197

LIST OF FIGURES

Figure I.1 Masonry buildings damaged by OOP mechanisms in most recent Italian seismic events	31
Figure II.1: Comparison between seismic responses of FB (a) and SFS (b) systems..	36
Figure II.2 Inertial SSI effects on spectral acceleration (NEHRP, 2012).....	37
Figure II.3: SFS models with different complexity levels related to the structure and soil: SDOF oscillator, MDOF system and continuum structural model on springs and dashpots (a, b, c) and on continuum soil model (d, e, f) (de Silva 2016).....	38
Figure II.4 Definition of replacement oscillator.....	40
Figure II.5 Variation of (a) f^*/f_0 and (b) ξ^* with σ	43
Figure II.6: Failure mechanisms of two buildings damaged by the 2016 Central Italy seismic sequence: (a) out-of-plane failures (Camerino, 2018), (b) in-plane failures (Visso, 2018).....	46
Figure II.7: In-plane failure mechanisms of URM walls: (a) tensile cracking and toe crushing (flexural failure mode); shear failure associated with (b) diagonal tension, (c) stepwise shear sliding and (d) bed-joint shear sliding	47
Figure II.8: Wall out of plane behaviour.....	49
Figure II.9: PSDM procedures: (a) multiple-stripe, (b) incremental dynamic, (c) cloud analysis.....	51
Figure III.1 Flowchart of the methodology adopted in this work.....	54
Figure III.2 SFS models with different basement configurations: (a) embedded floating foundation; (b) underground storey with load-bearing wall foundation	56
Figure III.3 Geometric properties of masonry sub-structures: (a) two (b) three and (c) four storeys.....	58
Figure III.4 SFS models of selected case studies with different foundation configuration: (a) homogeneous soil and underground storey; (b) homogeneous soil and embedded floating foundation; (c) layered soil and underground storey; (d) layered soil and embedded floating foundation (shear wave velocity profiles in m/s).	60
Figure III.5 Input noise for numerical dynamic identification of SFS systems: (a) accelerogram; (b) FFT and (c) soil transfer function along the FF vertical.....	62

Figure III.6 Dynamic response of three-storey SFS system ($h/b = 1.5$) with embedded floating foundation and homogeneous soil (A, B, C or D): (a) time histories and (b) FFTs of horizontal displacements at different structural elevations.	63
Figure III.7 Dynamic response of three-storey SFS system ($h/b = 1.5$) with underground storey and homogeneous soil (A, B, C or D): (a) time histories and (b) FFTs of horizontal displacements at different structural elevations.	64
Figure III.8 First modal shape of the SFS models on homogeneous soil type: (a) $h/b=1$, (b) $h/b=1.5$, (c) $h/b=2$	66
Figure III.9 Computation of radiation damping ratio: (a) unfiltered versus filtered time histories of roof horizontal displacement; (b) logarithmic displacement amplitude versus cycle number	70
Figure III.10 Definition of replacement oscillator of SFS system.....	72
Figure III.11 Regression models for σ -based analytical predictions: (a) structure with embedded floating foundation, (b) structure with underground storey.	74
Figure III.12 Regression models for σ -based predictions: (a) structure with embedded foundation, (b) structure with underground storey.	76
Figure III.13 Comparison between analytical (RO) and numerical (SSI) predictions: (a) structures with embedded foundation and SSI defined through σ ; (b) structures with underground storey.....	78
Figure III.14. Soil volume affected by horizontal foundation motion: (a) embedded floating foundation; (b) underground storey with bearing wall foundation.	79
Figure III.15 Comparison between analytical (RO) and numerical (SSI) predictions for structures with embedded foundation: (a) SSI defined through σ ; (b) SSI defined through σ_{eq} ; and (c) SSI defined through σ_{eq} computed with V_s NIST	81
Figure III.16 Comparison between analytical (RO) and numerical (SSI) predictions: (a) structures with embedded foundation and SSI defined through σ ; (b) structures with embedded foundation and SSI defined through σ_{eq} ; and (c) structures with underground storey.....	82
Figure IV.1 Flowchart of the methodology adopted in this work	84
Figure IV.2 SFS models of selected case studies founded on (a) homogeneous and (b) heterogeneous soil.....	85
Figure IV.3 2D finite difference models: (a) homogeneous and (b) heterogeneous soil profile.....	87

Figure IV.4 Profiles of (a) undrained strength, c_u , (b) initial shear stiffness, (c) shear wave velocity; (d) strain-dependent variation of normalized shear modulus and damping ratio according to the standard curves by Vucetic and Dobry (1991) vs hysteretic behaviour numerically simulated by sigmoidal function and Masing criteria.....	88
Figure IV.5 Variation of damping ratio with natural frequency: (a) single-control and (b) double-control frequency.....	90
Figure IV.6 Vertical stresses after static analysis under gravity loads: rubble stone masonry (a) $h/b = 1$ (b) $h/b = 2$; clay brick masonry (c) $h/b = 1$ and (d) $h/b = 2$..	93
Figure IV.7 Mohr Coulomb elasto-plastic constitutive model for (a) rubble stone and (b) clay brick masonry.	94
Figure IV.8 Dynamic response of Rs_1 on soil configurations A, D_{ho} , D_{he} : (a) time histories and (b) FFTs of horizontal displacements at different structural elevations.	96
Figure IV.9 Dynamic response of Rs_2 on soil configurations A, D_{ho} , D_{he} : (a) time histories and (b) FFTs of horizontal displacements at different structural elevations.	97
Figure IV.10 Dynamic response of Cb_1 on soil configurations A, D_{ho} , D_{he} : (a) time histories and (b) FFTs of horizontal displacements at different structural elevations.	98
Figure IV.11 Dynamic response Cb_2 on soil configurations A, D_{ho} , D_{he} : (a) time histories and (b) FFTs of horizontal displacements at different structural elevations.	99
Figure IV.12 Profiles of the displacement components of the SFS models: (a) rubble stone and (b) clay brick masonry structure.....	102
Figure IV.13 PGA- M_w -R distribution for the SIMBAD database	103
Figure IV.14 Set of the selected ground motions: (a) acceleration response spectra and (b) PGA- M_w -R distribution	104
Figure IV.15 Ground motion records used in the analyses: (a) accelerograms and (b) FFT	105
Figure IV.16 (a) Scheme of EDP, (b) time histories of σ_3 , (c) time histories of relative displacements, and (d) time histories of IDR (referred to ground motion ID4) ...	113
Figure IV.17 Soil amplification in terms of spectral ratios between free-field, at the foundation level, motion ($S_{a,s}$) and bedrock motion ($S_{a,b}$) for homogeneous (a) and heterogeneous (b) soil.....	116
Figure IV.18 Comparison between the max-mean and min S_a	117

Figure IV.19 Scatter plots of the maximum IDR for FB and compliant-base models versus the PGA for two-storey (a) rubble and (b) clay brick masonry structure, and for four-storey (c) rubble stone and (d) clay brick masonry structure computed for the selected set of ground motions	118
Figure IV.20 Scatter plots of the: maximum γ in FF condition versus maximum γ calculated in the SFS models for (a) homogeneous and (b) heterogeneous soil; maximum G/G_0 in FF condition versus maximum G/G_0 calculated in the SFS models for (c) homogeneous and (d) heterogeneous soil and maximum D in FF condition versus maximum D calculated in the SFS models for (e) homogeneous and (f) heterogeneous soil.....	119
Figure IV.21 Evolution of deformed shapes and plastic states of the two-storey, clay brick masonry structure, ID 1: (a) homogeneous soil and (b) heterogeneous soil	121
Figure IV.22 Evolution of deformed shapes and shear strains, ID 1: (a) homogeneous soil and (b) heterogeneous soil.....	122
Figure IV.23 Comparison between relative displacements and the corresponding inter-storey drift ratio (IDR) predicted for the two- and four-storey clay brick masonry structures on (a) homogeneous and (b) heterogeneous soil profiles.....	123
Figure IV.24 Comparison between (a) settlements, (b) foundation displacements and (c) rotations for the two- (left) and four-storey (right) clay brick masonry structures on homogeneous and heterogeneous soil profiles.....	124
Figure IV.25 Evolution of deformed shapes and plastic states of the four-storey, clay brick masonry structure, ID 1: (a) homogeneous soil and (b) heterogeneous soil	125
Figure IV.26 Evolution of deformed shapes and shear strains, ID 1: (a) homogeneous soil and (b) heterogeneous soil.....	126
Figure IV.27 EDP-IM relationships ($h/b = 1$; rubble stone masonry).....	129
Figure IV.28 EDP-IM relationships ($h/b = 2$; rubble stone masonry).....	130
Figure IV.29 EDP-IM relationships ($h/b = 1$; clay brick masonry)	131
Figure IV.30 EDP-IM relationships ($h/b = 2$; clay brick masonry)	132
Figure IV.31 Fragility functions ($h/b = 1$; rubble stone masonry)	136
Figure IV.32 Fragility functions ($h/b = 2$; rubble stone masonry)	137
Figure IV.33 Fragility functions ($h/b = 1$; clay brick masonry).....	138
Figure IV.34 Fragility functions ($h/b = 2$; clay brick masonry).....	139

Figure IV.35 Comparison between the fragility function of rubble stone and clay brick masonry structure for $h/b = 1$ and $h/b = 2$	140
Figure IV.36 Comparison between $R_F = IM_{50D} / IM_{50A}$ of (a) rubble stone and (b) clay brick masonry structure for $h/b = 1$ and $h/b = 2$	145
Figure IV.37 Comparison between $R_F = IM_{84D} / IM_{84A}$ of (a) rubble stone and (b) clay brick masonry structure for $h/b = 1$ and $h/b = 2$	146
Figure V.1 Location of the case studies on the Italian hazard map in terms of peak ground acceleration with a probability of exceedance equal to 10% in 50 years	148
Figure V.2 Proposed approach for the estimation of the frequency reduction ratio f^*/f_0	150
Figure V.3 Matera: (a) geological map with subsoil investigations (b) analysed buildings	151
Figure V.4 Geological sections relevant to the seven buildings analysed.....	153
Figure V.5 Comparison between the experimental and fixed-based periods	155
Figure V.6 Soil and foundation volumes, for each building, affected by inertial interaction	157
Figure V.7 Comparison between the experimental and analytical periods, the latter calculated with the traditional and the proposed approach	159
Figure V.8 (a) Soil profile, (b) V_s profiles measured through DH and MASW tests, (c) plan view of school and location of the surveys and (d) HVSR results.....	160
Figure V.9 (a) Plan view of the building (Brunelli et al 2020) and (b) soil and foundation volumes affected by the horizontal motion (section A-A/B-B)	163
Figure V.10 Comparison between the compliant base periods (T^*_{EXP} , T^*_{NUM} and T^*_{RO}) and the analytical periods calculated with the (a) traditional and (b) updated approach	164
Figure V.11 Sant'Agata de' Goti: (a) map; (b) aerial view; (c) geological section	166
Figure V.12 (a) Borehole layering, (b) V_P and V_S profiles.	168
Figure V.13 Comparison HVSR with amplification function at different depth	170
Figure V.14 Resonant column (RC) and cyclic torsional shear (CTS) tests on WGI: (a) G/G_0 - γ , (c) D - γ and on AD (b) G/G_0 - γ (d) D - γ relationships	171
Figure V.15 Variation of normalized shear stiffness (a) and damping (b) with shear strain assumed in the seismic response analyses.....	172
Figure V.16 Comparison between experimental data and hysteretic model: (a) WGI (b) AD.....	173

Figure V.17 Triaxial compression test results on WGI: (a) q - ϵ_a and (b) ϵ_v - ϵ_a relationships	174
Figure V.18 Triaxial compression test results on WGI: (a) stress paths; (b) failure points, (c) Mohr circles.....	175
Figure V.19 Numerical model (a) without cavities and (b) with cavities.....	177
Figure V.20 Input noise for numerical dynamic response of the hill: (a) accelerogram; (b) FFT	178
Figure V.21 Bedrock-surface transfer functions with and without cavities along vertical [V1-V10].....	179
Figure V.22 (a) Numerical model and (b) variability along the cross-section of the ratio PGA_s/PGA_b and f_{1soil} compared to the results of 1D seismic response analyses (V3, V7).....	180
Figure V.23 (a) Comparison between the spectral acceleration of the seven input motions on the average compatible with NTC spectrum for a flat rock outcrop; (b) accelerograms and (c) FFT of the three records used in the analyses.....	182
Figure V.24 (a) Numerical model, (b) variability along the cross-section of the ratio PGA_s/PGA_b , (c) of the amplification factor computed in the period range 0.1s-0.5s, (d) 0.5s-2.0s compared to the values computed through 1D analyses along verticals V3, V6.....	184
Figure V. 25 (a) Numerical model, shear strain contour at final t (b) no cavities and (c) with cavities (ARQ input motion)	185
Figure V.26 (a) Numerical model, shear strain contour at final t (b) no cavities and (c) with cavities (ALT input motion)	186
Figure V.27 (a) Numerical model, shear strain contour at final t (b) no cavities and (c) with cavities (BSC input motion)	187
Figure V.28 (a) Plan, (b) section of the ancient seminar and geometric survey of the underground level	189
Figure V.29 SFS numerical model of the ancient seminar	190
Figure V.30 Dynamic response of the SFS system: (a) time histories and (b) FFTs of horizontal displacements at different structural elevations.	191
Figure V.31 Profiles of maximum and residual displacements.....	192
Figure V.32 Evolution with time of (a) inelastic compressive strains and stresses and (b) plastic states (ARQ input motion)	193
Figure V.33 Evolution with time of (a) inelastic compressive strains and stresses and (b) plastic states (ALT input motion)	194

Figure V.34 Evolution with time of (a) inelastic compressive strains and stresses and (b) plastic states (BSC input motion).....	195
Figure V.35 Comparison between the foundation input motion (FIM) and free-field motion: (a) acceleration time histories and (b) acceleration spectra.....	196
Figure V.36 Fixed-base fragility functions for four-storey masonry buildings	198
Figure V.37 Fixed base and homogeneous D soil fragility functions for four-storey masonry buildings.....	199
A.A.1 Dynamic response of two-storey SFS system ($h/b = 1$) with embedded floating foundation and homogeneous soil (A, B, C or D): (a) time histories and (b) FFTs of horizontal displacements at different structural elevations.	215
A.A.2 Dynamic response of two-storey SFS system ($h/b = 1$) with embedded floating foundation and layered soil (C-B, D-B, D-C): (a) time histories and (b) FFTs of horizontal displacements at different structural elevations.	216
A.A.3 Dynamic response of two-storey SFS system ($h/b = 1$) with underground storey foundation and homogeneous soil (A, B, C or D): (a) time histories and (b) FFTs of horizontal displacements at different structural elevations.	217
A.A.4 Dynamic response of two-storey SFS system ($h/b = 1$) with underground storey foundation and layered soil (C-B, D-B, D-C): (a) time histories and (b) FFTs of horizontal displacements at different structural elevations.	218
A.A.5 Dynamic response of three-storey SFS system ($h/b = 1.5$) with embedded floating foundation and layered soil (C-B, D-B, D-C): (a) time histories and (b) FFTs of horizontal displacements at different structural elevations.	219
A.A.6 Dynamic response of three-storey SFS system ($h/b = 1.5$) with underground storey foundation and layered soil (C-B, D-B, D-C): (a) time histories and (b) FFTs of horizontal displacements at different structural elevations.	220
A.A.7 Dynamic response of four-storey SFS system ($h/b = 2$) with embedded floating foundation and homogeneous soil (A, B, C or D): (a) time histories and (b) FFTs of horizontal displacements at different structural elevations.	221
A.A.8 Dynamic response of four-storey SFS system ($h/b = 2$) with embedded floating foundation and layered soil (C-B, D-B, D-C): (a) time histories and (b) FFTs of horizontal displacements at different structural elevations.	222
A.A.9 Dynamic response of four-storey SFS system ($h/b = 2$) with underground storey foundation and homogeneous soil (A, B, C or D): (a) time histories and (b) FFTs of horizontal displacements at different structural elevations.	223

A.A.10 Dynamic response of four-storey SFS system ($h/b = 2$) with underground storey foundation and layered soil (C-B, D-B, D-C): (a) time histories and (b) FFTs of horizontal displacements at different structural elevations.	224
A.B.1 Evolution of deformed shapes and plastic states of the two-storey, clay brick masonry structure, ID 11: (a) homogeneous soil and (b) heterogeneous soil 226	
A.B.2 Evolution of deformed shapes and shear strains, ID 11: (a) homogeneous soil and (b) heterogeneous soil.....	227
A.B.3 Evolution of deformed shapes and plastic states of the two-storey, clay brick masonry structure, ID 12: (a) homogeneous soil and (b) heterogeneous soil.....	228
A.B.4 Evolution of deformed shapes and shear strains, ID 12: (a) homogeneous soil and (b) heterogeneous soil.....	229
A.B.5 Evolution of deformed shapes and plastic states of the four-storey, clay brick masonry structure, ID 11: (a) homogeneous soil and (b) heterogeneous soil.....	230
A.B.6 Evolution of deformed shapes and shear strains, ID 11: (a) homogeneous soil and (b) heterogeneous soil.....	231
A.B.7 Evolution of deformed shapes and plastic states of the four-storey, clay brick masonry structure, ID 12: (a) homogeneous soil and (b) heterogeneous soil.....	232
A.B.8 Evolution of deformed shapes and shear strains, ID 12: (a) homogeneous soil and (b) heterogeneous soil.....	233
A.B.9 Evolution of deformed shapes and plastic states of the two-storey, rubble stone masonry structure, ID 2: (a) homogeneous soil and (b) heterogeneous soil	234
A.B.10 Evolution of deformed shapes and shear strains, ID 2: (a) homogeneous soil and (b) heterogeneous soil.....	235
A.B.11 Evolution of deformed shapes and plastic states of the two-storey, rubble stone masonry structure, ID 5: (a) homogeneous soil and (b) heterogeneous soil	236
A.B.12 Evolution of deformed shapes and shear strains, ID 5: (a) homogeneous soil and (b) heterogeneous soil.....	237
A.B.13 Evolution of deformed shapes and plastic states of the two-storey, rubble stone masonry structure, ID 12: (a) homogeneous soil and (b) heterogeneous soil.....	238
A.B.14 Evolution of deformed shapes and shear strains, ID 12: (a) homogeneous soil and (b) heterogeneous soil.....	239
A.B.15 Evolution of deformed shapes and plastic states of the four-storey, rubble stone masonry structure, ID 2: (a) homogeneous soil and (b) heterogeneous soil	240

A.B.16 Evolution of deformed shapes and shear strains, ID 2: (a) homogeneous soil and (b) heterogeneous soil	241
A.B.17 Evolution of deformed shapes and plastic states of the four-storey, rubble stone masonry structure, ID 11: (a) homogeneous soil and (b) heterogeneous soil.....	242
A.B.18 Evolution of deformed shapes and shear strains, ID 11: (a) homogeneous soil and (b) heterogeneous soil	243
A.B.19 Evolution of deformed shapes and plastic states of the four-storey, rubble stone masonry structure, ID 12: (a) homogeneous soil and (b) heterogeneous soil.....	244
A.B.20 Evolution of deformed shapes and shear strains, ID 12: (a) homogeneous soil and (b) heterogeneous soil	245

LIST OF SYMBOLS

a	acceleration
a, b	parameter of the linear regression model (cloud method)
A	area of the j-th part of the SFS system
a, b, x_0	parameters sigmoidal function
a_0	dimensionless frequency factor
b	building width
B	foundation width
c	cohesion
C	damping matrix
c'	effective cohesion
c_θ	rotational dynamic damping coefficients
C_t	structural type coefficient
C_u	translational damping coefficients
c_u	translational dynamic damping coefficients
c_u	undrained strength
C_θ	rotational damping coefficients
D	cavity height
D	foundation depth
D	soil material damping
d_0	displacement out of plane capacity
D_0	initial value of the soil material damping
D_{5-95}	effective duration of the signal
E	Young's modulus
E_{Oed}	oedometric modulus
f^*	soil-foundation-structure fundamental frequency
f_0	fixed base fundamental frequency

f_{1d}	EC8-conforming fundamental frequency
f_{input}	predominant input frequency
f_n, f_m	Rayleigh damping parameters frequency interval
f_p, ξ_{min}	Rayleigh damping parameters
f_{soil}	soil fundamental frequency
G	shear modulus
G_0	shear stiffness at small strain
G_{eq}	equivalent shear modulus
h	building height
h_j	inter-storey height of the building
H	overall height
H_c	thickness of the Subappennines clays
I_A	Arias intensity
$I_{H(T1-T2)}$	Housner intensity
$I_{S(T1-T2)}$	integral of the spectral acceleration
K	bulk modulus
K	static translational and rotational stiffness
k'_θ	dynamic rotational springs stiffness
k'_u	dynamic translational springs stiffness
k_p	coefficient of passive earth pressure
k_θ	dynamic rotational springs stiffness
K_θ	embedded rotational springs static stiffness
k_{str}	single degree of freedom lateral stiffness
k_u	dynamic translational springs stiffness
K_u	embedded translational springs static stiffness
L	foundation length
m^*	equivalent mass
m_{str}	single degree of freedom oscillator mass

n	number of storeys
N	number of seismic record
P	probability of failure
p_j	weighting coefficient of the j-th part of the SFS system
p_a	atmospheric pressure
q	deviator stress
r	rigid circular foundation of radius
R^2	coefficient of determination
s	masonry thickness
s'	centre of the failure Mohr-Coulomb circles
$S_a(T^*)$	spectral acceleration at the fundamental period
$S_{a,avg}$	mean geometric spectral acceleration
$S_d(T^*)$	spectral displacement at the fundamental period
t	radius of the failure Mohr-Coulomb circles
t	time
T^*	soil-foundation-structure period
T^*_{EXP}	experimental period
T^*_{NUM}	numerical period
T^*_{RO}	replacement oscillator with dynamic impedance period
T_0	fixed base period
t_1	thickness of the shallow cover layer
T_{1d}	EC8-conforming fundamental period
t_2	thickness of the in-depth layer
t_l	input noise duration
U_{max}	maximum structure displacements
U_θ	displacement induced in the structure by the rotation of the foundation
U_{res}	residual displacements
U_{str}	flexural displacement of the soil-foundation-structural system

u_u	translational displacement of the foundation
V_P	compression wave velocities
V_P	NIST equivalent shear wave velocity
V_S	shear wave velocity
$V_{S,eq}$	equivalent shear wave velocity
$V_{S,30}$	EC8-conforming shear wave velocity
α, β	frequency dependent coefficients
α, β	damping ratio regression model parameters
α, β	σ -based regression model parameters
α_θ	rotational dimensionless factor
α_u	translational dimensionless factor
β_θ	rotational dimensionless factor
β_v	translational dimensionless factor
β	logarithmic standard deviation of the seismic demand model
δ	logarithmic decrement
δ	relative mass density
Δu_{str}	relative flexural displacements
ε_a	axial strain
ε_v	volumetric strain
ϕ	friction angle
ϕ_f	first-mode displacement
ϕ'	effective friction angle
Φ	lognormal cumulative distribution function
γ	unit weight
γ	shear strain
η	median of the seismic demand model
λ	wavelength
μ_{12}	soil impedance ratio

μ_s	friction coefficient
μ_β	mean value of β
μ_{R^2}	mean value of R^2
μ_{RF}	mean value of R_F
ν	Poisson's Ratio
θ	foundation rotation
ρ	mass density
ρ_{eq}	equivalent mass density
σ	stiffness ratio between the structure and the foundation soil
σ'_{v0}	vertical effective lithostatic stress
σ_0	compressive stress under static load
σ_1, σ_3	principal maximum and minimum stresses
σ_c	compressive strength
σ_{eq}	equivalent soil-structure stiffness parameter
σ_t	tensile strength
ω_0	fixed base uncoupled circular natural frequency
ω_θ	rotational uncoupled circular natural frequency
ω_u	translational uncoupled circular natural frequency
ξ	small strain damping ratio
ξ^*	Equivalent damping ratio
ξ_θ	rotational viscous damping
ξ_{rad}^*	SFS radiation damping ratio
ξ_{soil}	hysteretic soil damping ratio
ξ_{str}	structural damping ratio
ξ_{str}^*	soil-foundation-structure damping ratio
ξ_u	translational viscous damping

LIST OF ABBREVIATION

<i>AF</i>	amplification factor
<i>CID</i>	consolidated-drained triaxial compression test
<i>CTS</i>	cyclic torsional shear test
<i>DL</i>	damage level
<i>EDP</i>	engineering demand parameter
<i>FB</i>	fixed base
<i>FDM</i>	finite difference model
<i>FEM</i>	finite element model
<i>FFM</i>	free field motion
<i>FFT</i>	fast Fourier transform
<i>FIM</i>	foundation input motion
<i>FoS</i>	factor of safety
<i>HVSR</i>	horizontal/vertical spectral ratios
<i>IDA</i>	incremental dynamic analysis
<i>IDR</i>	inter-storey drift ratio
<i>IDR_{DL}</i>	inter-storey drift ratio damage level threshold
<i>IDR_u</i>	ultimate capacity inter-storey drift ratio
<i>IM</i>	intensity measure
<i>IM₅₀</i>	intensity measure at 50% of probability
<i>IP</i>	plasticity index
<i>LTHA</i>	linear time history analysis
<i>MC</i>	Mohr Coulomb criteria
<i>MIDR</i>	maximum inter-storey drift ratio
<i>MSA</i>	multiple-stripe analysis
<i>NLTHA</i>	nonlinear time history analysis

<i>OOP</i>	out of plane
<i>PGA</i>	peak ground acceleration
<i>PGD</i>	peak ground displacement
<i>PGV</i>	peak ground velocity
<i>PSDM</i>	probabilistic seismic demand models
<i>RC</i>	resonant column
<i>R_F</i>	reduction factor
<i>RIDR</i>	residual inter-storey drift
<i>RMDR</i>	residual-to-maximum drift ratio
<i>RO</i>	Replacement oscillator
<i>s.r.a.</i>	seismic response analyses
<i>SDOF</i>	single degree of freedom
<i>SFS</i>	soil-foundation-structure
<i>SSI</i>	soil-structure-interaction
<i>T</i>	Tresca criteria
<i>URM</i>	unreinforced masonry

ABSTRACT

In the recent years, due to the high vulnerability of masonry buildings, especially to local mechanisms of collapse, i.e. out of plane mechanisms, important tools have been developed to: (i) investigate the nonlinear response of masonry structure under earthquakes; (ii) analytically assess the 'seismic fragility' of such constructions in order to evaluate the expected damage. Usually, the models used for the seismic assessment consider the structure fixed at their base, neglecting the soil contribution. The interaction between soil and structure can significantly influence the seismic behaviour of masonry building and on the corresponding seismic fragility.

Based on those motivations the aim of this research study is to evaluate how the soil-structure-interaction influence the out of plane loaded masonry walls in elevation, in terms of: (i) linear dynamic properties; (ii) nonlinear behaviour and corresponding fragility; and (iii) analysis of real case studies of existing masonry buildings, at both territorial and local scale. To evaluate the influence in terms of linear properties, the numerical results of linear analyses on advanced 2D coupled soil-foundation-structure (SFS) interaction models were performed and compared with the analytical prediction based on the replacement oscillator approach. Regression models and a relative soil-structure stiffness parameter are proposed to quickly predict the frequency reduction induced by soil-structure-interaction, accounting for the presence of an embedded foundation, and a layered soil.

To evaluate the soil-structure-interaction on the nonlinear behaviour and the corresponding seismic fragility. Several archetype structures are considered, accounting for the variability in geotechnical and structural properties such as soil type, masonry type, and number of building stories. This selection reflects the most recurrent properties observed in the Italian and European built heritage. Advanced 2D coupled SFS nonlinear models are developed for each considered archetype building. A set of real records is used as input to cloud-based nonlinear time histories analyses (NLTHA), and the analysis results are used (1) to select optimal intensity measures (IMs) for the considered structural types; and (2) to generate fragility relationships for various structure-specific damage states, up to collapse. The comparison between the fragility relationships obtained for the different combinations of soil, masonry type and number of stories allows an explicit assessment of the influence of the SFS interaction on the seismic response and damage of masonry buildings.

Keywords: Historical masonry buildings; soil-structure-interaction; out of plane mechanisms; linear time history analysis; nonlinear time history analysis; fragility analysis.

I. INTRODUCTION

I.1. Framework and objectives of the study

Natural disasters over time have caused considerable damages to the built heritage, causing significant human and economic losses. According to the World Bank (IEG, 2007), the number of natural disasters has increased not only in magnitude but also in frequency. Certainly, earthquakes are one of the natural events with great impact on the world economy, particularly on the loss of life.

According to Daniell et al. (2011), a significant percentage of victims due to the strong earthquakes occurred in the period 1900-2011 was caused by the collapse of masonry buildings. In this respect, Italy is one of the European countries with the highest seismic risk relevant to buildings. This is produced on one hand by the medium-high level of seismic hazard and on the other by the high seismic vulnerability of existing buildings, as remarked even in the most recent years by destructive earthquakes that struck L'Aquila in 2009, Emilia Romagna in 2012 (Dolce and Di Bucci 2017), and Central Italy in 2016 (Di Ludovico et al. 2017; ReLuis, 2018a).

Based on the 2011 ISTAT census, 57% of the Italian building heritage consists of masonry buildings (most of them having less than four-storey), 93% of the residential buildings was constructed before the emanation of seismic codes (1987), and 58% of the masonry buildings was built more than sixty years ago. Therefore, a seismic risk assessment of masonry buildings has assumed a strategic role to reduce future earthquake losses. For this purpose, in recent years, important tools have been developed (i) to investigate nonlinear dynamic response of masonry structures under strong ground motion, and (ii) to analytically assess the 'seismic fragility' of such constructions, that is, the probability of reaching or exceeding a specified damage level given the intensity of ground shaking. The derivation of fragility models allows the assessment of the seismic vulnerability through loss/consequence functions and, ultimately, a probabilistic evaluation of seismic risk.

During an earthquake, unreinforced masonry (URM) structures may develop a complex behaviour because, depending on their construction characteristics, the load-bearing walls may be subjected to significant out-of-plane (OOP) lateral actions, resulting in local collapse mechanisms. Those phenomena usually induce a premature collapse of the structure, strongly limiting the ability to withstand seismic actions through a box-type behaviour and hence the in-plane resistance of load-bearing walls. Post-earthquake damage assessments (e.g. Augenti and Parisi 2010a; D'Ayala and Paganoni 2011; Ferreira et al. 2014; GEER 2016, 2017), numerical and experimental studies have shown that the vulnerability of existing masonry structures to OOP collapse mechanisms is particularly high in case of lacking/ineffective floor-to-wall and

wall-to-wall connections, heavy floors, and low strength-to-mass ratio of load-bearing walls, as shown by the examples in Figure I.1. These latter structural components are thus not able to resist inertia forces because of their low stiffness and strength in the out-of-plane direction. In some cases, OOP mechanisms are not simply associated with one-way vertical bending of masonry piers, delineating more complex movements related to, for instance, one-way horizontal bending of spandrels or two-way bending of walls close to building corners (D'Ayala et al. 1997; D'Ayala and Speranza 2003; Parisi and Augenti 2013).



Figure I.1 Masonry buildings damaged by OOP mechanisms in most recent Italian seismic events

Another aspect that can influence the seismic vulnerability of URM buildings is the interaction between the above-ground structure and the soil-foundation system. This is not usually considered in the seismic performance assessment of masonry buildings and vulnerability studies, which are typically carried out on fixed-base (FB) capacity models of the above-ground structure. Nonetheless, several benchmark analytical studies as well as experimental investigations have emphasised the influence of the underlying soil-foundation system on the dynamic response of the structure (e.g. Mylonakis and Gazetas 2000; Kausel 2010). More in detail, the soil-structure interaction (SSI) can produce:

- (i) a modification of the seismic input transmitted to the structure with respect to the free-field motion (kinematic interaction),
- (ii) a variation in the fundamental period and damping, influencing the seismic response of the structure (inertial interaction).

The combination of these effects can produce either beneficial or detrimental effects because the period elongation can either increase or decrease the seismic demand on

the structure (in terms of displacement, acceleration, and hence shear base force), influencing the seismic performance.

Another important SSI effect occurs under strong motion when the foundation swaying and/or rocking induce high cyclic strain levels in the surrounding soil until its yielding. The failure of the foundation soil contributes to the seismic energy dissipation, which may cause a reduction in displacement demand on structures (Faccioli et al. 1998; Shirato et al. 2008; Gazetas 2015). This has a beneficial effect on seismic performance of structures, particularly in the case of URM buildings that typically have low displacement capacity compared to other types of constructions (see experimental studies by, amongst others, Tomažević and Weiss, 2010, Augenti et al., 2011 and Kallioras et al., 2018).

To analyse the kinematic and inertial interaction, both uncoupled and coupled approaches for the modelling and analysis of soil-foundation-structure (SFS) systems have been proposed in the literature; to date, several codes of practice (e.g. NEHRP 2012) specify when and how to account for them.

In the uncoupled approaches, the kinematic and inertial interaction components are investigated separately ('sub-structure method'). By contrast, coupled approaches are the most accurate option to consider both kinematic and inertial interaction components at the same time. Usually, the foundation system of an existing masonry building is a relatively shallow beam/wall system made of masonry or, for recent constructions, other materials such as reinforced concrete. This means that the foundation stiffness is often comparable to that of the soil, resulting in a negligible kinematic interaction. Inertial interaction can be assessed through a soil-foundation-structure (SFS) system in which the dynamic impedance of the soil-foundation is simulated by a system of springs and dashpots, while the structure is modelled as a single-degree-of-freedom (SDOF) oscillator or a continuum system. In such a context, simple approaches have been proposed in the literature such as the replacement oscillator (RO) originally introduced by Veletsos and Meek (1974). Alternatively, SSI effects can be evaluated through a full dynamic analysis of a coupled SFS system that can be modelled through, for instance, the finite difference or finite element method. In this case, an adequately accurate characterization of the soil and structural system is required to obtain a realistic simulation of seismic behaviour.

All considerations above motivate the need to assess the effects of SSI on seismic performance and damage of masonry buildings, particularly to OOP failure mechanisms that frequently occur in ancient structures of historical urban centres. Thus, the aim of this work is three-fold:

- 1) to evaluate the effects of underground storeys and/or layered soil on dynamic properties of SFS systems consisting of OOP loaded masonry walls in elevation, comparing the prediction of analytical formulas based the replacement oscillator, RO, to numerical results of linear time history analysis (LTHA);

- 2) to assess SSI effects on the OOP behaviour and corresponding fragility of historical masonry buildings, based on nonlinear time history analysis (NLTHA) combined with the 'cloud analysis' approach, accounting for the variability in geotechnical and structural properties such as soil type, masonry type, and number of building storeys;
- 3) to implement numerical developments related to points (1) and (2) into the seismic assessment of real case studies of existing masonry buildings, at both territorial and local scale.

I.2. Outline of the thesis

After this introduction and before the last conclusive section - where results are summarised, and an outlook is provided - the core of the thesis consists of four chapters.

Chapter II describes the theoretical basis and modelling of soil-foundation-structure interaction, the qualitative behaviour of masonry buildings under earthquakes, and the methods for assessing seismic fragility based on nonlinear dynamic response analysis. Chapter III deals with SSI effects on the linear dynamic response of URM buildings based on parametric time history analyses of 2D interaction models reproducing transverse sections of representative SFS systems. These models considered a varying number of building storeys, assumed either the presence of an underground level or barely an embedded foundation, and accounted for variable subsoil conditions. A detailed description of the geometry, boundary conditions and material properties of the 2D SFS models, analysed through a widespread finite difference code, is first reported. Based on the analysis of models' response to a noise input in the frequency domain, the fundamental frequency and radiation damping of each SFS model are computed. Thereafter, LTHA results are compared to the simplified predictions based on the RO approach, in order to evaluate and overcome the significant limitations of the original method for assessing the seismic performance of historical masonry buildings, featured by uniformly distributed inertial mass and structural stiffness and frequently characterised by irregular underground storeys and/or foundations embedded in layered soil. An updated formulation of relative soil-structure stiffness ratio is thus proposed to evaluate whether SSI should be considered and, in such a case, to estimate the expected value of the fundamental frequency of the SFS system. In Chapter IV, SSI effects on nonlinear dynamic response and seismic fragility of URM buildings are investigated by making use of similar SFS models adopted in Chapter III, introducing nonlinear constitutive relationships for both the foundation soil and masonry structure. After a LTHA is performed for each model to evaluate the fundamental period, a set of 15 real ground motion records is selected and used as an acceleration input in NLTHA of SFS models. The seismic performance assessment

is expressed in terms of distribution of strains, displacements and accelerations throughout the SFS systems. NLTHA results are then used to develop fragility functions according to the following procedure:

- (i) selection of alternative intensity measures (IMs) for the considered structural types;
- (ii) definition of an engineering demand parameter (EDP);
- (iii) assumption of performance limit states for out-of-plane failure mechanisms;
- (iv) identification of the optimal IMs;
- (v) derivation of fragility models corresponding to increasing levels of OOP damage.

Chapter V presents the validation of the proposed methodologies and related results to real case studies in Italy. The updated simplified procedure based on the RO approach was tested to allow for a cost-effective and synthetic evaluation of the SSI effect at the scales of an urban centre as well as of a single building.

The validation at urban scale was carried out for the city of Matera, where a number of Horizontal/Vertical Spectral Ratios (HVSR) were recorded on free-field soil surface and buildings by CNR-IMAA (National Research Council of Italy - Institute of Methodologies for Environmental Analysis Tito Scalo, Potenza). In the validation study at building scale, the Pietro Capuzi school building at Visso was chosen because the structure was accurately monitored by the Italian Seismic Observatory of Structures (OSS, Italian Civil Protection Department), making available different records of the dynamic behaviour under ambient noise. Those records allowed for the comparison between the experimental periods and their analytical predictions.

In addition, the historical town of Sant'Agata de' Goti was selected as a third case study, where the effects of underground cavities on the seismic response of both the urban centre and a single historical building were investigated. To this aim, a comprehensive subsoil characterization was carried out through the integration of field and laboratory tests, leading to a detailed description of the geological cross-section of the hill where the town is settled, as well as of the SFS model. The dynamic response of both the hill and the building was evaluated through the following methods:

- (i) *free-field* analyses, in order to evaluate the effect of underground cavities on the seismic response of the hill, through both LTHA under an input noise and NLTHA under three strong reference input motions;
- (ii) SFS analyses, in order to evaluate the influence of nonlinearity on the seismic fragility of the complex soil-cavity-foundation-structure systems, through NLTHA under the same input motions of the hill.

II.SOIL-FOUNDATION-STRUCTURE INTERACTION AND BEHAVIOUR OF MASONRY BUILDINGS UNDER EARTHQUAKES

II.1. Soil-Structure Interaction: theoretical basis and modelling approaches

During an earthquake the dynamic behaviour of a structure can be significantly influenced by the interaction with the underlying soil and the foundation system (Mylonakis and Gazetas 2000; Kausel 2010). Generally, for the seismic assessment of building structures, fixed-base (FB) capacity models are adopted instead of soil-foundation-structure (SFS) in which the soil deformability is considered.

It is well known that the intensity of the seismic motion transmitted to a structure during an earthquake is influenced by earthquake source mechanism, in-depth wave propagation, site amplification and soil structure interaction (SSI) effects (Bielak 1974; Veletsos and Meek 1974; Stewart et al., 1999). The first three factors affect the so-called Free Field motion (FFM), while the SSI effects can modify the input motion transmitted to the structure and the structural response.

Two types of interaction can be observed between soil, structure and foundation:

- (i) *kinematic interaction*: due to the relative soil-foundation stiffness and the foundation embedment, the seismic motion transmitted from the foundation to the structure is modified with respect to the FFM into the so-called Foundation Input Motion (FIM) (Elsabee and Murray 1977; Kim and Stewart 2003; Conti et al., 2017);
- (ii) *inertial interaction*: the soil compliance to the structure motion produces the modification of the period and damping of the whole system, affecting the structural response in terms of displacements and/or accelerations, as well as inducing additional energy dissipation by means of wave radiation and hysteresis of soil (Gazetas 1983; Wolf 1985; Mylonakis et al., 2006; Givens et al., 2016);

In Figure II.1a and 1b, the responses of FB and SFS systems subjected to horizontal ground motion are compared each other. In the FB system, the lateral displacement on top of the structure is associated only to the structural deformation, denoted by u_{str} , being FIM and FFM coincident. Moreover, the energy associated with the oscillation of the structure is not transmitted through the foundation to the underlying soil. In the SFS system, instead, the total horizontal displacement of the structure can be expressed as the sum of three components, namely, u_{str} (i.e. soil assumed as rigid) and the others associated with swaying, u_u , and rocking oscillations, u_θ , of the base (i.e. structure assumed as rigid).

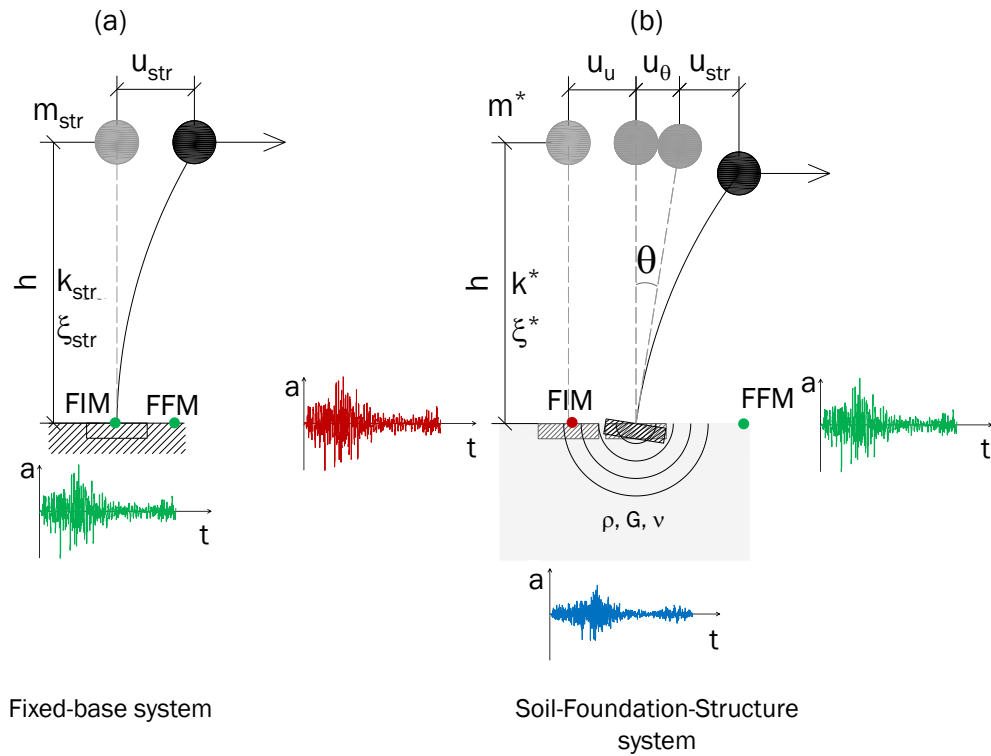


Figure II.1: Comparison between seismic responses of FB (a) and SFS (b) systems

In the case of existing masonry buildings, the foundation stiffness is often comparable to that of the soil, thus kinematic interaction can be neglected. In such hypothesis, the fundamental period increases from T_0 (FB system value) to T^* (SFS value); the structural damping ratio reduces from ξ_{str} to ξ_{str}^* , while the damping ratio of the soil-foundation system is due to both radiation phenomena, ξ_{rad} , and soil hysteresis, ξ_{soil} . This produces a total damping ratio of the SFS system $\xi^* = \xi_{str} + \xi_{rad} + \xi_{soil}$.

As shown in Figure II.2, the change in dynamic properties leads to an intensity of the seismic action transmitted to the base of the SFS system that is either higher or lower than the base shear imposed to the FB system, depending on the value of T_0 and hence, the mass-to-stiffness ratio of the above-ground structure. It follows that, for the Italian historical built heritage, where low-rise URM buildings are the most recurrent class of structures, SSI is usually expected to increase the seismic demand.

If the foundation is both embedded and stiffer with respect to the soil, the kinematic interaction cannot be neglected, since the FIM differs significantly from the FF; in other words, the foundation ‘filters’ the signal transmitted to the structure. As a result, the translational displacement, u_u , is reduced with respect to the free-field counterpart, but a higher rocking oscillation, u_θ , can be introduced (Conti et al., 2017).

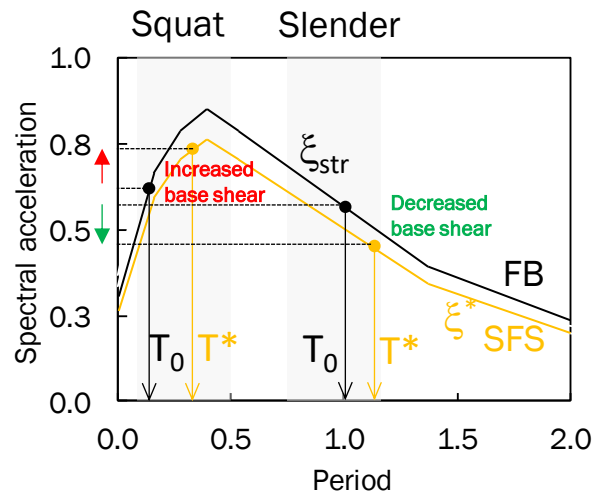


Figure II.2 Inertial SSI effects on spectral acceleration (NEHRP, 2012)

In order to account for SSI effects in seismic performance assessment, more or less refined models of soil and structure have been proposed in the literature, as depicted in Figure II.3. According to an increasing complexity level, the following alternative structural models can be adopted:

- a single-degree-of-freedom (SDOF) oscillator with mass m_{str} , height h , flexural stiffness k_{str} , and damping ratio ξ , which is characterised by a single vibration mode and, consequently, by a single natural period (Figure II.3a and 3d);
- a multi-degree-of-freedom (MDOF) oscillator with N lumped masses m_i , height h , stiffness matrix \mathbf{K} , and damping matrix \mathbf{D} , which is characterised by N vibration modes (Figure II.3b and 3e);
- a continuum model with mass density ρ , Young's Modulus E , Poisson's ratio ν , and a given shape and size, which is actually characterised by infinite vibration modes and can be discretised in accordance with a numerical technique, such as the finite element method (FEM) or finite difference method (FDM).

Regarding the soil, models with increasing complexity can be identified as follows:

- a combination of springs and dashpots with stiffness K_u , K_θ , and damping coefficients C_u , C_θ , related to the translational and rotational components of motion, respectively (Figure II.3a-b-c);
- a continuum model with mass density ρ , Young's Modulus E , Poisson's ratio ν , characterised by suitable in-depth and lateral extension as well as by reflecting or absorbing boundaries (Figure II.3d-e-f).

It should be noted that, if only horizontal components of seismic ground motion are considered, the number of stiffness and damping coefficients of the simplified soil model further increases in case of 3D systems. Indeed, their seismic response also depends on two horizontal displacements, two rotations in the vertical planes, and a torsional rotation around the vertical axis of the SFS model.

Needless to say, structure and soil properties can vary in the continuum models, depending on their degree of heterogeneity, as well as be more complex than the basic elastic parameters due to non-linear material behaviour.

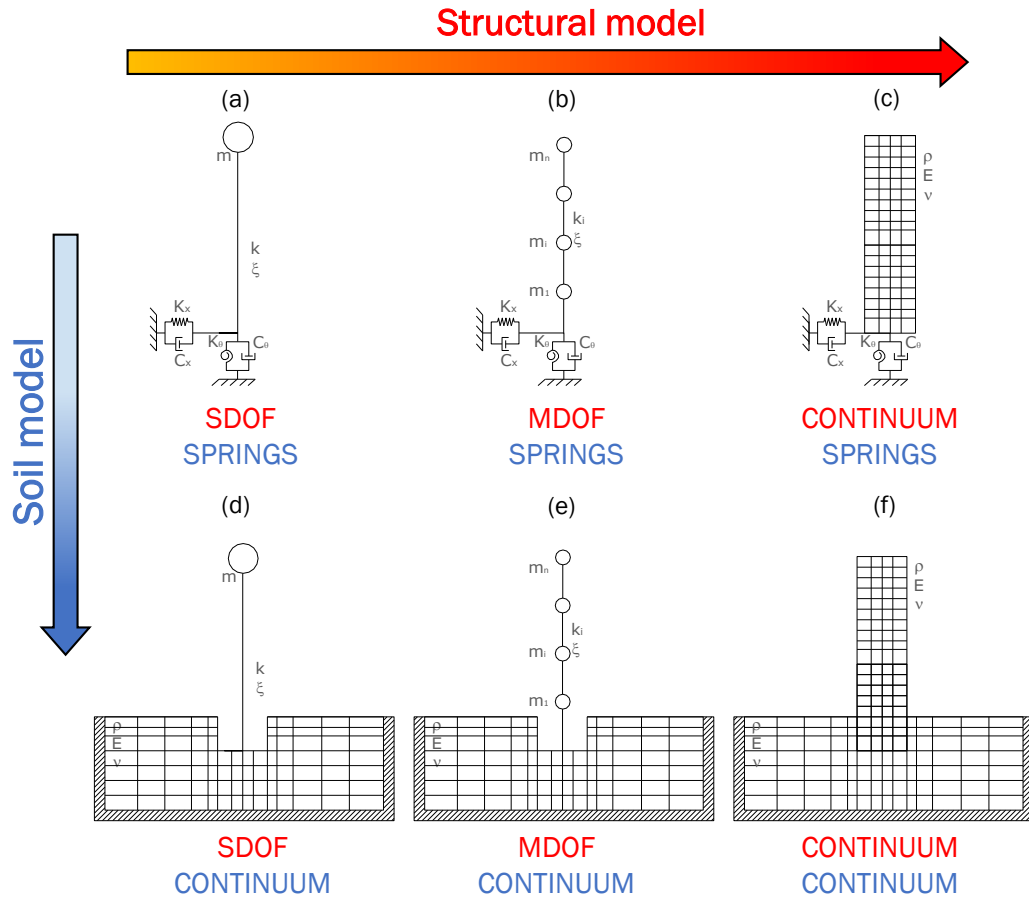


Figure II.3: SFS models with different complexity levels related to the structure and soil: SDOF oscillator, MDOF system and continuum structural model on springs and dashpots (a, b, c) and on continuum soil model (d, e, f) (de Silva 2016).

The kinematic and inertial interaction can be analysed through two different approaches depending on whether the effects are decoupled from each other or not, namely, uncoupled and coupled methods.

In the former, usually referred to as “sub-structure method”, the dynamic analysis is performed on a model in which foundation and structure are assumed to be stiff but mass-less, in order to obtain the signal at the foundation level, i.e. the foundation input motion (FIM). This latter can be therefore obtained by ‘filtering’ the FFM through suitable frequency-dependent kinematic interaction factors, $|I_u|$ and $|I_\theta|$ (Elsabee and

Murray 1977). FIM is then applied as inertia load to another model in which soil, foundation and structure are characterised by finite stiffness and mass. In a recent study, (Conti et al., 2018) also highlighted the influence of the foundation properties on the filtering of the FF motion, showing that the effect of the foundation-to-soil density ratio on the kinematic interaction factors increases with the foundation embedment and mass.

By contrast, coupled approaches such as those shown in Figure II.3d-e-f evaluate SSI effects simultaneously, by analysing full dynamic models including soil, foundation, and structure, leading to a most refined solution. The disadvantage of the coupled approach with respect to its uncoupled counterpart is not only the higher computational demand, but also the need for a rigorous calibration of all the parameters involved in the simulation. On the other hand, in the uncoupled approach a correct definition of equivalent properties is required to consider both nonlinearity and the particular characteristics of the single elements of the SFS system (i.e. irregular structure, irregular foundation shape, soil heterogeneity or irregular morphology).

Depending on the type of problem, different methods of analysis exist for the evaluation of SSI effects relevant to the SFS models described above, namely:

- (i) analytical solutions, for compliant-base SDOF systems (Figure II.3a and b);
- (ii) multi-modal response spectrum analysis for the model on springs (Figure II.3a-b-c);
- (iii) dynamic time history analysis (either linear or nonlinear) for the models in which soil and/or structure are modelled as continuum.

The simplest model for inertial interaction analysis is the compliant-base SDOF system (Figure II.4a). In this model, the structure is reduced to a SDOF on a foundation system, in which the stiffness is represented by two frequency-dependent and complex valued translational and rotational springs, coupled with as many dashpots simulating damping. Translational and rotational springs are associated with horizontal displacement u_u and rotation θ , and their frequency-dependent stiffness is respectively defined by $k_u(f^*)K_u$ and $k_\theta(f^*)K_\theta$. Similarly, translational and rotational dashpots are characterised by the damping coefficients C_u and C_θ .

Both the spring stiffnesses and the dashpot constants are derived from the foundation dynamic impedance functions \bar{K}_u and \bar{K}_θ , linking the force and the moment transmitted to the foundation to the corresponding translational and rotational motions. They are expressed by:

$$\bar{K}_u = k_u(f^*)K_u + i2\pi f^* c_u(f^*)C_u \quad (II.1)$$

$$\bar{K}_\theta = k_\theta(f^*)K_\theta + i2\pi f^* c_\theta(f^*)C_\theta \quad (II.2)$$

where:

- i is the imaginary unity;
- f^* is the fundamental frequency of the SFS system;
- $k_u(f^*)$ and $k_\theta(f^*)$ are translational and rotational dynamic stiffness coefficients; K_u and K_θ are translational and rotational components of the foundation static stiffness;
- $c_u(f^*)$ and $c_\theta(f^*)$ are the dynamic damping coefficients;
- C_u and C_θ are damping coefficients, accounting for the energy dissipated by waves spreading from the foundation (radiation damping) and soil hysteresis (material damping).

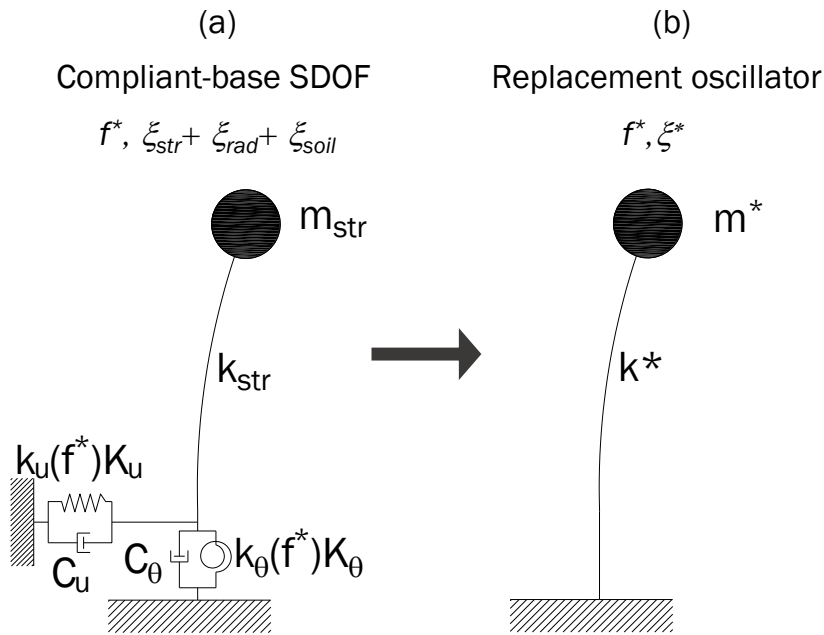


Figure II.4 Definition of replacement oscillator

To solve the compliant-base SDOF and calculate the SFS dynamic properties (T^* , ζ^*), the formulation mostly used in engineering applications was proposed by Veletsos and Meek (1974). The solution is based on the use of the replacement oscillator (RO), as shown in Figure II.4.b. The RO is a fixed-base SDOF system with equivalent mass m^* , lateral stiffness k^* and damping ratio ζ^* , properly calibrated to achieve the same dynamic behaviour of a compliant-base SDOF system.

In the Veletsos and Meek formulation, the structure is represented by a SDOF with mass m_{str} , stiffness k_{str} , damping ζ_{str} , and a rigid circular foundation of radius r , lying on a homogeneous half-space. The foundation-half space system is represented by a

combination of springs and dashpots, the former accounting for the soil flexibility and the latter simulating the energy dissipation, as usual.

The dynamic translational and rotational stiffnesses of springs, k'_u and k'_θ , and the damping coefficients of the associated dashpots are specialized as follows (Veletsos and Meek 1974):

$$k'_u = \alpha_u K; \quad c'_u = \beta_u \frac{Kr}{V_s} \quad (II.3)$$

$$k'_\theta = \alpha_\theta K; \quad c'_\theta = \beta_\theta \frac{Kr}{V_s} \quad (II.4)$$

where:

- K is the static translational-rotational stiffness of the foundation;
- r is the radius of the foundation;
- V_s is the shear wave velocity in the half-space;
- $\alpha_u, \alpha_\theta, \beta_u, \beta_\theta$ are dimensionless factors.

The foundation stiffness is defined as follows:

$$K = \frac{8}{2-\nu} Gr \quad (II.5)$$

where ν and G are respectively the Poisson's ratio and shear modulus of the half-space material. The dimensionless factors depend on ν and a dimensionless frequency parameter, used in all the impedance functions formulations, defined as follows:

$$a_0 = \frac{2\pi f^* r}{V_s} \quad (II.6)$$

The fundamental frequency of the RO can be assumed as equal to that of the compliant-base SDOF system. The total flexibility (or compliance) of this latter to dynamic loading can be taken as the sum of the flexibilities of each SFS component, that is:

$$\frac{1}{k^*} = \frac{1}{k_{str}} + \frac{1}{k_u} + \frac{h^2}{k_\theta} \quad (II.7)$$

By replacing Eq. II.7 in the well-known formula for the fundamental frequency of the SDOF:

$$f^* = \frac{1}{2\pi} \left(\sqrt{\frac{k^*}{m}} \right) \quad (II.8)$$

the fundamental frequency of the SFS system can be calculated through the following equation:

$$\frac{f^*}{f_0} = \frac{1}{\sqrt{1 + \frac{k_{str}}{k'_u} \left(1 + \frac{k'_u}{k'_\theta} h^2 \right)}} \quad (II.9)$$

Besides, the equivalent damping, ξ^* , is computed as follows:

$$\xi^* = \left(\frac{f^*}{f_0}\right)^3 \left[\xi_{str} + \frac{(2-\nu)\pi^4\delta}{2\sigma^3} \left(\frac{\beta_u}{\alpha_u^2} \frac{r^2}{h^2} + \frac{\beta_\theta}{\alpha_\theta^2} \right) \right] \quad (II.10)$$

where σ is the relative soil-structure stiffness, defined as:

$$\sigma = \frac{V_s}{f_0 h} \quad (II.11)$$

and δ is the relative mass density for the structure and soil, which is defined as:

$$\delta = \frac{m_{str}}{\rho\pi r^2 h} \quad (II.12)$$

where h is the height of the structure.

In Eq. (II.10), the first term on the right-hand side represents the structural contribution, whereas the second and third terms are the radiation damping associated with the horizontal and rotational components of the rigid-body foundation motion.

Both the expressions of frequency reduction and equivalent damping show that the response of the SFS system depends on three parameters, namely, σ , δ , ξ_{str} . In Figure II.5, f^*/f_0 and ξ^* are plotted against σ for three h/r values, related, respectively, to short ($h/r = 1$), squat ($h/r = 2$) and slender ($h/r = 5$) structures.

Given the structure properties (h , f_0) and the h/r ratio, as the soil deformability increases σ reduces, so the influence of SSI increases, causing a reduction in the fundamental frequency. The same variation in σ produces an increase in radiation damping, which has a significant impact on short structures and negligible effects on slender structures. This increase is caused by the dominance of translational modes with respect to the rotational modes on the foundation motion; indeed, the foundation rotation produces less radiation damping compared to the foundation translation (Givens et al., 2016). With reference to the displacement, Wolf (1985) observed that the slender the structure, the higher the total displacement whereas the flexural displacement decreases as σ reduces.

A recent study by Karatzia and Mylonakis (2019) has shown the limitation of the wave parameter, i.e. $1/\sigma$, as an independent variable in parametric SSI analyses, since the period variation is a stiffness-related problem, not a mass-related one. They demonstrate, with reference to a structure consisting of a cylindrical column that by substituting in the wave parameter expression, the extended structural flexural stiffness, moment of inertia (to evaluate the fixed-base frequency) and shear wave velocity expressions, the wave parameter depends on the relative mass ratio. They proposed an alternative formulation of the classical SSI equation to calculate f^*/f_0 in which all associated dimensionless groups of parameters are independent and suitable for parametric investigation.

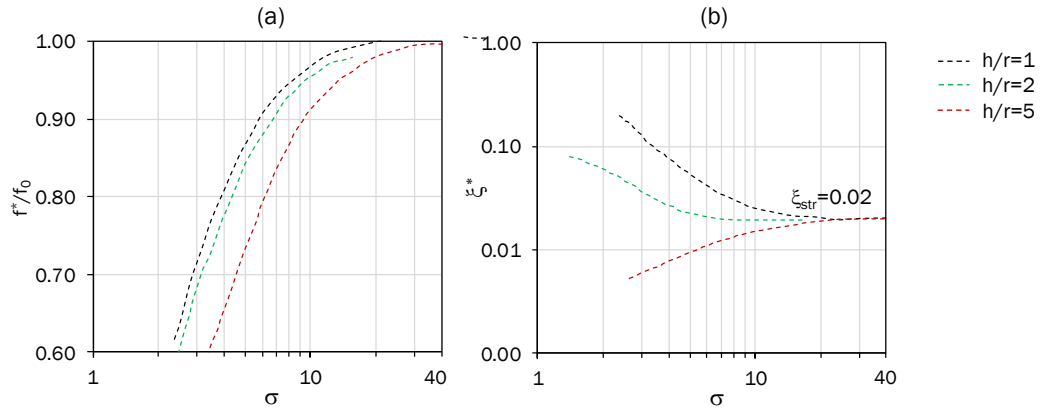


Figure II.5 Variation of (a) f^*/f_0 and (b) ξ^* with σ

A more recent solution for the evaluation of the frequency reduction (period elongation) is that proposed by Maravas et al. (2014), which is based on the compliant-base SDOF. In that study, an exact analytical solution was proposed. The difference between the formulation by Maravas et al. (2014) and that proposed by Veletsos and Meek (1974) consists in the equation used to derive the exact solution for radiation damping. Specifically, Maravas et al. (2014) used Eq. (II.7), by introducing complex-valued and frequency-dependent impedances, and obtaining the following expression:

$$\xi^* = S \left[\frac{\xi_u}{\omega_u^2 (1 + 4\xi_u^2)} + \frac{\xi_\theta}{\omega_\theta^2 (1 + 4\xi_\theta^2)} + \frac{\xi_{str}}{\omega_0^2 (1 + 4\xi_{str}^2)} \right] \quad (\text{II.13})$$

where:

- ξ_u and ξ_θ are energy loss coefficients that are similar to viscous damping ratios and equal to the ratio between the imaginary and two times the real parts of the impedance functions;
- ξ_{str} is the structural damping;
- ω_u , ω_θ and ω_0 are the uncoupled circular natural frequencies of the system, respectively under swaying oscillation of the base, rocking oscillation and oscillation of the fixed-base structure;
- S is a factor defined by Eq. (II.13) and it is used to calculate the fundamental frequency, f^* , as follows:

$$S = \left[\frac{1}{\omega_u^2 (1 + 4\xi_u^2)} + \frac{1}{\omega_\theta^2 (1 + 4\xi_\theta^2)} + \frac{1}{\omega_0^2 (1 + 4\xi_{str}^2)} \right]^{-1} \quad (\text{II.14})$$

$$f^* = \frac{S}{2\pi(1 + 4\xi^{*2})} \quad (\text{II.15})$$

The formulations proposed above consider a shallow, circular, rigid foundation resting on a homogenous linear or viscoelastic/hysteretic half-space and permits to introduce the hysteretic damping ζ_{soil} into Eqs. (II.10) and (II.13).

The sensitivity of inertial interaction to the foundation depth has been mostly investigated by modifying the springs' stiffness and damping coefficients (Gazetas 1991; Avilés and Pérez-Rocha 1996, 1998; de Silva et al. 2018). Equivalent properties are required to consider the flexibility (Pitilakis and Karatzetzou, 2015) and complex geometry of foundations, as well as the presence of a layered soil (Gazetas 1983; Stewart et al. 2003).

The above procedures can be used for both a quick estimation of SSI effects, and to calculate the seismic demand on a structure as spectral displacement and/or acceleration of the SFS with period T^* and damping ζ^* . On the other hand, some aspects of this approach represent a significant limitation in seismic performance assessment of historical masonry buildings, namely:

- (i) the transformation of a complex structure with diffused mass and stiffness into a SDOF system, and the consequent definition of the effective lumped parameters (inertia mass and flexural stiffness) associated with the fundamental mode of vibration of the fixed-base structure;
- (ii) the difficult issue of considering the presence of irregularities such as underground storeys or foundations embedded in layered soil.

It follows that for most historical masonry buildings a more refined approach should be adopted, referring to numerical simulations in which the SFS system is regarded as a coupled model. Full dynamic analyses can be carried out using FEM or FDM; both methods produce a set of algebraic equations to solve, derived in different ways. In FDM, algebraic expressions, written in terms of the field variables (e.g., stress or displacement) at discrete points in space, replace the derivative in the set of governing equations (Itasca,2011). In contrast, in FEM the field quantities (e.g., stress and displacement) vary throughout each element in a certain way, using shape functions controlled by suitable parameters. The formulation involves the adjustment of these parameters to minimize error terms or energy terms.

Based on the aims of this dissertation, FDM is preferred over FEM because the former ensures a higher accuracy level in the resolution of dynamic problems. FD models and the definition of each parameter will be discussed in Chapters III and IV, in relation to linear and nonlinear dynamic analyses, respectively.

II.2. Seismic response and damage of masonry buildings

In historical centres of many European countries, like Italy, the most widespread structural typology is that of URM buildings, which are composed of several load-bearing masonry walls with relatively flexible floor diaphragms (Magenes and Calvi 1997). Such buildings are characterised by a huge variety of materials, geometric shapes in plan and elevation, wall sections and construction details, according to the local tradition and depending on the historical period in which they were manufactured. It is well known that masonry is a composite material, made of units (i.e. bricks, blocks or stones) and joints (with or without mortar). Masonry units are referred to as stones if they are made of natural material (e.g. limestone, tuff), whereas bricks and blocks are typically of artificial nature (e.g. fired clay bricks, adobe bricks, cement blocks). Joints are generally filled with air, hydraulic, hybrid, or even mud mortar, the latter being the case of adobe masonry. With respect to other materials (e.g. steel, fibre-reinforced polymers) but similarly to normal concrete, the ratio between the tensile and compressive strength of the unreinforced masonry is very low (approximately ranging between 0.05 and 0.1) due to weak mechanical properties of the mortar and low unit-mortar bond performance.

In the past, URM structures were designed according to some rules-of-thumb to ensure stability to gravity loads through the self-weight of horizontal and vertical components (e.g. vaults and walls), neglecting the effects of seismic loading. Based on the examination of existing masonry buildings (e.g. data acquisition for buildings without structural failures), treatises of the XIX century, such as those by Rondelet and Curoni (Augenti and Parisi, 2019), empirically proposed the thickness of the wall section, s , to be sized mainly depending on the following building features:

- the number of stories, n , following the empirical equation (Augenti and Parisi 2019):

$$s = 0.45 + 0.12n \quad (\text{II.16})$$

- the diaphragms typology: horizontal like one-way joist systems composed of steel I-beams and perforated flat bricks, traditional wooden floors, or a system of vaults.

Nonetheless, the wall section morphology was defined on the basis of building techniques and the common type of material locally available at the construction site. For example, in the case of the Italian historical centres, three wall textures can be assumed representative of the masonry walls (De Felice 2011): (i) rubble, (ii) roughly squared, (iii) cut stones. Besides, three types of masonry units can be identified for North, Central and South Italy, respectively clay bricks, limestones, and tuff stones.

As described in Section II.1, the consideration of the foundation system is of paramount importance to better understand the dynamic response of the structure. Historical masonry buildings are frequently characterised by irregular underground

storeys or foundations embedded in layered soil. Shallow masonry foundations were generally adopted by deepening and widening the load-bearing walls below the ground floor. In most cases, an embedment of few meters was deemed sufficient to ensure building safety against gravity loads, so an underground floor with the function of crawl space or cellar to store food was built.

The damages observed after strong earthquakes have highlighted the high vulnerability of historical masonry buildings, mostly caused by poor quality of masonry, irregular distribution of mass and stiffness, weak connections between orthogonal walls as well as between walls and horizontal diaphragms, flexible horizontal diaphragms, and absence of seismic requirements at the time of the construction.

Under seismic loading, the URM building exhibits a complex behaviour, depending on whether the local response of one or more load-bearing walls prevails on the global response. According to the literature (see e.g. Giuffrè, 1993) and knowledge provided through post-earthquake damage inspections, two types of failure mechanisms, strictly related to the type of behaviour, can be identified:

- *first-mode mechanisms*, associated with flexural or overturning behaviours (out-of-plane response), such as the vertical overturning and corner failure shown in Figure II.6a;
- *second-mode mechanisms*, associated with in-plane response of masonry walls that may fail in shear or flexure, as shown in Figure II.6b.



Figure II.6: Failure mechanisms of two buildings damaged by the 2016 Central Italy seismic sequence: (a) out-of-plane failures (Camerino, 2018), (b) in-plane failures (Visso, 2018)

Several laboratory tests and post-earthquake reconnaissance studies (e.g. Augenti & Parisi, 2010) have shown that three alternative failure modes can occur in a wall subjected to in-plane lateral loading, that is:

- flexural (or rocking) failure, which consists of the formation of horizontal tensile cracks (cracking) at low-to-moderate levels of lateral loading, followed by compressive cracks (crushing) at opposite toes of the most stressed cross sections (Figure II.7a);
- shear failure: typical of squat panels or panels subjected to medium-high axial load; increasing the horizontal actions, two types of cracks are formed in the sections in which the shear strength is attained: (i) diagonal cracks (Figure II.7d), develop along the longitudinal plane, involving the blocks, (ii) stepwise (Figure II.7e) and/or horizontal cracks (Figure II.7f) which follow the path of the joints (sliding).

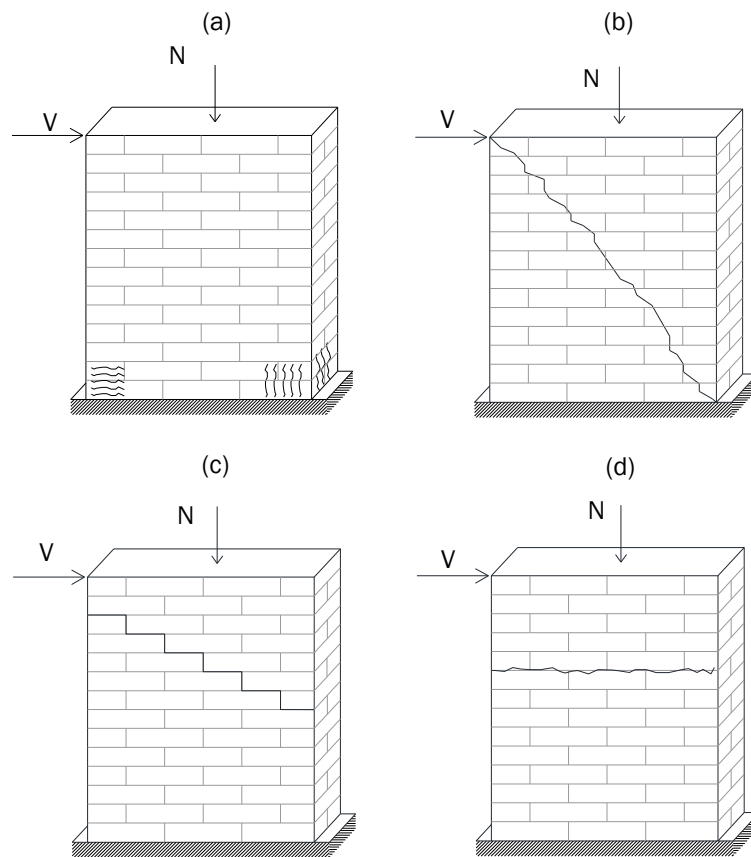


Figure II.7: In-plane failure mechanisms of URM walls: (a) tensile cracking and toe crushing (flexural failure mode); shear failure associated with (b) diagonal tension, (c) stepwise shear sliding and (d) bed-joint shear sliding

OOP damage mechanisms are the source of the most recurrent types of local collapse observed during post-earthquake damage inspections (e.g., Augenti and Parisi, 2010; Bruneau, 1994; D'Ayala and Paganoni, 2011; D'Ayala and Speranza, 2003; Penna et al., 2014; Sorrentino et al., 2014). Such failures typically occur in the case of, for instance, free-standing elements (e.g. parapets, tympanums, statues), masonry walls made of poor-quality masonry, and walls with lacking/ineffective connections to transverse walls or floors. For these types of elements, the seismic ground motion produces significant OOP excitations, resulting into a failure mechanism that is mainly controlled by the geometry (slenderness, type of constraint) (Lagomarsino, 2015). Indeed, a typical mechanism under seismic loading is the formation of one or more pseudo-rigid macro-blocks in the building structure, which reach collapse due to the loss of stability or rocking/overturning of a unique block.

Assuming a masonry element with no tensile strength, the pseudo-static equilibrium is reached if the line of thrust lies inside the element. Under seismic loading, the line of thrust can reach the outer surface, causing the formation of a hinge and the fragmentation of the original element into two blocks that experience a relative rotation with respect to each other. If two or more hinges develop, a kinematic mechanism is activated, and the equilibrium limit state is lost.

In the literature, different approaches for seismic assessment of URM buildings against local collapse mechanisms have been proposed and are classified as follows: (i) forced-based approach; (ii) displacement-based approach.

The force-based approach consists of the application of the limit equilibrium analysis through the kinematic theorem. Given a failure mechanism, the minimum load multiplier of horizontal forces (taken as a fraction of gravity loads) is calculated according to the virtual work equation, allowing the evaluation of the acceleration capacity (available resistance) to be compared with the acceleration demand (required resistance).

The displacement-based approach also relies upon limit equilibrium analysis, but it follows the progressive degradation of lateral resistance (or horizontal load multiplier) under increasing control displacement. The displacement-based approach is thus a large-displacement analysis that actually allows the whole failure mechanism to be simulated from its activation to the total loss of stability. The importance of displacement-based analysis has been demonstrated by different studies (Doherty et al. 2002; Lam et al. 2003; Derakhshan et al. 2013; Lagomarsino 2015), which have highlighted that URM walls subjected to dynamic loading can resist accelerations higher than those corresponding to their static strength. This is motivated by the fact that URM walls behave as rigid bodies subjected to rocking, also developing energy dissipation at location of crushing toes. Besides, cracks can develop even under low-intensity earthquakes, so the survivability of URM walls strongly depends on acceptable levels of displacement capacity.

The aforementioned studies have proposed different displacement-based approaches, which are based on a capacity curve in the form of force-displacement relationship (Figure II.8) that is modified with respect to that of a rigid body (Housner 1963) to better fit the real performance. To describe the OOP behaviour, Housner (1963) proposed a model in which the horizontal displacements occur when rocking is activated (dashed line in Figure II.8). Nevertheless, due to the masonry deformability and the progressive formation of a hinge (the eccentricity of the resulting forces is greater than the middle third), the masonry follows an initial elastic branch until the rocking is activated. Then, the OOP behaviour of the URM wall is described by a descending branch of the capacity curve, which is quite similar to that of a rigid body as the dynamic behaviour is mainly controlled by the geometric nonlinearity of the system (red line in Figure II.8). Based on this approach, Lagomarsino (2015) proposed the performance levels for the assessment of rocking masonry structures. Specifically, the following damage levels (DLs) were proposed (Figure II.8):

- DL1 corresponding to the elastic limit of the initial branch of the bi-linear model;
- DL2 corresponding to the activation of the rocking (obtained by the intersection between the initial branch and that provided by incremental kinematic analysis);
- DL3 corresponding to a post-peak strength degradation (provided that important connections do not fail):

$$d_{DL2} \leq d_{DL3} = 0.25d_0 \quad (\text{II.17})$$

where d_0 is the displacement at which OOP load capacity vanishes;

- DL4 corresponding to the near collapse due to the overturning:

$$d_{DL4} = 0.4d_0 \quad (\text{II.18})$$

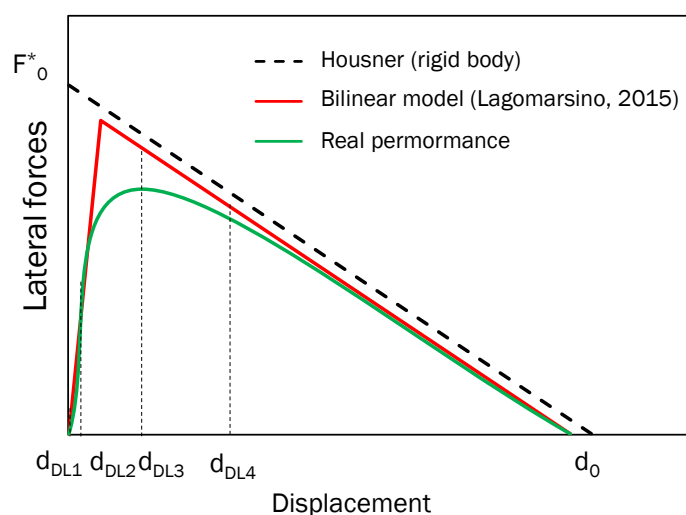


Figure II.8: Wall out of plane behaviour

It is noted that the definition of such DLs plays a key role in the derivation of fragility curves for probabilistic vulnerability assessment, as discussed in Section II.3 and implemented in Chapter IV. Indeed, performance levels must be defined to set proper thresholds for the engineering demand parameter. In this dissertation, the DLs proposed by Lagomarsino (2015) will be assumed.

II.3. Methods for seismic fragility analysis

Seismic fragility analysis is an essential step in probabilistic seismic risk assessment of URM buildings, because it allows evaluating the probability of the structure to exceed a prescribed performance limit state given an intensity measure of the seismic event. The cumulative distribution function of the performance limit state is defined as 'fragility function'. Porter (2019) defines the fragility function as "*the mathematical function that expresses the probability that some undesirable events (an element reaches a defined limit state) occurs as a function of some measure of environmental excitation (a measure of acceleration, displacement in an earthquake)*". Based on this definition, with reference to a structure, the limit state is represented in terms of one or more engineering demand parameters (EDPs), whereas the magnitude of the environmental excitation is described through a scalar or vector-valued intensity measure (IM). Thus, the relationship between EDP and IM significantly influences the fragility function.

To evaluate the EDP-IM relationship, different probabilistic seismic demand models (PSDMs) have been proposed in the literature: each one of them corresponds to a nonlinear time history analysis (NLTHA) procedure based on a real or artificial ground motion.

Three main PSDMs can be identified: (i) multiple-stripe analysis (MSA); (ii) incremental dynamic analysis (IDA); and (iii) cloud analysis. All these procedures can be used to determine the median (or mean) relationship between EDP and IM, and an associated measure of uncertainty (Mackie and Stojadinovic 2005).

The main difference between the three above-mentioned procedures is the selected set of ground motions, which must cover a wide range of intensity measures in order to describe the structural behaviour until the collapse.

MSA (Baker, 2007; Jalayer and Cornell, 2009) is characterised by several stripe response analyses (Figure II.9a) performed at the same IM value. For each stripe analysis, the set of ground motions is properly scaled to obtain the corresponding IM (i.e. spectral acceleration at the fundamental period of the analysed structure). The counted median and standard deviation of EDP are evaluated along the single stripe, by defining the 16th, 50th and 84th percentiles curves.

In the IDA method (Vamvatsikos and Cornell, 2002), instead, different curves describing the structural dynamic response (blue curves in Figure II.9b) are obtained

by progressively scaling to different IM values the intensity of each ground motion. In this procedure, the counted median and standard deviation are still evaluated by defining the 16th, 50th and 84th percentiles curves.

The last procedure is the cloud analysis (Jalayer, 2003; Jalayer et al., 2015) in which the selected set of ground motions is un-scaled and characterised by different spectral acceleration content (Baker and Cornell 2006). Consequently, the seismic demand is represented by a “cloud” of points (see Figure II.9c) in the EDP-IM space.

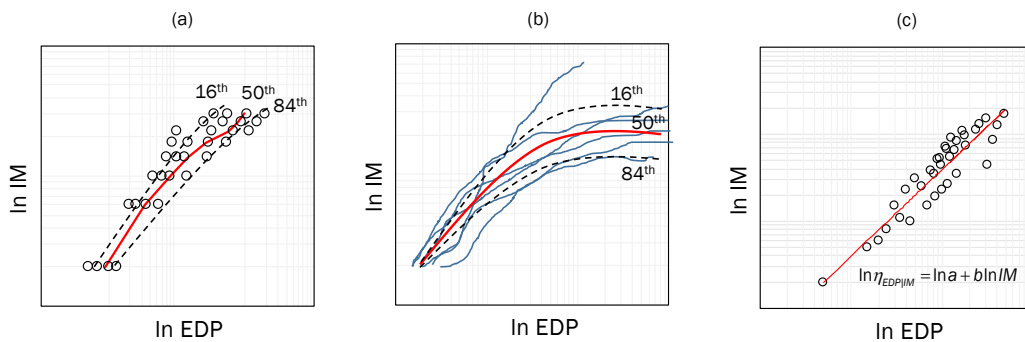


Figure II.9: PSDM procedures: (a) multiple-stripe, (b) incremental dynamic, (c) cloud analysis

In the study by Jalayer et al. (2015), the authors compared the results of IDA and cloud analysis, highlighting the huge sensitivity of the cloud method to the selection and number of ground motions to use in the NLTHA with respect to IDA. Based on a comparison of analysis results in the EDP-IM space, it appears that the selection of ground motions should be carried out so that data points which exceed the limit state threshold can be visualised.

If the ground motions set is adequately selected, the cloud method represents a valid alternative procedure to the IDA and MSA, also ensuring the following advantages: (i) lower number of NLTHAs to run, (ii) ease of application to general cases due to the linearity of the EDP-IM relationship (i.e. to perform parametric analysis), and (iii) the use of an optimal IM reduces the dependence from hazard parameters such as magnitude and distance.

Each PSDM is based on different steps (Mackie and Stojadinović, 2005):

- 1) select the ground motions set;
- 2) model the selected structure (i.e. through FD model);
- 3) run NLTHA;
- 4) estimate $\eta_{EDP|IM}$ and $\sigma_{\ln(EDP)|IM}$, which are respectively the conditional median and standard deviation of the natural logarithm of the seismic demand parameter.

For MSA and IDA, the statistical parameters are evaluated from the 16th, 50th and 84th percentile curves (see Jalayer, 2003, Jalayer and Cornell, 2007). In the cloud method, instead, the statistical parameters are obtained by fitting the “cloud” of points in Figure II.9c with a power function predicting the median EDP for a given value of IM, by the following expression in the arithmetical space:

$$\eta_{EDP|IM} = aIM^b \quad (II.19)$$

or in the logarithmic space as follows:

$$\ln \eta_{EDP|IM} = \ln a + b \ln IM \quad (II.20)$$

In the above equations, a and b are the parameters of the linear regression model, and the logarithmic standard deviation $\beta_{EDP|IM} = \sigma_{\ln(EDP)|IM}$, assumed to be constant in the IMs range (hypothesis of homoscedasticity), is equal to (Jalayer, 2003):

$$\beta_{EDP|IM} = \sqrt{\frac{\sum_{i=1}^N [\ln(edp_i) - \ln(aim_i^b)]^2}{N-2}} \quad (II.21)$$

where: edp_i and im_i are respectively the EDP obtained from NLTHA under the i -th ground motion represented by IM; and N is the number of seismic input motions. Thus, the value of $\beta_{EDP|IM}$ can be used to estimate the dispersion of the data with respect to the linear regression, in order to choose the optimal IM (see Section IV.2.2). Eq. (II.19) can be rewritten in the natural logarithmic plane because the EDP is assumed to be conditionally lognormally distributed upon the values of IMs.

For the aim of this dissertation (see Chapter I), the structural fragility functions are derived through the cloud method, so three parameters (i.e. $\ln a$, b and β) of the fragility model are estimated. The fragility function describes the lognormal cumulative distribution function (Φ) of exceeding a DL for a given IM (Porter 2019):

$$P[EDP > EDP_{DL} | IM = im] = \Phi\left(\frac{\ln(IM / \eta_{DL})}{\beta_{DL}}\right) \quad (II.22)$$

where: EDP_{DL} is the EDP threshold corresponding to the prescribed damage level; η_{DL} is the median capacity of the asset to resist the damage level; and β_{DL} is the logarithmic standard deviation of the capacity of the asset to resist the damage level.

The derivation of numerical fragility relationships is usually carried out by considering a fixed-base structure (Couto et al., 2020; Minas & Galasso, 2019; Rota et al., 2010; Simões et al., 2019; Simões et al., 2020) and neglecting the soil-foundation-structure (SFS) interaction, the effects of which can be beneficial or detrimental, as discussed in Section II.1. Several recent studies (Khosravikia et al., 2018; Cavalieri et al., 2020; de

Silva, 2020; Petridis and Pitilakis, 2020) have highlighted the importance of taking into account the SFS interaction mechanisms.

Khosravikia et al., (2018) have studied the role of SSI on the seismic losses by investigating the seismic response of an uncoupled system (similar to Figure II.3a) by varying the number of storeys and the foundation configuration in order to define two groups of structures: stiff and flexible systems lying on three soil categories. Using Monte Carlo simulation, a wide range of ground motions was accounted for. Analysis results showed that SSI is beneficial in the case of structures on very deformable soils regardless of their slenderness ratio and the foundation embedment, mitigating losses with an effectiveness that increases with the structure height. Conversely, in the case of deformable soils, SSI can lead to detrimental effects, resulting in an increase of seismic losses.

Petridis and Pitilakis (2020) have investigated both the influence of SSI and nonlinear soil behaviour on the seismic fragility of reinforced concrete (RC) structures, varying the number of storeys and the soil conditions (described in terms of shear wave velocity, cohesion and mass density). The structures were modelled using RC moment resisting frames whereas the foundation system, in order to account the inertial effects, was modelled both as beam on nonlinear Winkler foundation (BNWF) and as a system of elastic springs and dashpots. Fragility functions were derived using IDA, showing that the nonlinear behaviour of the soil during the seismic motion influences significantly the vulnerability of the SFS system with respect to the SSI effects only. Such an effect was more evident for the soft soil profile.

Few researches have produced fragility curves for a wide range of soils and building models (usually on RC structures). This knowledge gap is mostly due to the high computational demand and modelling effort, which are usually tolerated in case of specific studies. For this reason, Petridis and Pitilakis (2020) proposed a method to modify the existing fragility curves for FB structures to take into account not only SSI effects but also soil nonlinearity in large-scale risk assessment. The proposed fragility modifiers were obtained as ratios between the median values of the SFS system and FB system, to be multiplied by the median value of the FB fragility curve for each DL.

Based on the above observations and research studies, the role of SSI in the seismic performance of a building is clearly significant. Due the large computational and modelling effort, it is necessary to provide simpler tools to account for SSI effects, not only in terms of variation of dynamic response parameters, but also in terms of seismic fragility of masonry buildings founded on deformable soils. As above shown, very few studies are available on coupled models for such a kind of SFS systems. This issue is addressed in the following sections, in the attempt to investigate the effects of soil-foundation-structure interaction on both linear (Chapter III) and nonlinear dynamic response, as well as on seismic fragility (Chapter IV), of masonry buildings typical of the Italian peninsula.

III.EFFECTS OF SFS INTERACTION ON LINEAR DYNAMIC RESPONSE OF MASONRY BUILDINGS

Most simplified analytical approaches proposed in the literature or suggested by codes of practice are used for a quick estimation of the fundamental frequency variation (f^*/f_0) and the amount of radiation damping induced by dynamic SFS interaction. The accuracy of existing closed-form solutions may be limited because they were derived through SDOF structural models with shallow rigid foundation placed on a homogeneous, linear elastic half-space. Equivalent parameters should be calibrated to apply the analytical formulations for complex soil-foundation configurations, which are rather recurrent in the Italian and European built heritage. To this aim, the effectiveness of those formulations in capturing the dynamic out-of-plane response of single load-bearing walls within URM buildings – which may have either a shallow foundation or an underground storey embedded in layered soil – needs to be investigated. The methodology used in this thesis is summarised in the flowchart in Figure III.1. Based on the analytical solutions for homogeneous soil, three regression models corresponding to as many h/b ratios were obtained. Being the results of the analytical predictions significantly different with respect to those of the numerical predictions, an equivalence criterion was calibrated to update the soil-structure stiffness ratio, in order to more accurately evaluate f^*/f_0 .

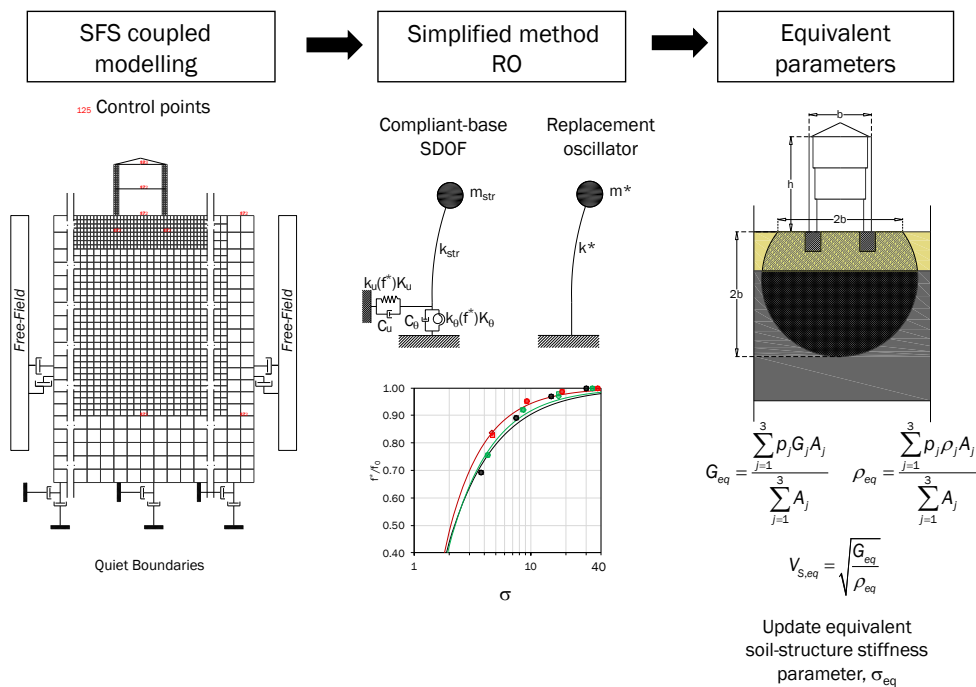


Figure III.1 Flowchart of the methodology adopted in this work

III.1. Selected case studies and capacity models

A parametric analysis was performed in order to assess the modification of periods and damping ratios of masonry structures, due to SSI. Some parameters which control the soil-structure interaction were varied, i.e. configuration of building basements (embedded “floating” foundation and underground floor), soil shear wave velocity profile of layered, structural height.

The geometrical configuration considered for the 2D FD analyses (Piro et al. 2020), is shown in Figure III.2, is the transverse section of an historical masonry building (Piro et al. 2017; Vuoto et al. 2018) (Chapter V.3.2), the latter being representative of recurrent constructions located in the Euro-Mediterranean region (see D’Ayala and Speranza, 2003; Augenti and Parisi, 2019).

SFS systems were developed in FLAC 2D ver. 7.0 (Itasca, 2011) according to the finite difference (FD) method. Two subsoil configurations were distinctly considered and associated with code-conforming ground types, namely, homogeneous and layered soil. This latter subsoil configuration consists of two layers, i.e. a shallow cover with thickness t_1 and an in-depth formation with thickness t_2 .

Two configurations of building basements were also adopted, as follows:

- (i) embedded “floating” foundation with depth $D < t_1$ (Figure III.2a);
- (ii) underground storey with load bearing wall foundation, reaching a depth $D = t_1$ (Figure III.2b).

In other words, two different configurations were adopted in terms of transversal wall base connection, the first with independent embedded footings (Figure III.2a) and the second with a massive underground foundation (Figure III.2b). Therefore, a different behaviour in terms of kinematic interaction is expected between the two foundation-soil systems configurations, being that pertaining to the hypogea level characterised by a stiffer behaviour.

The seismic bedrock was simulated through an additional layer with finite thickness, which was placed below the in-depth formation and characterised by the properties of ground type A according to Eurocode 8 (EC8) (CEN 2004) and Italian Building Code (MIT 2018).

The elevation of each masonry structure consisted of two slender load-bearing walls connected to each other by single-span floor systems and a pitched roof. The thickness of the walls was reduced along the building height, leading to a fairly homogeneous distribution of vertical stresses from the ground floor to the top.

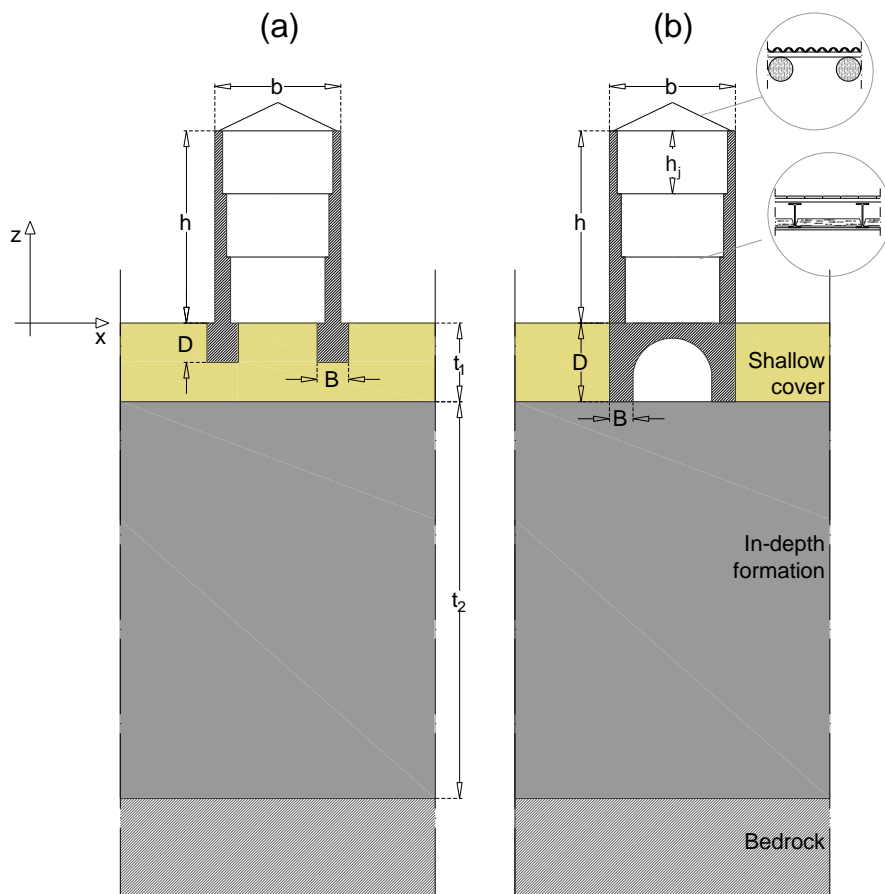


Figure III.2 SFS models with different basement configurations: (a) embedded floating foundation; (b) underground storey with load-bearing wall foundation

By contrast, inter-storey height was assumed to be constant along the building height. Floor and roof systems were modelled through one-dimensional (1D) beam elements with pinned connections to load-bearing walls. Each structural model was assumed to have variable height, h , and width, b , whereas an invariant depth of 30 m (equal to t_1+t_2 in Figure III.2), was assigned to the bedrock. As observed in many historical buildings (Augenti and Parisi, 2019), shallow foundations were assumed to be made of the same masonry type of the structure above ground. The inertia mass of the structure was defined by the size and mass density of masonry walls and floor elements. The inertia mass of the roof was incorporated in that of the upper floor element. Being the parametric study addressed to examine SSI effects well below structural and geotechnical failure states, FD models of soil, foundation and structure were analysed by assuming a linear elastic behaviour of materials. Accordingly, the damping ratios of the soil and structural materials (respectively denoted as ζ_{soil} and ζ_{str}

below) were set to 0.1%, assuming very low strain levels under low-amplitude excitations. The soil was modelled as a medium with variable sets of values for shear wave velocity, V_s , mass density, ρ , shear modulus, G , and Poisson's ratio, ν . Constant properties were used for the floors and the masonry, this latter regarded as an equivalent homogeneous material according to the macro-modelling approach (Lourenço 1996). Such hypothesis allows for assessing the macroscopic behaviour of masonry components (i.e. walls and foundations), overlooking a detailed description of local stress/strain fields within individual masonry constituents (i.e. bricks/stones and mortar joints). The macro-modelling approach significantly reduces the computational cost and was successfully validated for a number of historical masonry types (see e.g. Parisi et al., 2019).

Alternative configurations of building basement (i.e. embedded floating foundation or underground storey), soil (i.e. homogeneous or layered), as well as three variants of tuff stone masonry structure with different number of storeys (i.e. 2, 3 or 4) were generated for the SFS system. Four types of soil, denoted as A, B, C and D according to EC8 (CEN, 2004), were alternatively assigned to homogeneous subsoil models. Three combinations of shallow cover and in-depth formation were assumed in the case of layered soil, namely C-B, D-B and D-C. Preliminary analyses showed that other combinations of soil layers that did not produce significant SSI effects on the building sub-structures considered in this study.

A multi-parametric analysis was carried out by keeping constant the following properties:

- (i) thickness of shallow cover and in-depth formation, which was assumed equal to $t_1 = 5$ m and $t_2 = 25$ m, respectively;
- (ii) width and inter-storey height of the building, which were respectively set to $b = 8$ m and $h_j = 4$ m according to typical sizes detected in historical buildings (see e.g. Augenti and Parisi, 2019);
- (iii) mass density and Poisson's ratio of structural materials, i.e. masonry and homogenised (ideal) material of floor- and roof-equivalent beam elements.

The depth of the embedded foundation was set to $D = 2.5$ m, whereas the height of the underground storey was set to $D = t_1 = 5$ m. According to the inter-storey height considered, the structural systems with 2, 3 and 4 storeys above ground had aspect ratios h/b equal to 1, 1.5 and 2, respectively. The subsoil domain was assumed to have a width of 50 m and a bedrock depth of 30 m. The top of the bedrock was included in the domain through a finite layer with thickness of 5 m. The infinite extension of bedrock in depth was simulated by dashpots that were assigned to the bottom nodes and were oriented along the normal and shear directions. To minimise the model size, free-field boundary conditions were imposed to the vertical sides of soil volume, simulating an ideal horizontally layered soil profile connected to the main-grid domain through viscous dashpots. The soil was discretised into a mesh of quadrilateral

elements, the size of which was defined by satisfying the criterion by Kuhlemeyer and Lysmer (1973) for accurate modelling of shear wave propagation up to a frequency of 25 Hz. In proximity of the structure the height of the quadrilateral elements was reduced in order to approximate the dimensions (length and height) of a single brick of the masonry thickness. The latter was set based on the thickness of the historical buildings in Piro et al (2017) as shown in Figure III.3.

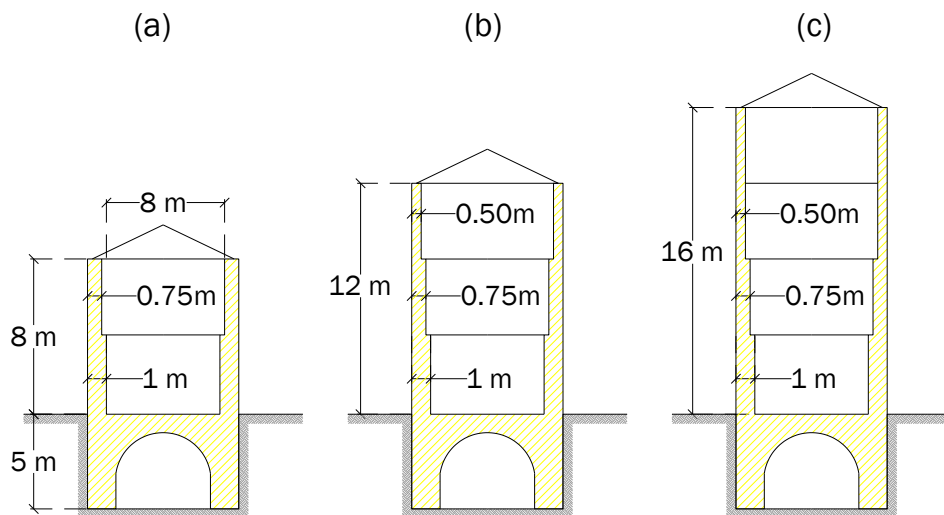


Figure III.3 Geometric properties of masonry sub-structures: (a) two (b) three and (c) four storeys

Figure III.4 shows the FD models that were developed for the case-study SFS systems by considering homogeneous (Figure III.4a-b) and layered (Figure III.4c-d) subsoil configurations and different basement configurations: underground storey (Figure III.4a-c) and embedded floating foundation (Figure III.4b-d). Shear wave velocity profiles are reported on the right-hand side of Figure III.4, with different colours and line types. Table III.1 outlines physical and mechanical properties of soils, masonry and homogeneous material of floor-equivalent beam elements. The shear wave velocity was assigned as mean value of the range related to each category defined by EC8 (CEN, 2004), The soil density and Poisson's ratio were realistically assumed as respectively increasing and decreasing with V_s and representative of gravel (A, B), dense sand (C) and loose sand (D). Mean properties of tuff stone masonry were defined according to experimental results by Augenti and Parisi (2010b). Floor and roof systems were modelled through beam elements with 1 m-wide homogenised cross section, assuming (i) floor systems to be composed of steel I-beams, tiles and poor

filling material (i.e. mixed steel-tile systems), and (ii) the pitched roof to be made of timber elements (see circles in Figure III.2b).

Table III.1. Physical and mechanical properties of materials.

Material	V_s (m/s)	ρ (kg/m ³)	E (MPa)	G (MPa)	ν
Soil type A/Bedrock	1200	2200	7608	3170	0.20
Soil type B	600	2000	1800	720	0.25
Soil type C	300	1800	421	162	0.30
Soil type D	150	1600	97	36	0.35
Tuff stone masonry	-	1600	1080	360	0.49
Homogenised floor	-	1750	30,000	12,500	0.20
Homogenised roof	-	300	1300	542	0.20

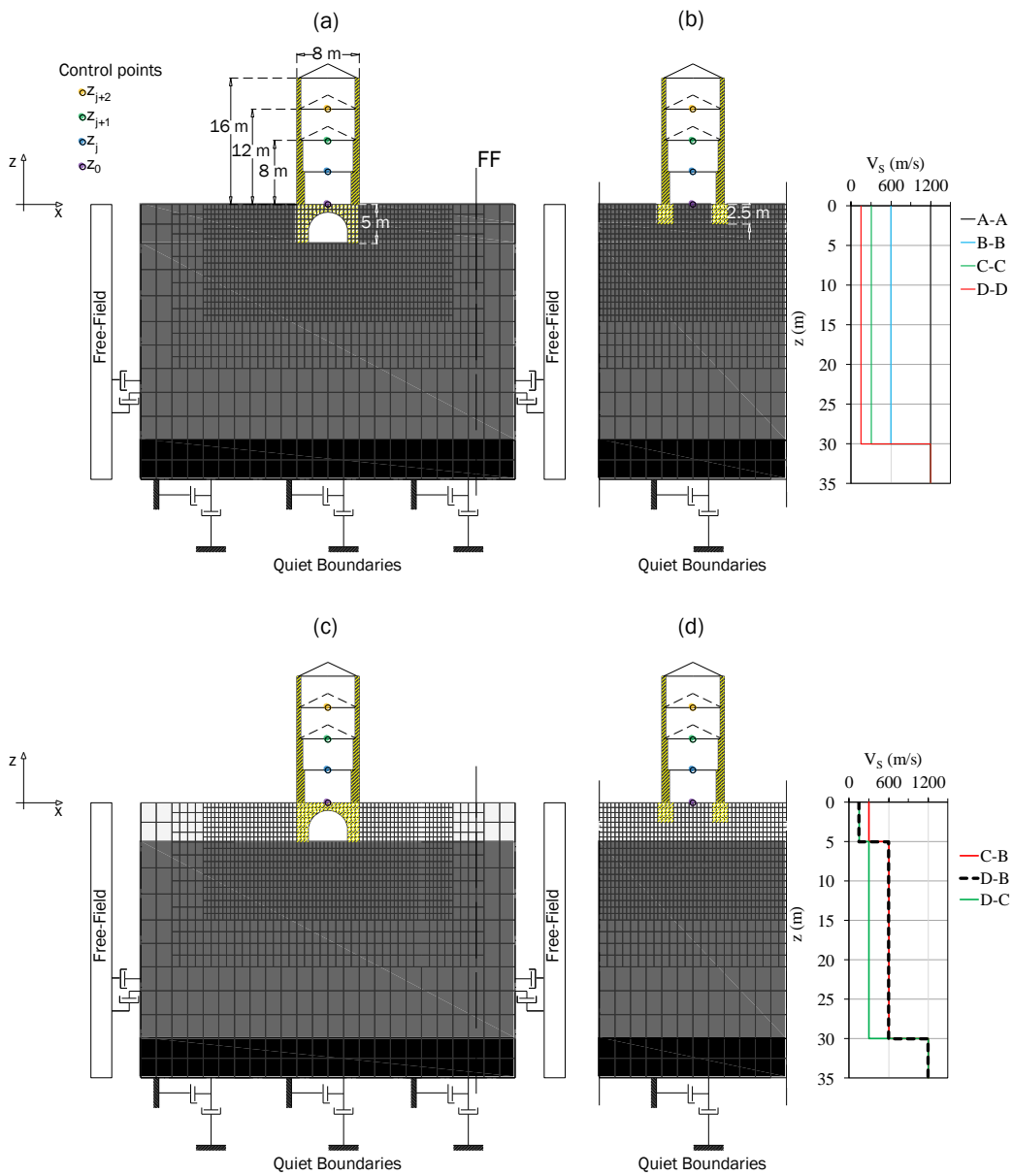


Figure III.4 SFS models of selected case studies with different foundation configuration: (a) homogeneous soil and underground storey; (b) homogeneous soil and embedded floating foundation; (c) layered soil and underground storey; (d) layered soil and embedded floating foundation (shear wave velocity profiles in m/s).

III.2. Full time history analysis of SFS interaction model

III.2.1. Fundamental frequency variation

Forty-two plane-strain dynamic analyses of SFS models were carried out in the time domain with the FD code FLAC 2D ver. 7.0 (Itasca, 2011). Initial conditions of static equilibrium under gravity loads were reproduced by simulating the following phases: (1) excavation until the foundation depth; (2) construction of the underground storey/embedded foundations; and (3) construction of the above-ground structure. Given that FLAC software is not able to perform modal analysis, the procedure developed by de Silva et al. (2018) was used to compute the fundamental frequency of each SFS system. The SFS model was subjected to a noise signal with duration $t_1 = 10$ s (Figure III.5a) and frequency range [1 Hz, 25 Hz] (Figure III.5b), which was applied as a shear stress time-history at the bedrock. The structural response was numerically monitored over 20 s to record the free-vibration behaviour of the SFS system after the end of the forced-vibration stage. Figure III.5c shows the transfer functions for each soil configuration computed as the ratio between the Fast Fourier Transform (FFT) of the *free-field* acceleration at surface and at bedrock depth along the vertical FF in Figure III.4. Dotted lines identify the fundamental frequencies f_A , f_B , f_C , f_D of homogeneous subsoil volumes associated with the selected code-conforming categories (i.e. A, B, C and D).

The fundamental frequency, f^* , of each SFS system was associated with the peaks of the FFT of the control point displacements (Figure III.4) during the free-vibration stage. Figure III.6a and b show the dynamic response of the three-storey structure ($h/b = 1.5$) with direct foundation embedded in homogeneous soils A, B, C and D, in terms of displacement time histories at different elevations from $z = 0$ to $z = 12$ m (see control points in Figure III.4) and FFT computed in the free-vibration stage, respectively. The same results are shown in Figure III.7 for the structure with underground storey. In both cases, f^* is clearly highlighted by spectral peaks, whereas dashed lines indicate the soil fundamental frequencies, denoted as f_{soil} . The comparison between the displacement time histories and FFT during the free oscillation highlights that, moving from soil type A to C, the soil fundamental frequency approaches the frequency of the structure $f_0 = 2.94$ Hz. Consequently, the peak displacement amplitudes at each elevation gradually increase due to soil-building resonance.

A slight but non-negligible reduction of fundamental frequency of the SFS system under increasing soil deformability is shown by the structure with embedded foundation (Figure III.6) (f^* from 2.94 Hz to 2.70 Hz), whereas the frequency of the structure with underground storey (Figure III.7) was found to be much less affected by the soil type (f^* from 2.94 Hz to 2.82 Hz).

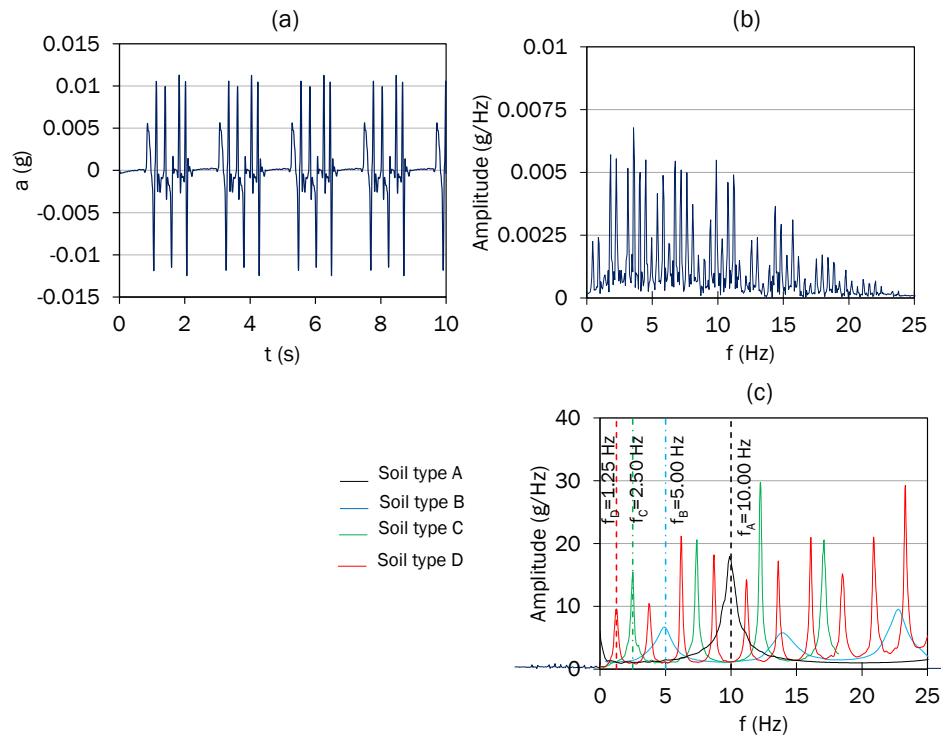


Figure III.5 Input noise for numerical dynamic identification of SFS systems: (a) accelerogram; (b) FFT and (c) soil transfer function along the FF vertical.

In this latter case, the above-ground structure tends to behave as a fixed-base system, due to the massive underground structure. In the case of homogeneous soil D, the FFT highlights two amplitude peaks: one is associated with f_{soil} , as highlighted in the enlargements of displacement time histories plotted in the last chart of Figure III.6a, where the horizontal displacement at $z = 12$ m follows the foundation motion with the same frequency; the other pertains to f^* , confirming that the dynamic behaviour is influenced by soil motion when the relative soil-structure stiffness is low (de Silva et al. 2019a; Piro et al. 2020).

For the case $h/b=1$ and $h/b=2$, both on homogeneous and layered soil, the same representation is reported in Appendix A.1.

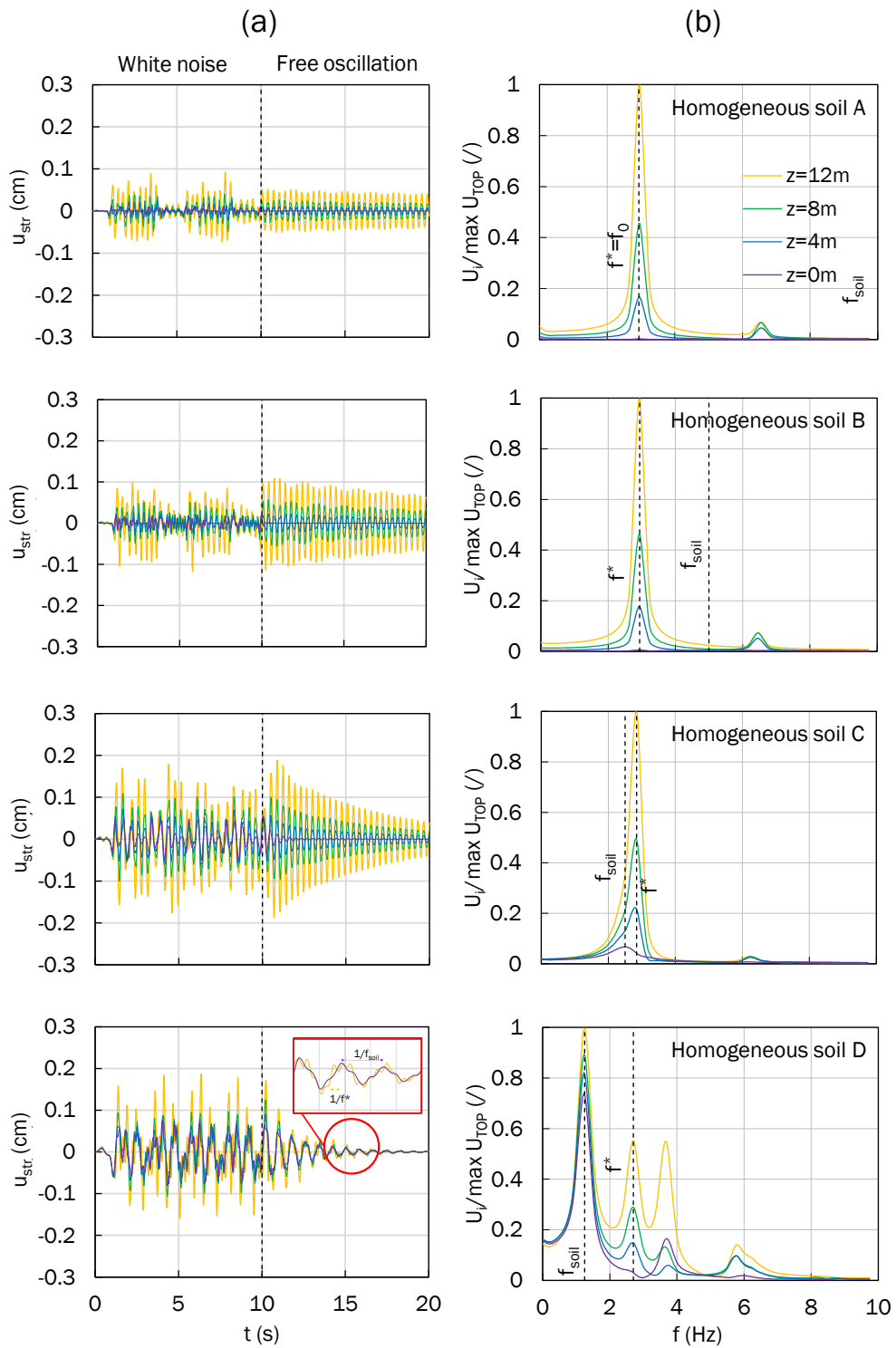


Figure III.6 Dynamic response of three-storey SFS system ($h/b = 1.5$) with embedded floating foundation and homogeneous soil (A, B, C or D): (a) time histories and (b) FFTs of horizontal displacements at different structural elevations.

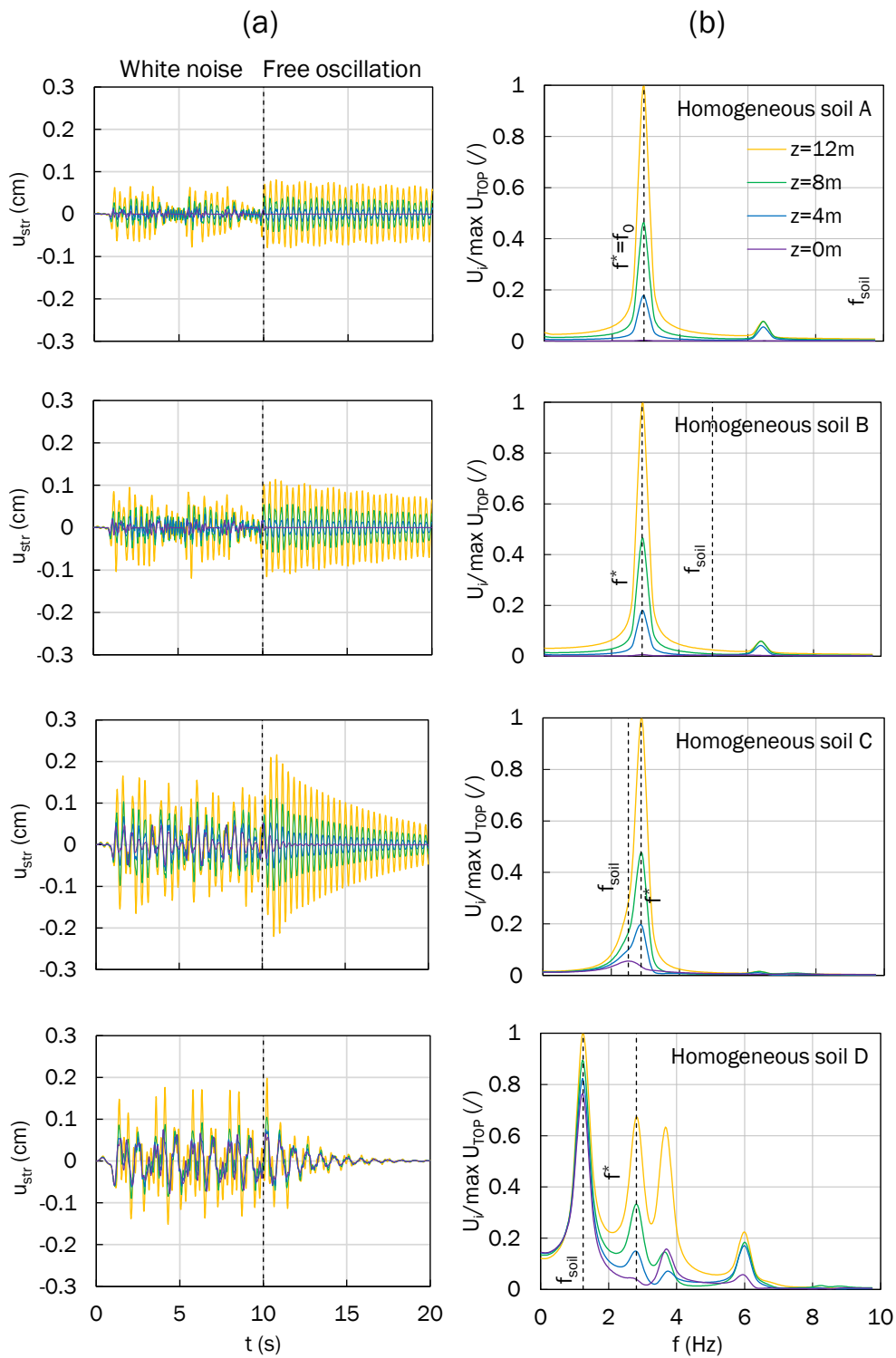


Figure III.7 Dynamic response of three-storey SFS system ($h/b = 1.5$) with underground storey and homogeneous soil (A, B, C or D): (a) time histories and (b) FFTs of horizontal displacements at different structural elevations.

Table III.2 and Table III.3 provide a summary of fundamental frequencies of the soil and SFS systems with embedded foundation and underground storey, respectively. The fundamental frequency of fixed-base structural systems, f_0 , was computed by assuming homogeneous soil type A. The numerical results confirm that the fixed-base frequency mainly depends on the aspect ratio of the above-ground structure, rather than the basement system, with an appreciable difference (5.01 vs 4.92 Hz) only for the squat structure with $h = b$. Such a difference can be ascribed to the presence of the void, which may be more influential for the squat structure.

Table III.2. Fundamental frequencies of soil and SFS systems with embedded foundation ($b/D = 3.2$)*.

Soil configuration	Soil layering	f_{soil} (Hz)	f^* (Hz)		
			$h/b=1$	$h/b=1.5$	$h/b=2$
Homogeneous	A	10.00	5.01	2.94	2.02
	B	5.00	4.92	2.94	2.02
	C	2.50	4.64	2.85	1.97
	D	1.25	3.69	2.70	1.91
Layered	C-B	4.30	4.64	2.85	2.00
	D-B	3.30	4.18	2.73	1.94
	D-C	2.50	4.15	2.64	1.94

Table III.3 Fundamental frequencies of soil and SFS systems with underground storey ($b/D=1.6$) *.

Soil configuration	Soil layering	f_{soil} (Hz)	f^* (Hz)		
			$h/b=1$	$h/b=1.5$	$h/b=2$
Homogeneous	A	10.00	4.92	2.94	2.02
	B	5.00	4.89	2.91	2.02
	C	2.50	4.83	2.88	2.02
	D	1.25	3.69	2.82	2.02
Layered	C-B	4.30	4.83	2.91	2.02
	D-B	3.30	4.70	2.88	2.02
	D-C	2.50	4.64	2.85	1.97

* Bold characters indicate fundamental frequencies of fixed-base systems (i.e. $f^* = f_0$).

As already noted by comparing Figure III.6 and Figure III.7, Table III.2 and Table III.3, the presence of the underground storey causes a lower frequency drop with respect to the case of embedded foundation. As expected, this effect tends to vanish as slenderness increases. The same trend is observed in modal shape represented in

terms of flexural displacement u_{str} , normalised with respect to the flexural displacement of the top (see Figure III.7), where the structure on different soil type, tends to follow the same modal shape of the FB. For $h > b$ and layered soil configurations, the SFS frequency for embedded foundation approaches the frequency corresponding to the same homogeneous case related to the top layer.

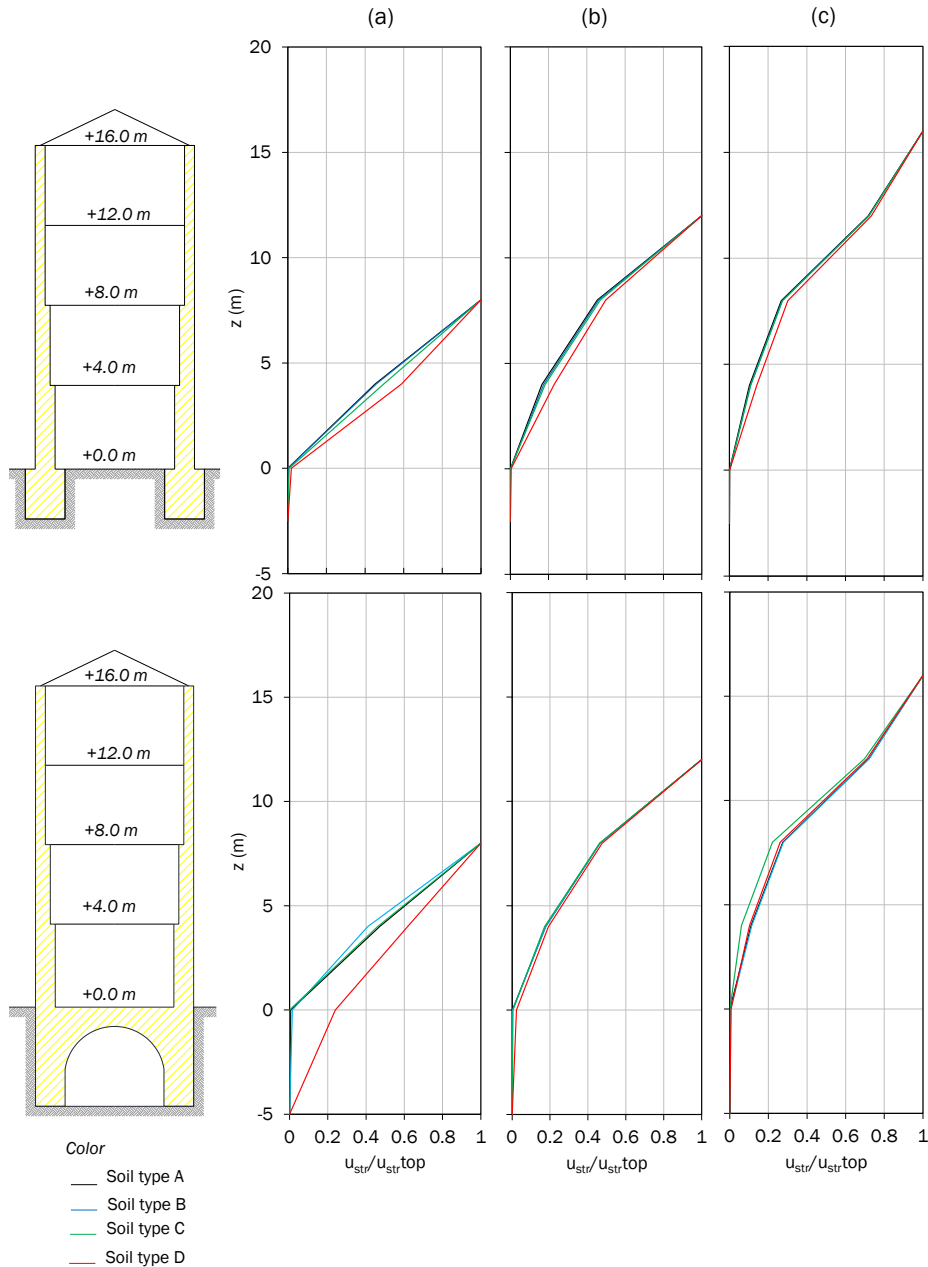


Figure III.8 First modal shape of the SFS models on homogeneous soil type: (a) $h/b=1$, (b) $h/b=1.5$, (c) $h/b=2$

Furthermore, Figure III.8, highlight how the wall, especially for the first two floors, is subjected to the same rotation. To quantify the lateral “deformation” of each storey, the inter-storey drift ratio (IDR) was computed, as the relative displacement at the j -th floor divided by and the inter-storey height of the building, based on the following equation:

$$IDR_j = \frac{u_{strj+1} - u_{strj}}{h_j} \quad (III.1)$$

The resulting values are listed in Table III.4 and Table III.5. A small difference between the IDRs corresponding to the first two floor ($z_j \div z_{j+1} = -5 \div 0$) is induced by the foundation rotation only for the case with $h/b = 1$ and underground level.

Table III.4. Inter-storey drift ratio of the SFS systems with embedded foundation

Soil layering	$z_j \div z_{j+1}$ (m)	IDR _i (%)		
		$h/b = 1$	$h/b = 1.5$	$h/b = 2$
A	-2.5÷0	0.0000	0.0000	0.0000
	0÷4	0.0098	0.0037	0.0037
	4÷8	0.0119	0.0065	0.0060
	8÷12	-	0.0122	0.0164
	12÷16	-	-	0.0103
B	-2.5÷0	0.0000	0.0001	0.0000
	0÷4	0.0051	0.0075	0.0034
	4÷8	0.0060	0.0125	0.0052
	8÷12	-	0.0235	0.0142
	12÷16	-	-	0.0089
C	-2.5÷0	0.0001	0.0001	0.0001
	0÷4	0.0025	0.0095	0.0066
	4÷8	0.0025	0.0152	0.0100
	8÷12	-	0.0280	0.0271
	12÷16	-	-	0.0169
D	-2.5÷0	0.0003	0.0001	0.0000
	0÷4	0.0061	0.0021	0.0033
	4÷8	0.0044	0.0025	0.0038
	8÷12	-	0.0047	0.0101
	12÷16	-	-	0.0063

Table III.5 Interstorey drift ratio of the SFS systems with underground storey

Soil layering	$z_j \div z_{j+1}$ (m)	IDR_i (%)		
		$h/b=1$	$h/b=1.5$	$h/b=2$
A	-5÷0	0.0001	0.0001	0.0000
	0÷4	0.0057	0.0061	0.0036
	4÷8	0.0065	0.0101	0.0054
	8÷12	-	0.0188	0.0146
	12÷16	-	-	0.0092
B	-5÷0	0.000	0.0001	0.0001
	0÷4	0.0008	0.0080	0.0034
	4÷8	0.0012	0.0131	0.0051
	8÷12	-	0.0245	0.0138
	12÷16	-	-	0.0086
C	-5÷0	0.0000	0.0002	0.0000
	0÷4	0.0008	0.0107	0.0020
	4÷8	0.0009	0.0184	0.0052
	8÷12	-	0.0342	0.0155
	12÷16	-	-	0.0098
D	-5÷0	0.0014	0.0002	0.0001
	0÷4	0.0028	0.0019	0.0009
	4÷8	0.0028	0.0032	0.0016
	8÷12	-	0.0058	0.0045
	12÷16	-	-	0.0029

Table III.6 allows a comparison between estimates of fundamental frequencies computed in accordance with EC8 (CEN, 2004) and those derived from dynamic analysis of fixed-base structural systems.

EC8-conforming estimates of fundamental period, T_{1d} , were obtained as follows:

$$T_{1d} = C_t h^{3/4} \quad (III.2)$$

where: C_t is a structural type coefficient, which was set to 0.05 as provided by EC8 (CEN, 2004) in the case of masonry buildings; and H is the overall height (in metres) of the structure computed from the foundation level (i.e. $H = h + D$).

Table III.6. Comparison between EC8-conforming and numerical estimates of fundamental frequency.

b/D	h/b	f_0 (Hz)	f_{1d} (Hz)	
			H	h
3.2	1	5.01	3.43	4.20
	1.5	2.94	2.70	3.10
	2	2.02	2.24	2.50
1.6	1	4.92	2.92	4.20
	1.5	2.94	2.38	3.10
	2	2.02	2.04	2.50

Thus, the fundamental frequency according to EC8 (CEN, 2004) was simply defined as $f_{1d} = 1/T_{1d}$. Regardless of the ratio b/D , and hence the basement type, Eq. (III.2) produced an underestimation of the fixed-base fundamental frequency for SFS systems with h/b ranging from 1 to 1.5; the opposite is observed when $h/b = 2$. The fixed-base fundamental frequency for SFS systems were also compared with the f_{1d} values computed considering the aboveground height, h . It is observed that, for SFS models with $h/b = 1$, with both embedded foundation and underground level, the frequency is lower than that numerically predicted, on the other hand for $h/b = 1.5$ and $h/b = 2$ the frequency values are greater.

III.2.2. Evaluation of radiation damping

Dynamic analysis of SFS systems under noise signal was also used to evaluate the radiation damping ratio.

For each SFS model, the displacement time history was filtered to identify peak amplitudes. Figure III.9a shows the filtered (red line) and unfiltered (black line) time histories of the horizontal displacement recorded on top of the three-storey structure ($h/b = 1.5$) with underground storey ($b/D = 1.6$) embedded in homogeneous soil D. For each filtered time history, the natural logarithmic amplitude was then computed and plotted against the cycle number, as shown in Figure III.9b. The slope of the linear regression line, i.e. the logarithmic decrement δ , was used to calculate the equivalent damping ratio, ξ^* , as follows:

$$\xi^* = \sqrt{\frac{\delta^2}{4\pi^2 + \delta^2}} \approx \frac{\delta}{2\pi} \quad (\text{III.3})$$

which turns out to be equal to the radiation damping ratio, given that $\xi_{str} = 0.1\%$ was assigned to the structural model.

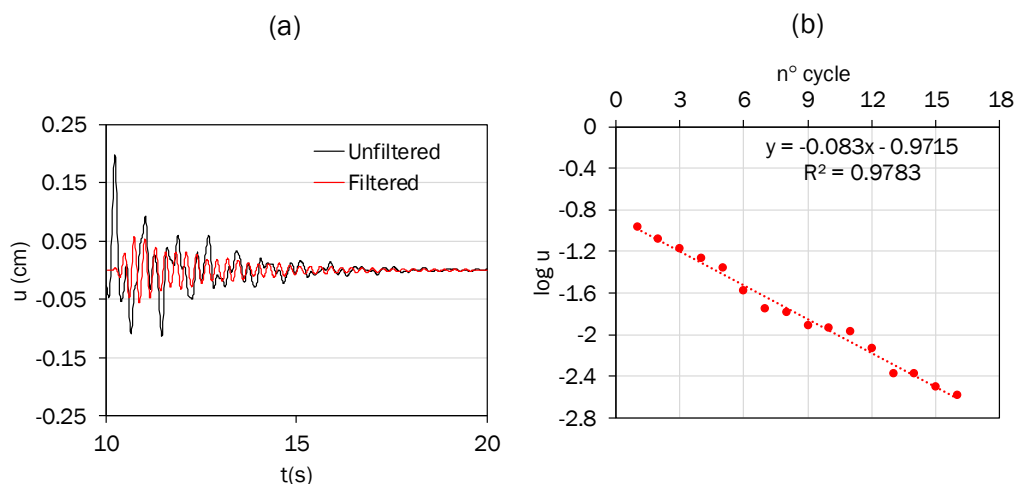


Figure III.9 Computation of radiation damping ratio: (a) unfiltered versus filtered time histories of roof horizontal displacement; (b) logarithmic displacement amplitude versus cycle number

Table III.7 and Table III.8 summarize radiation damping ratios related to SFS systems with embedded floating foundation and underground storey, respectively.

In most cases, radiation damping tends to rise up as the soil deformability increases, as shown by the apparently increasing decay of free vibration in Figure III.6a and Figure III.7a. It is observed that when the SFS system frequency, f^* , is greater than the fundamental frequency of the soil, f_{soil} (cases A and B) the structural top displacement amplitude decreases slowly with time, indicating low radiation damping, ξ_{rad} . On the contrary, for soil types C and D, f^* is lower than the fundamental frequency of the soil and the structural top displacement amplitude decreases rapidly with time, indicating high values of ξ_{rad} . The above trends are reflected in the radiation damping ratios reported in Table III.7. Such a behaviour may be associated to the theoretical mobilization of radiation damping in the soil for frequencies higher than the fundamental frequency of the soil (Gazetas 1991b).

Conversely, ξ_{rad} decreases as the slenderness of the structure increases from 1 to 1.5. The presence of the underground storey generally leads to higher values of radiation damping, because of the larger contact surface between the structure and soil, particularly in homogeneous soil configurations denoted as C and D.

Table III.7 Radiation damping ratios of SFS systems with embedded foundation.

Soil configuration	Soil layering	ζ_{rad} (%)		
		$h/b=1$	$h/b=1.5$	$h/b=2$
Homogeneous	A	0.24	0.11	0.05
	B	0.99	0.42	0.22
	C	3.36	1.66	1.08
	D	3.79	2.64	2.24
Layered	C-B	1.26	0.53	0.30
	D-B	1.98	0.61	0.38
	D-C	5.44	2.76	1.32

Table III.8 Radiation damping ratios of SFS systems with underground storey.

Soil configuration	Soil layering	ζ_{rad} (%)		
		$h/b=1$	$h/b=1.5$	$h/b=2$
Homogeneous	A	0.21	0.27	0.26
	B	0.91	0.31	0.27
	C	1.04	1.87	0.77
	D	4.05	3.26	2.56
Layered	C-B	1.40	0.51	0.27
	D-B	1.80	0.44	0.32
	D-C	3.66	3.06	0.94

It is worth remembering that very low values of both structural and soil hysteretic damping ratios were assumed, in order to isolate the effect of radiation damping. Since very low strain levels are mobilised in the soil by the low-amplitude input motions adopted in this study, the contribution of the low-strain soil damping can basically be added to the values reported in Table III.7 and Table III.8, as usually done in the application of the RO approach (Givens et al. 2016).

III.3. Simplified analysis: the replacement oscillator model

As described in Section II.1, the application of simplified methods to predict the fundamental period and damping ratio of a URM building resting on soft soil is difficult. The reliability of the most simplified approach was checked against the dynamic analysis results presented in Section III.2. The simplest model to study the inertial effect is represented by the replacement oscillator (Chapter II), solved with the analytical solution proposed by Veletsos and Meek (1974).

The equivalent mass, m^* , is typically set equal to the inertia mass of the above-ground structure involved in the dynamic motion (i.e. $m^* = m_{str}$). In this study, the mass m_{str} was assumed as the effective inertia mass corresponding to the fundamental mode of vibration of the fixed-base structure, as follows:

$$m_{str} = \sum_{j=1}^n m_j \phi_j \quad (III.4)$$

where: j denotes a floor level; n is the number of floor levels; m_j is the inertia mass of the j -th floor level; and ϕ_j is the first-mode displacement of the j -th floor level.

The fundamental modal shape of the fixed-base structure (Figure III.10a) was computed through dynamic analysis of the SFS system with firm soil, i.e. soil type A (see Figure III.8) under a noise input signal.

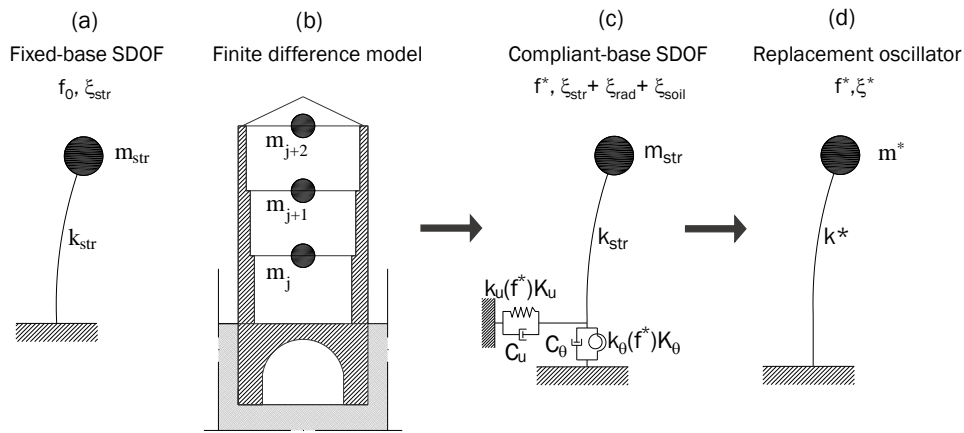


Figure III.10 Definition of replacement oscillator of SFS system

The same time history analysis allowed for evaluating the fundamental frequency of the fixed-base system, f_0 , so that the stiffness of an equivalent fixed-base SDOF (Figure III.10a) could be computed as follows:

$$k_{str} = 4\pi f_0^2 m_{str} \quad (III.5)$$

The equivalent damping ratio, ζ^* , is assumed to be the sum of structural damping, radiation damping and soil damping, i.e. $\zeta^* = \zeta_{str} + \zeta_{rad} + \zeta_{soil}$. In this study, soil material damping, ζ_{soil} , was not considered in accordance with the approach proposed by Veletsos and Meek (1974), which was implemented to calculate the fundamental period and equivalent damping ratio of the oscillators replacing the SFS systems. Moreover, this study investigates the SFS interaction under very low strain levels, where ζ_{soil} is generally negligible. The structural damping, ζ_{str} , was assumed as low as 0.1% to directly quantify the radiation damping of the SFS system in the replacement oscillator model.

The foundation impedance functions \bar{K}_u and \bar{K}_θ assigned to the base of the SDOF model were calculated according to the Eqs. (II.1) and (II.2). The translational and rotational components of the static stiffness, as well as the radiation damping coefficients, were calculated using the formulas proposed by Gazetas (1991) accounting for the different embedment of the structure with embedded foundation and underground storey:

$$K_{w,sup} = [2GL / (2 - \nu)](2 + 2.50\chi^{0.85}) \quad (III.6)$$

$$K_{u,sup} = K_{w,sup} - [0.2 / (0.75 - \nu)]GL[1 - (B/L)] \quad (III.7)$$

$$K_w = K_{w,sup} \left[1 + 0.15(D/B)^{0.5} \right] \left\{ 1 + 0.52[(h/B)(A_w/L^2)]^{0.4} \right\} \quad (III.8)$$

$$K_u = K_{u,sup} (K_w / K_{w,sup}) \quad (III.9)$$

$$K_{\theta,sup} = [G / (1 - \nu)] I_{bx}^{0.75} (L/B)^{0.25} [2.4 + 0.5(B/L)] \quad (III.10)$$

$$K_\theta = K_{\theta,sup} \left\{ 1 + 1.26(d/B) \left[1 + (d/B)(d/D)^{-0.2} (B/L)^{0.5} \right] \right\} \quad (III.11)$$

$$C_{u,sup} = \rho V_s A_b \quad (III.12)$$

$$C_{\theta,sup} = (\rho V_{La} I_{bx}) \quad (III.13)$$

$$C_u = C_{u,sup} + \rho V_s A_w \quad (III.14)$$

$$C_\theta = C_{\theta,sup} + \rho I_{bx} (d/B) \left\{ V_{La} (d^2/B^2) + 3V_s + V_s (B/L) \left[1 + (d^2/B^2) \right] \right\} \eta_\theta \quad (III.15)$$

where the subscript “sup” means that the static stiffness was calculated neglecting the foundation embedment, K_{wsup} and K_w are the translational (lateral direction) static stiffness; L , B and D are, respectively the length, width and depth of the foundation; d is the constant effective-contact height, in this cases equal to D ; I_{bx} is the area moments of inertia along the x axes of the soil-foundation contact area, A_w , is the sidewall-soil contact area, $\chi = A_b / 4L$; A_b is the base area; V_{La} is the Lysmer’s analogue wave velocity; and $\eta_\theta = 0.25 + 0.65\sqrt{a_0} (d/D)^{-a_0/2} (D/B)^{-1/4}$. The dynamic coefficients k_u

were estimated from the plots reported in the study of Gazetas (1991) while k_θ are estimated as:

$$k_\theta \cong k_{\theta,\text{sup}} \cong 1 - 0.20a_0 \quad (\text{III.16})$$

The fundamental frequency f^* of the RO (equal to that of the flexible-base SDOF system) was calculated in accordance with Eq. (II.9), by replacing the terms k'_u and k'_θ with the real part of Eqs. (III.9) and (III.11).

Figure III.11 a and b show the analytical f^*/f_0 for RO (rhombus symbols) obtained from Eq. (II.9) for the embedded foundation and the underground storey, respectively, against the relative soil-structure stiffness parameter σ , computed through Eq. (II.11).

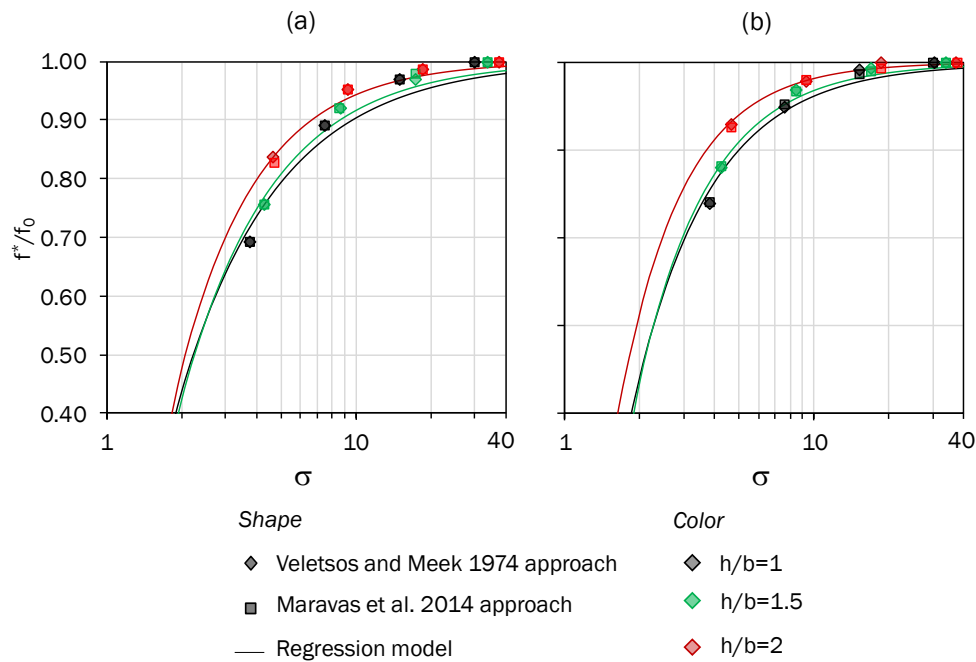


Figure III.11 Regression models for σ -based analytical predictions: (a) structure with embedded floating foundation, (b) structure with underground storey.

In all cases, the foundation length L was set to 1 m in accordance with the procedure for the computation of inertia masses and gravity loads. For both the basement configurations, σ was found to range in the intervals [3.75,30], [3.91,34.50] and [4.70,37.50] for structural systems with h/b equal to 1, 1.5 and 2, respectively. For the same aspect ratios, f^*/f_0 was found to range in the following intervals: [0.69,1.00], [0.76,1.00] and [0.84,1.00] in the case of SFS systems with embedded floating foundation; [0.89,1.00], [0.92,1.00] and [0.95,1.00] in the case of SFS systems with underground storey.

No direct relationship between σ and f^*/f_0 was defined in the study by Veletsos and Meek (1974), so the following function was fitted to each analytical data set related to a given aspect ratio h/b and represented by continuous lines in Figure III.11:

$$\frac{f^*}{f_0} = \alpha \sigma^\beta + 1 \quad (III.17)$$

where α and β are regression coefficients, which are listed in Table III.9 together with the coefficient of determination R^2 . The power law function was constrained to unity at high σ -values, i.e. the fixed-base frequency is obtained for structures on rigid soil. Those curves allow the comparison between analytical predictions and numerical results, as described in Section III.4. It can be noted that, for each basement configuration, a good agreement between analytical data sets and regression models was found.

The analytical solutions of the procedure proposed by Maravas et al. (2014), which are based on Eqs. (II.13), (II.14) and (II.15), are also shown in Figure III.11a and b (. The values of the uncoupled circular natural frequencies of the system ω_u , ω_θ and ω_0 were calculated as:

$$\omega_u = \sqrt{\frac{\text{Re}(\bar{K}_u)}{m_{str}}} \quad (III.18)$$

$$\omega_\theta = \sqrt{\frac{\text{Re}(\bar{K}_\theta)}{m_{str}h^2}} \quad (III.19)$$

$$\omega_0 = \sqrt{\frac{k_{str}}{m_{str}}} \quad (III.20)$$

Whereas the corresponding values of viscous damping ratios, ξ_u , ξ_θ were computed as:

$$\xi_u = \frac{\text{Im}(K_u)}{2\text{Re}(\bar{K}_u)} \quad (III.21)$$

$$\xi_\theta = \frac{\text{Im}(K_\theta)}{2\text{Re}(\bar{K}_\theta)} \quad (III.22)$$

As shown in Figure III.11, a good agreement between the two procedures was found. The analytical damping ratios, ξ_{rad} , were computed by Eq. (II.10), in which the dimensionless factors $\alpha_u, \alpha_\theta, \beta_u$ and β_θ are replaced, respectively, by the dynamic stiffness coefficients $k_u(f^*)$ and $k_\theta(f^*)$ and the dynamic damping coefficients $c_u(f^*)$ and $c_\theta(f^*)$ of Gazetas formulas.

Nonlinear regression analysis was also carried out on the analytical damping ratios, through the following exponential function:

$$\xi_{rad} = \alpha \exp(-\beta\sigma) \quad (III.23)$$

where α and β are regression coefficients, which are listed in Table III.9 together with the coefficient of determination R^2 . Figure III.12 shows regression lines together with each set of numerical results up to $\xi_{rad} = 20\%$, which was the graphical upper bound used originally by Veletsos and Meek (1974).

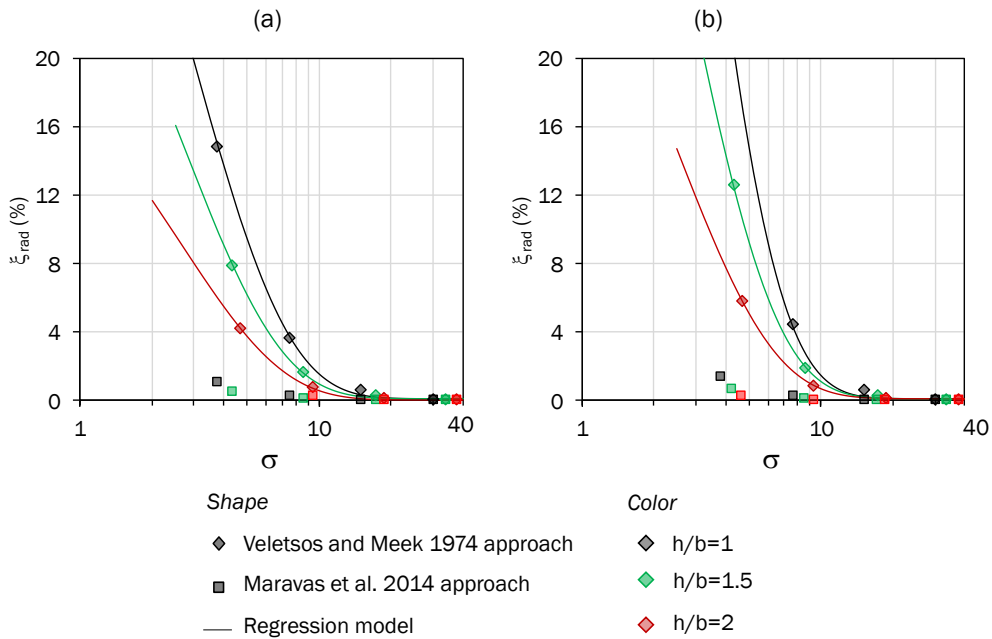


Figure III.12 Regression models for σ -based predictions: (a) structure with embedded foundation, (b) structure with underground storey.

Table III.9. Regression coefficients and coefficient of determination of regression models for estimation of fundamental frequency and radiation damping ratio.

b/D	h/b	f			ξ_{rad}		
		α	β	R^2	α	β	R^2
	1	-1.20	-1.09	0.92	60	0.37	1.00
3.2	1.5	-1.33	-1.20	0.99	42	0.39	1.00
	2	-1.37	-1.38	0.99	25	0.38	1.00
	1	-0.95	-1.41	1.00	158	0.47	1.00
1.6	1.5	-1.04	-1.53	1.00	83	0.44	1.00
	2	-0.94	-1.70	0.99	42	0.43	1.00

Regression coefficients α and β as well as the coefficient of determination are listed in Table III.9. It is noted that regression analysis was carried out over the whole set of data points, that is, without removing data associated with $\xi_{rad} > 20\%$. The procedure proposed by Maravas et al. (2014) was also used to derive analytical estimates of ξ_{rad} , which are compared to regression models in Figure III.12a and b. In all cases, the procedure by Maravas et al. (2014) produced a significant underestimation of ξ_{rad} .

III.4. Comparison between full dynamic and simplified analyses

Figure III.13a and c show the values of f^* listed in Table III.2 and Table III.3 normalised to those of the fixed-based systems (first rows in the same tables) and plotted against the soil-structure stiffness parameter σ corresponding to the shear wave velocity of the shallow cover, as suggested by Veletsos and Meek (1974).

The regression curves obtained from response predictions of the RO described above, are shown in Figure III.13. As expected, the fundamental frequency of structures with embedded floating foundation (Figure III.13a) reduces with decreasing σ , and hence the soil stiffness. This effect is confirmed to be practically negligible in the presence of underground storey, except for the models with soil type D (Figure III.13). In the latter case, the classical calibration of the soil-structure stiffness parameter through the shear wave velocity of the foundation soil can produce an underestimation of SFS interaction effects and the presence of the more deformable lateral soil needs to be taken into account.

Dynamic analysis results confirm the analytical trend line, but the former are quite scattered, especially for models with layered soil. Such a dispersion is due to the hypothesis of rigid foundation placed on ground surface of a homogeneous half-space, in the Veletsos and Meek (1974) approach.

To this aim, an equivalent soil-structure stiffness parameter, σ_{eq} , was defined by properly modifying the shear wave velocity. Such modified velocity is herein defined as equivalent shear wave velocity and is denoted by $V_{s,eq}$.

This parameter was computed in the soil volume expected to be excited by the foundation motion. Such a volume was assumed to have depth and surface width equal to twice the building width b , which is compatible with the soil volume usually affected by the presence of a structure.

It is worth noting that Gazetas (1983) and Stewart et al. (2003) suggested that the soil affected by the foundation swaying and rocking extends to a depth less than half the foundation width, which is almost coincident with the depth of the upper soil layer for the analysed case studies. Nevertheless, although the depth of the effective soil volume is typically set to $b/2$ in the computation of impedance functions, there is no general consensus on the soil volume mobilised during earthquake excitation because of the huge variability in the structural response.

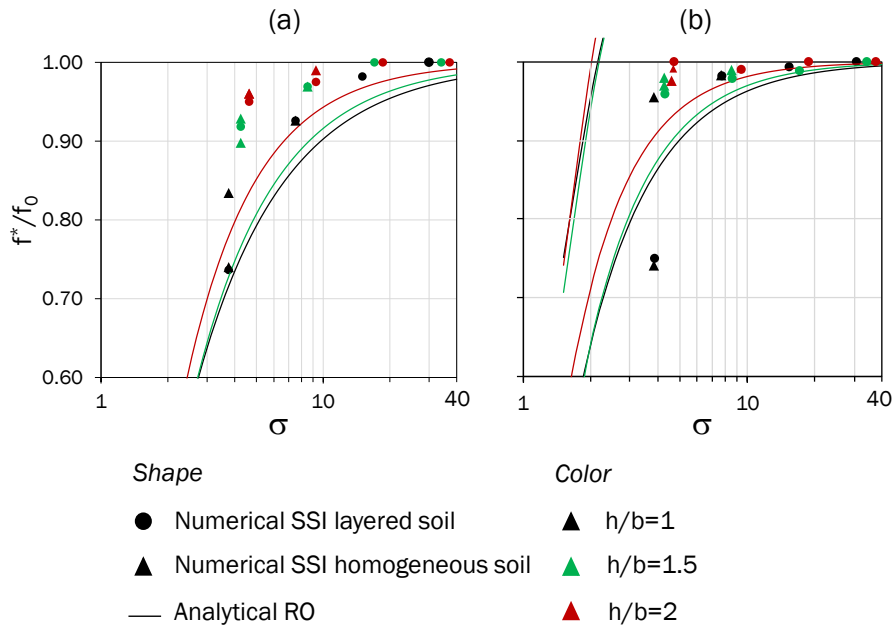


Figure III.13 Comparison between analytical (RO) and numerical (SSI) predictions: (a) structures with embedded foundation and SSI defined through σ ; (b) structures with underground storey.

As shown in Figure III.14, the aforementioned volume includes fractions of the top and bottom soil layers, the structure and the void space of the underground storey. Such components of the SFS system can be respectively numbered as 1, 2, 3 and 4, so that an equivalent shear modulus G_{eq} and an equivalent mass density ρ_{eq} can be defined through the following equations:

$$G_{eq} = \frac{\sum_{j=1}^3 \rho_j G_j A_j}{\sum_{j=1}^4 A_j} \quad (III.24)$$

$$\rho_{eq} = \frac{\sum_{j=1}^3 \rho_j \rho_j A_j}{\sum_{j=1}^4 A_j} \quad (III.25)$$

where G_j , ρ_j , A_j and p_j respectively stand for the shear modulus, mass density, area and weighting coefficient of the j -th part of the SFS system ($j = 1, \dots, 4$). In case of homogeneous soil, G_1 and G_2 turn out to be equal.

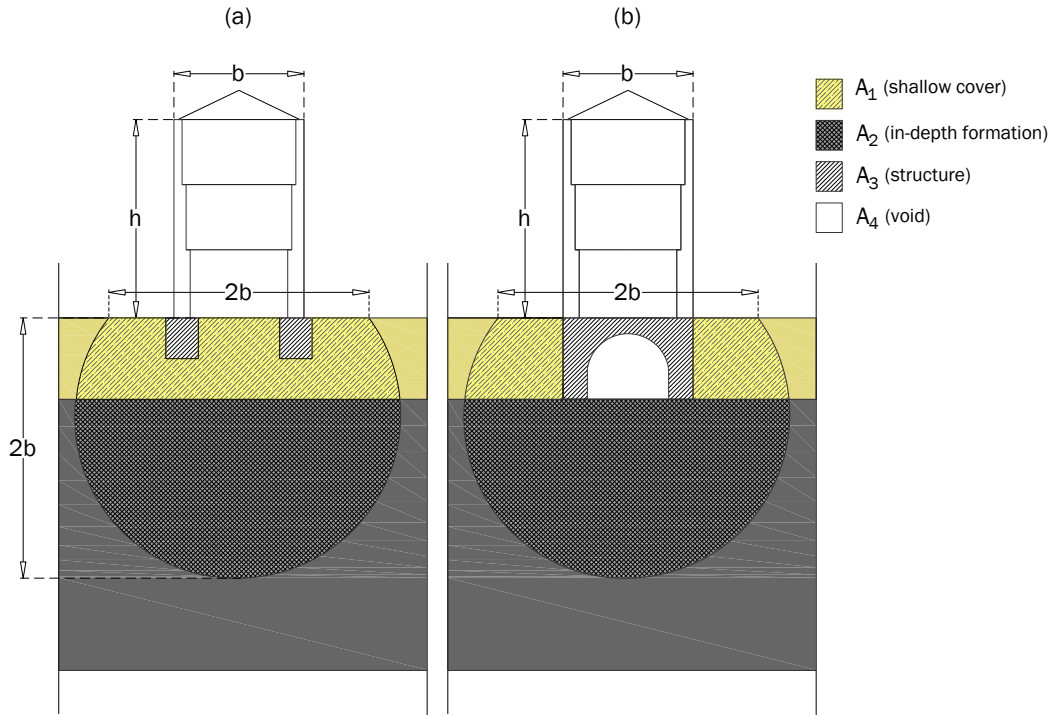


Figure III.14. Soil volume affected by horizontal foundation motion: (a) embedded floating foundation; (b) underground storey with bearing wall foundation.

Thus, the equivalent shear wave velocity of the SFS system can be computed as follows:

$$V_{S,eq} = \sqrt{\frac{G_{eq}}{\rho_{eq}}} \quad (III.26)$$

The weighting coefficients p_j need to be numerically calibrated because they depend on the ratios between properties of the SFS system. In this way, the same extension of the soil volume can be used for different soil-foundation configurations, because the relevance of each component in the different SFS systems is governed by the variability of the weighting coefficients.

The coefficients p_1 , p_2 and p_3 were obtained by minimising the difference, Δ , between σ_{eq} (equal to $V_{S,eq}/hf_0$) and the value of σ to be used in Eq. (III.17) in order to compute the ratio f^*/f_0 given by each numerical analysis, $\sigma(f^*/f_0)_{num}$. Such calibration allows reducing the dispersion of numerical results with respect to analytical data. To compute the weighting coefficients for each set, it was also imposed that each coefficient was less than or equal to unity.

The calibration was performed in numerical cases in which the soil flexibility reduced the frequency ratio f^*/f_0 down to 97%, the latter cut-off level is shown by a dashed, horizontal black line in Figure III.15. The calibration was not performed on the structures with underground floor, because the frequency ratio f^*/f_0 was lower than 0.97 only in four of the SFS models analysed.

Figure III.15b highlights how the scatter of numerical data sets obtained for the embedded foundation decreases if σ is replaced by the soil-structure stiffness parameter σ_{eq} , computed from the equivalent shear wave velocity through Eq. (III.26). Table III.10 outlines the values of the calibrated coefficients associated with the contribution of shallow cover, in-depth formation and basement system, i.e. p_1 , p_2 and p_3 respectively. The estimates of p_1 indicate that the flexibility of the top soil layer significantly influences the dynamic SFS interaction, especially in the case of relatively stiff foundation soil (see, for instance, the output for D-B layering). Indeed, horizontal displacements of the SFS systems are more influenced by the flexibility of lateral soil, rather than that of the in-depth formation, as confirmed by p_2 values mostly close or equal to zero. The latter result is consistent with the low depth of the soil volume affected by the foundation motion reported in the literature.

Table III.10.Weighting coefficients for definition of σ_{eq}

h/b	Soil layering	p_1	p_2	p_3	$\sigma(f^*/f_0)_{num}$	σ_{eq}	Δ
1	C-C	0.00	0.00	1.00	13.5	11.9	1.7
	D-D	1.00	0.04	0.18	4.1	4.1	0.0
	D-B	1.00	0.04	0.03	6.0	6.0	0.0
	D-C	1.00	0.02	0.00	4.1	4.1	0.0
	C-B	0.59	0.80	1.00	13.5	13.5	0.0
1.5	D-D	0.10	0.00	1.00	10.4	10.4	0.0
	D-B	1.00	0.25	1.00	11.5	11.5	0.0
	D-C	0.29	0.39	1.00	8.5	8.4	0.1
2	D-D	0.06	0.03	1.00	11.0	11.0	0.0
	D-B	1.00	0.30	1.00	13.0	13.0	0.0
	D-C	0.00	0.03	1.00	13.0	12.9	0.1

Furthermore, for all h/b ratios the effect of foundation stiffness (p_3 values) is predominant when f^* is approaching to f_{soil} . For squat structures ($h/b = 1$), when f^* is greater than f_{soil} the effect of the soil stiffness is predominant. For slender structures ($h/b = 1.5$ and $h/b = 2$), when f^* is lower than f_{soil} both shallow cover and foundation stiffness are predominant.

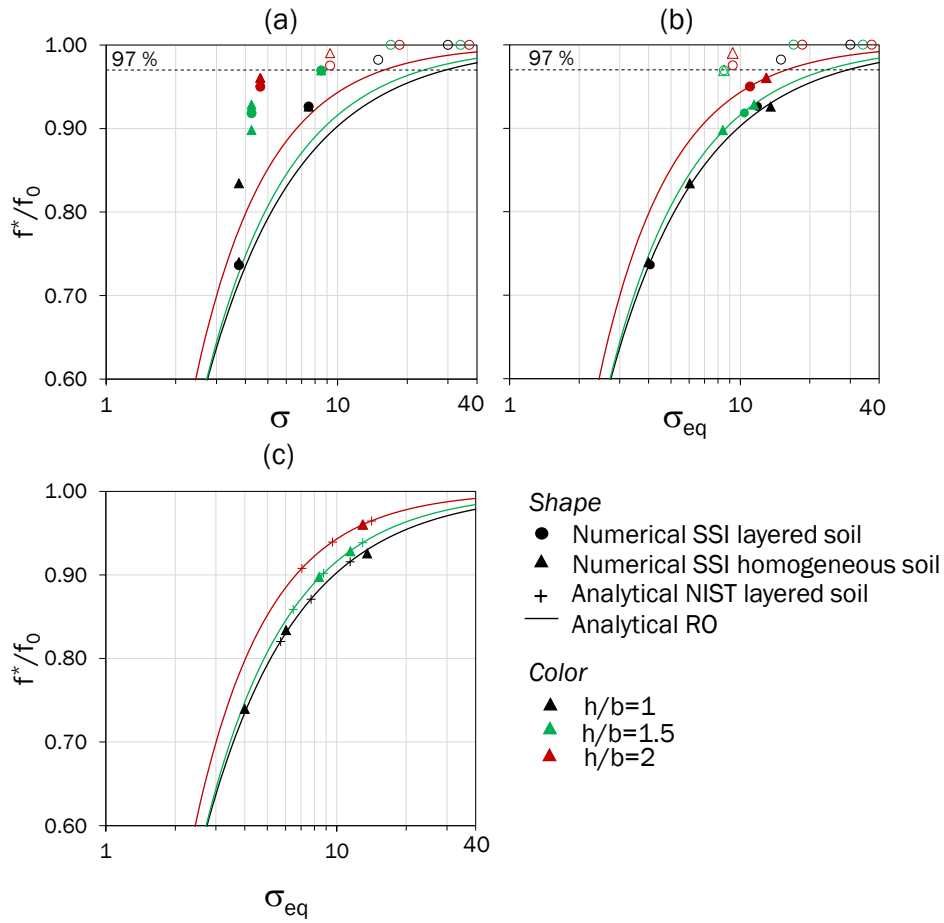


Figure III.15 Comparison between analytical (RO) and numerical (SSI) predictions for structures with embedded foundation: (a) SSI defined through σ ; (b) SSI defined through σ_{eq} ; and (c) SSI defined through σ_{eq} computed with V_{sNIST} .

In practice-oriented procedures in NIST (NEHRP, 2012), the concept of averaging a continuously or piecewise inhomogeneous soil to obtain equivalent homogeneous properties for SSI modelling has been included and also, implemented in real cases of urban units (Rovithis et al. 2017). The soil-structure stiffness parameter was also defined in NIST based on the shear wave velocity. For each layered soil configuration, an average shear wave soil velocity, $V_{s,avg}$, was computed, considering the effective depth of soil volume affected by horizontal foundation motion, $z_p=2b$, as follows:

$$V_{s,avg} = \frac{z_p}{\sum_{i=1}^N \left(\frac{\Delta z_i}{V_s(z_i)} \right)} \quad (III.27)$$

where Δz_i is the thickness of the soil layer and $V_s(z_i)$ is the corresponding shear wave velocity.

Figure III.15c shows the comparison between the numerical data set against σ_{eq} , and the ratio f^*/f_0 computed through Eq. (III.17) using the NIST value of σ (cross in Figure III.15c). It can be observed that as the structure slenderness increases the difference between the ratio f^*/f_0 predicted by the NIST and the proposed procedure tends to decrease.

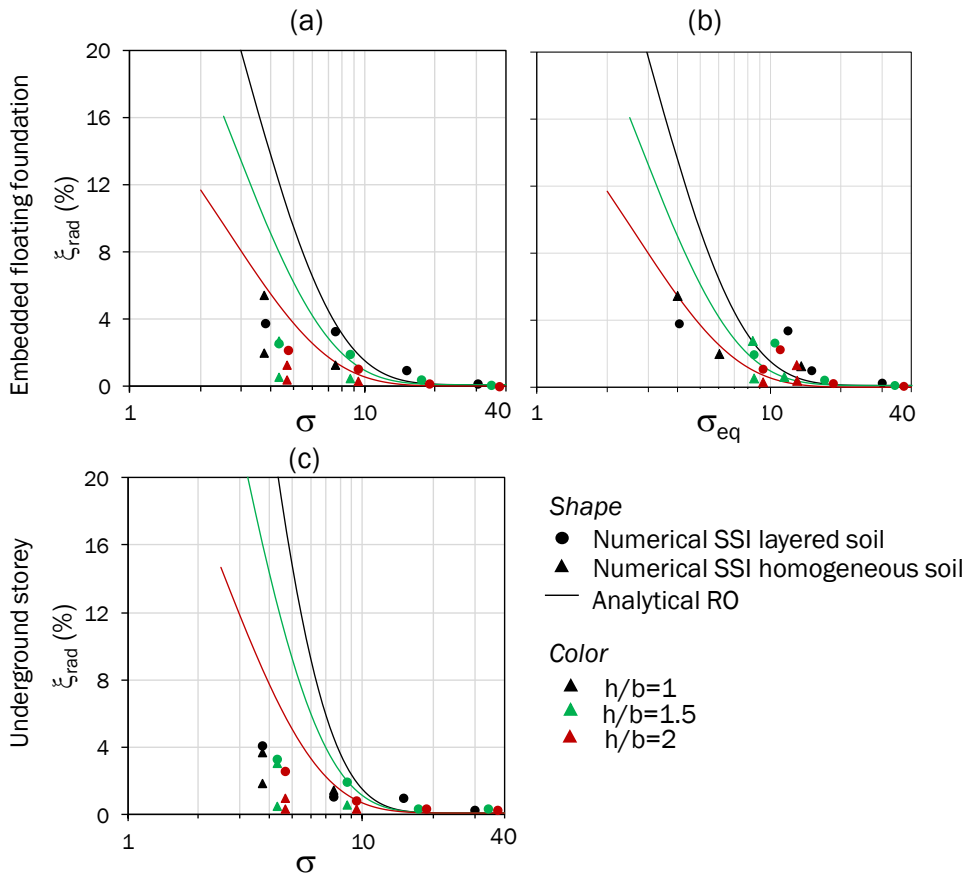


Figure III.16 Comparison between analytical (RO) and numerical (SSI) predictions: (a) structures with embedded foundation and SSI defined through σ ; (b) structures with embedded foundation and SSI defined through σ_{eq} ; and (c) structures with underground storey.

Figure III.16 shows the radiation damping ratio computed from numerical results through the procedure described in Section III.2. As the soil stiffness decreases (corresponding to lower values of σ), the energy dissipation capacity of the SFS system increases. In all cases, the numerical estimate of damping ratio (dots in Figure III.16) appears, especially for soil type D, lower than the analytical prediction (solid lines in Figure III.16). The difference between numerical results and analytical predictions can

be mainly ascribed to the fact that the 2D foundation generated in FLAC software (Itasca, 2011) neglects the out-of-plane dimension and is made of deformable material. By contrast, a circular rigid plate is assumed in the RO model. Further investigations are necessary to clarify this effect.

However, the radiation damping ratio obtained from dynamic analysis under noise input motion rarely exceeds $\xi_{rad} = 6\%$, which is a value expected to be significantly exceeded by the hysteretic damping ratio associated with soil nonlinear behaviour under earthquake strong motion.

Figure III.16b shows the radiation damping ratio plotted against σ_{eq} . Even in this case, if $\sigma_{eq} \leq 10$, the analytical predictions are greater than their numerical counterparts. Conversely, if $\sigma_{eq} > 10$, the RO approach produces rather the same estimates of the numerical models or even an underestimation of ξ_{rad} .

IV.EFFECTS OF SFS INTERACTION ON NONLINEAR DYNAMIC RESPONSE AND SEISMIC FRAGILITY OF MASONRY BUILDINGS

The previous linear time history analyses (LTHA) of transverse sections of masonry buildings have highlighted the effects of SFS interaction on their dynamic response when the loadbearing walls are laterally loaded outside their own plane. As a result, the parametric LTHA have allowed the derivation of a simplified model for a quick assessment of the modification of fundamental period and damping according to the RO approach. Nonetheless, the influence of SFS interaction on the activation of limit states for both out-of-plane (OOP) mechanisms of masonry walls and plastic straining in the soil-foundation system needs to be investigated using nonlinear time history analyses (NLTHA). In this way, on one hand the characteristics of the input motion can be explicitly considered and on the other, the nonlinear behaviour of the soil, foundation and structure can be taken into account. NLTHA also produces the ability to identify the best intensity measures (IMs) correlated with seismic damage, allowing the development of fragility functions for seismic vulnerability assessment of masonry buildings. The methodology used in this thesis is summarised in the flowchart shown in Figure IV.1. The procedure follows the steps briefly discussed in Section II.3 and described in detail in this chapter.

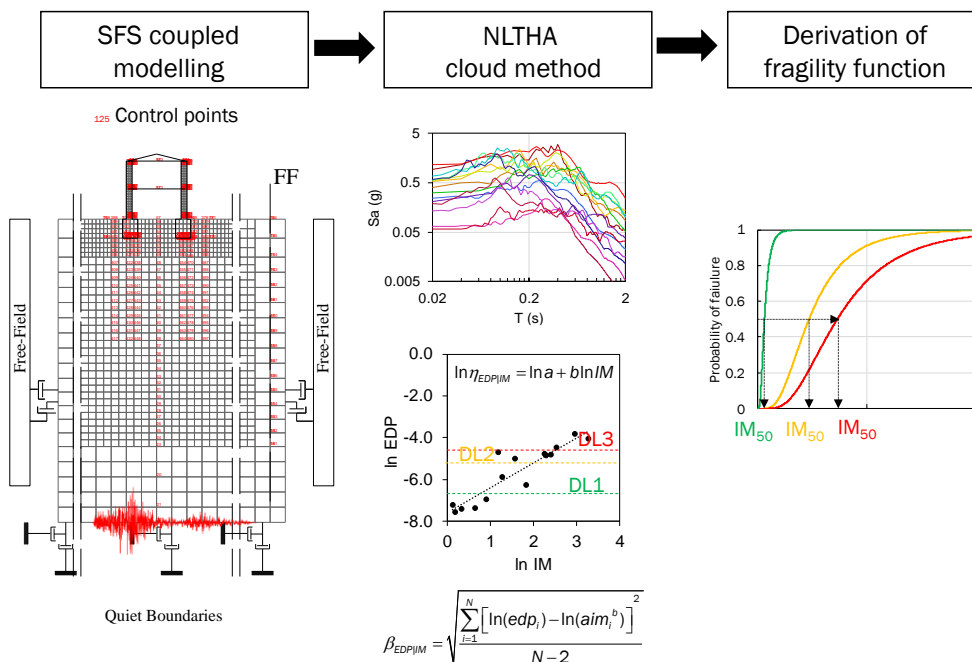


Figure IV.1 Flowchart of the methodology adopted in this work

IV.1. Nonlinear SFS interaction models

SFS interaction was further investigated through NLTHA of similar SFS models considered in Chapter III, assigning them a nonlinear behaviour of both the soil and masonry. Previous studies observed that, under strong motions, the foundation motion induce cyclic high strain levels in the surrounding soil until its yielding. Such failure of the foundation soil contributes to the dissipation of seismic energy, causing a reduction in displacement demand on structures (Faccioli et al. 1998; Shirato et al. 2008; Gazetas 2015). The masonry nonlinearity, instead, is taken into account in order to better reproduce the OOP behaviour under seismic motion, because spread cracks form as a result of tensile and compressive failure, influencing the OOP failure and collapse. Two different masonry types (described in Section IV.1.1) that are rather recurrent in the Italian and European built heritage were investigated.

The reference fixed-base conditions were again assumed as corresponding to a SFS model characterised with ground type A (i.e. outcropping bedrock). Two soft soil conditions were considered, both representative of a clayey soil type D according to EC8 CEN (2004).

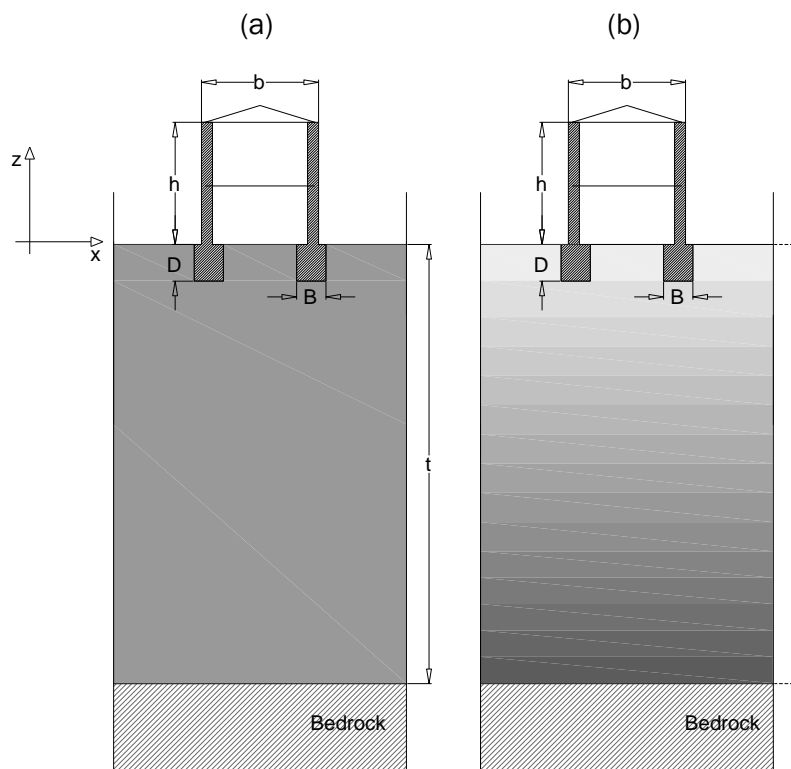


Figure IV.2 SFS models of selected case studies founded on (a) homogeneous and (b) heterogeneous soil.

Stiffness and strength parameters were assumed as either constant (homogeneous profile, D_{ho}) or variable with depth (heterogeneous profile, D_{he}) as qualitatively shown in Figure IV.2 and described in detail in the following sub-section.

With respect to the parametric study described in Chapter III, only the embedded “floating” foundation and the structural system characterised by two or four-storey ($h/b = 1$ and $h/b = 2$) were considered. The SFS systems with underground level were excluded because SSI effects in this case were observed as less significant.

Table IV.1 reports the acronyms used in this Chapter to identify the twelve SFS configurations.

Table IV.1 SFS models acronyms

N° of storey	Masonry material	Soil configuration	Abbreviation
Two	Rubble stone	Soil A	Rs_1_A
Two	Rubble stone	Soil D_{ho}	Rs_1_ D_{ho}
Two	Rubble stone	Soil D_{he}	Rs_1_ D_{he}
Four	Rubble stone	Soil A	Rs_2_A
Four	Rubble stone	Soil D_{ho}	Rs_2_ D_{ho}
Four	Rubble stone	Soil D_{he}	Rs_2_ D_{he}
Two	Clay brick	Soil A	Cb_1_A
Two	Clay brick	Soil D_{ho}	Cb_1_ D_{ho}
Two	Clay brick	Soil D_{he}	Cb_1_ D_{he}
Four	Clay brick	Soil A	Cb_2_A
Four	Clay brick	Soil D_{ho}	Cb_2_ D_{ho}
Four	Clay brick	Soil D_{he}	Cb_2_ D_{he}

IV.1.1. Model description

The complete SFS models adopted for NLTHA, are shown in Figure IV.3. The discretization of the model into the mesh represented in Figure IV.3 followed the same criteria adopted in Chapter III. With respect to the models used in LTHA, the masonry wall thickness was reduced from 1.00m to 0.75m based on Eq. (II.16).

To evaluate both the soil and structure response, several control points were set along the structure axis (see coloured points) and below the foundation level along the verticals a_{sx} and a_{dx} down to 16 m depth, which represents the thickness of the soil volume affected by horizontal foundation motion.

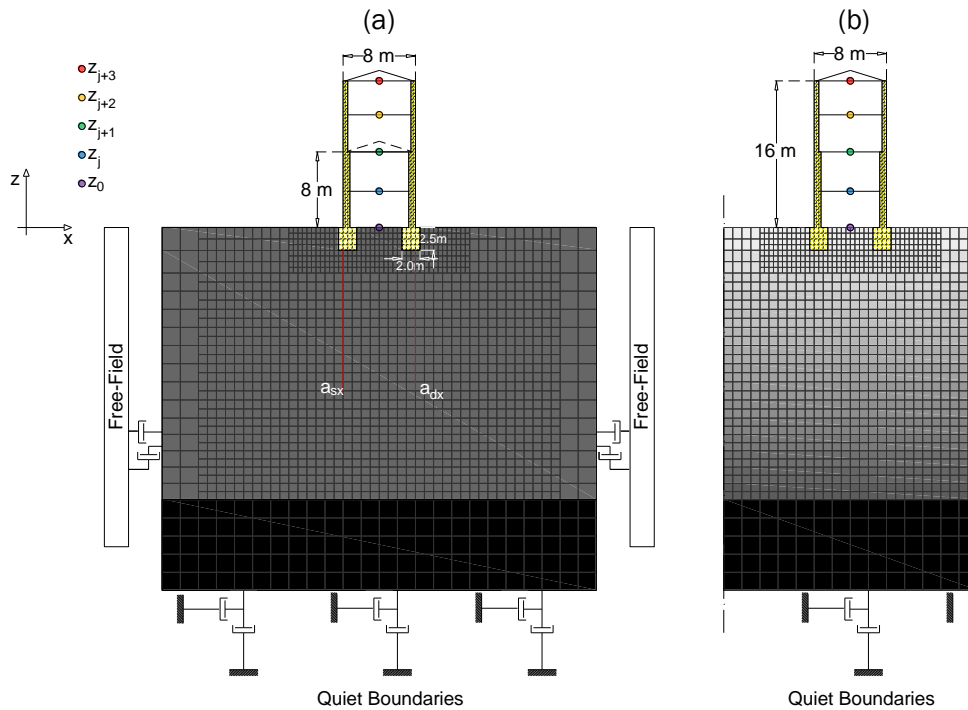


Figure IV.3 2D finite difference models: (a) homogeneous and (b) heterogeneous soil profile.

Table IV.2 summarises the physical and mechanical properties of soil types A, D_{ho} and D_{he} . For ground type A (bedrock) a linear elastic behaviour was assumed as in Chapter III. By contrast, a limit shear strength was assumed for soil types D_{ho} and D_{he} through a Tresca constitutive model (T), characterised by an undrained strength, c_u .

The homogeneous and heterogeneous soil profiles selected for this study were thought as representative, respectively, of a lightly overconsolidated clay and a normally consolidated clay with medium plasticity, by assuming a plasticity index $IP = 30\%$ for the homogeneous (D_{ho}) and $IP = 20\%$ for the heterogeneous (D_{he}) profile.

Figure IV.4a, b, and c compare the variation of the strength and stiffness properties of both profiles with depth.

The variations of both shear stiffness at small strains and undrained strength with depth in the heterogeneous soil profile follow the model adopted by Capatti et al. (2017). The undrained strength (cyan line in Figure IV.4a) was assumed as linearly increasing with the vertical effective lithostatic stress, σ'_{v0} , according to the relationship: $c_u = 0.35\sigma'_{v0}$ (Calabresi and Manfredini 1976), except for a shallow layer of dry crust with constant c_u from the surface to 2.5m. Due to the light overconsolidation, for soil type D_{ho} the undrained strength was set constant with depth (red line in Figure IV.4a) and higher than that of the heterogeneous soil profile.

Table IV.2 Physical and mechanical properties of the soil types

Soil type / Material	ρ (kg/m ³)	V_s (m/s)	K (MPa)	G_0 (MPa)	ν (-)	c_u (MPa)	D_0 (%)
A/Bedrock	2200	1200	4224	3168	0.20	-	1%
D_{ho} / light o.c. clay (homogeneous)	1600	150	1788	36	0.49	0.10	2%
D_{he} / n.c. clay (heterogeneous)	1600	100 191	915 2970	18 60	0.49	0.01 0.07	2%

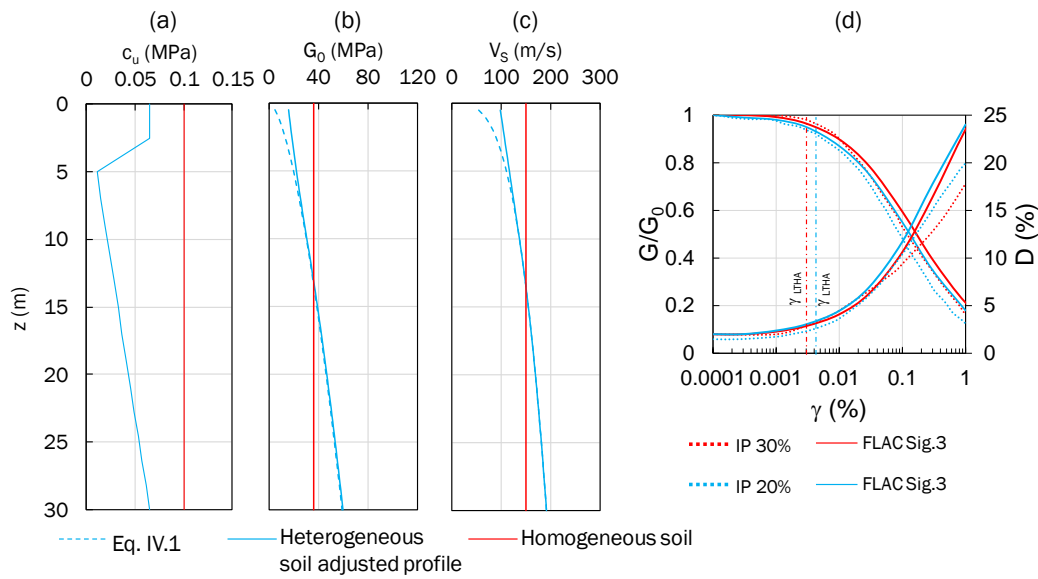


Figure IV.4 Profiles of (a) undrained strength, c_u , (b) initial shear stiffness, (c) shear wave velocity; (d) strain-dependent variation of normalized shear modulus and damping ratio according to the standard curves by Vucetic and Dobry (1991) vs hysteretic behaviour numerically simulated by sigmoidal function and Masing criteria

The small strain shear stiffness, G_0 , was also assumed as constant for soil type D_{ho} (red line in Figure IV.4c), and corresponding to a constant value $V_s = 150$ m/s (red line in Figure IV.4d). In the case of soil type D_{he} , instead, G_0 increases with the mean effective lithostatic stress p' (dotted cyan line in Figure IV.4c) as follows:

$$\frac{G_0}{p_a} = S \left(\frac{p'}{p_a} \right)^n \quad (IV.1)$$

where p_a is the atmospheric pressure, S and n are two parameters expressed as a function of IP , through the following empirical correlations (D'onofrio and Silvestri 2001):

$$S = 217 + 806 \exp\left(-\frac{IP}{19}\right) \quad (IV.2)$$

$$n = 0.67 - 0.162 \exp\left(-\frac{IP}{23}\right) \quad (IV.3)$$

The profile of V_s (dashed blue line in Figure IV.4d) was obtained as the square root of the ratio between G_0 (Eq. IV.1) and the mass density ρ .

In the FD models the adjusted profiles (solid blue lines in Figure IV.4b and c) were used and obtained by considering linear trends tangent to the theoretical curves (dashed lines) for a depth lower than 10 m, in order to avoid unrealistic null velocity and stiffness at the ground level.

For both soft soil profiles, a pre-failure hysteretic behaviour was assumed. The strain-dependent variation of normalized shear modulus, G/G_0 , was described by the standard curves suggested by Vucetic and Dobry (1991) for the plasticity indexes $IP = 20\%$ and $IP = 30\%$ (dotted lines in Figure IV.4d). The standard curves were implemented in the numerical model by fitting them through 'sigmoidal' functions (Mánica et al. 2014), represented as solid lines in Figure IV.4d, corresponding to the following expression:

$$\frac{G}{G_0} = \frac{a}{1 + \exp\left(\frac{-(\log(\gamma) - x_0)}{b}\right)} \quad (IV.4)$$

where a , b and x_0 are three parameters, reported in Table IV.3. The hysteretic damping was obtained by applying the well-known Masing criteria (Hardin and Drnevich 1972). To verify the model calibration, the cyclic response of a cubic soil sample was numerically simulated at shear strain levels increasing from $\gamma=0.0001\%$ to $\gamma=1\%$, and the corresponding variation of the hysteretic damping was calculated from the shear stress-strain (τ - γ) loops. The comparison between the simulated (solid line) and standard G/G_0 : γ and D : γ curves (dotted lines) is shown in Figure IV.4d; in the same figure, the dash-dotted lines indicate the amount of the maximum shear strain, γ_{LTHA} , mobilized in the soil under the white noise input adopted for the dynamic identification analyses reported in the following Section IV.1.2. Such strain level was obtained as the maximum value between the mean γ computed along the verticals a_{sx} and a_{dx} (see Figure IV.3) down to a depth of 16m. The low degree of non-linearity and hysteresis mobilized at such values of γ_{LTHA} confirms the reliability of the assumption of linear behaviour in the dynamic identification analyses.

Table IV.3 Sigmoidal function parameters

Soil type	a	b	x ₀
D _{ho} / light o.c. clay (homogeneous)	1.02	-0.60	-0.80
D _{he} / n.c. clay (heterogeneous)	1.02	-0.60	-0.90

The energy dissipation at very small strains, for both dynamic identification analyses (LTHA) and NLTHA, was simulated through a Rayleigh approach. As well known, the damping matrix **C** involved in the dynamic equilibrium of a complex system, e.g. MDOF, FEM or FDM, can be expressed as a linear combination of the mass **M** and the stiffness **K** matrixes as follows (Chopra 1995):

$$\mathbf{C} = \alpha\mathbf{M} + \beta\mathbf{K} \quad (IV.5)$$

where α and β are two frequency-dependent coefficients. The former coefficient is relevant to a system with mass-proportional damping (light blue dotted line in Figure IV.5a), whereas the latter is related to a system with stiffness-proportional damping (green dotted line in Figure IV.5a). The damping ratio, ξ , for the n -th mode of vibration (red solid line in Figure IV.5a) can be expressed as follows:

$$\xi_n = \frac{1}{2} \left(\frac{\alpha}{\omega_n} + \beta\omega_n \right) \quad (IV.6)$$

where ω_n is the natural frequency associated with the n -th mode.

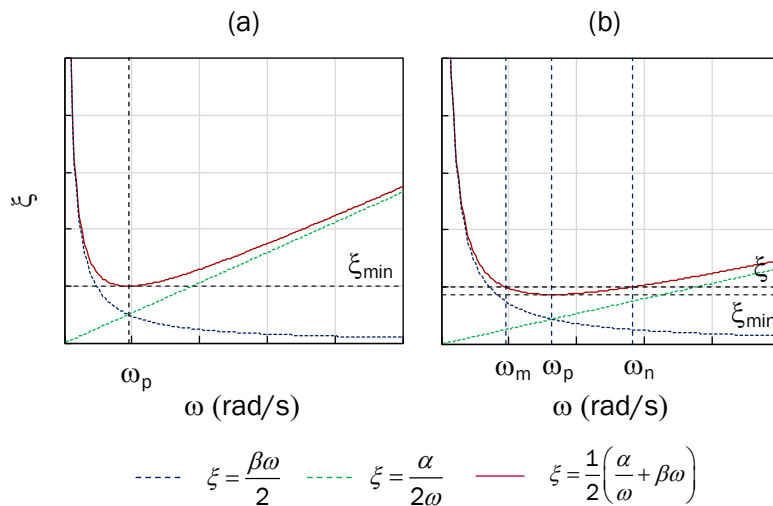


Figure IV.5 Variation of damping ratio with natural frequency: (a) single-control and (b) double-control frequency

The two coefficients can be calculated following two approaches: the single-control frequency (Figure IV.5a) or the double-control frequencies (Figure IV.5b). In the former approach, the coefficients α and β are calculated as:

$$\alpha = \omega_p \xi_{\min} \quad (IV.7)$$

$$\beta = \frac{\xi_{\min}}{\omega_p} \quad (IV.8)$$

by setting, usually, ω_p (or the frequency f_p) as the natural frequency of the system and ξ_{\min} as the experimental small-strain damping, D_0 . For the double-control frequencies approach, instead, the coefficients α and β are calculated as follows:

$$\alpha = \xi \frac{\omega_m \omega_n}{\omega_m + \omega_n} \quad (IV.9)$$

$$\beta = \xi \frac{2}{\omega_m + \omega_n} \quad (IV.10)$$

by assuming the same damping ratio, ξ , for two modes, m (ω_m) and n (ω_n), selected in the frequency range that mostly influence the system response.

The two approaches lead to the same damping curve if the following conditions are met:

$$\omega_p = \frac{2\omega_m \omega_n}{\sqrt{4\omega_m \omega_n}} \quad (IV.11)$$

$$\xi_{\min} = \frac{\xi}{\sqrt{4\omega_m \omega_n}} \frac{1}{\omega_m \omega_n} \quad (IV.12)$$

The approach implemented in FLAC software is the single-control frequency. This can be a limitation when the Rayleigh damping has to be calibrated for SSI analyses, since both the fundamental frequency of the system and the predominant frequency of the input motion influence the SFS system response.

More specifically, two disadvantages are related to this type of approach:

- (i) what is the value to assign to f_p between the fundamental frequency of the system and the predominant input frequency, f_{input} (which can be assumed for instance, equal to the median frequency of the input motion, as suggested by Rathje et al., 1998);
- (ii) the system results overdamped at all frequencies lower or greater than f_p .

For the above reasons, the parameters of the single control frequency approach were calibrated through Eq. (IV.11) and Eq. (IV.12) according to the curve obtained with the double-control frequencies method.

In both LTHA and NLTHA, two different f_p were calculated for the structure and the soil, as well as two different reference damping values were assigned to the masonry (i.e.

5%) and to the soil (i.e. D_0 in Table IV.2). The sets of control frequencies, f_m and f_n , were evaluated, respectively, as follows:

- f_m as the minimum value between the fundamental soil frequency, f_{soil} , the fundamental fixed-base frequency, f_0 , or the input frequency, f_{input} ;
- f_n as $5f_{soil}$ or $5f_0$ if f_{input} was smaller than f_{soil} or f_0 , otherwise $f_n = f_{input}$.

In Section IV.1.2 and Section IV.2.4 the corresponding values are listed.

Two different types of masonry were considered, namely, rubble stone masonry and clay brick masonry. As the aim of the study was to obtain seismic fragility curves for classes of buildings through the cloud method, the masonry was modelled as an equivalent homogeneous material adopting the Mohr-Coulomb (MC) elasto-plastic constitutive model to limit the computational work. The elastic parameters, i.e. ρ , K and G , were set equal to the median values reported in Table C.8.5.1 of the Italian Building Code Commentary (MIT, 2019) for existing masonry buildings, as listed in Table IV.4. By contrast, the values of the strength parameters (friction angle, ϕ , and cohesion, c) reported in Table IV.4 were respectively set based on the friction coefficient, μ_s , and the MC criterion, by the following procedure.

Firstly, μ_s was computed following the expression (Augenti and Parisi 2019):

$$\mu_s = \frac{0.17}{\sqrt[3]{\sigma_0/\sigma_c}} \quad (IV.13)$$

at two values of σ_0/σ_c , respectively equal to:

- (i) the ratio between the compression stress, σ_0 , at the base of the above-ground structure under the static load computed through FLAC software (Figure IV.6) and the compression strength, σ_c , equal to the value reported in Table C.8.5.1 (MIT, 2019);
- (ii) $\sigma_0/\sigma_c = 1/3$, which is the typical stress level suggested by the code for the computation of the secant elastic moduli.

Thereafter, the tangent of the mean value of μ_s was assumed as the friction angle ϕ .

Table IV.4 Physical and mechanical properties of the selected masonry types

Material	ρ^* (kg/m ³)	G^* (MPa)	K^* (MPa)	σ_c (MPa)	σ_t (MPa)	μ^* (-)	ϕ (°)	c (MPa)
Rubble stone masonry	1900	290	14500	1.5*	0.15	0.53	27°	0.45
Clay brick masonry	1600	500	25000	3.45*	0.35	0.88	36°	0.87

*mean value.

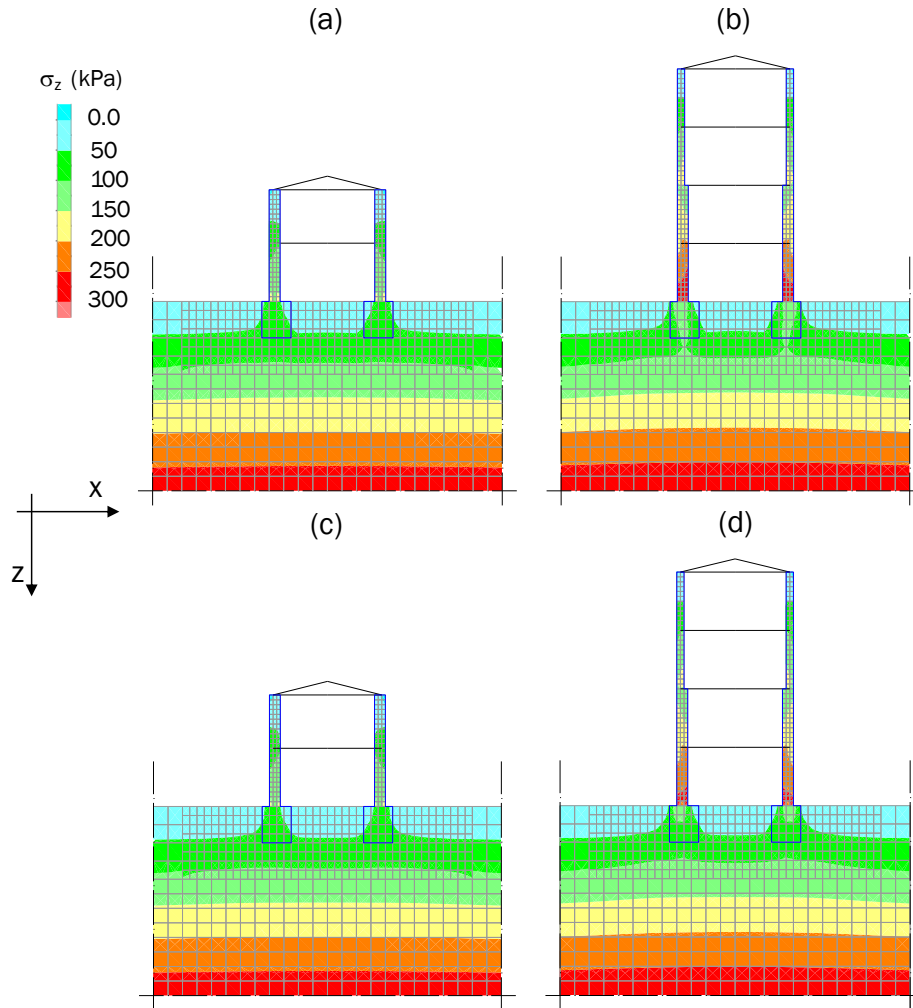


Figure IV.6 Vertical stresses after static analysis under gravity loads: rubble stone masonry (a) $h/b = 1$ (b) $h/b = 2$; clay brick masonry (c) $h/b = 1$ and (d) $h/b = 2$.

The cohesion, c , instead, was back-calculated based on the MC criterion. Assuming the compression strength positive, the shear failure envelope in the σ_1 - σ_3 plane (Figure IV.7) can be expressed as follows:

$$f_s = \sigma_1 - \sigma_3 k_p - 2c\sqrt{k_p} = 0 \quad (\text{IV.14})$$

where σ_1 and σ_3 are, respectively, the principal maximum and minimum stresses; k_p is the coefficient of passive earth pressure equal to:

$$k_p = \frac{1 + \sin\phi}{1 - \sin\phi} \quad (\text{IV.15})$$

By setting the maximum compressive strength, σ_c , the cohesion, c , is computed as:

$$c = \frac{\sigma_c}{2\sqrt{k_p}} \quad (IV.16)$$

A tensile cut-off equal to $\sigma_t=1/10 \sigma_c$ was also implemented in the model through tension failure criterion (Figure IV.7):

$$f_t = \sigma_3 - \sigma_t = 0 \quad (IV.17)$$

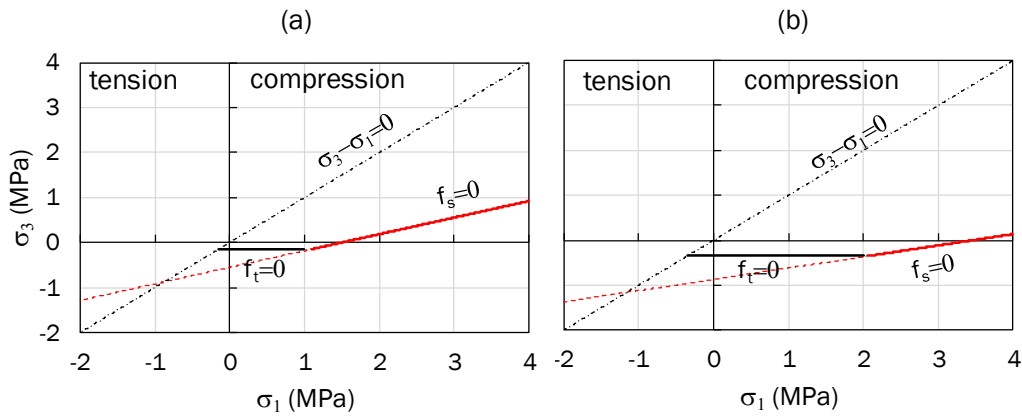


Figure IV.7 Mohr Coulomb elasto-plastic constitutive model for (a) rubble stone and (b) clay brick masonry.

The obtained values of c and ϕ , reported in Table IV.4, are also quite similar to those reported in the literature (i.e. Binda et al., 1994; Milosevic et al., 2013).

As described in Section III.1, the masonry walls are connected through 1D beam elements with the properties summarised in Table IV.5.

Table IV.5 Physical and mechanical properties of the floor beam materials

Structural component	ρ (kg/m ³)	E (MPa)	A (m ²)
Steel floor slab	1350	30000	0.35
Wooden roof truss	300	1300	0.31

IV.1.2. Numerical dynamic identification

A preliminary Numerical Dynamic Identification Analysis (NDIA) was performed on each configuration of soil and structure, in order to evaluate the corresponding frequencies, f_0 , and f^* (and hence the fundamental period of the SFS system, T^*). Those values were calculated using the same procedure described in Section III.2.

Differently from Chapter III, Rayleigh damping was assigned to both soil and structure, and the same noise signal with duration $t_1 = 5$ s (instead of 10s) to reduce the computational work. Therefore, the structural response was numerically monitored over 10 s to record the free-vibration behaviour of the SFS system after the end of the forced-vibration stage.

Table IV.6 outlines the values adopted for f_p and ξ_{min} . To define the correct intervals of frequencies for the structure, the NDIA on FB model was firstly performed with zero damping.

Table IV.6 Rayleigh damping parameters for different materials

Material	h/b	f_{soil} (Hz)	f_0 (Hz)	f_{input} (Hz)	f_m (Hz)	f_n (Hz)	f_p (Hz)	ξ_{min} (-)
Soil type A	-	10.0	-	-	3.24	10.00	5.70	0.017
Soil type D _{ho}	-	1.25	-	-	1.25	6.25	2.80	0.015
Soil type D _{he}	-	1.37	-	-	1.37	6.85	3.06	0.015
Rubble stone	1	-	2.56	3.24	2.56	12.80	5.72	0.037
	2	-	0.97	-	0.9	4.85	2.17	0.037
Clay brick	1	-	3.09	-	3.09	15.45	6.91	0.037
	2	-	1.14	-	1.14	5.40	2.55	0.037

The plots in Figure IV.8 a and b show, for each soil configuration (A, D_{ho} and D_{he}), the dynamic response of the two-storey rubble stone masonry building, respectively, in terms of displacement time histories at different elevations (a) and FFT computed in the free-vibration stage normalised to the maximum displacement resulting at the control points. The same results are shown in Figure IV.9, Figure IV.10 and Figure IV.11 for the rubble stone masonry structure with four storeys and the clay brick masonry building with two and four-storeys.

In each case, the SFS fundamental frequency, f^* , is clearly highlighted by spectral peaks, as also f_{soil} for the homogeneous and heterogenous type D soils. A slight but non-negligible reduction in the fundamental frequency of the SFS system under increasing soil deformability is shown by the two-storey structures, both in the case of rubble stone masonry building (Figure IV.8b) (f^* from 2.56Hz to 2.36Hz) and clay brick masonry building (Figure IV.10b) (f^* from 3.09Hz to 2.78Hz). Conversely, the fundamental frequency of the four-storey structures was found to be much less

affected by the soil type, evidencing $f^* = 0.97\text{Hz}$ and $f^* = 1.20\text{Hz}$ for the rubble stone and clay brick masonry structures.

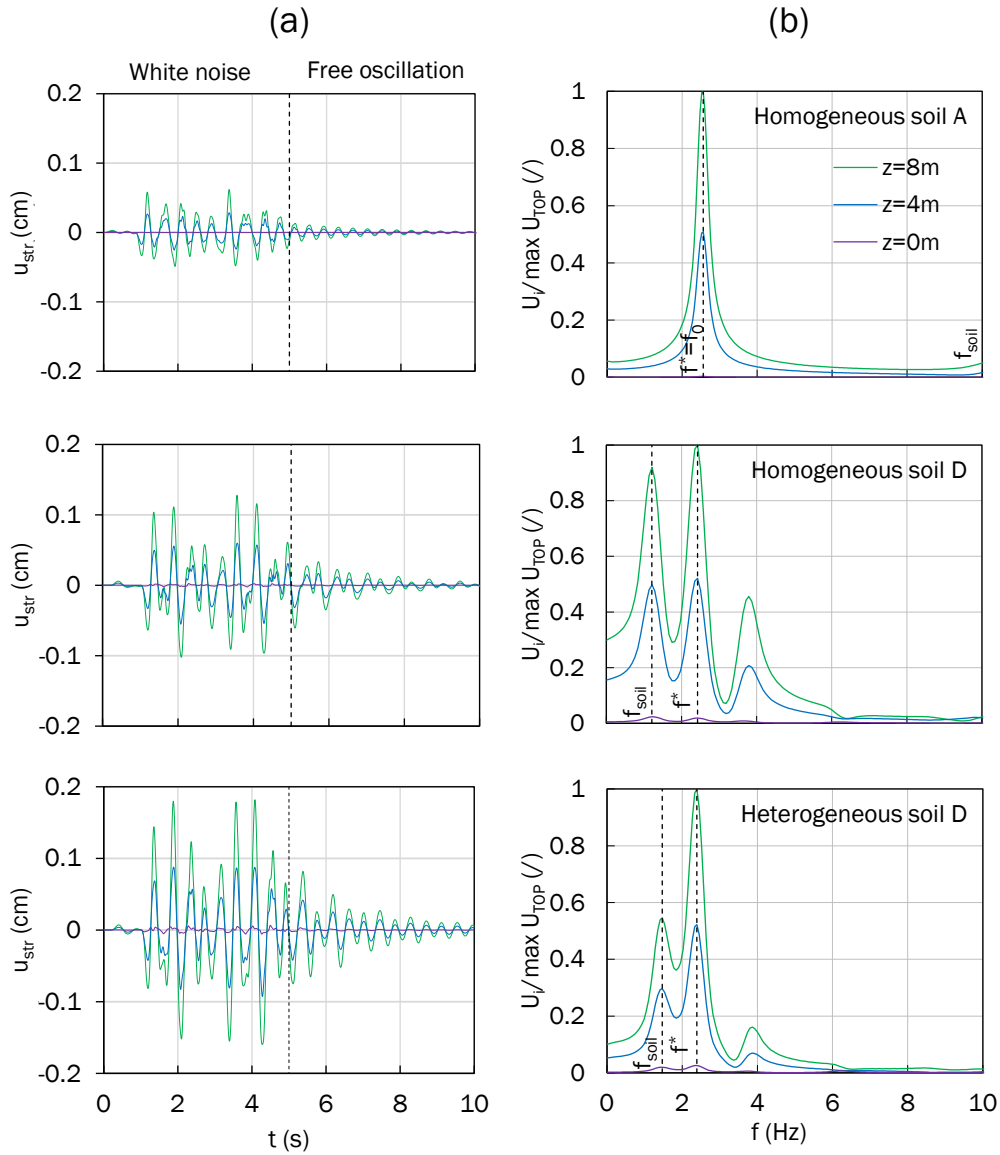


Figure IV.8 Dynamic response of Rs_1 on soil configurations A, D_{ho}, D_{he}: (a) time histories and (b) FFTs of horizontal displacements at different structural elevations.

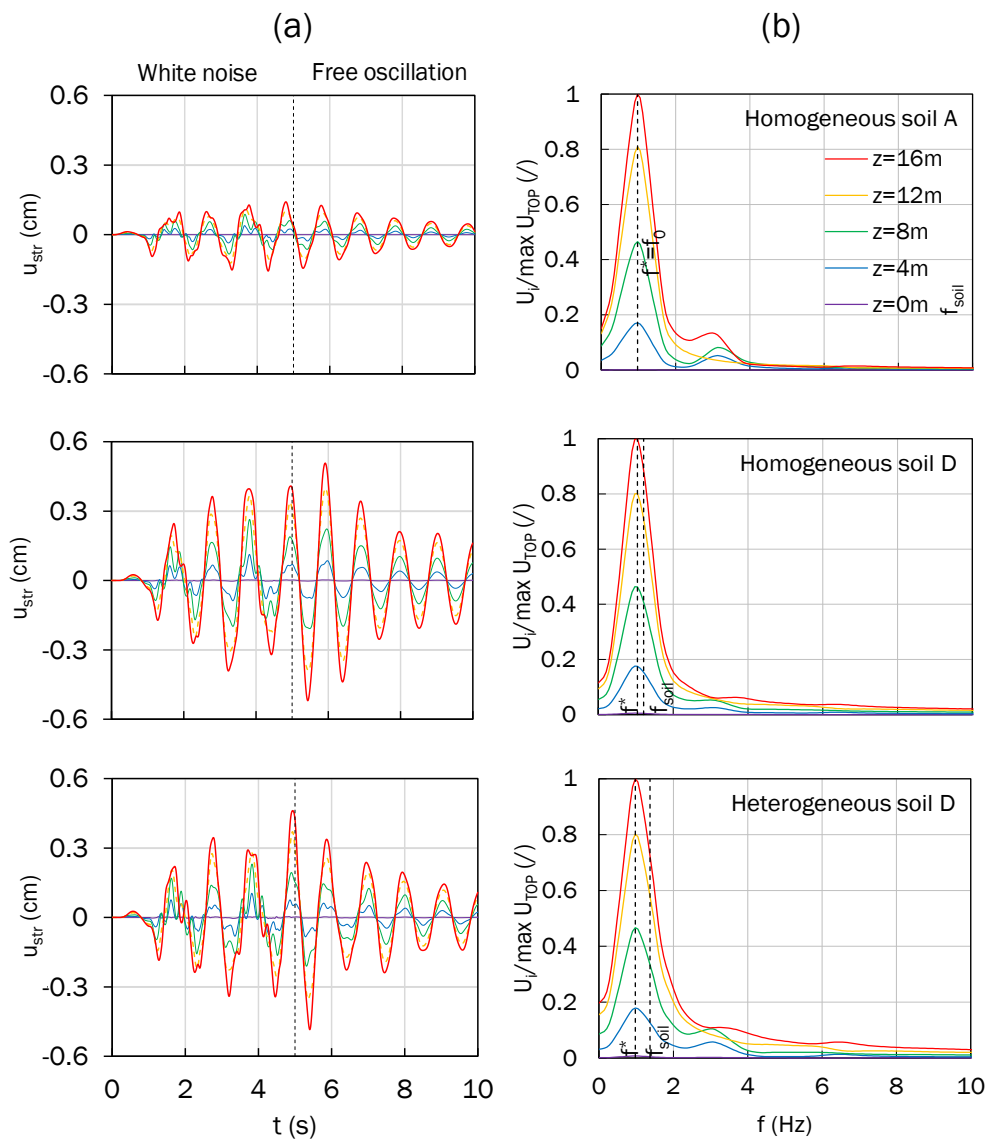


Figure IV.9 Dynamic response of Rs_2 on soil configurations A, D_{ho}, D_{ne}: (a) time histories and (b) FFTs of horizontal displacements at different structural elevations.

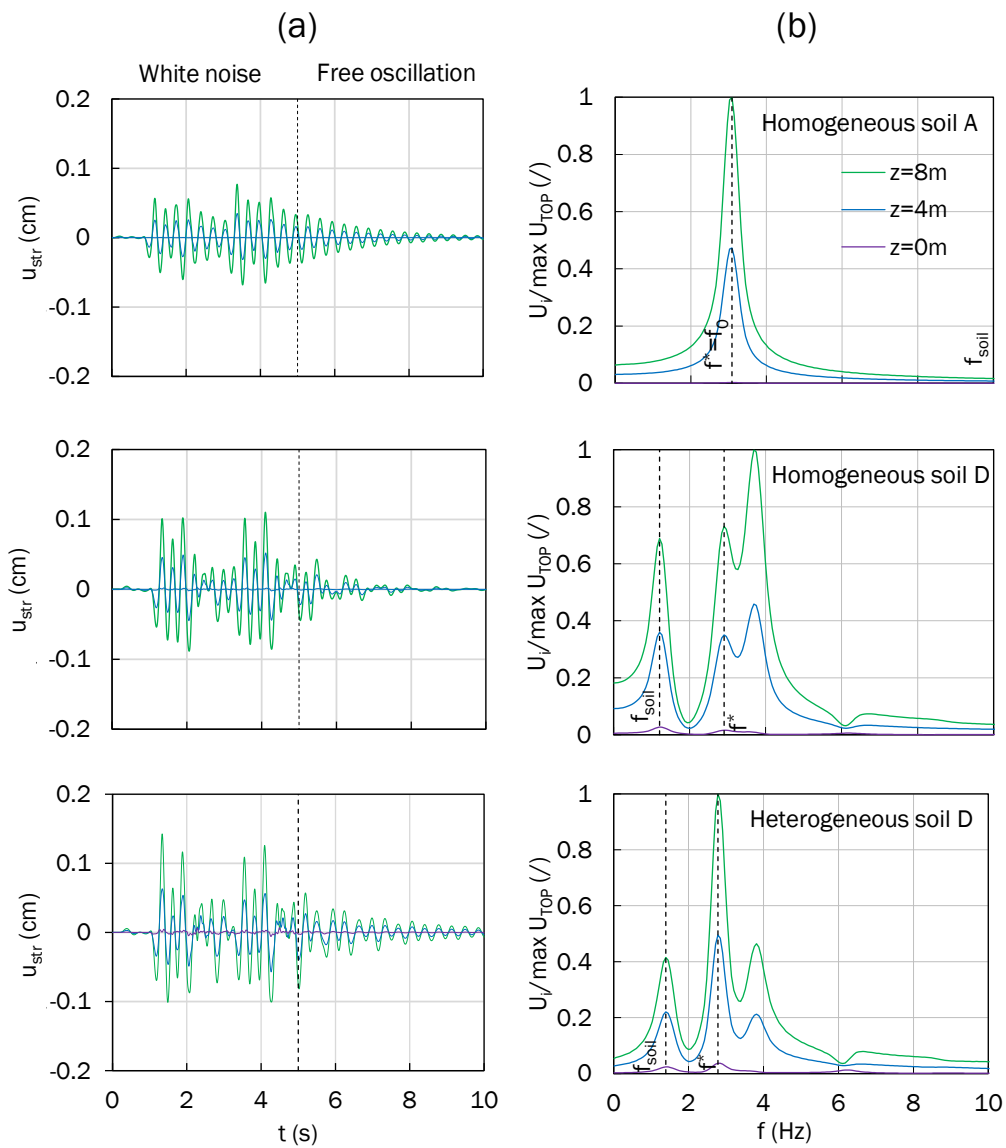


Figure IV.10 Dynamic response of Cb_1 on soil configurations A, D_{no}, D_{ne}: (a) time histories and (b) FFTs of horizontal displacements at different structural elevations.

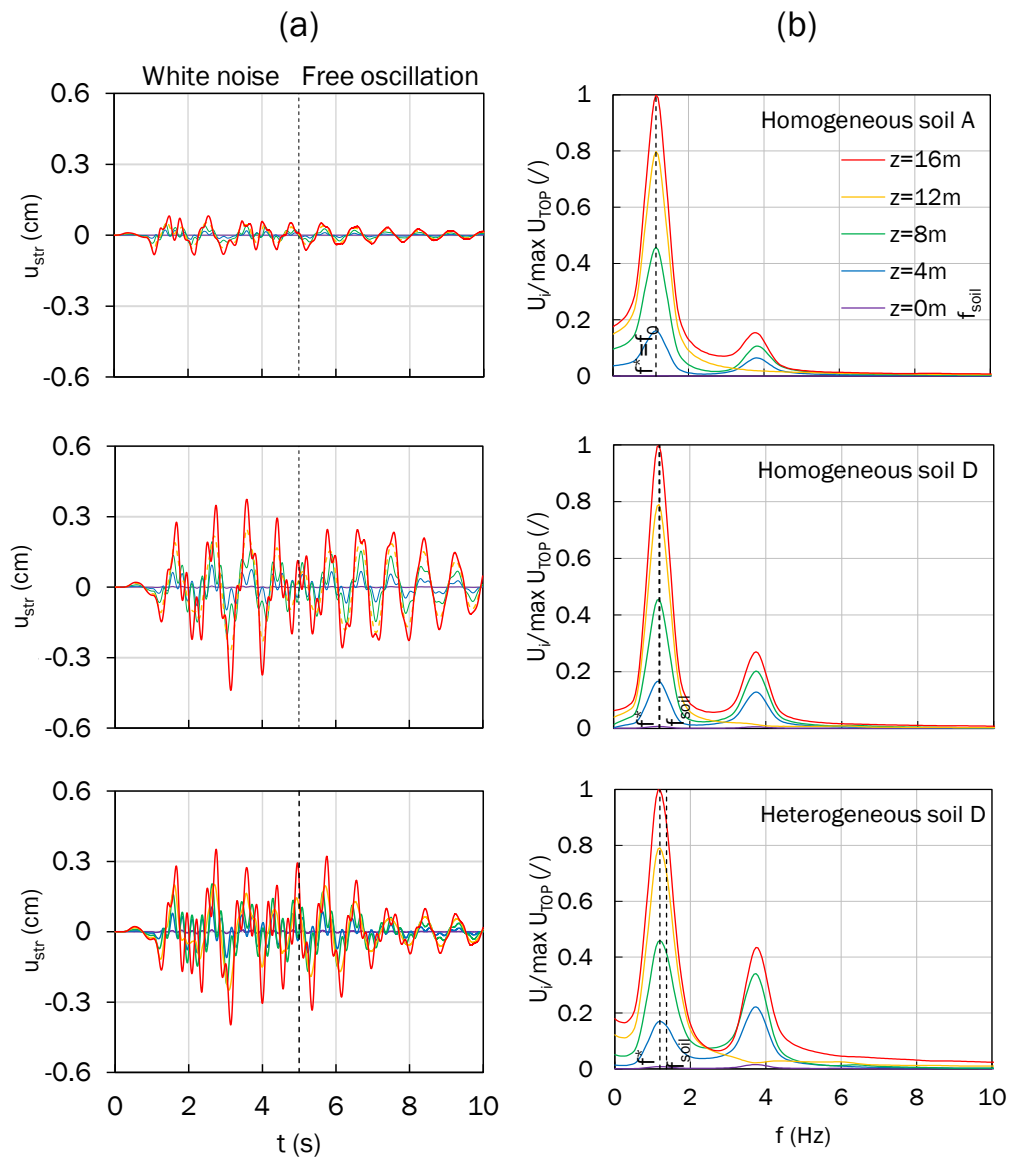


Figure IV.11 Dynamic response Cb_2 on soil configurations A, D_{no}, D_{he}: (a) time histories and (b) FFTs of horizontal displacements at different structural elevations.

In the case of squat structures ($h/b = 1$) with either soil D_{he} or D_{ho} , the FFT highlights two amplitude peaks that are respectively associated with f_{soil} and f^* , confirming that the dynamic behaviour is influenced by soil motion when the relative soil-structure stiffness is low (de Silva et al. 2018; Piro et al. 2020). By contrast, in the case of slender structures the FFT highlights only the amplitude peaks associated with the structural modes, i.e. the second mode at 4Hz in Figure IV.11b. It is also noted that the fixed-base fundamental frequency, f_0 , of the clay brick masonry structure is close to f_{soil} of soil D_{ho} causing an increase of displacements (Figure IV.11b).

Table IV.7 provides a summary of fundamental frequencies of the soil and SFS systems.

Table IV.7 Fundamental frequencies of soil and SFS systems

Structure material	Soil type	f_{soil} (Hz)	f^* (Hz)	
			$h/b = 1$	$h/b = 2$
Rubble stone	A	10.00	2.56	0.97
	D_{ho}	1.25	2.43	0.97
	D_{he}	1.37	2.39	0.97
Clay brick	A	10.00	3.09	1.20
	D_{ho}	1.25	2.91	1.20
	D_{he}	1.37	2.78	1.20

Figure IV.12 shows the comparison between the three components of the total SFS displacements (i.e. u_{str} , u_u and u_θ) of the two and four-storey masonry structure. It can be observed that the displacements induced by the rotation of the foundation are quite small with respect to those induced by the foundation translation. As already observed in Section III.2 and reported in Table IV.8 the IDR, calculated with Eq. (III.1) for $h/b = 1$, are quite similar for both the storeys (red characters in Table IV.8).

Table IV.8 Inter-story drift ratio of the SFS systems

Soil type	$Z_j \div Z_{j+1}$ (m)	<i>Rs masonry building</i>		<i>Cb masonry building</i>	
		<i>IDR_j (%)</i>		<i>IDR_j (%)</i>	
		<i>h/b = 1</i>	<i>h/b = 2</i>	<i>h/b = 1</i>	<i>h/b = 2</i>
A	-2.5÷0	0.0000	0.0000	0.0000	0.0000
	0÷4	0.0014	0.0036	0.0028	0.0016
	4÷8	0.0014	0.0062	0.0032	0.0029
	8÷12	-	0.0072	-	0.0034
	12÷16	-	0.0040	-	0.0020
D _{ho}	-2.5÷0	0.0001	0.0004	0.0001	0.0003
	0÷4	0.0024	0.0138	0.0014	0.0078
	4÷8	0.0023	0.0235	0.0016	0.0142
	8÷12	-	0.0276	-	0.0166
	12÷16	-	0.0162	-	0.0105
D _{he}	-2.5÷0	0.0005	0.0003	0.0005	0.0003
	0÷4	0.0058	0.0101	0.0038	0.0066
	4÷8	0.0056	0.0170	0.0042	0.0118
	8÷12	-	0.0197	-	0.0135
	12÷16	-	0.0117	-	0.0085

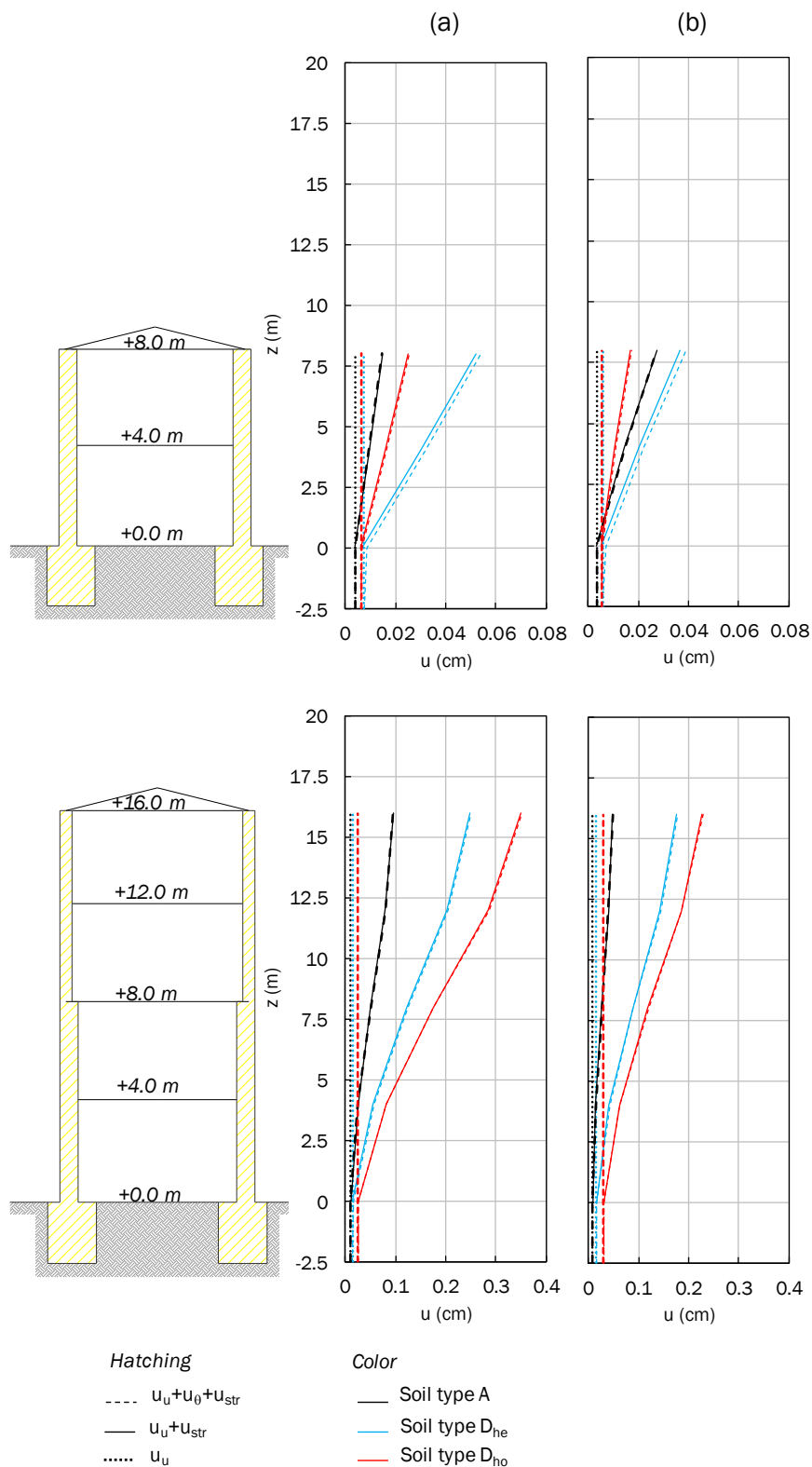


Figure IV.12 Profiles of the displacement components of the SFS models: (a) rubble stone and (b) clay brick masonry structure

IV.2. Cloud analysis

IV.2.1. Selection of strong ground motion records

As described in Section II.3 the construction of fragility curves through the cloud analysis method needs the definition of a set of ground motions to account for the record-to-record variability (Jalayer et al. 2015), which represents the only source of uncertainty considered in this study.

The database used is SIMBAD (Selected Input Motions for displacements-Based Assessment and Design) by Smerzini et al., (2014). The database counts 467 records (each constituted by the three components of the ground motion), which were generated by 130 seismic events occurred all around the world. The distribution of the 467 records, divided by soil type, is depicted in Figure IV.13, in terms of peak ground acceleration (PGA) of the X component versus moment magnitude (M_w) and epicentral distance (R).

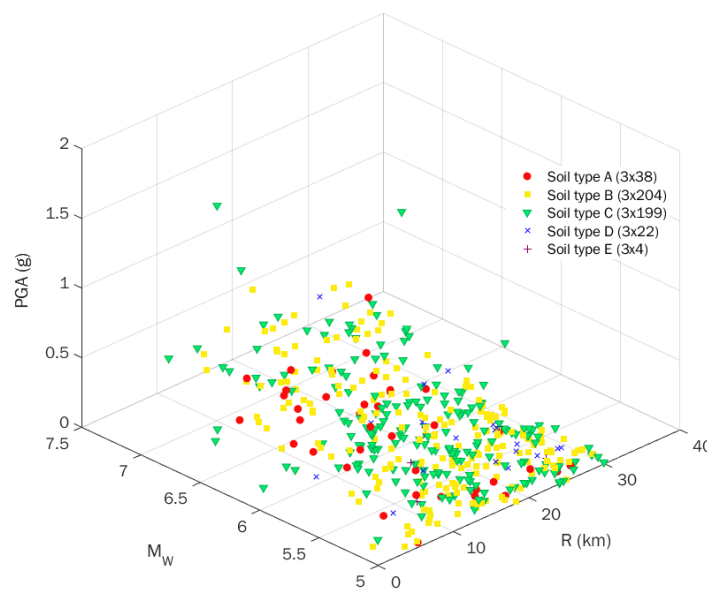


Figure IV.13 PGA- M_w - R distribution for the SIMBAD database

A set of 15 ground motions was selected in order to analyse the dynamic structural response, based on the following criteria:

- to consider a wide range of $S_a(T^*)$, i.e. [0.01g - 3.00g], for structures with either $h/b = 1$ or $h/b = 2$ to study the behaviour of the structures until the collapse;
- to avoid records of the same seismic events;
- to select records on soil types A and B ($V_{s30} > 500$ m/s), being site effects properly analysed in the coupled SFS analysis.

Figure IV.14a and b show the acceleration spectra and the PGA-M_w-R distribution of the selected ground motions. The red and black dashed lines identify the limits of the range of the SFS fundamental periods, whereas the green dashed-dotted lines represent the soil fundamental periods.

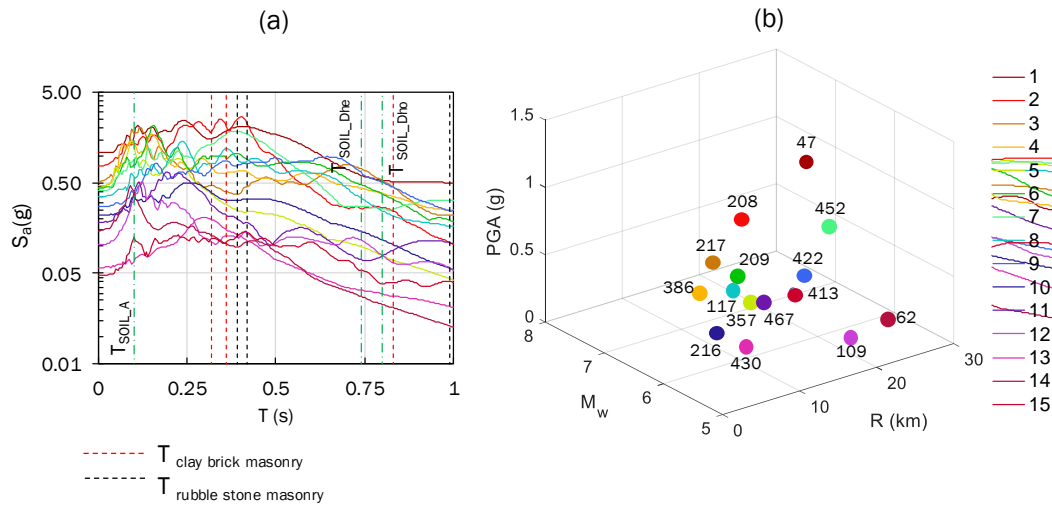


Figure IV.14 Set of the selected ground motions: (a) acceleration response spectra and (b) PGA-M_w-R distribution

Table IV.9 Properties of the selected records.

ID	ID _{SIM}	Earthquake	Date	M _w	R (km)	Soil type	V _{s30} (m/s)	Comp.	PGA (g)
1	47	Rumoi	14-12-2004	5.7	8.08	B	579	X	1.15
2	208	Duzce	12-11-1999	7.1	27.16	B	481	Y	0.91
3	217	Olfus	29-05-2008	6.3	8.89	A	/	X	0.67
4	386	Christchurch	13-06-2011	6	5.10	A*	/	Y	0.57
5	357	Christchurch	22-02-2011	5.6	8.42	A*	/	X	0.55
6	209	Bingol	01-05-2003	6.3	11.79	B	529	Y	0.52
7	452	Loma Prieta	18-10-1989	6.9	28.57	A	1428	X	0.47
8	117	South Iceland	21-06-2000	6.4	12.15	B	/	Y	0.40
9	422	Friuli 1 st S	06-05-1976	6.4	21.72	B	522	X	0.31
10	216	Parkfield	28-09-2004	6	7.14	A	1340	X	0.25
11	467	Kozani MS	13-05-1995	6.5	16.69	A	/	X	0.21
12	109	Anza	12-06-2005	5.2	18.45	A	/	Y	0.18
13	430	Friuli 4 th S	15-09-1976	5.9	10.04	A	901	Y	0.13
14	62	Kyushu	09-09-1996	5.7	27.04	A	889	Y	0.06
15	413	Irpinia	23-11-1980	6.9	23.77	A	1149	Y	0.06

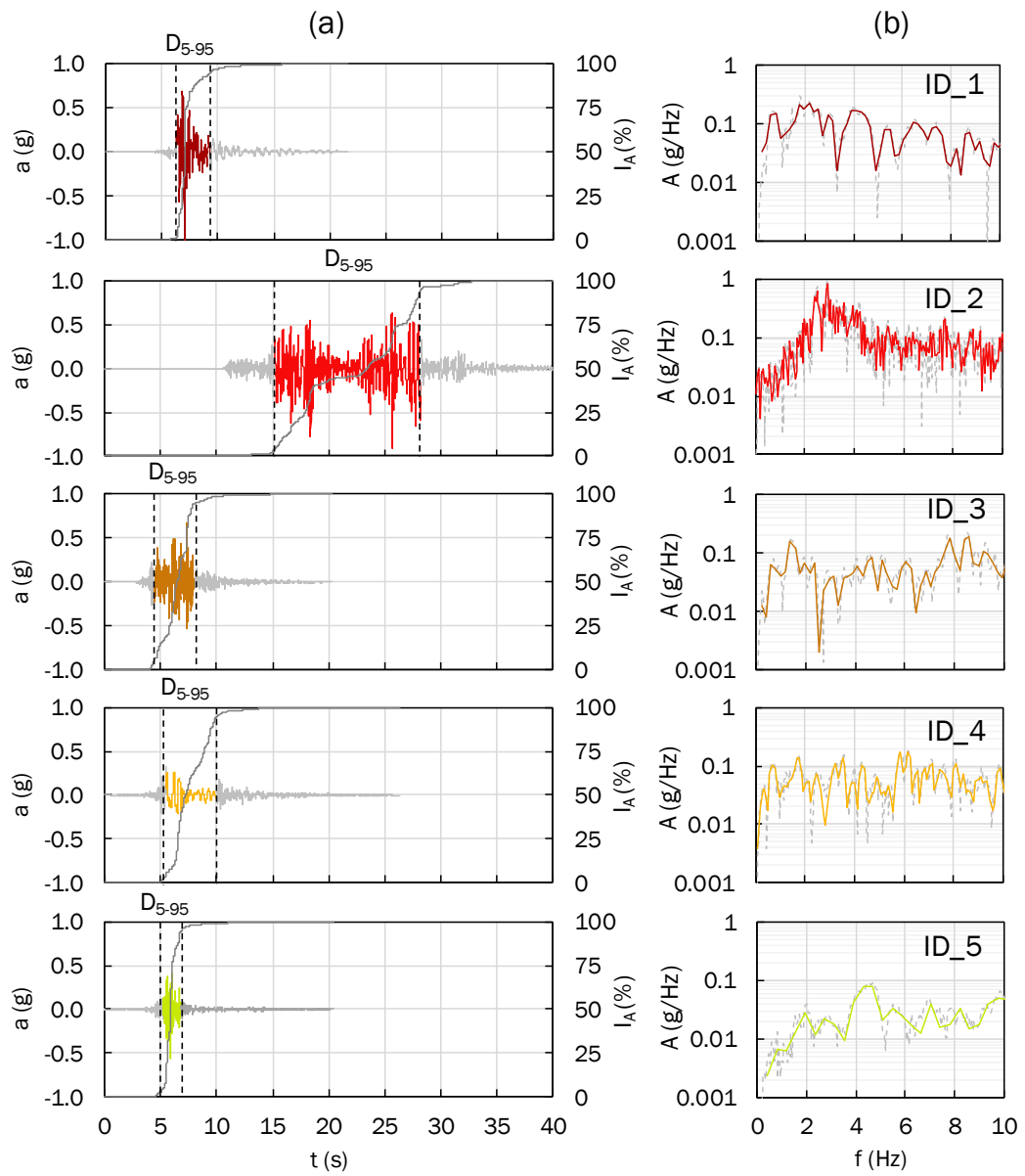


Figure IV.15 Ground motion records used in the analyses: (a) accelerograms and (b) FFT

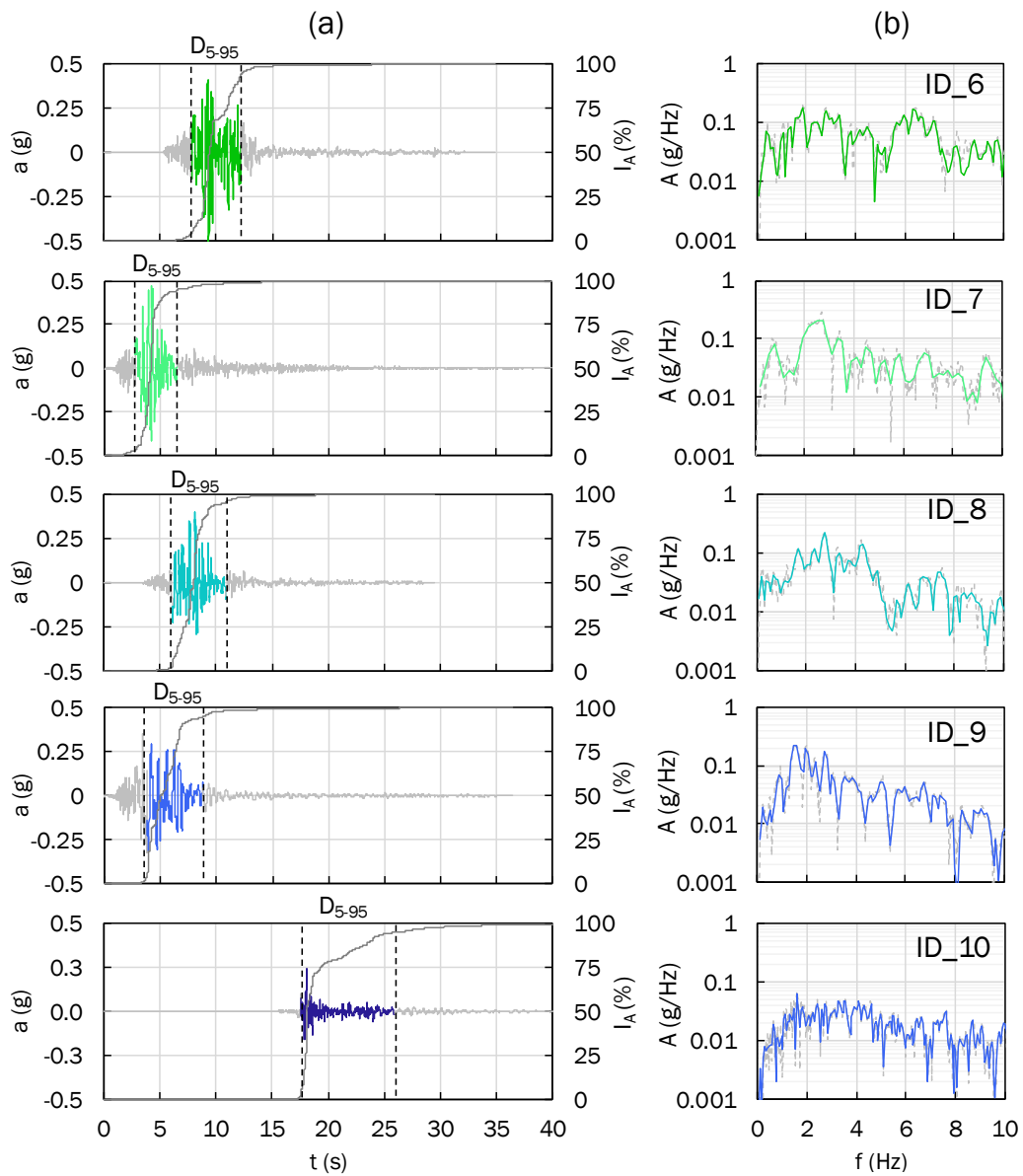


Figure IV.15 Continued

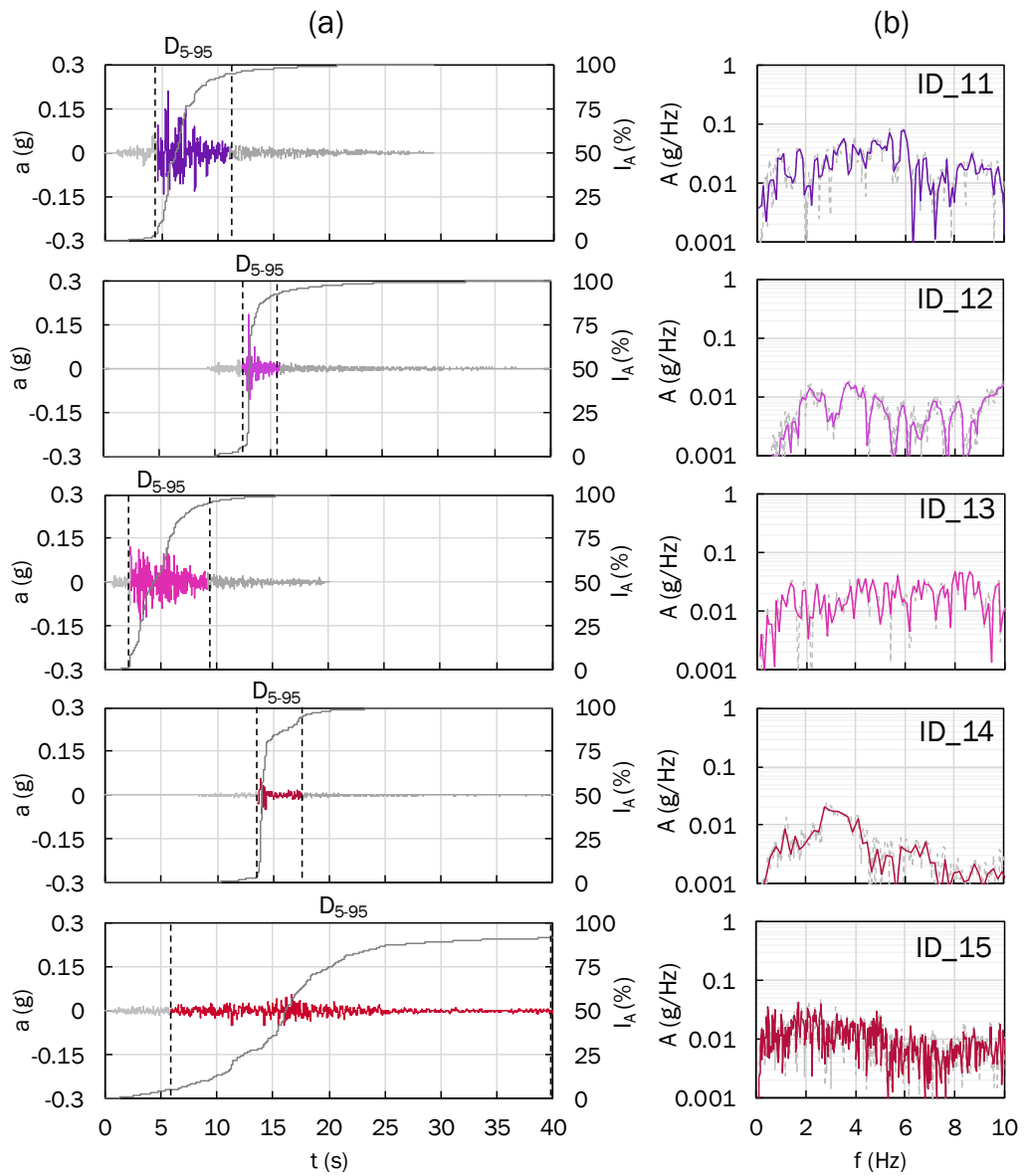


Figure IV.15 Continued

In Table IV.9 the main properties of each selected ground motion are reported; in Figure IV.15 the accelerogram and the corresponding FFT of each ground motion are shown. A total number of 180 NLTHAs on SFS models were carried out using signals windowed over the significant duration D_{5-95} (coloured accelerograms), estimated between the 5%-95% of the Arias Intensity (I_A) to reduce the computational work.

IV.2.2. Intensity measures

To predict the demand of a structure, an intensity measure (IM) is required. The structural response, defined by an engineering demand parameter (EDP), can be expressed as a function of the IM through Eq. (II.19).

The IMs considered and tested in this study, can be grouped as follows:

- (i) peak measures: i.e. *PGA*, peak ground displacement, *PGD* and peak ground velocity, *PGV*;
- (ii) spectral measures:
 - first mode spectral acceleration $S_a(T^*)$;
 - mean geometric spectral acceleration:

$$S_{a,avg} = \sqrt{S_a(T^*)S_a(1.5T^*)} \quad (IV.18)$$

that considers an elongation of the fundamental period until $1.5T^*$ due to the nonlinear behaviour

- first mode spectral displacement $S_d(T^*)$
- (iii) integral measures:

- integral of the spectral acceleration:

$$I_{S_a} = \int_{T_1}^{T_2} S_a(T) dT \quad (IV.19)$$

evaluated between two periods, for instance those typically used in the microzonation studies, i.e. $[T_1-T_2] = 0.1 - 0.5s$ and $[T_1-T_2] = 0.1 - 2.0s$;

- Housner intensity, i.e. the integral of the spectral velocity $S_v(T)$:

$$I_H = \int_{T_1}^{T_2} S_v(T) dT \quad (IV.20)$$

evaluated in the same period intervals.

The choice of the IM to use in the EDP-IM correlation (see Section II.2) can significantly influence the uncertainty in the adopted PSDM and consequently the fragility functions. Hence, the selection of a proper IM assumes a major importance. In the literature the

criteria to select an optimal IM are efficiency, sufficiency and hazard computability (Minas and Galasso 2019). Efficiency indicates that the selected IM allows the best prediction of the EDP values, as it provides the lowest dispersion, $\beta_{EDP|IM}$ (see Eq.II.21), of $\eta_{EDP|IM}$ and/or the highest value of the coefficient of determination R^2 . Sufficiency means a statistical independence of the IM on other earthquake parameters, e.g. R and M_w . Hazard computability is related to the ability to assess seismic hazard at a given site through the selected IM. Currently, hazard maps as well as real-time shakemaps are represented in terms of PGA or S_a at specific periods, so the use of other IMs is more computationally demanding. For the aim of this study, the criterion used to select the optimal IM is the efficiency. All the IMs listed above were computed for the reference input motions, rather than the free-field surface motions or the FIM computed through NLTHA. Table IV.10 outlines the values of the peak and integral IMs computed for each selected ground motion, which are all independent of the soil and structure properties. On the other hand, the spectral IMs (S_a , $S_{a,avg}$ and S_d) depend on T^* , thus must be evaluated for each soil type and type of masonry structure; Table IV.11, Table IV.12, Table IV.13 and Table IV.14 summarise their values for the different SFS systems analysed

Table IV.10 Peak and integral IM values of selected records

	PGA (m/s ²)	PGV (m/s)	PGD (cm)	I _{H0.1-0.5s} (cm)	I _{H0.1-2s} (cm)	I _{Sa0.1-0.5s} (m/s)	I _{Sa0.1-2s} (m/s)
1	11.29	73.32	9.92	40.06	180.60	8.54	17.72
2	8.92	36.26	7.36	37.88	72.86	7.95	7.15
3	6.59	32.20	6.85	13.32	88.09	3.47	8.64
4	5.55	39.23	9.59	15.61	94.51	3.75	9.27
5	5.43	12.14	1.06	8.69	18.69	2.32	1.83
6	5.11	34.27	10.28	20.19	82.70	4.60	8.11
7	4.64	33.95	8.03	27.93	97.77	5.50	9.59
8	3.92	26.00	10.34	18.90	72.81	3.95	7.14
9	3.09	30.08	6.34	15.74	80.05	3.16	7.85
10	2.41	14.58	1.42	7.58	24.86	1.63	2.44
11	2.04	8.46	1.47	6.13	23.74	1.55	2.33
12	1.81	3.86	0.29	2.69	5.55	0.66	0.54
13	1.27	6.35	1.12	3.51	15.33	0.92	1.50
14	0.63	3.33	0.46	2.75	7.84	0.57	0.77
15	0.55	5.06	2.01	2.45	15.40	0.52	1.51

IV.EFFECTS OF SFS INTERACTION ON NONLINEAR DYNAMIC RESPONSE AND SEISMIC
FRAGILITY OF MASONRY BUILDINGS

Table IV.11 Spectral IMs of selected records for two-storey rubble stone masonry buildings
($h/b = 1$).

	Soil A			Soil D _{ho}			Soil D _{he}		
	S _a (T*) (m/s ²)	S _{a,avg} (m/s ²)	S _d (T*) (cm)	S _a (T*) (m/s ²)	S _{a,avg} (m/s ²)	S _d (T*) (cm)	S _a (T*) (m/s ²)	S _{a,avg} (m/s ²)	S _d (T*) (cm)
1	22.30	16.41	6.02	22.51	15.43	9.58	22.03	14.30	10.32
2	27.05	11.53	8.16	27.80	10.66	11.84	19.96	8.25	9.35
3	4.19	4.49	1.49	4.84	5.26	2.06	5.23	5.97	2.45
4	7.71	7.26	1.95	7.70	7.11	3.28	7.06	6.47	3.31
5	2.62	2.02	1.02	2.44	1.84	1.04	2.42	1.80	1.13
6	11.03	9.72	3.43	9.96	8.98	4.24	8.88	8.11	4.16
7	19.90	11.15	5.44	18.98	9.88	8.08	17.46	8.51	8.18
8	10.18	8.40	3.92	9.18	7.87	3.91	9.70	7.85	4.54
9	8.30	8.79	2.95	8.70	9.26	3.71	8.97	9.56	4.20
10	3.49	2.94	1.11	3.55	2.82	1.51	3.60	2.69	1.69
11	2.18	1.86	0.77	1.91	1.67	0.81	1.81	1.54	0.85
12	1.00	0.68	0.35	1.11	0.66	0.47	1.18	0.65	0.55
13	1.36	1.31	0.43	1.52	1.35	0.32	1.38	1.27	0.65
14	1.49	0.93	0.59	1.34	0.84	0.57	1.20	0.76	0.56
15	1.30	1.25	0.37	1.46	1.26	0.62	1.33	1.12	0.62

Table IV.12 Spectral IMs of selected records for four-storey rubble stone masonry buildings
($h/b = 2$).

	Soil A			Soil D _{ho}			Soil D _{he}		
	S _a (T*) (m/s ²)	S _{a,avg} (m/s ²)	S _d (T*) (cm)	S _a (T*) (m/s ²)	S _{a,avg} (m/s ²)	S _d (T*) (cm)	S _a (T*) (m/s ²)	S _{a,avg} (m/s ²)	S _d (T*) (cm)
1	4.81	4.77	11.94	4.81	4.77	11.94	4.81	4.77	11.94
2	1.21	0.88	3.00	1.21	0.88	3.00	1.21	0.88	3.00
3	2.40	2.18	5.97	2.40	2.18	5.97	2.40	2.18	5.97
4	3.07	2.90	7.62	3.07	2.90	7.62	3.07	2.90	7.62
5	0.41	0.28	1.02	0.41	0.28	1.02	0.41	0.28	1.02
6	2.04	1.70	5.06	2.04	1.70	5.06	2.04	1.70	5.06
7	3.15	2.56	7.82	3.15	2.56	7.82	3.15	2.56	7.82
8	1.82	1.59	4.51	1.82	1.59	4.51	1.82	1.59	4.51
9	2.81	1.71	6.97	2.81	1.71	6.97	2.81	1.71	6.97
10	0.64	0.49	1.59	0.64	0.49	1.59	0.64	0.49	1.59
11	1.19	0.59	2.95	1.19	0.59	2.95	1.19	0.59	2.95
12	0.13	0.08	0.33	0.13	0.08	0.33	0.13	0.08	0.33
13	0.63	0.35	1.56	0.63	0.35	1.56	0.63	0.35	1.56
14	0.27	0.18	0.67	0.27	0.18	0.67	0.27	0.18	0.67
15	0.48	0.45	1.20	0.48	0.45	1.20	0.48	0.45	1.20

Table IV.13 Spectral IMs of selected records for two-storey clay brick masonry buildings
($h/b = 1$).

	Soil A			Soil D _{ho}			Soil D _{ne}		
	S _a (T*) (m/s ²)	S _{a,avg} (m/s ²)	S _d (T*) (cm)	S _a (T*) (m/s ²)	S _{a,avg} (m/s ²)	S _d (T*) (cm)	S _a (T*) (m/s ²)	S _{a,avg} (m/s ²)	S _d (T*) (cm)
1	17.35	17.89	4.79	19.39	17.85	6.02	20.39	17.75	6.69
2	24.27	16.12	6.69	26.30	14.35	8.16	23.02	12.47	7.56
3	5.09	5.43	1.40	4.80	4.88	1.49	4.57	4.84	1.50
4	6.68	6.13	1.84	6.29	5.92	1.95	6.46	6.12	2.12
5	3.76	2.92	1.04	3.28	2.59	1.02	3.07	2.40	1.01
6	10.89	9.71	3.00	11.07	9.93	3.43	10.31	9.56	3.38
7	15.04	13.41	4.15	17.53	13.16	5.44	18.69	12.77	6.13
8	9.35	8.34	2.58	12.62	9.39	3.92	13.13	9.70	4.31
9	8.33	9.14	2.30	9.52	9.16	2.95	9.56	9.10	3.14
10	3.90	3.65	1.08	3.59	3.36	1.11	3.51	3.24	1.15
11	2.88	1.82	0.80	2.49	1.92	0.77	2.40	1.93	0.79
12	1.27	1.06	0.35	1.13	0.92	0.35	1.08	0.86	0.35
13	1.17	1.09	0.32	1.38	1.32	0.43	1.42	1.37	0.47
14	2.18	1.35	0.60	1.90	1.19	0.59	1.74	1.11	0.57
15	1.34	1.20	0.37	1.21	1.11	0.37	1.19	1.13	0.39

Table IV.14 Spectral IMs of selected records for two-storey clay brick masonry buildings
($h/b = 2$).

	Soil A			Soil D _{ho}			Soil D _{ne}		
	S _a (T*) (m/s ²)	S _{a,avg} (m/s ²)	S _d (T*) (cm)	S _a (T*) (m/s ²)	S _{a,avg} (m/s ²)	S _d (T*) (cm)	S _a (T*) (m/s ²)	S _{a,avg} (m/s ²)	S _d (T*) (cm)
1	5.26	5.01	9.18	5.26	5.01	9.18	5.26	5.01	9.18
2	2.59	1.59	4.52	2.59	1.59	4.52	2.59	1.59	4.52
3	4.74	3.59	8.27	4.74	3.59	8.27	4.74	3.59	8.27
4	3.62	3.39	6.31	3.62	3.39	6.31	3.62	3.39	6.31
5	0.67	0.39	1.16	0.67	0.39	1.16	0.67	0.39	1.16
6	3.78	1.98	6.60	3.78	1.98	6.60	3.78	1.98	6.60
7	2.89	2.69	5.04	2.89	2.69	5.04	2.89	2.69	5.04
8	2.51	1.95	4.38	2.51	1.95	4.38	2.51	1.95	4.38
9	4.58	2.88	7.99	4.58	2.88	7.99	4.58	2.88	7.99
10	1.04	0.69	1.82	1.04	0.69	1.82	1.04	0.69	1.82
11	1.06	0.84	1.84	1.06	0.84	1.84	1.06	0.84	1.84
12	0.18	0.12	0.32	0.18	0.12	0.32	0.18	0.12	0.32
13	0.71	0.53	1.25	0.71	0.53	1.25	0.71	0.53	1.25
14	0.35	0.23	0.61	0.35	0.23	0.61	0.35	0.23	0.61
15	0.45	0.48	0.79	0.45	0.48	0.79	0.45	0.48	0.79

IV.2.3. Engineering demand parameter and performance limit states for out-of-plane failure mechanisms

The engineering demand parameter selected to represent the OOP behaviour is the maximum inter-storey drift ratio (computed over all storeys), denoted as MIDR. For each analysis, the IDR was calculated according to the following equation:

$$IDR_j = \frac{u_{strj+1} - u_{strj}}{h_j} = \frac{\Delta u_{strj}}{h_j} \quad (III.1)$$

(also represented in Figure IV.16a) considering the time histories, at each control point (see Figure IV.3), of the relative flexural displacements, Δu_{str} , as shown in Figure IV.16b. The displacements related to the foundation rotation and translation were subtracted from u_{str} in order to consider only the response of the structure.

A static pushover analysis was not carried out, so the damage levels (DLs)/thresholds for OOP failure mechanisms were defined considering the values suggested by Lagomarsino (2015).

The DLs are defined as rate of the ultimate limit state in which the collapse of the wall is caused by the overturning, which takes place when the IDR is equal to (Lagomarsino 2015):

$$IDR_u = \frac{s}{2h} \quad (IV.21)$$

where s is the masonry wall thickness. In the case of rubble stone masonry, IDR_u was reduced by 35% (De Felice 2011) in order to account for nonlinearity effects and possible loss of the masonry integrity. Based on the limit states described in Section II.3, which are expressed as ratios of $d_0=s/2$, three IDR thresholds corresponding to as many DLs were defined to calculate the fragility functions:

- (i) DL1 corresponding to the formation of the tensile cracks at the toe of the wall, which was identified as IDR associated with the attainment of the tensile strength of masonry (see Figure IV.16b);
- (ii) DL2 corresponding to the activation of the rocking mechanism, which was assumed to be attained when IDR reaches:

$$IDR_{DL2} = 0.25IDR_u \quad (IV.22)$$

- (iii) DL3 near collapse due to overturning, which was assumed to be attained when IDR reaches:

$$IDR_{DL3} = 0.4IDR_u \quad (IV.23)$$

Figure IV.16b, c, and d show the time history of the minimum principal stress, σ_3 evaluated in the quadrilateral zone (red fill in Figure IV.16), the relative displacements,

and the corresponding IDR, respectively, in the case of two-storey clay brick masonry structure subjected to the input motion ID_4. It can be observed how as the tensile strength was reached, σ_3 does not assume negative values.

Table IV.15 summarises the IDR thresholds associated with different DLs and adopted to compute the fragility functions.

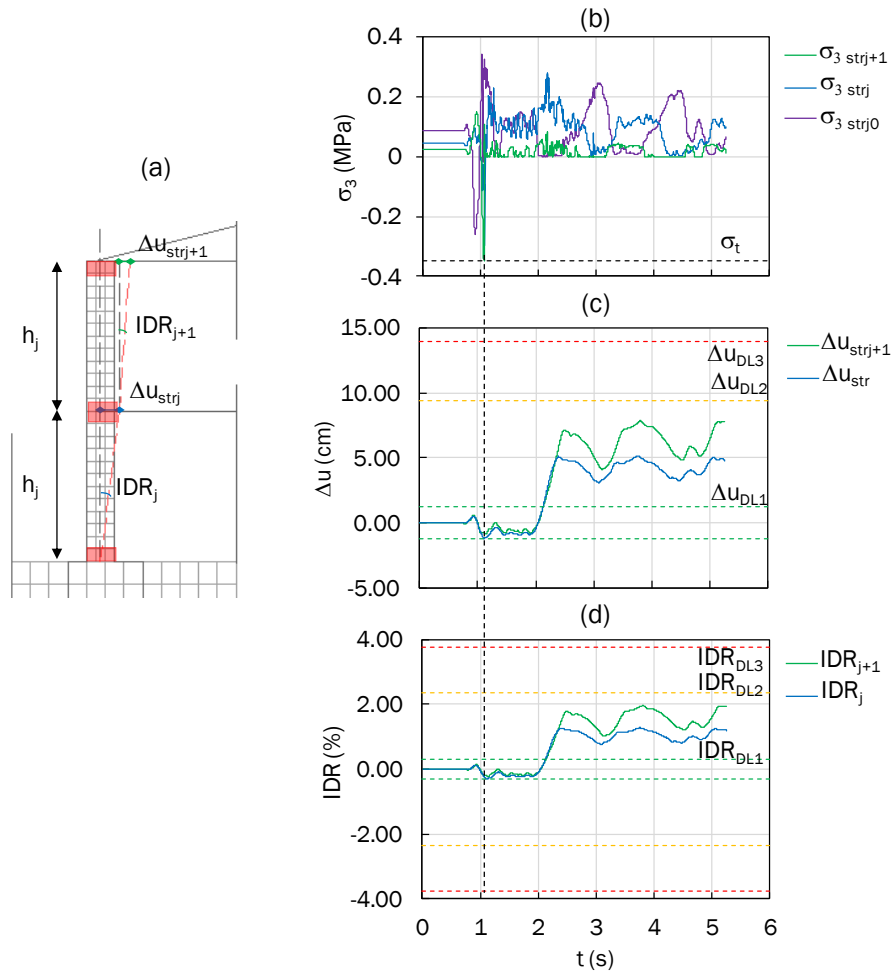


Figure IV.16 (a) Scheme of EDP, (b) time histories of σ_3 , (c) time histories of relative displacements, and (d) time histories of IDR (referred to ground motion ID4)

Table IV.15 IDR thresholds associated with different DLs

	DL1	DL2	DL3
$h/b = 1$ Rubble stone masonry	0.18%	1.52%	2.44%
$h/b = 2$ Rubble stone masonry	0.17%	1.02%	1.60%
$h/b = 1$ Clay brick masonry	0.30%	2.34%	3.80%
$h/b = 2$ Clay brick masonry	0.47%	1.56%	2.50%

IV.2.4. Setting of the Rayleigh damping ratio

NLTHA was carried out with FLAC software under the assumption of total stress analysis. As described in Section IV.1.1 Rayleigh damping was also assigned in addition to hysteretic damping. The control frequency, f_p , and the critical damping, ξ_{min} , were calculated following the procedure described in Section IV.1.1. They were applied to the numerical identification (Section IV.1.2) and to each ground motion, as summarised in Table IV.16 for the soil, and in Table IV.17 for the structures.

Table IV.16 Rayleigh damping parameters adopted for the soil in the analyses

ID	A ($f_{soil}=10$ Hz)					D _{ho} ($f_{soil}=1.25$ Hz)				D _{he} ($f_{soil}=1.37$ Hz)			
	f_{input} (Hz)	f_m (Hz)	f_n (Hz)	f_p (Hz)	ξ_{min} (%)	f_m (Hz)	f_n (Hz)	f_p (Hz)	ξ_{min} (%)	f_m (Hz)	f_n (Hz)	f_p (Hz)	ξ_{min} (%)
1	2.2	2.2	10.0	4.7	1.5	1.3	6.1	2.7	1.5	1.4	6.8	3.0	1.5
2	3.3	3.3	10.0	5.8	1.7	1.3	6.1	2.7	1.5	1.4	6.8	3.0	1.5
3	4.1	4.2	10.0	6.5	1.8	1.3	8.6	3.2	1.3	1.4	8.6	3.4	1.4
4	4.0	4.0	10.0	6.4	1.8	1.3	6.1	2.7	1.5	1.4	6.8	3.0	1.5
5	6.5	2.9	10.0	5.4	1.7	1.3	6.1	2.7	1.5	1.4	6.8	3.0	1.5
6	2.9	2.9	10.0	5.4	1.7	1.3	6.1	2.7	1.5	1.4	6.8	3.0	1.5
7	2.5	2.5	10.0	5.0	1.6	1.3	6.1	2.7	1.5	1.4	6.8	3.0	1.5
8	2.6	2.7	10.0	5.2	1.6	1.3	6.1	2.7	1.5	1.4	6.8	3.0	1.5
9	1.9	2.0	10.0	4.4	1.5	1.3	6.1	2.7	1.5	1.4	6.8	3.0	1.5
10	2.8	2.8	10.0	5.3	1.7	1.3	6.1	2.7	1.5	1.4	6.8	3.0	1.5
11	3.6	3.6	10.0	6.0	1.8	1.3	6.1	2.7	1.5	1.4	6.8	3.0	1.5
12	6.3	6.3	18.9	10.9	1.7	1.3	11.3	3.7	1.2	1.4	4.1	2.4	1.7
13	2.9	2.9	10.0	5.4	1.7	1.3	8.0	3.1	1.4	1.4	8.0	3.3	1.4
14	2.8	2.9	14.4	6.4	1.5	1.3	6.1	2.7	1.5	1.4	6.8	3.0	1.5
15	1.9	2.0	10.0	4.5	1.5	1.3	6.1	2.7	1.5	1.4	6.8	3.0	1.5

Table IV.17 Rayleigh damping parameters adopted for the structures in the analyses.

ID	h/b=1 Stone $f_0=2.56$ Hz					h/b=2 Stone $f_0=0.97$ Hz				h/b=1 Brick $f_0=3.09$ Hz				h/b=1 Brick $f_0=1.14$ Hz			
	f_{Input} (Hz)	f_m (Hz)	f_n (Hz)	f_p (Hz)	ξ_{min} (%)	f_m (Hz)	f_n (Hz)	f_p (Hz)	ξ_{min} (%)	f_m (Hz)	f_n (Hz)	f_p (Hz)	ξ_{min} (%)	f_m (Hz)	f_n (Hz)	f_p (Hz)	ξ_{min} (%)
1	2.2	2.2	12.8	5.4	3.7	1.0	4.9	2.2	3.7	2.2	11.2	5.0	3.7	1.20	6.0	2.7	3.7
2	3.3	2.6	12.8	5.7	3.7	1.0	4.9	2.2	3.7	3.0	15.2	6.8	3.7	1.20	6.0	2.7	3.7
3	4.2	2.6	12.8	5.7	3.7	1.0	4.9	2.2	3.7	3.0	15.2	6.8	3.7	1.20	6.0	2.7	3.7
4	4.0	2.6	12.8	5.7	3.7	1.0	4.9	2.2	3.7	3.0	15.2	6.8	3.7	1.20	6.0	2.7	3.7
5	2.9	2.6	12.8	5.7	3.7	1.0	4.9	2.2	3.7	2.9	14.7	6.6	3.7	1.20	6.0	2.7	3.7
6	2.9	2.9	9.3	4.1	3.7	1.0	4.9	2.2	3.7	2.9	14.7	6.6	3.7	1.20	6.0	2.7	3.7
7	2.5	2.5	12.7	5.7	3.7	1.0	4.9	2.2	3.7	2.5	12.7	5.7	3.7	1.20	2.5	1.8	4.7
8	2.7	2.6	12.8	5.7	3.7	1.0	4.9	2.2	3.7	2.7	13.4	6.0	3.7	1.20	2.7	1.8	4.6
9	2.0	2.0	8.1	3.6	3.7	1.0	4.9	2.2	3.7	2.0	9.9	4.4	3.7	1.20	6.0	2.7	3.7
10	2.8	2.8	8.1	3.6	3.7	1.0	4.9	2.2	3.7	2.8	14.1	6.3	3.7	1.20	6.0	2.7	3.7
11	3.6	2.6	12.8	5.7	3.7	1.0	4.9	2.2	3.7	3.0	15.2	6.8	3.7	1.20	6.0	2.7	3.7
12	6.3	2.6	12.8	5.7	3.7	1.0	6.3	2.5	3.4	3.0	15.2	6.8	3.7	1.20	6.3	2.8	3.7
13	2.9	2.6	12.8	5.7	3.7	1.0	4.9	2.2	3.7	2.9	14.7	6.6	3.7	1.20	6.0	2.7	3.7
14	2.9	2.6	12.8	5.7	3.7	1.0	4.9	2.2	3.7	2.9	14.4	6.4	3.7	1.20	2.9	1.9	4.6
15	2.0	2.0	8.4	3.8	3.7	1.0	4.9	2.2	3.7	2.0	9.9	4.4	3.7	1.20	6.0	2.7	3.7

IV.2.5. Performance assessment of SFS components

The soil amplification in *free-field* conditions was firstly investigated in terms of spectral ratios, $S_{a,s}/S_{a,b}$, between free-field surface motion and bedrock motion. The former acceleration spectra were obtained from the acceleration time histories predicted at the foundation level ($z=-2.5\text{m}$) in *free-field* conditions, i.e. at a distance of 18m from the structural model. The comparison between the spectral ratios computed at the foundation level for the soil configurations, D_{ho} and D_{he} , is shown in Figure IV.17a, and b, respectively.

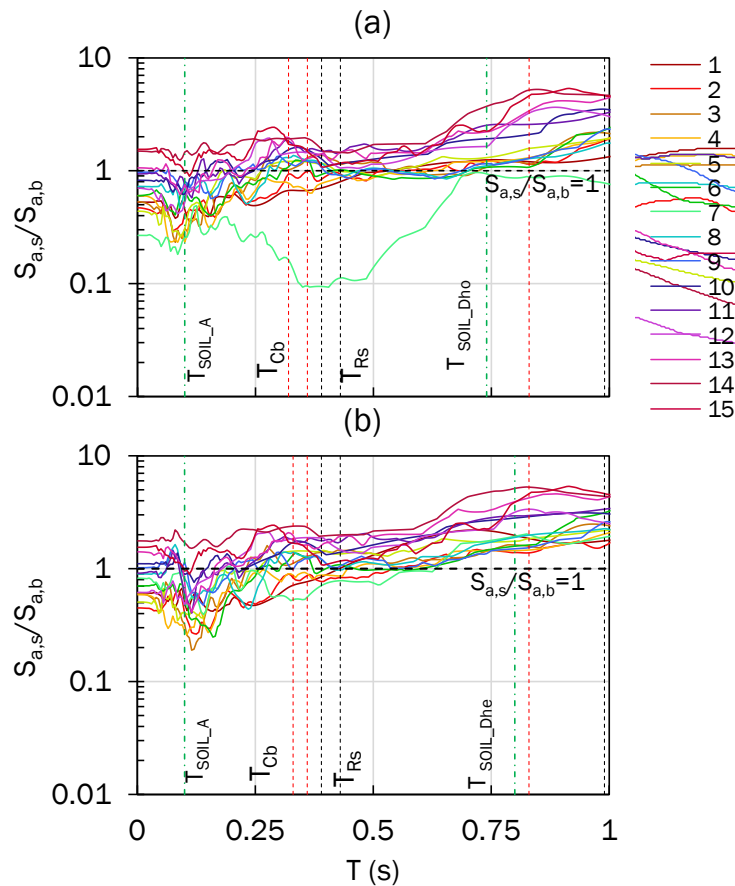


Figure IV.17 Soil amplification in terms of spectral ratios between free-field, at the foundation level, motion ($S_{a,s}$) and bedrock motion ($S_{a,b}$) for homogeneous (a) and heterogeneous (b) soil.

Under strong motions, significant reduction of PGA and of the spectral amplitudes (i.e. spectral ratios lower than unity) can be observed in the period range of the two-storey buildings, for both soft soil profiles. On the contrary, for weak motions the spectral amplitudes result amplified, $S_{a,s}/S_{a,b} > 1$, especially for the heterogeneous soil profile.

In the period range of four-storey buildings, instead, for both weak and strong motions the spectral amplitudes result amplified.

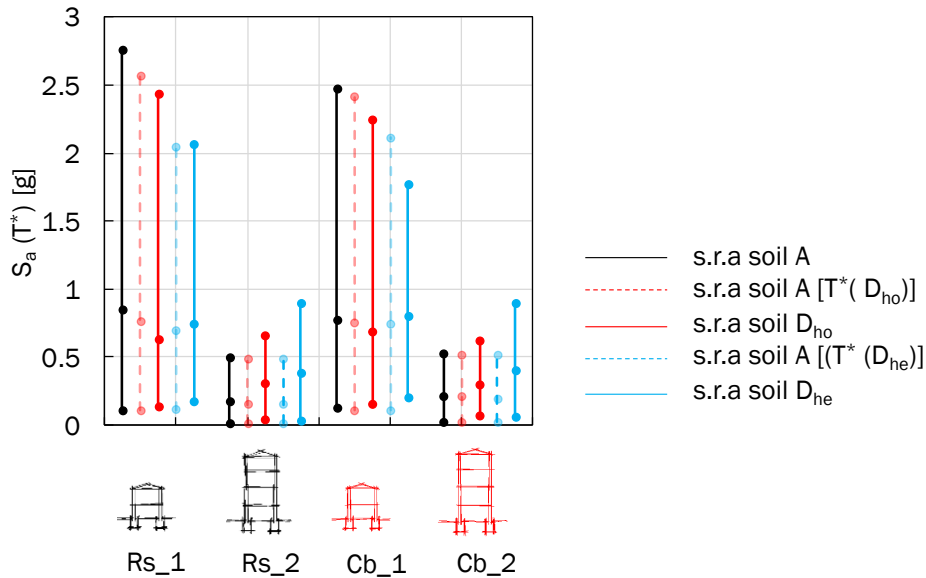


Figure IV.18 Comparison between the max-mean and min S_a .

This is also observed in Figure IV.18 which compares, for each building typology, the variations in maximum, mean and minimum values of S_a computed over all the ground motions to those associated with the input motions. It can be observed that, as max S_a is significantly reduced for the strong input motions, especially for the two-storey structures, the same does not occur for min S_a which instead increases for each building typology, highlighting the site amplification effects. The significant reduction of PGA and S_a , in case of strong motions, is a consequence of large shear strains, and of the related increase of mobilized damping.

Figure IV.19 shows the maximum values of IDR (MIDR) over all storeys as calculated according to Eq. (III.1) for all the 180 NLTHA. To better understand the SSI effects, the fixed base MIDR (black hollow circles) is also plotted.

Figure IV.20 reports the comparisons in terms of maximum shear strain, γ , maximum G/G_0 ratio and maximum damping ratio, D , between the *free-field* condition and the compliant-base models (i.e. D_{ho} and D_{he}), indicated as SFS. The latter were calculated as the maximum value between the mean γ , G/G_0 and D along the vertical a_{sx} and a_{dx} (see Figure IV.3) down to 16m, which represents the depth of the volume involved in the foundation motion (equal to $2b$), and in which higher strain levels are reached, (see shear strain contours in Figure IV.22 and Figure IV.26). The analysis results are

aggregated by soil configuration, i.e. homogeneous soil D (D_{ho}) Figure IV.20a, c, e and heterogeneous soil D (D_{he}) Figure IV.20b, d, f.

It can be observed that the MIDR predicted by the compliant-base models (i.e. D_{ho} and D_{he}) is greater with respect to the FB conditions, due to both site and SSI effects. On the other hand, the MIDR predicted by the homogeneous soft soil profile results, on average, lower with respect to the heterogeneous profile, since in the former case lower shear strains are reached in the soil volume affected by the foundation motion. On the contrary, for strong motions the MIDR calculated for the homogeneous soft soil profile results higher with respect to the heterogeneous profile, since higher shear strains are reached in the soil volume affected by the foundation motion, leading to a higher damping ratio, and lower stiffness (see G/G_0 in Figure IV.20), as shown by comparing Figure IV.20.

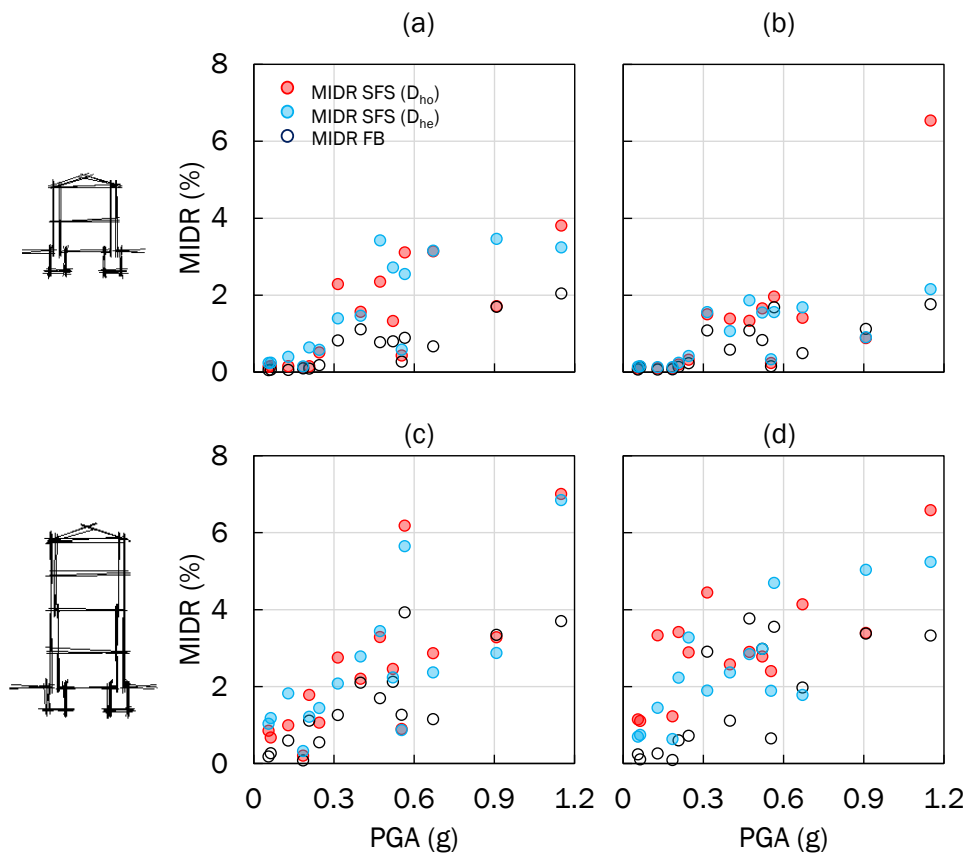


Figure IV.19 Scatter plots of the maximum IDR for FB and compliant-base models versus the PGA for two-storey (a) rubble and (b) clay brick masonry structure, and for four-storey (c) rubble stone and (d) clay brick masonry structure computed for the selected set of ground motions

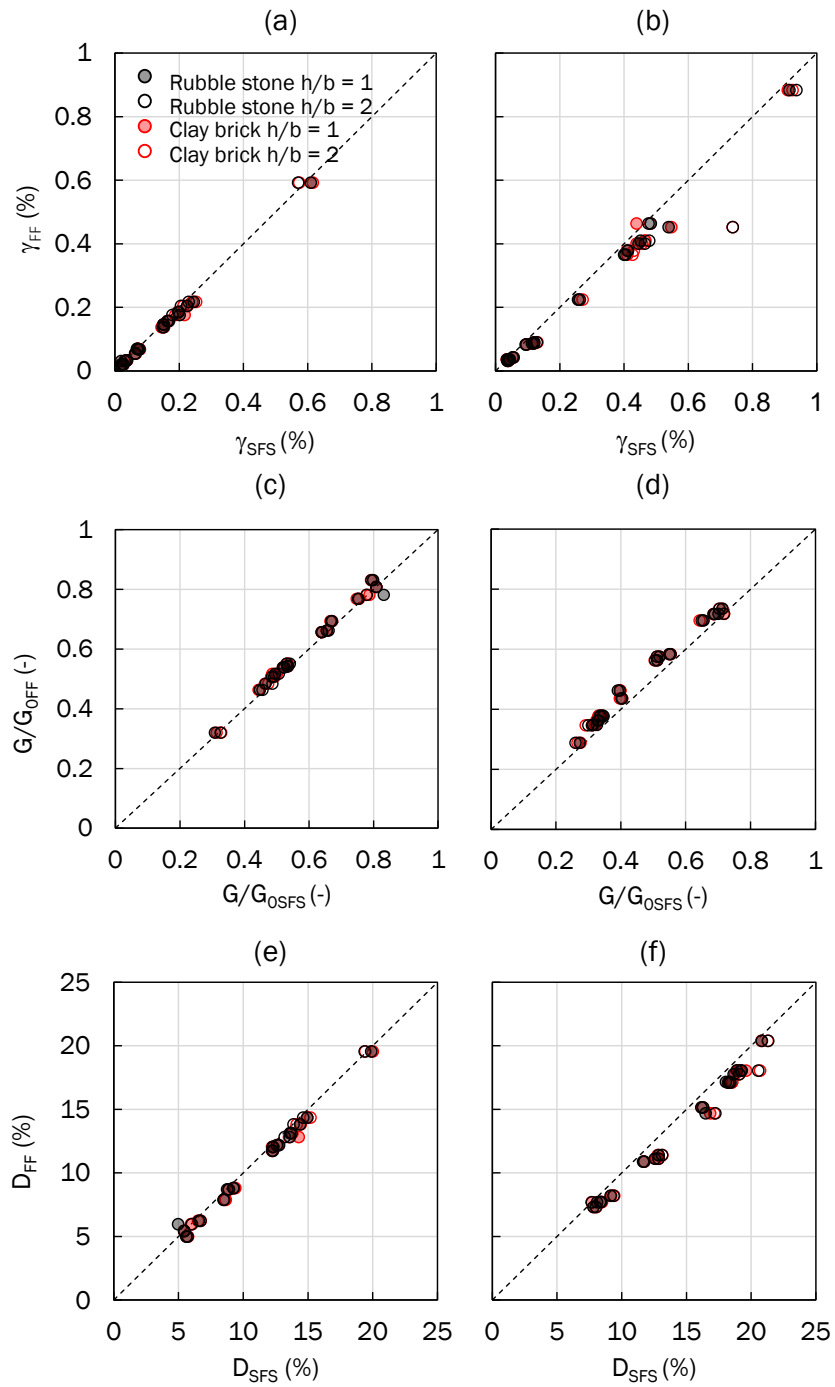


Figure IV.20 Scatter plots of the: maximum γ in FF condition versus maximum γ calculated in the SFS models for (a) homogeneous and (b) heterogeneous soil; maximum G/G_0 in FF condition versus maximum G/G_0 calculated in the SFS models for (c) homogeneous and (d) heterogeneous soil and maximum D in FF condition versus maximum D calculated in the SFS models for (e) homogeneous and (f) heterogeneous soil

Generally, the MIDR values of the four-storey structures are greater than the two-storey ones, mainly due to the reduced masonry thickness (from 0.75m to 0.50m) and consequentially to lower ultimate IDR capacity. The masonry material also influences the dynamic response: in fact, the rubble stone structures are more vulnerable with respect to the clay brick structures. An exception is represented by the four-storey clay brick masonry, for which the MIDR values are higher, mainly due to resonance effects between the soil and the building, since no significant differences are observed in the comparison with the FB MIDR.

To better understand the significant reduction for ID_1, observed for both $h/b = 1$ and $h/b = 2$ clay brick masonry structure, the performance assessment of the SFS components can be represented through the comparison between soil D_{ho} and soil D_{he} , in terms of:

- (i) evolution with time, at four different instants, of both plastic states and shear strain;
- (ii) relative displacements and the corresponding IDR;
- (iii) settlements, displacements and rotation at the foundation level.

The same results for both rubble stone and clay brick masonry under three ground motions, i.e. those characterized by the highest, mean and lowest $S_a(T^*)$, are reported in Appendix B.

Figure IV.21 and Figure IV.22 represent the evolution with time of plastic states and shear strain, respectively. As above mentioned, the clay brick structure on soil D_{he} presents less widespread plastic zones with respect to soil D_{ho} , i.e. less zones in which the tensile strength is reached (yellow zones), mainly due to the failure of the lower soil layers (red zone) where the failure envelope is reached. As apparent in Figure IV.22 large strain levels are attained in these zones, inducing high hysteretic damping and, consequently, a lower motion transmitted to the structure (see Figure IV.17c).

With reference to $h/b = 1$ and $h/b = 2$, Figure IV.23 and Figure IV.24 show in detail the comparison between the relative displacements and the corresponding IDR (Figure IV.23), and the comparison in terms of foundation settlements, displacements, and drift, for the two soil profiles.

The same representations were used for the four-storey clay brick structure results, shown in Figure IV.25, Figure IV.26. Also, in this case the soil failure had a beneficial effect on the structure response, leading to less plastic zones with respect to soil D_{ho} . As for the two-storeys structure, the plastic zones are mainly triggered at the toe of the walls, representing the initial phase of the rocking mechanism (Section II.2), and in the following instants develop along the entire height. An important difference between the two and four-storey structures is the extension of the plastic zones around the foundation, which are not only in the lateral side areas but also below the foundation, due to the higher foundation rotation, θ (see Figure IV.24c).

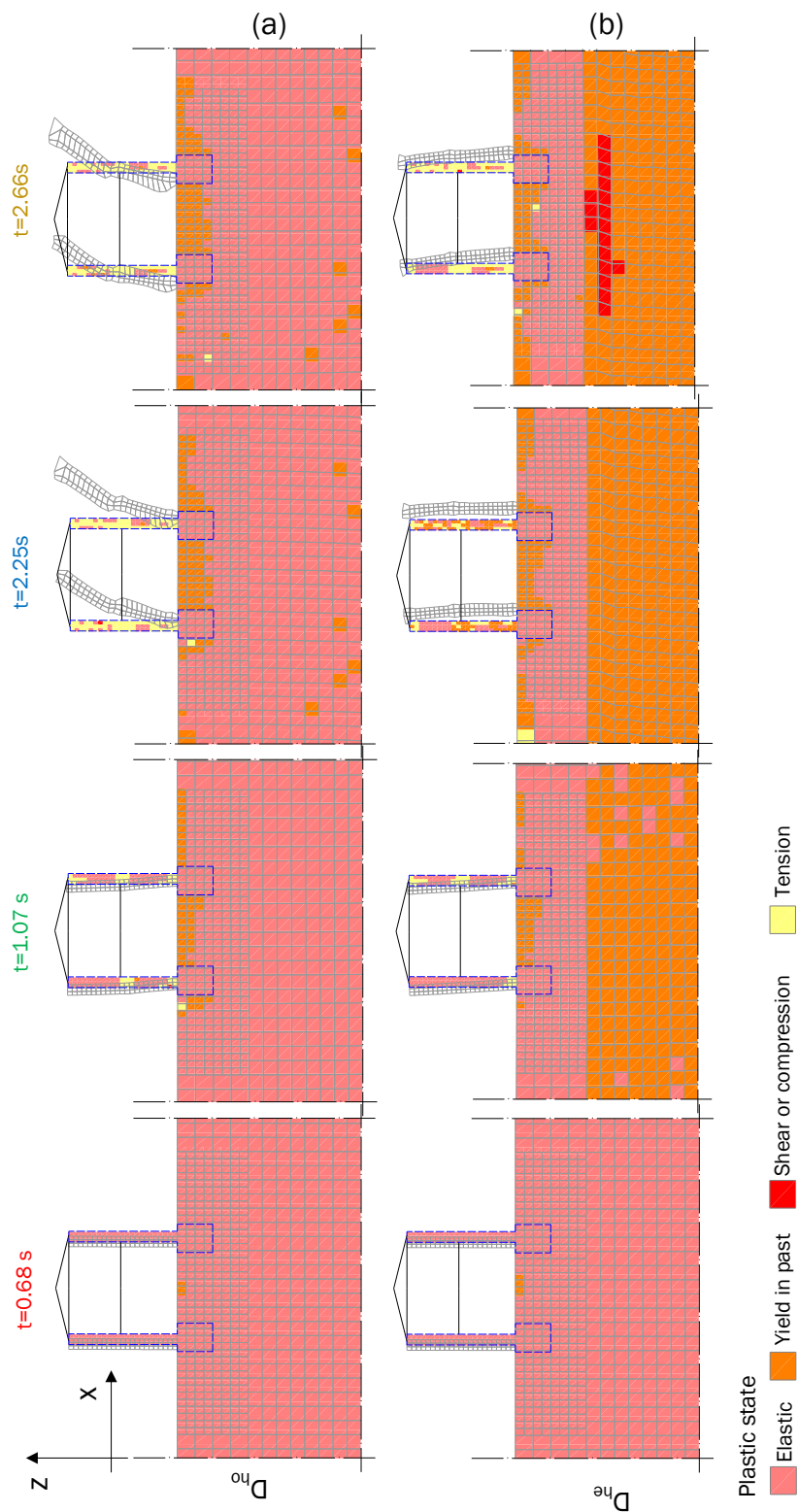


Figure IV.21 Evolution of deformed shapes and plastic states of the two-storey, clay brick masonry structure, ID 1: (a) homogeneous soil and (b) heterogeneous soil

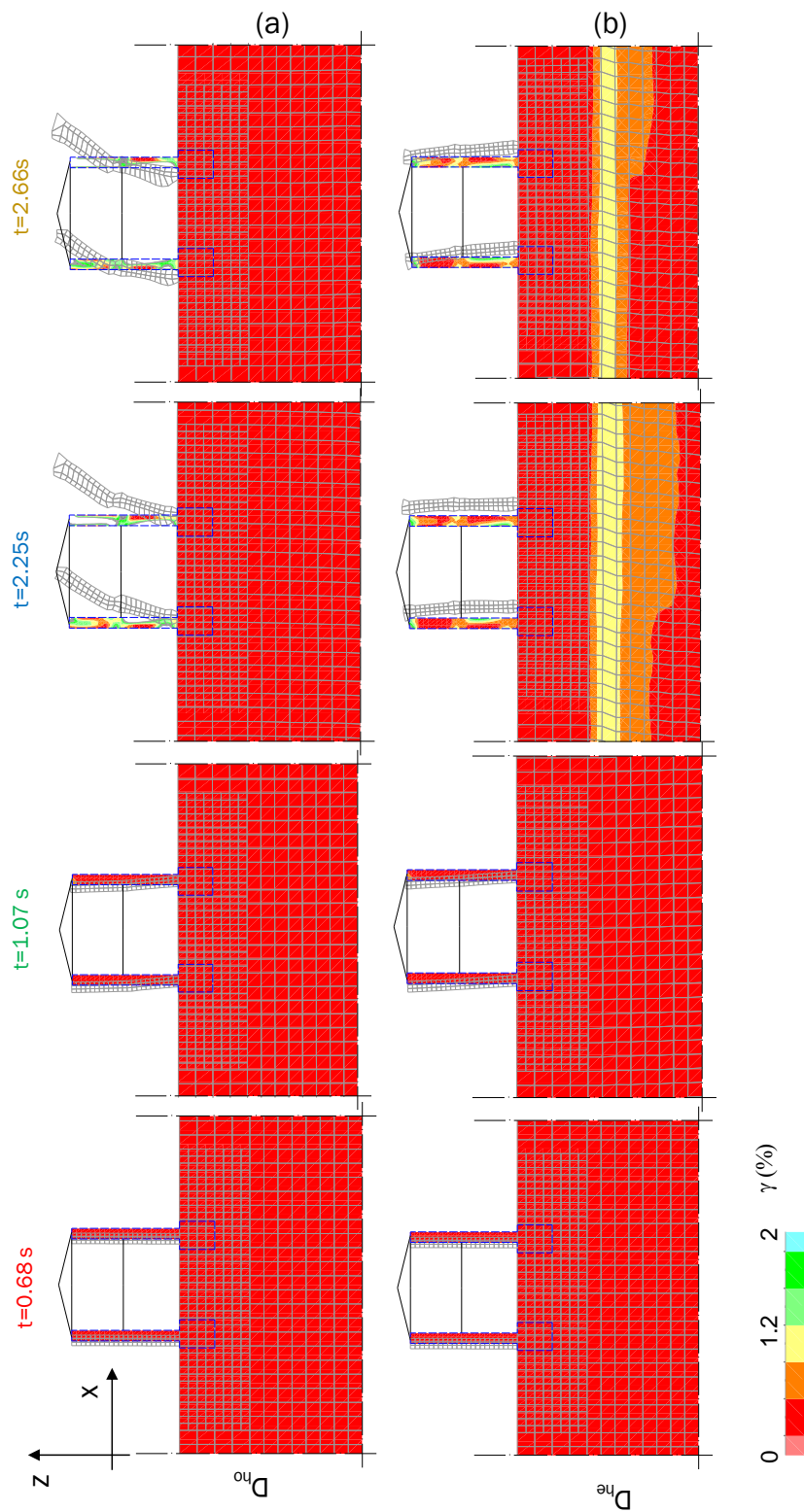


Figure IV.22 Evolution of deformed shapes and shear strains, ID 1: (a) homogeneous soil and (b) heterogeneous soil

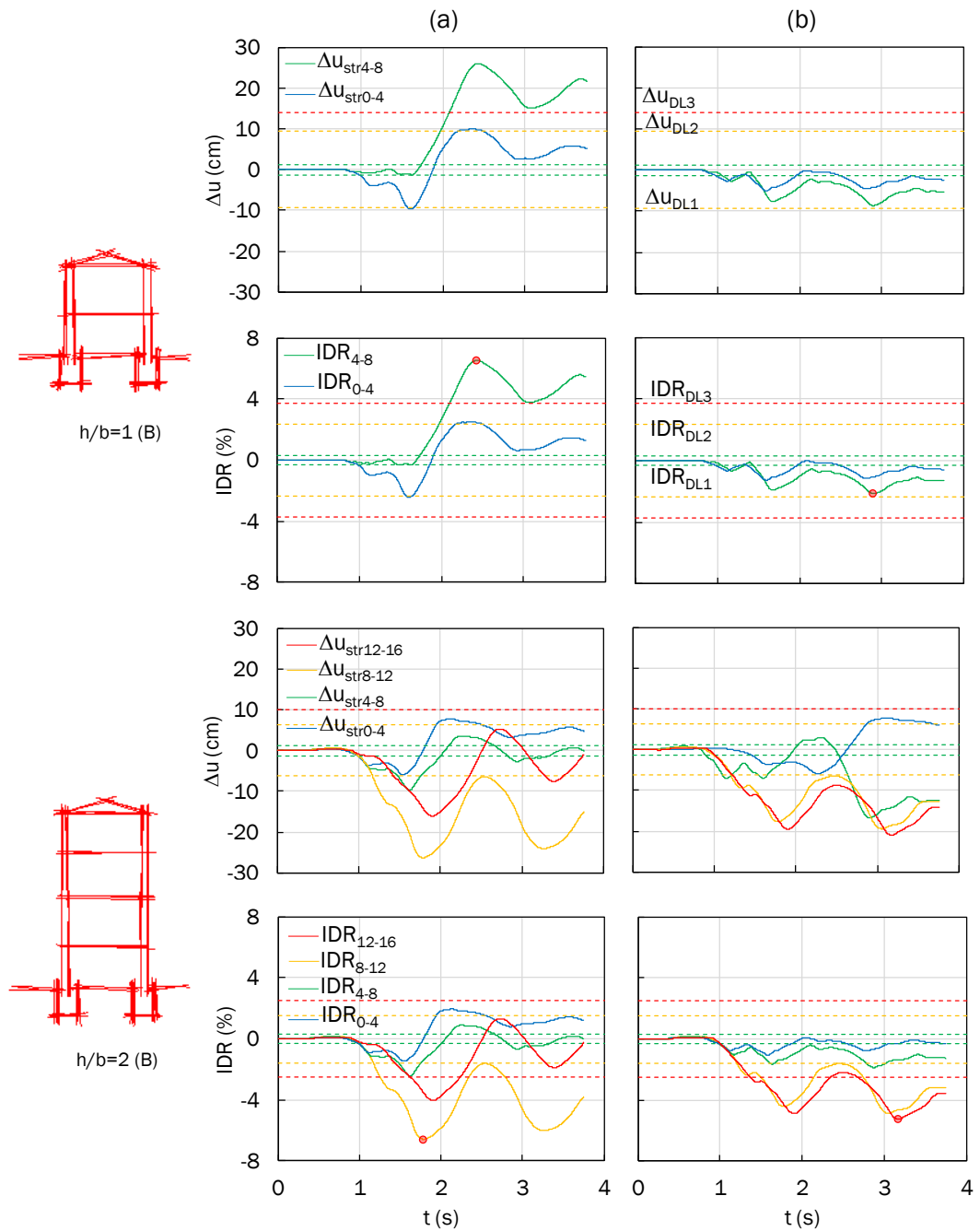


Figure IV.23 Comparison between relative displacements and the corresponding inter-storey drift ratio (IDR) predicted for the two- and four-storey clay brick masonry structures on (a) homogeneous and (b) heterogeneous soil profiles

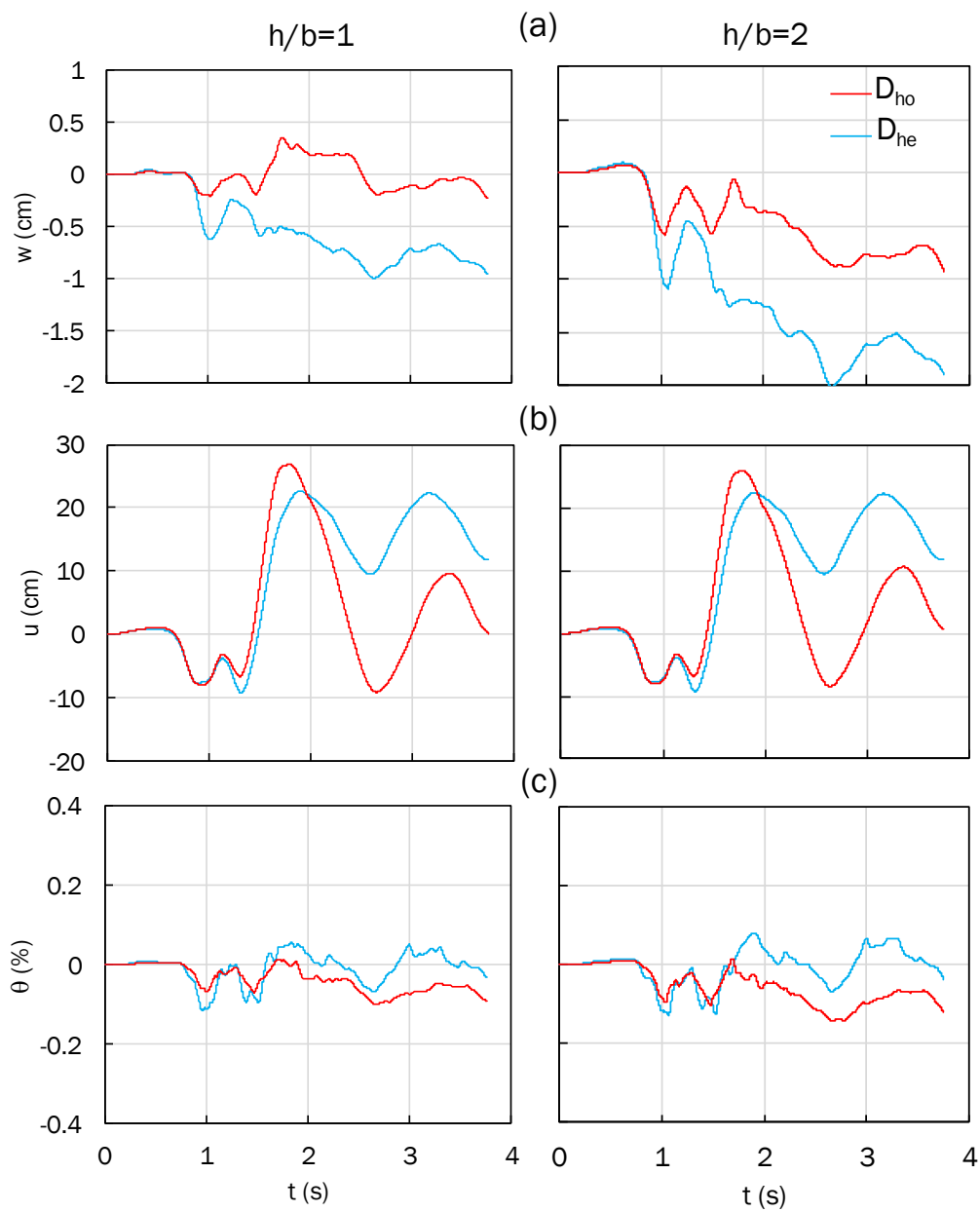


Figure IV.24 Comparison between (a) settlements, (b) foundation displacements and (c) rotations for the two- (left) and four-storey (right) clay brick masonry structures on homogeneous and heterogeneous soil profiles.

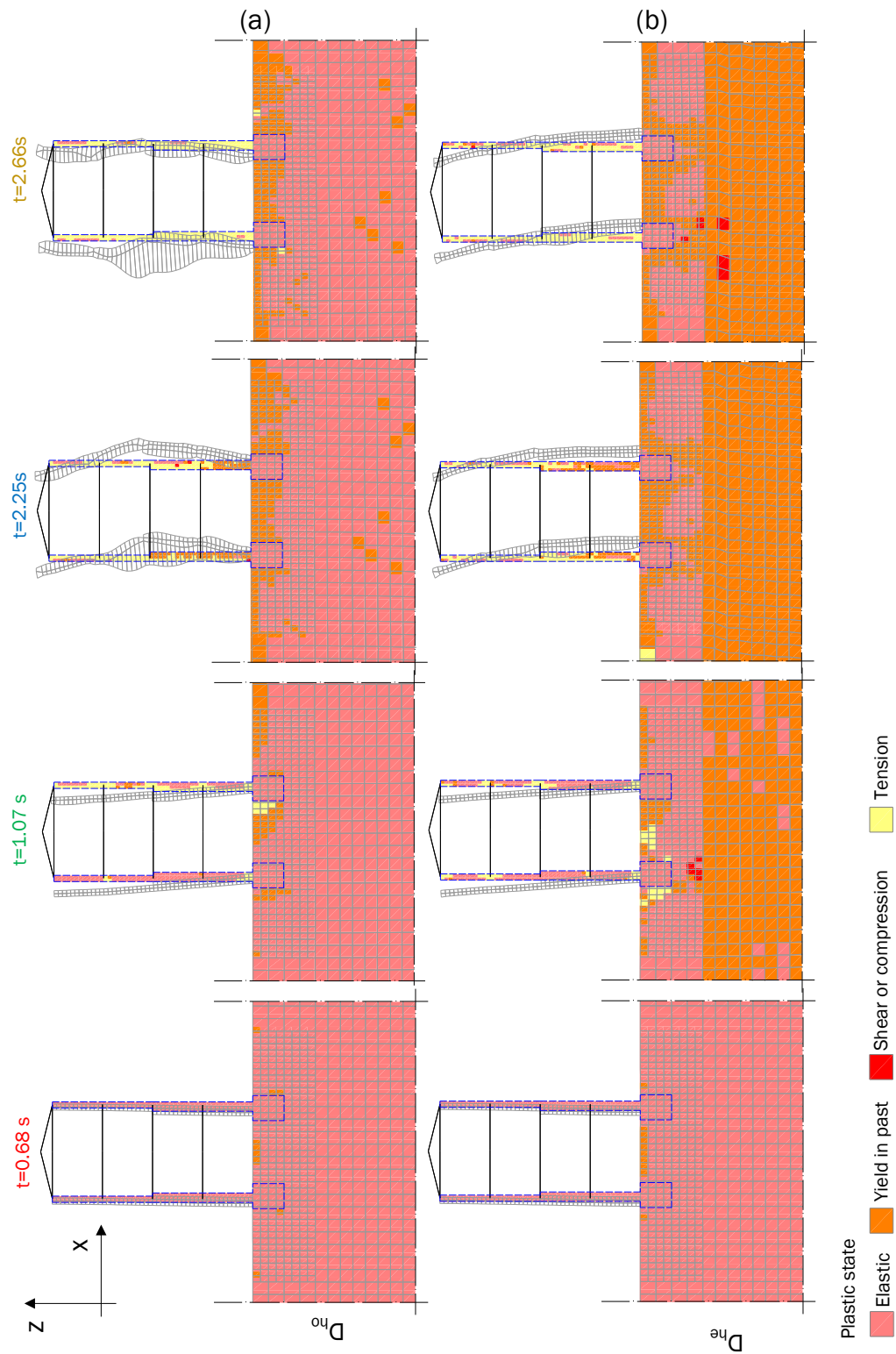


Figure IV.25 Evolution of deformed shapes and plastic states of the four-storey, clay brick masonry structure, ID 1: (a) homogeneous soil and (b) heterogeneous soil

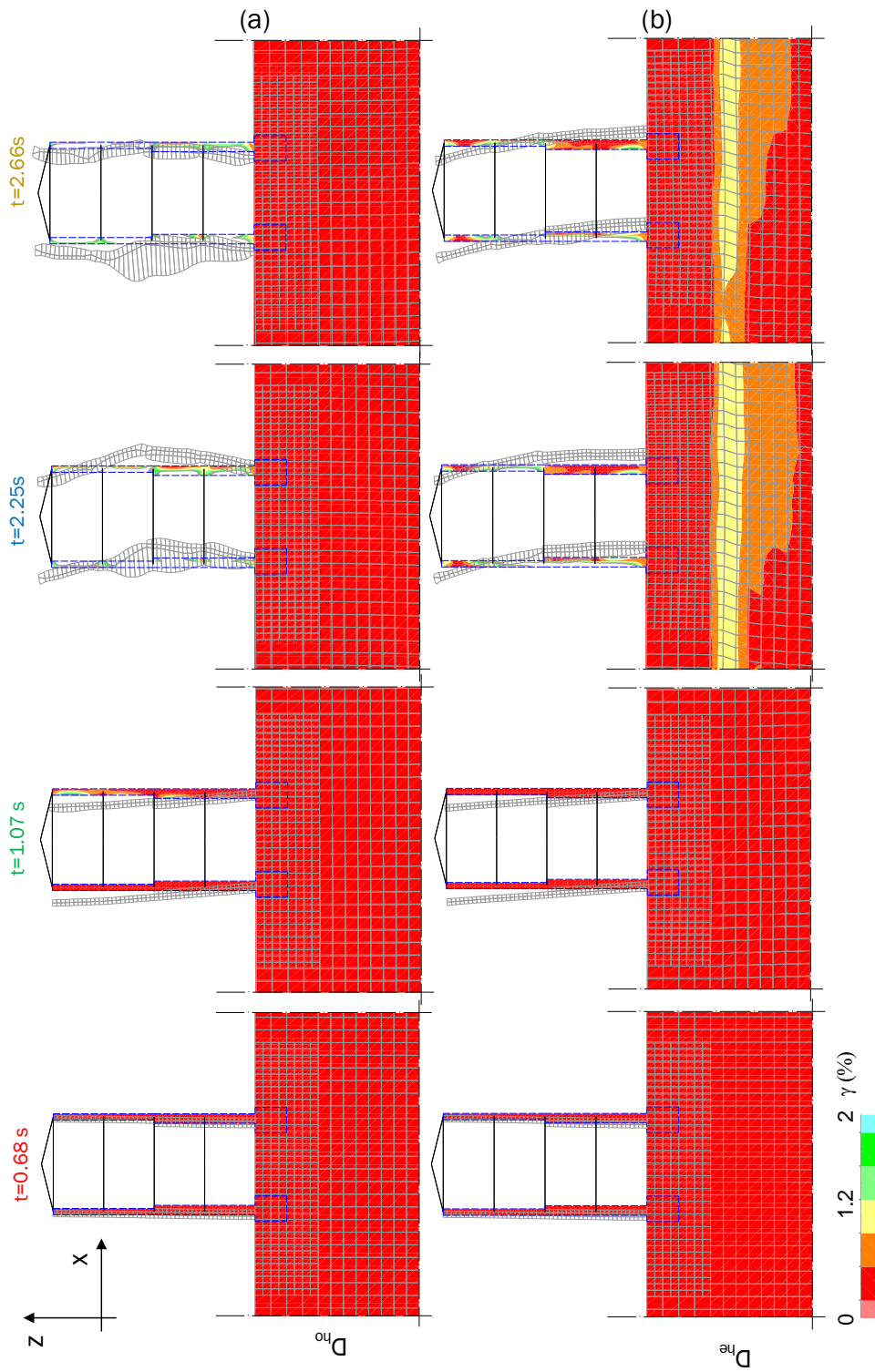


Figure IV.26 Evolution of deformed shapes and shear strains, ID 1: (a) homogeneous soil and (b) heterogeneous soil

IV.3. Seismic fragility

IV.3.1. Demand analysis

Based on the cloud analysis method, the demand model (Section II.3) depends on three parameters: i.e. $\ln a$, b and $\beta_{EDP|IM}$ (Section II.3), obtained by the relationships expressed in Section II.3 and reported below:

$$\ln \eta_{EDP|IM} = \ln a + b \ln IM \quad (II.20)$$

$$\beta_{EDP|IM} = \sqrt{\frac{\sum_{i=1}^N [\ln(edp_i) - \ln(aim_i^b)]^2}{N-2}} \quad (II.21)$$

where edp_i and im_i are respectively the EDP obtained from the NLTHA under the i -th ground motion represented by im_i and N is the number of input motions adopted in the analyses.

Table IV.18 reports the calculated values of $\ln a$ and b (see Eq. II.20) and the standard deviation $\beta_{EDP|IM}$ Eq. (II.21) for each h/b value, masonry type and IM adopted.

Firstly, the IMs described in Section IV.2.2 were tested based on the criterion of efficiency, i.e. for each of the 10 IMs, the values of the standard deviation $\beta_{EDP|IM}$ and coefficient of determination, R^2 , were compared, in order to detect the IM that best predicts the considered EDP.

The lowest $\beta_{EDP|IM}$ and the corresponding R^2 are highlighted in red in Table IV.18, showing that the optimal IM is the PGV almost for all the SFS models. Indeed, the median value of both $\beta_{EDP|IM}$ and R^2 , μ_β and μ_{R^2} , corresponding to the single IM for all the SFS models, are the lowest.

The scatter bi-logarithmic plots of MIDR versus the IMs for each subsoil condition, i.e. soil A (black circle), soil D_{ho} (red circle) and soil D_{he} (blue circle) are shown in Figure IV.27, Figure IV.28, Figure IV.29 and Figure IV.30. These latter are respectively related to rubble stone masonry structures with $h/b = 1$ and $h/b = 2$, and clay brick masonry structures with $h/b = 1$ and $h/b = 2$. The dotted lines represent the linear regression with the corresponding equation and R^2 . The dashed horizontal lines represent the thresholds associated with the damage levels (see Section IV.2.3).

As summarised by the values in Table IV.18, the scatter plots highlight the optimal IMs, i.e. $I_{H0.1-2.0s}$, $I_{Sa0.1-2.0s}$ and PGV, pointing out that the commonly adopted $S_a(T^*)$ is characterised by having, a relatively lower μ_{R^2} (0.80) and higher value of μ_β (0.47) with respect to the above optimal IMs.

IV.EFFECTS OF SFS INTERACTION ON NONLINEAR DYNAMIC RESPONSE AND SEISMIC FRAGILITY OF MASONRY BUILDINGS

Table IV.18 Standard deviation, $\beta_{EDP|IM}$ and probabilistic seismic demand (regression) models

		$\beta_{EDP IM}$									
		$S_a(T^*)$	$S_{a,avg}$	$S_d(T^*)$	I_H (0.1-0.5s)	I_H (0.1-2.0s)	I_{Sa} (0.1-0.5s)	I_{Sa} (0.1-2.0s)	PGA	PGV	PGD
Rs_1	FB	0.47	0.43	0.45	0.35	0.57	0.37	0.57	0.58	0.41	0.68
	D _{ho}	0.63	0.46	0.63	0.57	0.44	0.59	0.44	0.77	0.38	0.61
	D _{he}	0.45	0.38	0.45	0.37	0.32	0.35	0.32	0.60	0.33	0.44
Rs_2	FB	0.62	0.65	0.62	0.52	0.55	0.48	0.55	0.67	0.53	0.63
	D _{ho}	0.27	0.28	0.27	0.50	0.31	0.51	0.31	0.68	0.41	0.40
	D _{he}	0.34	0.32	0.34	0.49	0.36	0.50	0.36	0.62	0.43	0.40
Cb_1	FB	0.46	0.38	0.46	0.45	0.46	0.50	0.46	0.74	0.40	0.59
	D _{ho}	0.66	0.51	0.66	0.56	0.43	0.58	0.43	0.79	0.40	0.64
	D _{he}	0.51	0.38	0.51	0.44	0.32	0.46	0.32	0.64	0.30	0.47
Cb_2	FB	0.42	0.51	0.42	0.46	0.38	0.45	0.38	0.74	0.34	0.55
	D _{ho}	0.36	0.36	0.36	0.44	0.39	0.42	0.39	0.42	0.37	0.46
	D _{he}	0.47	0.50	0.47	0.37	0.45	0.35	0.45	0.41	0.39	0.53
μ_{β}		0.47	0.43	0.47	0.46	0.42	0.46	0.42	0.64	0.39	0.53
R ²											
Rs_1	FB	0.88	0.90	0.89	0.93	0.83	0.93	0.83	0.82	0.91	0.75
	D _{ho}	0.79	0.89	0.79	0.83	0.90	0.82	0.90	0.69	0.93	0.81
	D _{he}	0.85	0.89	0.85	0.90	0.92	0.91	0.92	0.73	0.92	0.85
Rs_2	FB	0.72	0.69	0.72	0.81	0.78	0.83	0.78	0.67	0.79	0.71
	D _{ho}	0.92	0.91	0.92	0.72	0.90	0.72	0.90	0.50	0.82	0.83
	D _{he}	0.81	0.84	0.81	0.62	0.79	0.61	0.79	0.38	0.71	0.74
Cb_1	FB	0.86	0.91	0.86	0.87	0.86	0.84	0.86	0.65	0.90	0.78
	D _{ho}	0.78	0.86	0.78	0.84	0.90	0.82	0.90	0.68	0.92	0.79
	D _{he}	0.80	0.89	0.80	0.85	0.92	0.84	0.92	0.68	0.93	0.83
Cb_2	FB	0.91	0.86	0.91	0.89	0.92	0.89	0.92	0.71	0.94	0.84
	D _{ho}	0.66	0.66	0.66	0.50	0.61	0.55	0.61	0.55	0.64	0.46
	D _{he}	0.61	0.56	0.61	0.76	0.64	0.78	0.64	0.70	0.74	0.51
μ_{R2}		0.80	0.82	0.80	0.79	0.83	0.79	0.83	0.65	0.84	0.74

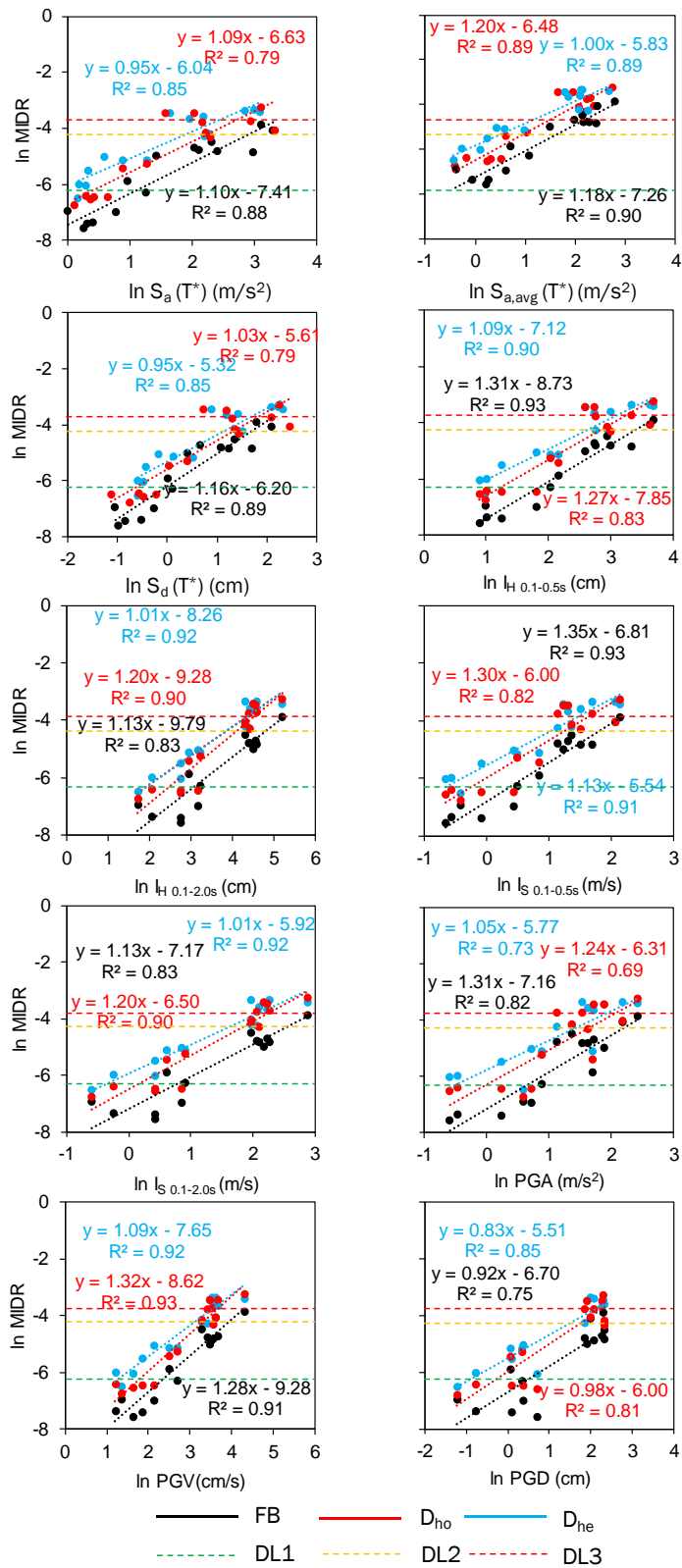


Figure IV.27 EDP-IM relationships ($h/b = 1$; rubble stone masonry)

IV.EFFECTS OF SFS INTERACTION ON NONLINEAR DYNAMIC RESPONSE AND SEISMIC FRAGILITY OF MASONRY BUILDINGS

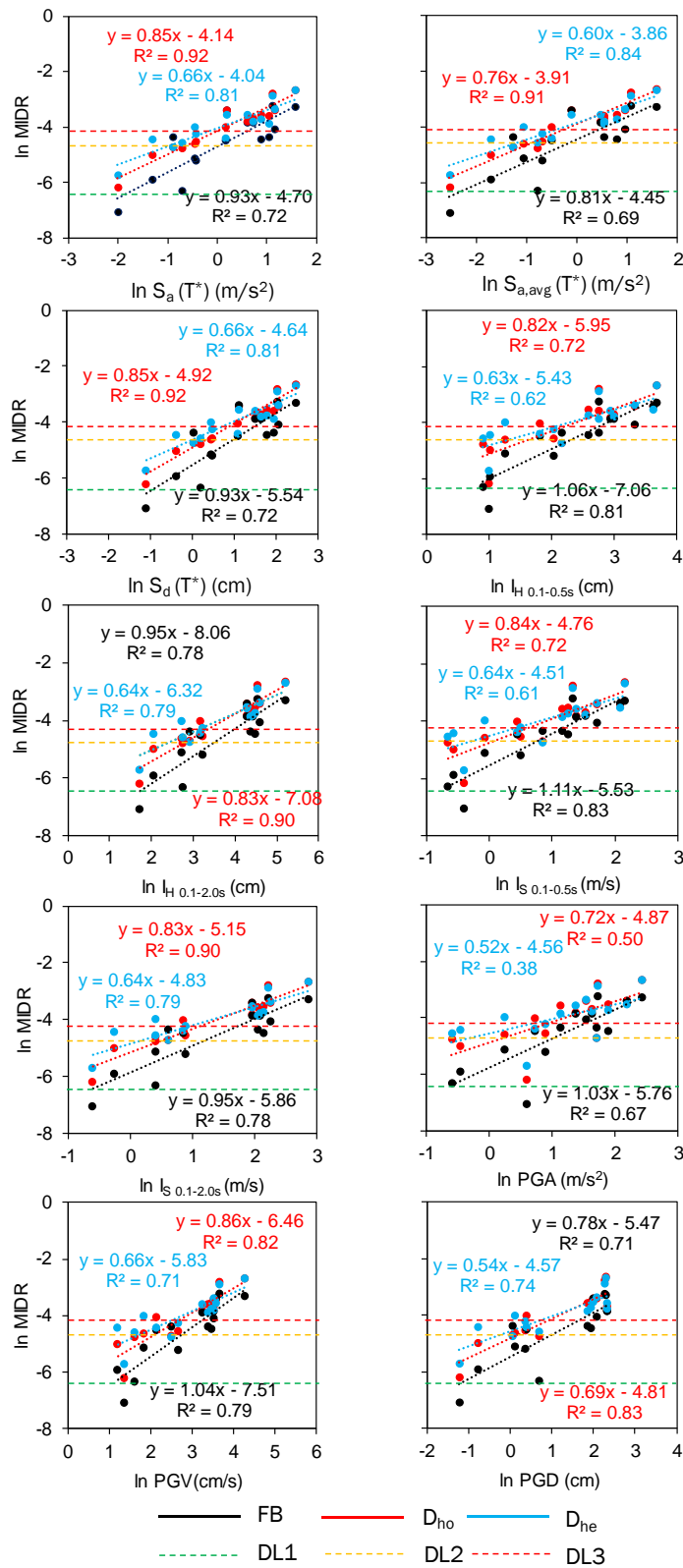


Figure IV.28 EDP-IM relationships ($h/b = 2$; rubble stone masonry)

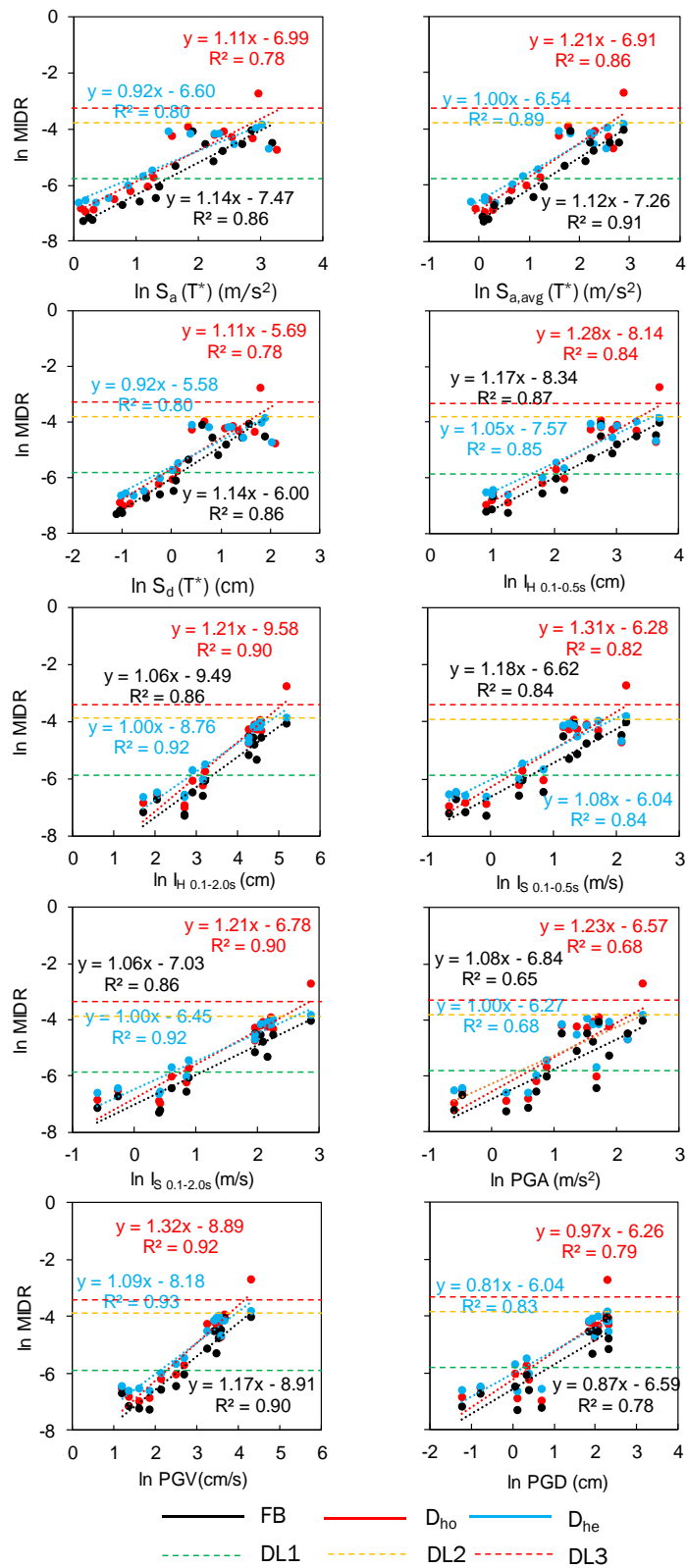


Figure IV.29 EDP-IM relationships ($h/b = 1$; clay brick masonry)

IV.EFFECTS OF SFS INTERACTION ON NONLINEAR DYNAMIC RESPONSE AND SEISMIC FRAGILITY OF MASONRY BUILDINGS

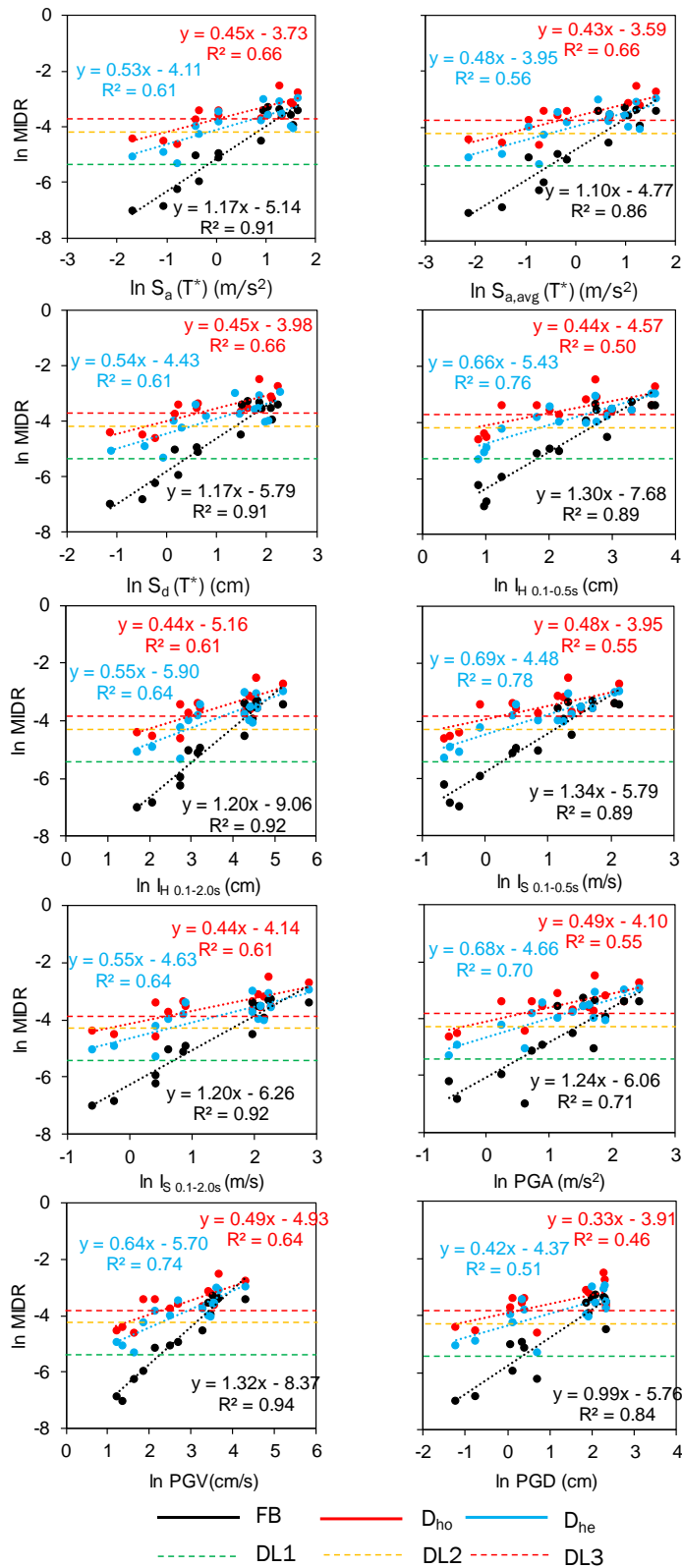


Figure IV.30 EDP-IM relationships ($h/b = 2$; clay brick masonry)

IV.3.2. Derivation of fragility curves

After the computation of the regression parameters and standard deviation for each IM and soil-structure configuration, the fragility functions for each selected DL (Section IV.2.3), set the DL threshold, were derived according to the following equation (see Section II.3):

$$P[EDP > EDP_{DL} | IM = im] = \Phi \left(\frac{\ln(IM / \eta_{DL})}{\beta_{DL}} \right) \quad (II.22)$$

where η_{DL} is the median capacity of the asset to resist the damage level; and β_{DL} is the logarithmic standard deviation of the capacity of the asset to resist the damage level. Figure IV.31 represents a set of fragility functions for the two-storey rubble stone masonry building. Using the same representation, the sets of fragility functions, for the $h/b = 2$ rubble stone masonry and the $h/b = 1$ and $h/b = 2$ clay brick masonry, are shown, respectively in Figure IV.32, Figure IV.33 and Figure IV.34.

When SSI and site effects are taken into account in the dynamic response, it follows that:

- for Rs_1 (see Figure IV.31) the FB model fragility function is shifted further to the right with respect to the soil D models, leading to a significant underestimation of the probability of damage, P ; also, comparing the fragility functions derived for the D soils, by considering the heterogeneity in the soil model, P is higher with respect to the homogenous case, mainly due to the site amplification;
- in contrast to Rs_1 case, for Rs_2 (see Figure IV.32), as well as for Cb_1 and Cb_2, the fragility functions representatives of the heterogenous soil, given IM, have a lower P with respect to the homogeneous soil because of the beneficial effects of the site effects on the structural response;
- except for high values of IM, for Cb_1 (see Figure IV.33) the fragility function related to the FB model is shifted further to the right with respect to the soft soil conditions;
- for Cb_2 (see Figure IV.34) the homogeneous soil led to a higher probability of damage with respect to the heterogenous soil since resonance phenomena may have occurred, being f_0 close to f_{soil} .

Given the number of storeys, the influence of the masonry type and soil conditions, on the fragility for each DL implies:

- for Rs_1 (thicker lines), a higher probability of failure at each DL due to the higher deformability and lower strength of that masonry type with respect to the corresponding Cb_1 model;

- for Cb_2, at DL1 and DL2 resonance phenomena shift the fragility function further to the left, leading to a greater probability of failure with respect to the rubble stone masonry.

What described above is depicted in Figure IV.35, which shows the influence of the masonry type and soil configuration, given the number of storeys, on the fragility for each DL, expressed in terms of the optimal IMs for both the heights (*PGV* and *Is0.1-2.0s*) as well as in terms of $S_a(T^*)$.

The fragility functions parameters, i.e. standard deviation β_{DL} and median $\eta_{DL}=IM_{50}$ (IM corresponding to $P = 50\%$), for all the SFS models, are summarised in Table IV.19, Table IV.20, Table IV.21, Table IV.22, highlighting the above-mentioned aspects. For example, if the two-storey masonry structure and DL3 are considered, the PGV_{50} is reduced from 121.6 cm/s to 69.4 cm/s (i.e. almost one half) in the case of homogenous soft soil and to 90.6 cm/s in the case of heterogeneous profile.

Table IV.23 outlines the reduction factor of IM_{50} with respect to soil A, for both D_{ho} and D_{he} soils. Such a factor is defined as follows:

$$R_F = \frac{IM_{50D}}{IM_{50A}} \quad (IV.24)$$

Similarly, to the factor proposed by Petridis and Pitilakis (2020), R_F quantifies the influence of SSI and site effects on OOP seismic fragility of masonry structures. It represents the distance between the fragility functions, and a value lower or higher than unity implies that the combination of seismic amplification and SSI is detrimental or beneficial on the building fragility, respectively. The comparisons between the R_F for each DL, given the number of storeys and the masonry type, are shown as histograms in Figure IV.36. For sake of completeness, the R_F are reported for all the IMs (optimal and not optimal), since the optimal IM can vary depending on the SFS model considered.

It can be noted that:

- in all cases, R_F is lower than unity, i.e. both SSI and site effects lead to detrimental effects on the OOP behaviour of the structure;
- for two-storey structures, R_F increases as the deformability of the masonry type decreases; the opposite occurs for the four-storey structures, with R_F decreasing with the stiffness of the masonry type, due to the resonance phenomena (except for DL3 for the heterogeneous soil profile);
- set the masonry type, as the structure height increases, R_F on average increases;
- comparing the average value over all the IMs, indicated as μ_{RF} , the difference between R_{F_Dho} and R_{F_Dhe} is reduced as the DL approaches collapse;

- moving from a given DL to that immediately higher, the distance between the function relevant to fixed (soil A) and compliant base (soil D) on average decreases for D_{ho} and increases for D_{he} .

If the 84th percentile is considered, R_F is computed as follows:

$$R_F = \frac{IM_{84D}}{IM_{84A}} \quad (IV.25)$$

The comparisons between the reduction factors computed for each DL, given the number of storeys and the masonry type, are shown in Figure IV.37. It can be observed that on average R_F increases especially with respect to DL3, highlighting that both site amplification and SSI are beneficial, especially for clay brick masonry structures, with respect to the reduction factor computed in terms of IM_{50} .

IV.EFFECTS OF SFS INTERACTION ON NONLINEAR DYNAMIC RESPONSE AND SEISMIC FRAGILITY OF MASONRY BUILDINGS

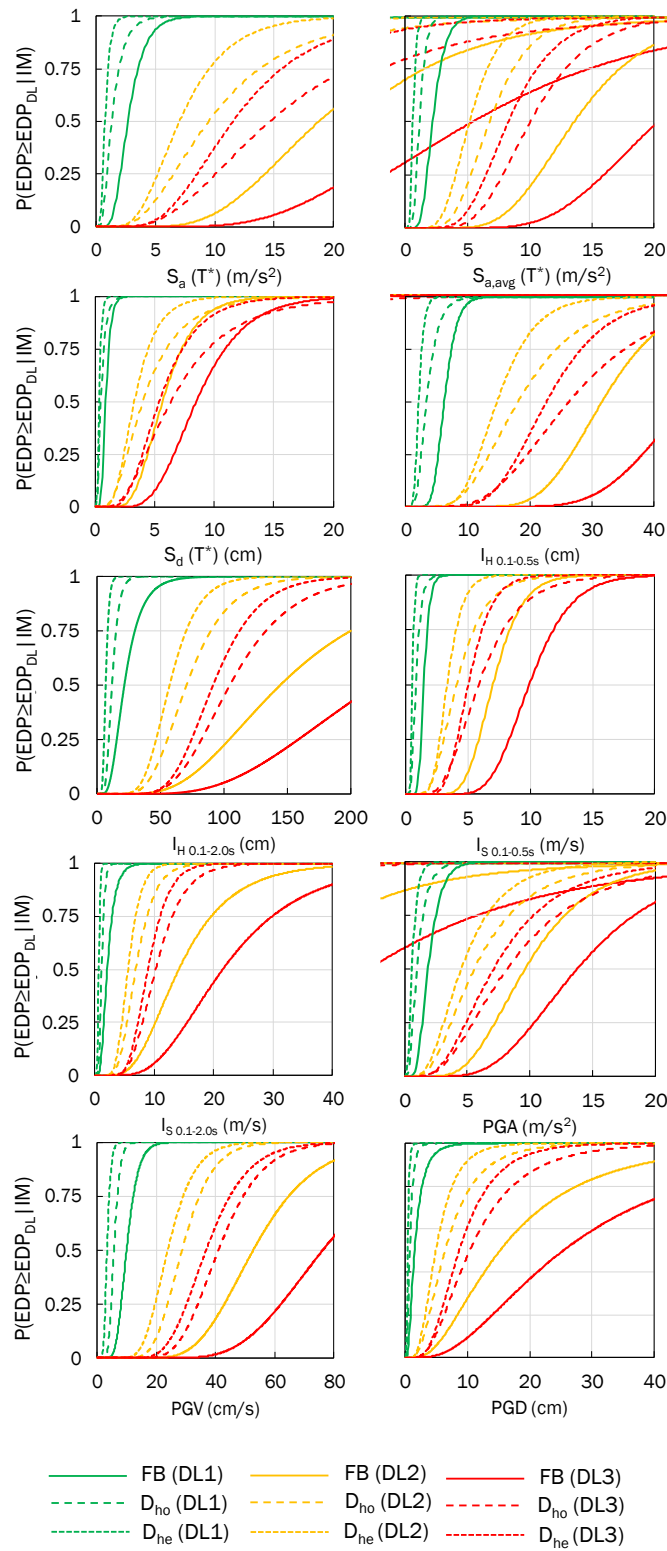


Figure IV.31 Fragility functions ($h/b = 1$; rubble stone masonry)

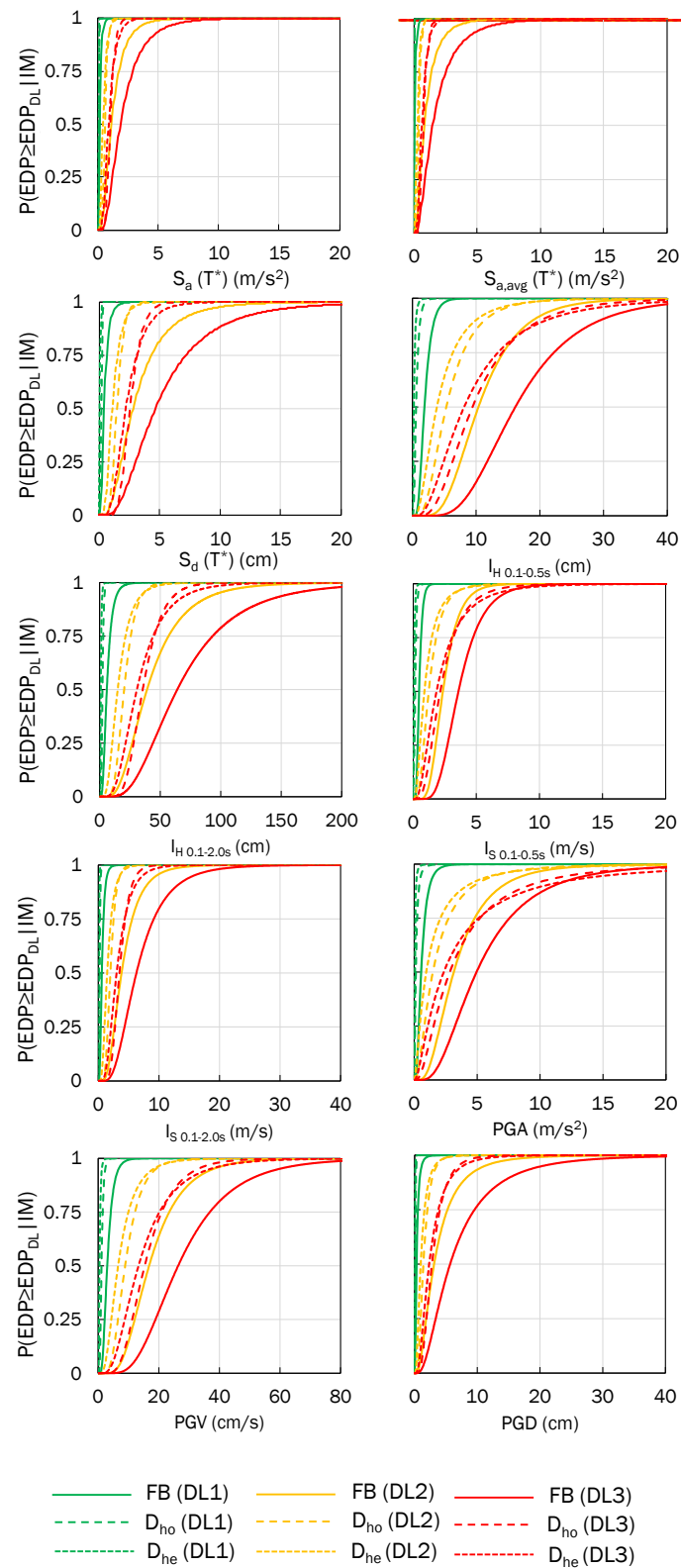


Figure IV.32 Fragility functions ($h/b = 2$; rubble stone masonry)

IV.EFFECTS OF SFS INTERACTION ON NONLINEAR DYNAMIC RESPONSE AND SEISMIC FRAGILITY OF MASONRY BUILDINGS

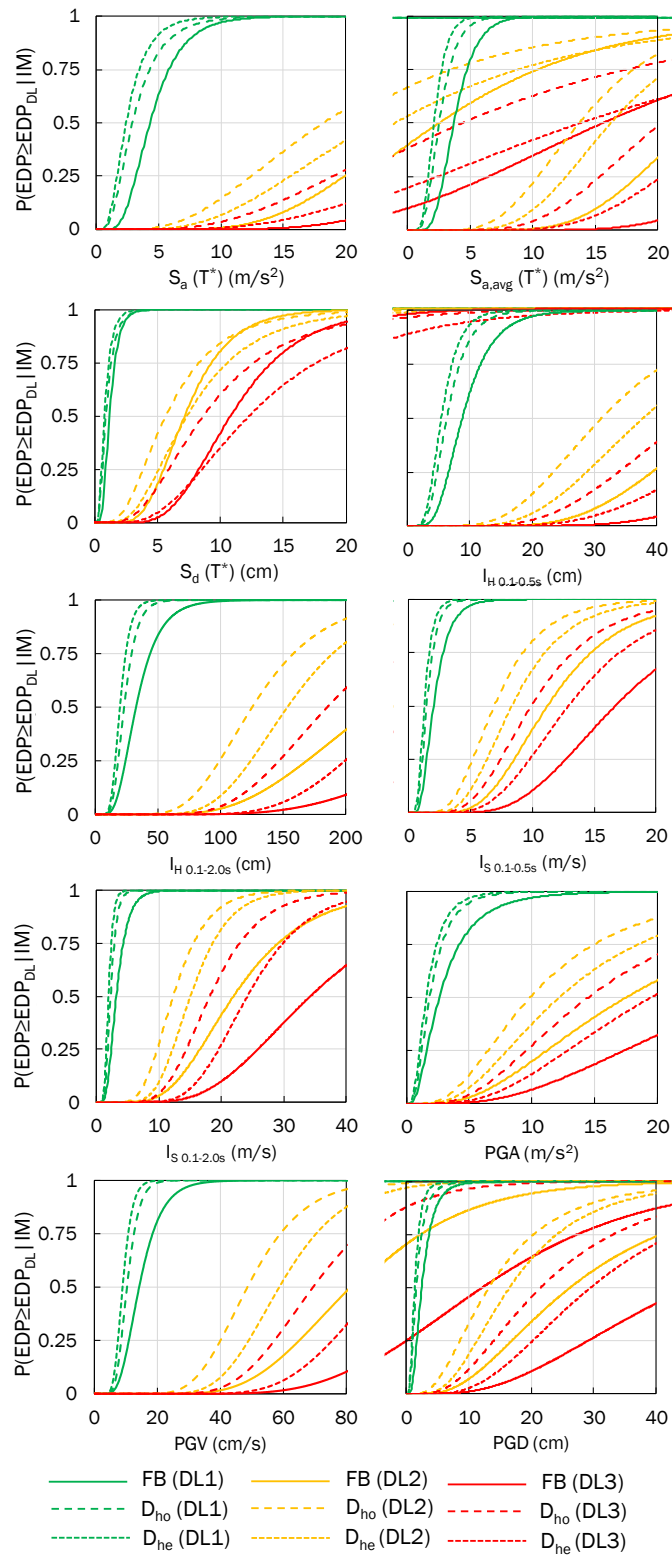


Figure IV.33 Fragility functions ($h/b = 1$; clay brick masonry)

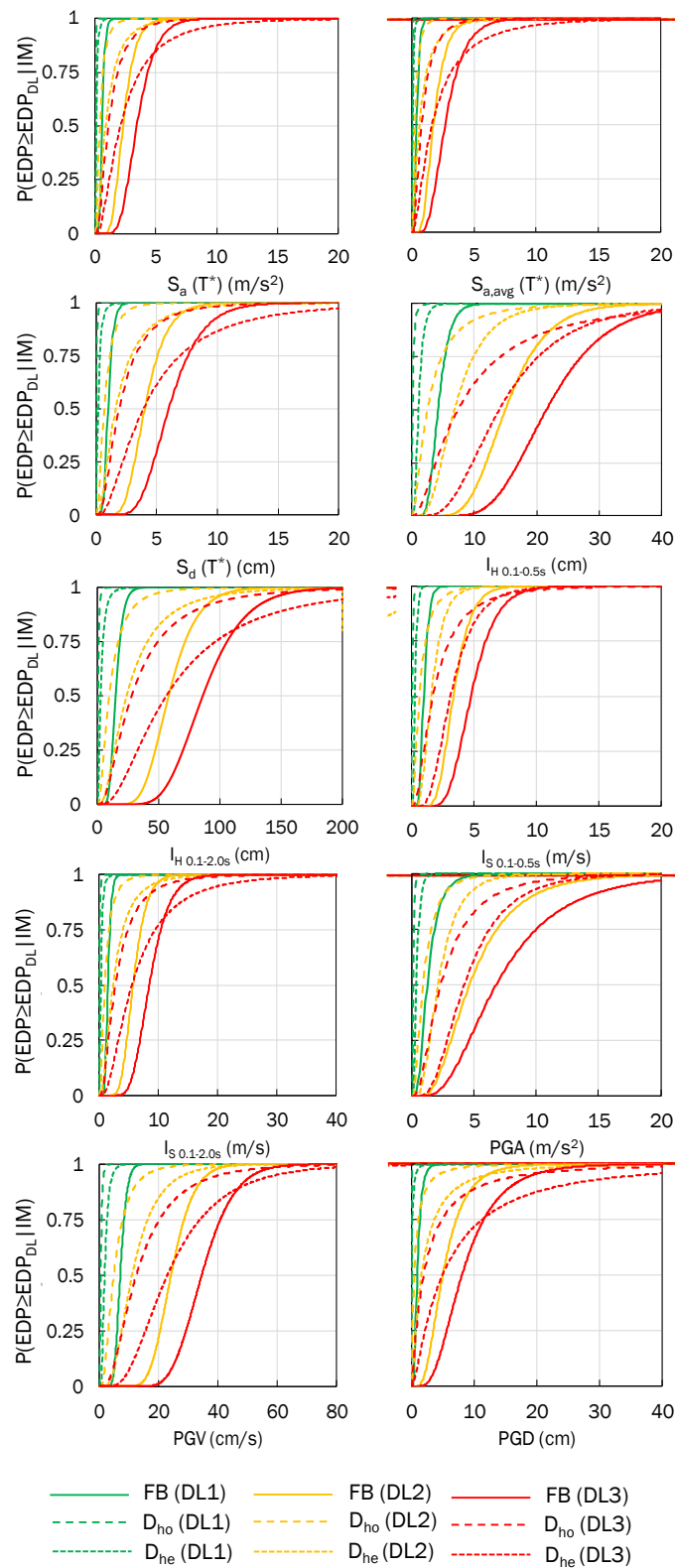


Figure IV.34 Fragility functions ($h/b = 2$; clay brick masonry)

IV.EFFECTS OF SFS INTERACTION ON NONLINEAR DYNAMIC RESPONSE AND SEISMIC FRAGILITY OF MASONRY BUILDINGS

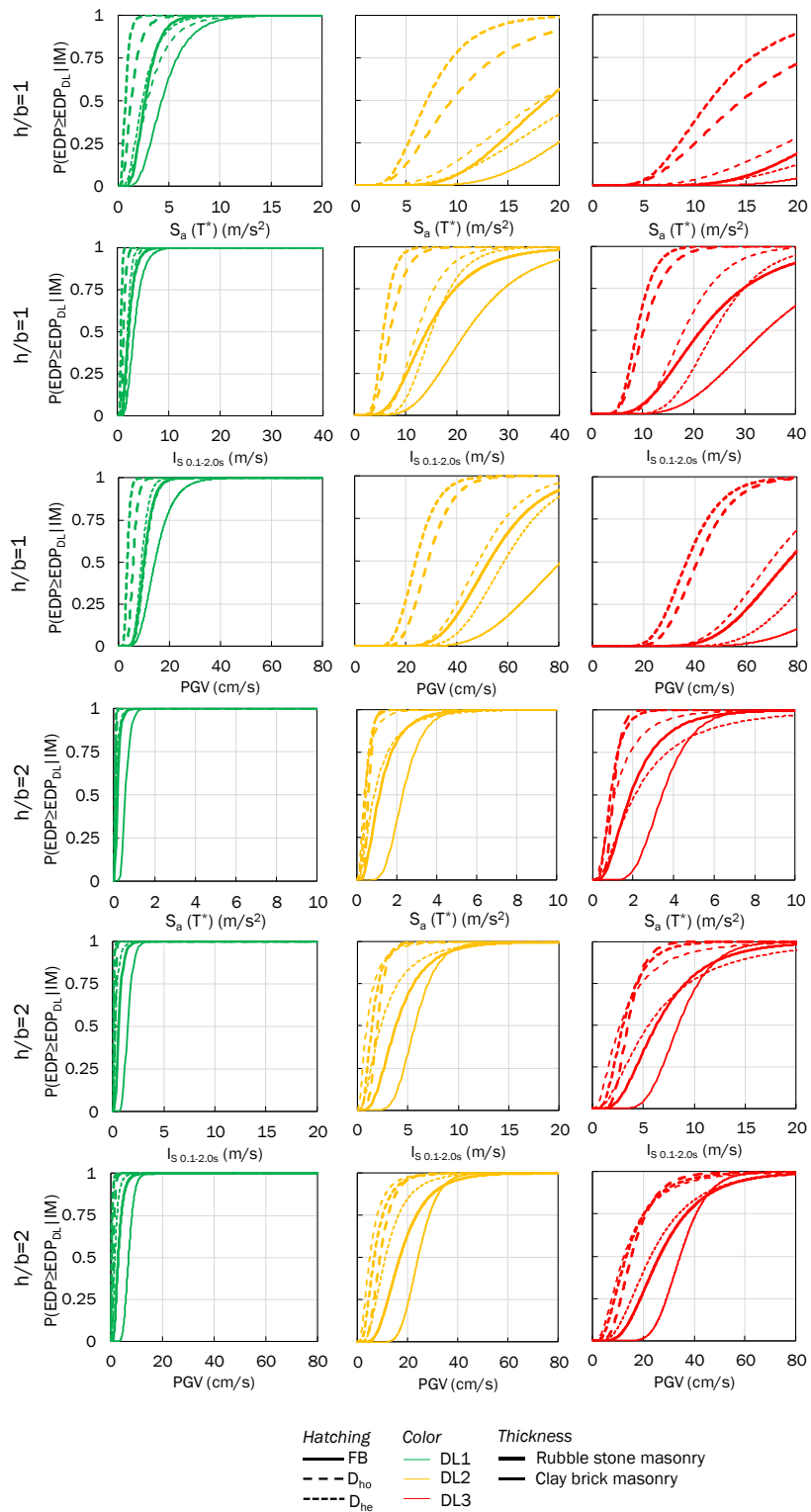


Figure IV.35 Comparison between the fragility function of rubble stone and clay brick masonry structure for $h/b = 1$ and $h/b = 2$

Table IV.19 Fragility functions parameters of two-storey rubble stone masonry structures

	A				D _{ho}				D _{he}			
	β_{DL}	DL1	DL2	DL3	β_{DL}	DL1	DL2	DL3	β_{DL}	DL1	DL2	DL3
		η_{DL}	η_{DL}	η_{DL}		η_{DL}	η_{DL}	η_{DL}		η_{DL}	η_{DL}	η_{DL}
S _a (T [*])	0.41	2.7	18.8	28.9	0.56	1.3	9.5	14.6	0.45	0.7	7.0	11.5
S _{a,avg}	0.36	2.2	13.6	20.3	0.37	1.1	6.8	10.0	0.36	0.6	5.2	8.3
S _d (T [*])	0.37	0.9	5.7	8.5	0.59	0.5	4.0	6.4	0.45	0.3	3.3	5.4
I _{H_0.1-0.5s}	0.25	6.2	31.7	45.4	0.43	3.3	18.1	26.3	0.32	2.1	14.7	22.7
I _{H_0.1-2.0s}	0.48	21.5	144.3	219.6	0.36	11.8	70.5	104.6	0.31	6.8	57.1	91.4
I _{Sa_0.1-0.5s}	0.26	1.4	7.0	9.9	0.43	0.8	4.1	5.8	0.30	0.5	3.3	5.0
I _{Sa_0.1-2.0s}	0.48	2.1	14.2	21.5	0.36	1.2	6.9	10.3	0.31	0.7	5.6	9.0
PGA	0.42	1.9	9.6	13.8	0.60	1.0	5.6	8.2	0.55	0.6	4.5	7.1
PGV	0.30	9.9	52.7	76.2	0.28	5.7	28.6	41.0	0.29	3.3	23.9	36.8
PGD	0.71	1.5	15.3	25.5	0.60	0.7	6.4	10.4	0.51	0.4	4.9	8.7

Table IV.20 Fragility functions parameters of four-storey rubble stone masonry structures

	A				D _{ho}				D _{he}			
	β_{DL}	DL1	DL2	DL3	β_{DL}	DL1	DL2	DL3	β_{DL}	DL1	DL2	DL3
		η_{DL}	η_{DL}	η_{DL}		η_{DL}	η_{DL}	η_{DL}		η_{DL}	η_{DL}	η_{DL}
S _a (T [*])	0.64	0.2	1.1	1.9	0.31	0.07	0.6	1.0	0.50	0.03	0.4	0.9
S _{a,avg}	0.78	0.1	0.8	1.5	0.36	0.04	0.4	0.8	0.51	0.01	0.3	0.7
S _d (T [*])	0.64	0.4	2.8	4.7	0.31	0.18	1.5	2.6	0.50	0.07	1.1	2.2
I _{H_0.1-0.5s}	0.47	1.9	10.4	16.2	0.59	0.58	5.3	9.4	0.75	0.22	3.8	8.1
I _{H_0.1-2.0s}	0.56	5.9	39.1	64.1	0.35	2.29	20.2	35.5	0.54	0.91	14.8	30.7
I _{Sa_0.1-0.5s}	0.41	0.5	2.4	3.6	0.58	0.14	1.2	2.1	0.75	0.05	0.9	1.8
I _{Sa_0.1-2.0s}	0.56	0.6	3.8	6.3	0.35	0.22	2.0	3.5	0.54	0.09	1.5	3.0
PGA	0.63	0.5	3.1	4.9	0.91	0.12	1.5	2.8	1.16	0.03	1.0	2.3
PGV	0.49	3.0	16.8	26.4	0.46	1.08	8.9	15.3	0.62	0.43	6.6	13.3
PGD	0.78	0.3	3.1	5.7	0.56	0.10	1.4	2.8	0.72	0.03	1.0	2.3

IV.EFFECTS OF SFS INTERACTION ON NONLINEAR DYNAMIC RESPONSE AND SEISMIC
FRAGILITY OF MASONRY BUILDINGS

Table IV.21 Fragility functions parameters of two-storey clay brick masonry structures

	A				D _{ho}				D _{he}			
	β_{DL}	DL1	DL2	DL3	β_{DL}	DL1	DL2	DL3	β_{DL}	DL1	DL2	DL3
		η_{DL}	η_{DL}	η_{DL}		η_{DL}	η_{DL}	η_{DL}		η_{DL}	η_{DL}	η_{DL}
S _a (T*)	0.45	4.3	25.9	39.2	0.57	2.9	18.2	27.8	0.54	2.4	22.4	37.4
S _{a,avg}	0.37	3.7	22.9	35.0	0.41	2.5	13.7	20.3	0.37	2.1	16.3	26.1
S _d (T*)	0.45	1.2	7.1	10.8	0.57	0.9	5.7	8.6	0.54	0.8	7.3	12.3
I _{H_0.1-0.5s}	0.43	8.8	50.4	75.5	0.42	6.3	31.2	45.2	0.41	5.4	37.9	59.4
I _{H_0.1-2.0s}	0.44	32.5	223.8	349.1	0.35	23.0	125.3	185.3	0.31	19.6	153.4	246.4
I _{Sa_0.1-0.5s}	0.48	2.0	11.2	16.7	0.43	1.4	6.9	9.9	0.41	1.2	8.3	12.9
I _{Sa_0.1-2.0s}	0.44	3.2	22.0	34.3	0.35	2.3	12.3	18.2	0.31	1.9	15.0	24.2
PGA	0.71	2.6	17.5	27.1	0.62	1.9	9.9	14.5	0.62	1.6	12.2	19.5
PGV	0.39	14.2	81.3	121.6	0.29	10.3	48.6	69.4	0.27	8.9	58.7	90.6
PGD	0.56	2.5	26.2	45.2	0.64	1.6	13.2	21.5	0.56	1.3	16.5	29.5

Table IV.22 Fragility functions parameters of four-storey clay brick masonry structures

	A				D _{ho}				D _{he}					
	β_{DL}	DL1	DL2	DL3	β_{DL}	DL1	DL2	DL3	β_{DL}	DL1	DL2	DL3		
		η_{DL}	η_{DL}	η_{DL}		η_{DL}	η_{DL}	η_{DL}		η_{DL}	η_{DL}	η_{DL}	η_{DL}	
S _a (T*)	0.35	0.6	2.3	3.4	0.78	0.03	0.4	1.1	0.85	0.1	0.9	2.1	0.35	0.6
S _{a,avg}	0.45	0.4	1.7	2.7	0.81	0.02	0.3	0.8	1.00	0.1	0.6	1.6	0.45	0.4
S _d (T*)	0.35	1.0	4.0	6.0	0.78	0.05	0.7	1.9	0.85	0.2	1.6	3.9	0.35	1.0
I _{H_0.1-0.5s}	0.34	4.2	15.0	21.6	0.97	0.16	2.5	7.4	0.54	1.1	6.9	14.0	0.34	4.2
I _{H_0.1-2.0s}	0.31	14.9	58.2	86.0	0.84	0.64	9.6	27.9	0.80	2.7	23.8	56.2	0.31	14.9
I _{Sa_0.1-0.5s}	0.33	1.0	3.4	4.8	0.84	0.05	0.6	1.7	0.49	0.3	1.6	3.1	0.33	1.0
I _{Sa_0.1-2.0s}	0.31	1.5	5.7	8.4	0.84	0.06	0.9	2.7	0.80	0.3	2.3	5.5	0.31	1.5
PGA	0.58	1.2	4.6	6.8	0.81	0.08	0.9	2.3	0.58	0.4	2.1	4.2	0.58	1.2
PGV	0.25	7.0	24.1	34.5	0.72	0.42	4.8	12.4	0.58	1.7	11.0	22.9	0.25	7.0
PGD	0.53	1.0	5.0	8.1	1.34	0.01	0.5	2.0	1.21	0.1	1.6	5.0	0.53	1.0

SOIL-STRUCTURE INTERACTION EFFECTS ON SEISMIC RESPONSE OF MASONRY BUILDINGS

Table IV.23 Reduction factor for the fixed base fragility functions ($R_{F_Dhe}=IM_{50Dhe}/IM_{50A}$ and $R_{F_Dho}=IM_{50Dho}/IM_{50A}$)

	DL1		DL2		DL3			DL1		DL2		DL3	
	R_{F_Dho}	R_{F_Dhe}	R_{F_Dho}	R_{F_Dhe}	R_{F_Dho}	R_{F_Dhe}		R_{F_Dho}	R_{F_Dhe}	R_{F_Dho}	R_{F_Dhe}	R_{F_Dho}	R_{F_Dhe}
$S_a(T^*)$	0.49	0.28	0.50	0.37	0.51	0.40		0.44	0.18	0.53	0.39	0.55	0.48
$S_{a,avg}$	0.52	0.28	0.50	0.38	0.49	0.41		0.41	0.16	0.49	0.35	0.50	0.43
$S_d(T^*)$	0.55	0.39	0.71	0.58	0.75	0.64		0.44	0.18	0.53	0.39	0.55	0.48
$I_{H_0.1-0.5s}$	0.54	0.33	0.57	0.46	0.58	0.50		0.31	0.12	0.51	0.37	0.58	0.50
$I_{H_0.1-2.0s}$	0.55	0.32	0.49	0.40	0.48	0.42		0.39	0.16	0.52	0.38	0.55	0.48
$I_{Sa_0.1-0.5s}$	0.55	0.35	0.58	0.47	0.59	0.51		0.31	0.11	0.52	0.38	0.60	0.52
$I_{Sa_0.1-2.0s}$	0.55	0.32	0.49	0.40	0.48	0.42		0.39	0.16	0.52	0.38	0.55	0.48
PGA	0.52	0.31	0.58	0.47	0.59	0.52		0.22	0.05	0.47	0.30	0.57	0.47
PGV	0.57	0.34	0.54	0.45	0.54	0.48		0.36	0.15	0.53	0.39	0.58	0.50
PGD	0.48	0.25	0.42	0.32	0.41	0.34		0.32	0.11	0.45	0.31	0.49	0.41
μ_{RF}	0.53	0.32	0.54	0.43	0.54	0.46		0.36	0.14	0.51	0.36	0.55	0.48
$S_a(T^*)$	0.68	0.56	0.70	0.86	0.71	0.95		0.05	0.17	0.17	0.38	0.32	0.61
$S_{a,avg}$	0.68	0.57	0.60	0.71	0.58	0.75		0.04	0.13	0.15	0.35	0.30	0.61
$S_d(T^*)$	0.76	0.66	0.79	1.03	0.80	1.14		0.05	0.18	0.17	0.41	0.32	0.65
$I_{H_0.1-0.5s}$	0.72	0.62	0.62	0.75	0.60	0.79		0.04	0.26	0.17	0.46	0.34	0.65
$I_{H_0.1-2.0s}$	0.71	0.60	0.56	0.69	0.53	0.71		0.04	0.18	0.17	0.41	0.32	0.65
$I_{Sa_0.1-0.5s}$	0.72	0.62	0.62	0.74	0.59	0.77		0.05	0.28	0.19	0.47	0.36	0.66
$I_{Sa_0.1-2.0s}$	0.71	0.60	0.56	0.69	0.53	0.71		0.04	0.18	0.17	0.41	0.32	0.65
PGA	0.71	0.61	0.56	0.70	0.53	0.72		0.06	0.29	0.19	0.45	0.34	0.62
PGV	0.73	0.63	0.60	0.72	0.57	0.74		0.06	0.24	0.20	0.46	0.36	0.66
PGD	0.65	0.54	0.50	0.63	0.48	0.65		0.01	0.10	0.09	0.32	0.24	0.62
μ_{RF}	0.71	0.60	0.61	0.75	0.59	0.79		0.05	0.20	0.17	0.41	0.32	0.64

IV.EFFECTS OF SFS INTERACTION ON NONLINEAR DYNAMIC RESPONSE AND SEISMIC FRAGILITY OF MASONRY BUILDINGS

Table IV.24 Reduction factor for the fixed base fragility functions ($R_{F_Dhe}=IM_{84Dhe}/IM_{84A}$ and $R_{F_Dho}=IM_{84Dho}/IM_{84A}$)

	DL1		DL2		DL3		DL1		DL2		DL3	
	R_{F_Dho}	R_{F_Dhe}										
$S_a (T^*)$	0.57	0.29	0.58	0.39	0.59	0.42	0.31	0.15	0.38	0.34	0.39	5.33
$S_{a,avg}$	0.52	0.28	0.51	0.38	0.50	0.41	0.27	0.13	0.32	0.27	0.33	0.33
$S_d (T^*)$	0.69	0.42	0.88	0.63	0.93	0.69	0.31	0.15	0.38	0.34	0.39	0.41
$I_{H_0.1-0.5s}$	0.64	0.36	0.68	0.50	0.69	0.54	0.35	0.15	0.58	0.49	0.66	0.66
$I_{H_0.1-2.0s}$	0.48	0.26	0.43	0.33	0.42	0.35	0.32	0.15	0.42	0.37	0.45	0.47
$I_{Sa_0.1-0.5s}$	0.65	0.36	0.69	0.49	0.70	0.52	0.36	0.16	0.62	0.53	0.71	0.72
$I_{Sa_0.1-2.0s}$	0.48	0.26	0.43	0.33	0.42	0.35	0.32	0.15	0.42	0.37	0.45	0.47
PGA	0.62	0.35	0.69	0.53	0.70	0.58	0.29	0.09	0.62	0.51	0.75	0.80
PGV	0.55	0.33	0.53	0.45	0.52	0.48	0.35	0.17	0.51	0.44	0.56	0.57
PGD	0.43	0.21	0.38	0.27	0.37	0.28	0.26	0.10	0.36	0.30	0.39	0.39
μ_{RF}	0.56	0.31	0.58	0.43	0.58	0.46	0.32	0.14	0.46	0.40	0.51	1.02
$S_a (T^*)$	0.76	0.61	0.79	0.95	0.80	1.05	0.07	0.28	0.26	0.63	0.49	1.01
$S_{a,avg}$	0.71	0.57	0.62	0.71	0.60	0.75	0.06	0.23	0.22	0.61	0.43	1.06
$S_d (T^*)$	0.86	0.73	0.89	1.12	0.90	1.24	0.07	0.30	0.26	0.68	0.49	1.08
$I_{H_0.1-0.5s}$	0.71	0.60	0.61	0.73	0.59	0.77	0.07	0.32	0.31	0.56	0.64	0.80
$I_{H_0.1-2.0s}$	0.64	0.53	0.51	0.60	0.48	0.62	0.07	0.29	0.28	0.67	0.55	1.07
$I_{Sa_0.1-0.5s}$	0.69	0.58	0.59	0.69	0.56	0.72	0.09	0.33	0.32	0.56	0.60	0.77
$I_{Sa_0.1-2.0s}$	0.64	0.53	0.51	0.60	0.48	0.62	0.07	0.29	0.28	0.67	0.55	1.07
PGA	0.65	0.55	0.51	0.63	0.49	0.65	0.08	0.29	0.24	0.46	0.43	0.63
PGV	0.66	0.56	0.54	0.64	0.52	0.66	0.10	0.34	0.32	0.64	0.58	0.93
PGD	0.70	0.54	0.54	0.63	0.51	0.65	0.03	0.19	0.21	0.64	0.55	1.22
μ_{RF}	0.70	0.58	0.61	0.73	0.59	0.77	0.07	0.29	0.27	0.61	0.53	0.96

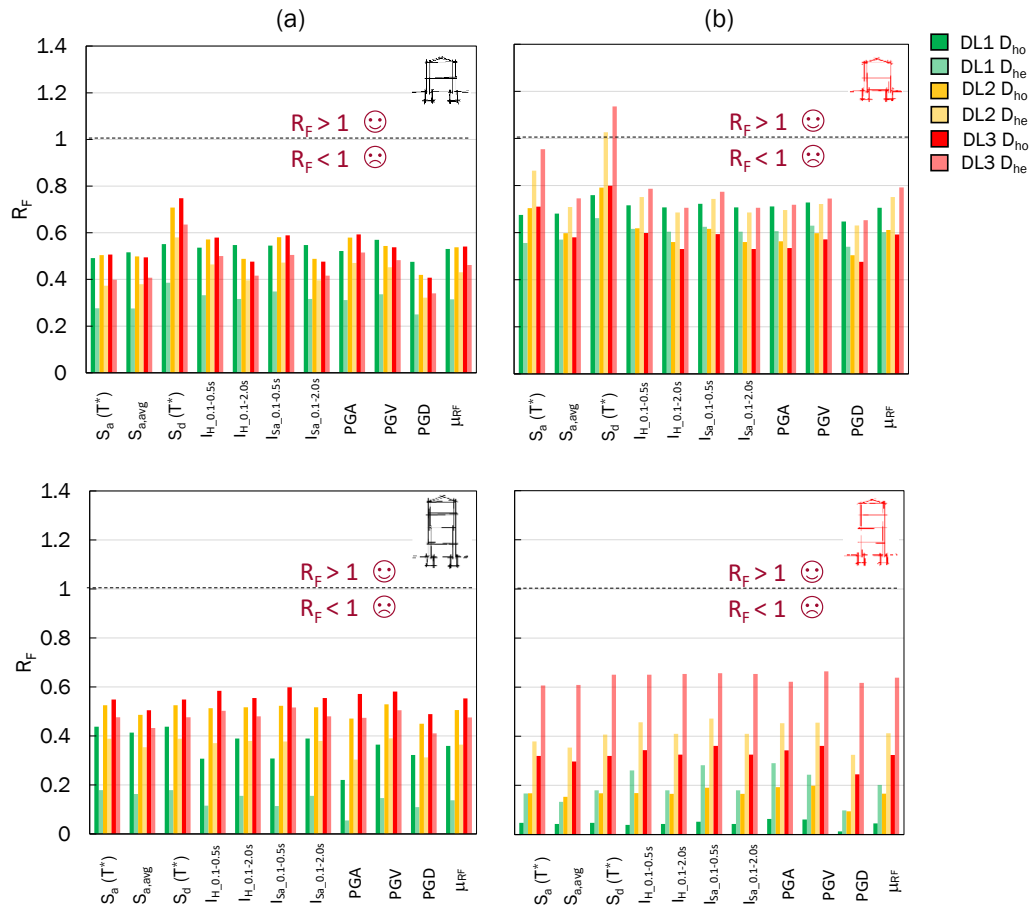


Figure IV.36 Comparison between $R_F = IM_{50D} / IM_{50A}$ of (a) rubble stone and (b) clay brick masonry structure for $h/b = 1$ and $h/b = 2$

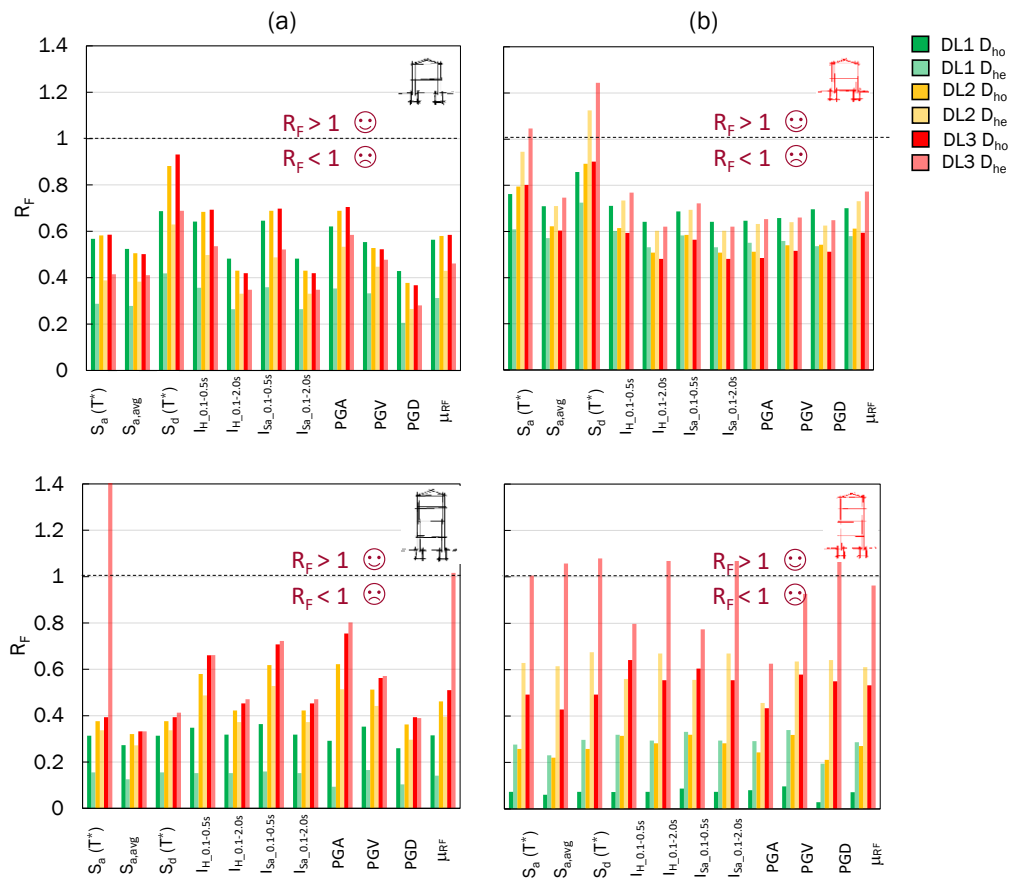


Figure IV.37 Comparison between $R_F = IM_{84D} / IM_{84A}$ of (a) rubble stone and (b) clay brick masonry structure for $h/b = 1$ and $h/b = 2$

V.APPLICATIONS TO CASE STUDIES

Accounting soil-structure interaction and site effects lead to a different response of masonry walls laterally loaded outside their own plane, with respect to the fixed-base condition. In particular the linear response (Chapter III) was influenced in terms of variation of the initial fundamental period and damping, while in terms of both the activation of out-of-plane failure and collapse of masonry walls, (Chapter IV) a significantly underestimation with respect to the fixed-base conditions was recognized. In Chapter III a procedure for a quick estimation of the frequency variation was proposed calibrating, on the numerical results and for different soil and foundation configuration, weighting coefficients were calibrated, in order to evaluate the relative soil-structure stiffness. In Chapter IV, instead, sets of fragility functions were derived for different soil configuration and structure types, in order to predict the probability of failure. The proposed procedure was applied firstly at urban scale on the historical centre of Matera (MT), and then at building scale on the Pietro Capuzi school located in Visso (MC). The prediction of the fragility functions, instead, were compared on the NLTHA results of an Ancient seminar located in the historical village of Sant'Agata de' Goti (BN), where also a NLTHA on the transversal section of the village were performed. The three case studies, as shown in the Italian hazard map (Figure V.1), fall in two areas where significant seismic actions are expected at the site, PGA [0.15g - 0.18g] for Matera (MT) and Sant'Agata de'Goti (BN) and PGA [0.20g - 0.23g] for Visso (MC). The first two case studies were selected due to the availability of single-station recordings of seismic ambient noise (on both structure and soil) and permanent accelerometers records for Matera and the school building respectively. Sant'Agata de' Goti instead, was chosen because a detailed soil and structure characterization was available.

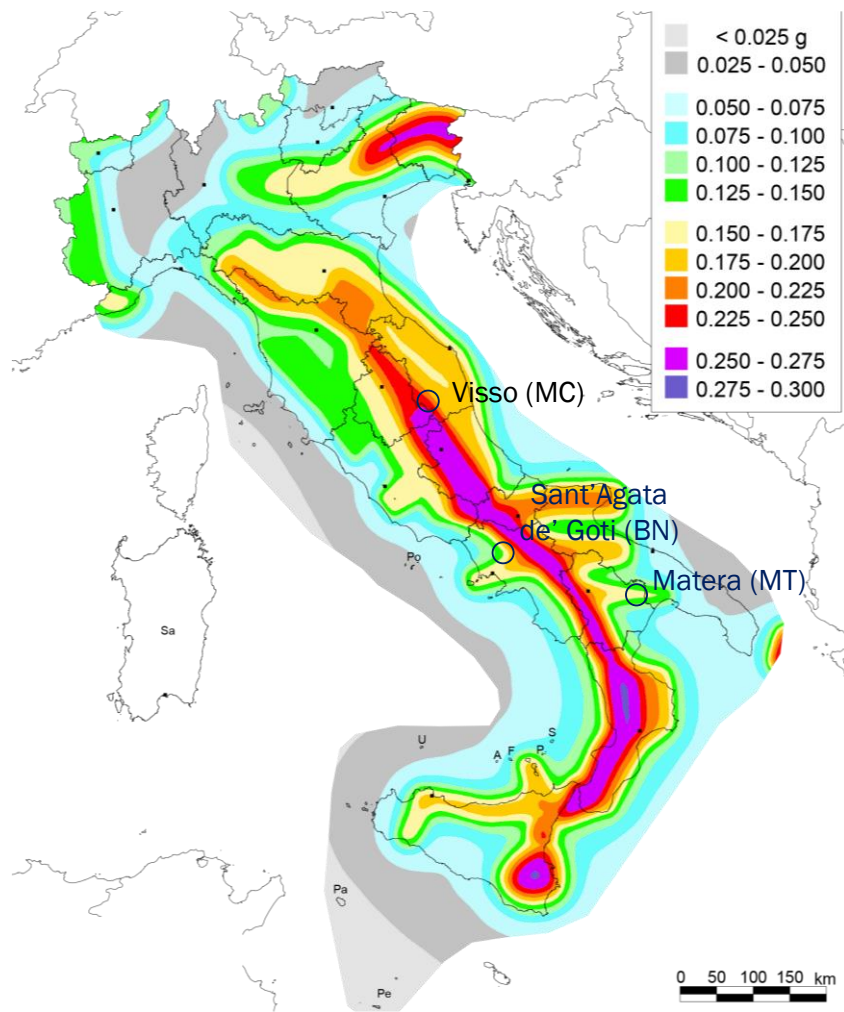


Figure V.1 Location of the case studies on the Italian hazard map in terms of peak ground acceleration with a probability of exceedance equal to 10% in 50 years

V.1. The proposed analytical approach

A simplified procedure for quick assessment of the frequency modification was proposed in Chapter III. A set of weighting coefficients were calibrated to properly modifying the shear wave velocity, $V_{s,eq}$, and consequently calculate the equivalent soil-structure stiffness parameter, σ_{eq} , to take into account the influence of both foundation embedment and soil layering. Also, depending on the h/b ratio, regression models for estimation of fundamental frequency and radiation damping ratio were provided. Nonetheless, since the analyses used as reference to calibrate the regression coefficients cannot capture the 3D nature of the radiation mechanism, the regression model for the estimation of ξ_{rad} is not considered. In addition, the proposed formula for the estimation of f^* can be applied when σ_{eq} is higher than 2 (considering the same lower bound of σ used in the Veletsos and Meek (1974) and Maravas et al., (2014), formulations).

Figure V.2 shows the workflow of the proposed approach. To apply the modified approach, it is necessary to know:

- the V_s profile and the physical, mechanical properties (G , ρ) of the materials in the volume affected by the horizontal motion (soil and foundation);
- the depth, D , and the width, B , of the foundations;
- the height, h , and the fixed-base frequency, f_0 , of the structure.

The weighting coefficients, p_i , were chosen by comparing the seismic impedance ratios between the soil layers, μ with those obtained from the parametric study (Chapter III). Based on the equations reported in Chapter III Eqs (III.24), (III.25) and (III.26), the equivalent properties, respectively, G_{eq} , ρ_{eq} and $V_{s,eq}$, were computed:

$$G_{eq} = \frac{\sum_{j=1}^3 p_j G_j A_j}{\sum_{j=1}^3 A_j} \quad (III.24)$$

$$\rho_{eq} = \frac{\sum_{j=1}^3 p_j \rho_j A_j}{\sum_{j=1}^3 A_j} \quad (III.25)$$

$$V_{s,eq} = \sqrt{\frac{G_{eq}}{\rho_{eq}}} \quad (III.26)$$

Knowing $V_{s,eq}$, h and f_0 , the equivalent soil-structure stiffness parameter, σ_{eq} , is computed through the following expression:

$$\sigma_{eq} = \frac{V_{s,eq}}{hf_0} \quad (V.1)$$

Given h/b ratio, the corresponding regression coefficients, α and β , were chosen and the frequency variation, f^*/f_0 , is computed through the following expression:

$$\frac{f^*}{f_0} = \alpha \sigma^\beta + 1 \tag{III.17}$$

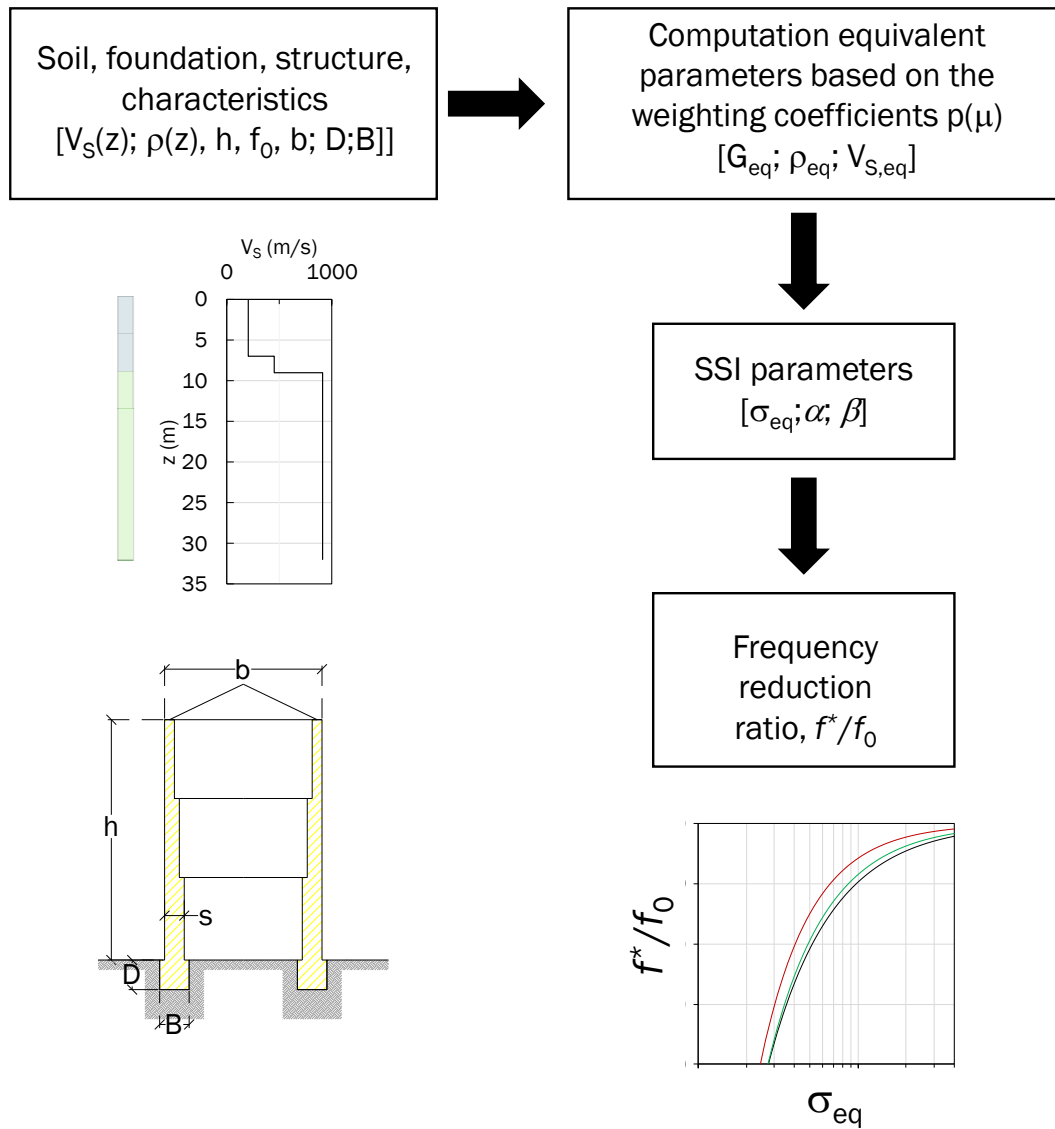


Figure V.2 Proposed approach for the estimation of the frequency reduction ratio f^*/f_0

V.2. The case study of Matera buildings

Matera (Figure V.3) is a historical city located in Southern Italy, well-known for its peculiar geomorphological setting which strongly conditioned its urban development. With its historical centre of the Sassi UNESCO World Heritage Site Matera has been appointed as European Capital of Culture 2019. It is one of the main test sites of the Research project CLARA “*Cloud platform and smart underground imaging for natural risk assessment - Smart Cities and Communities and Social Innovation*” (<http://www.smartcities-clara.eu/>), promoted by a large public-private partnership with the participation of three institutes of CNR (IMAA, IREA, ISTC), OGS Trieste, University of Ferrara, University of Roma-La Sapienza, University of Enna and University of Catania.

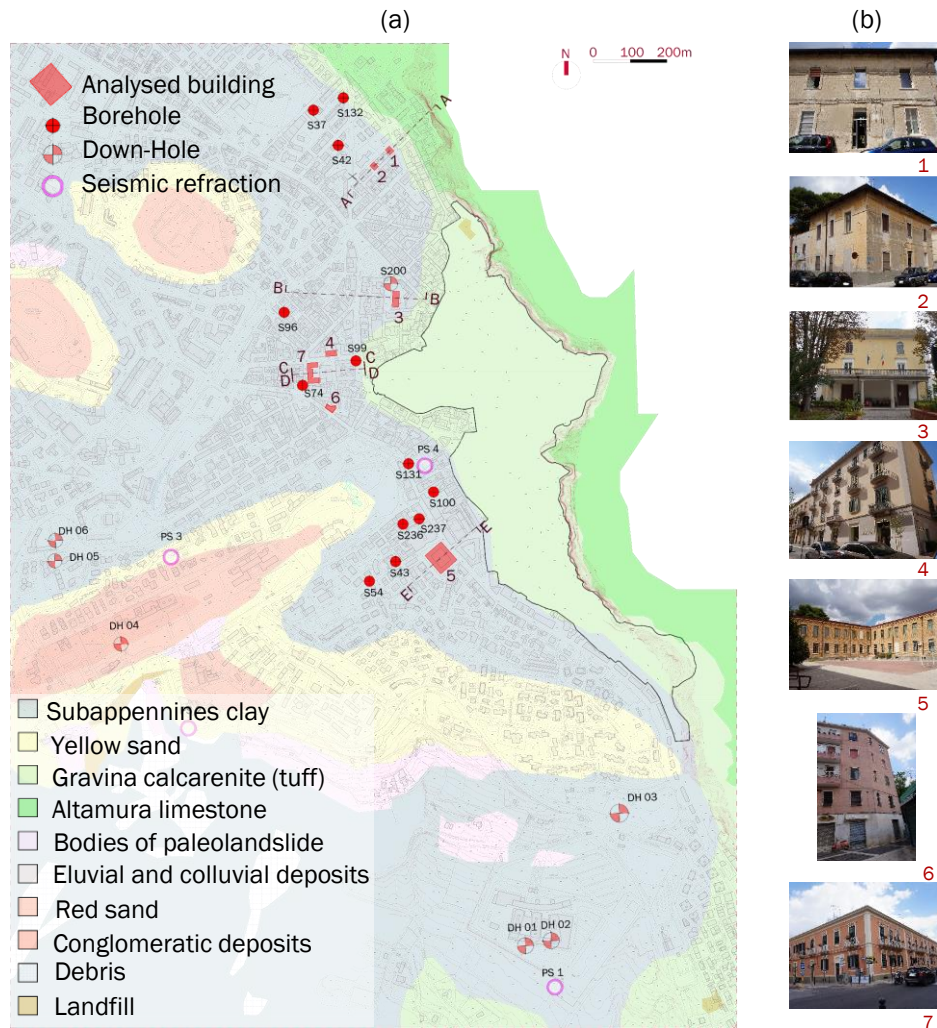


Figure V.3 Matera: (a) geological map with subsoil investigations (b) analysed buildings

In the framework of this project, a total of 230 single-station recordings (134 on the soil surface and 96 on masonry and reinforced concrete buildings) of seismic ambient noise were carried out by CNR-IMAA at Tito Scalo (Potenza) and analysed with the Horizontal to Vertical Spectral Ratio technique (Gallipoli et al., 2020).

The main geological formations outcropping in the North-West and South-East of the urban center, as well as in the “Sassi” area, showed in Figure V.3a, are represented by Altamura limestone and Gravina calcarenites. The latter formation is covered by the Subappennines clay and other overlying materials, with thickness varying from a few meters, near the Sassi area, to 40-50 m inwards.

To validate the procedure described in Section III.4, a set of 7 masonry buildings, shown in Figure V.3b, was selected, since located on deformable soil and characterized by a structural configuration similar to those considered in the parametric study described in Chapter III, i.e. were built between the 1919 and 1980; the loadbearing walls made up of tuff masonry; had a number of storeys between two and four; had a regular development in plan and height.

The subsoil was widely investigated in the past years by numerous boreholes, down-hole and seismic refraction tests (Gallipoli and Lupo, 2012). In order to integrate the existing experimental data, in 2020 in the framework of the ReLUIS project, a borehole (S 200 in Figure V.3a) was drilled down to 53m near one of the analysed buildings (# 3 in the same map), and a downhole test was performed in the borehole.

Following the boreholes layering near the buildings, four geological sections, shown in Figure V.4, were drafted to define the soil profile for each case. The same figure reports the elevation and distance of the boreholes with respect to the section, as well as the schematic geometry of the overlying buildings and the frequency values measured by Gallipoli et al. (2020) either on the ground surface (f_{soil}) or on the top of the structure (f^*_{EXP}); note that sections CC and DD differ only for the overlying buildings and the relevant frequencies.

As shown in the sections, the thickness of the clay increases from 7m to 30 m moving from East to West, i.e. with increasing distance from the terrace ridge overlooking the Sassi area; only in the case of sections AA and BB the Gravina calcarenite was intercepted by three drillings.

In Table V.1 the main characteristics of the 7 buildings are outlined, i.e. height, h , width, b , the experimental frequency for the structure, f^*_{EXP} , and the soil, f_{soil} , and the thickness of the Subappennines clays, H_c (from #4 to #7 the thickness was assumed from the geological section, hypothesizing a slope of 22% for the Gravina calcarenite)

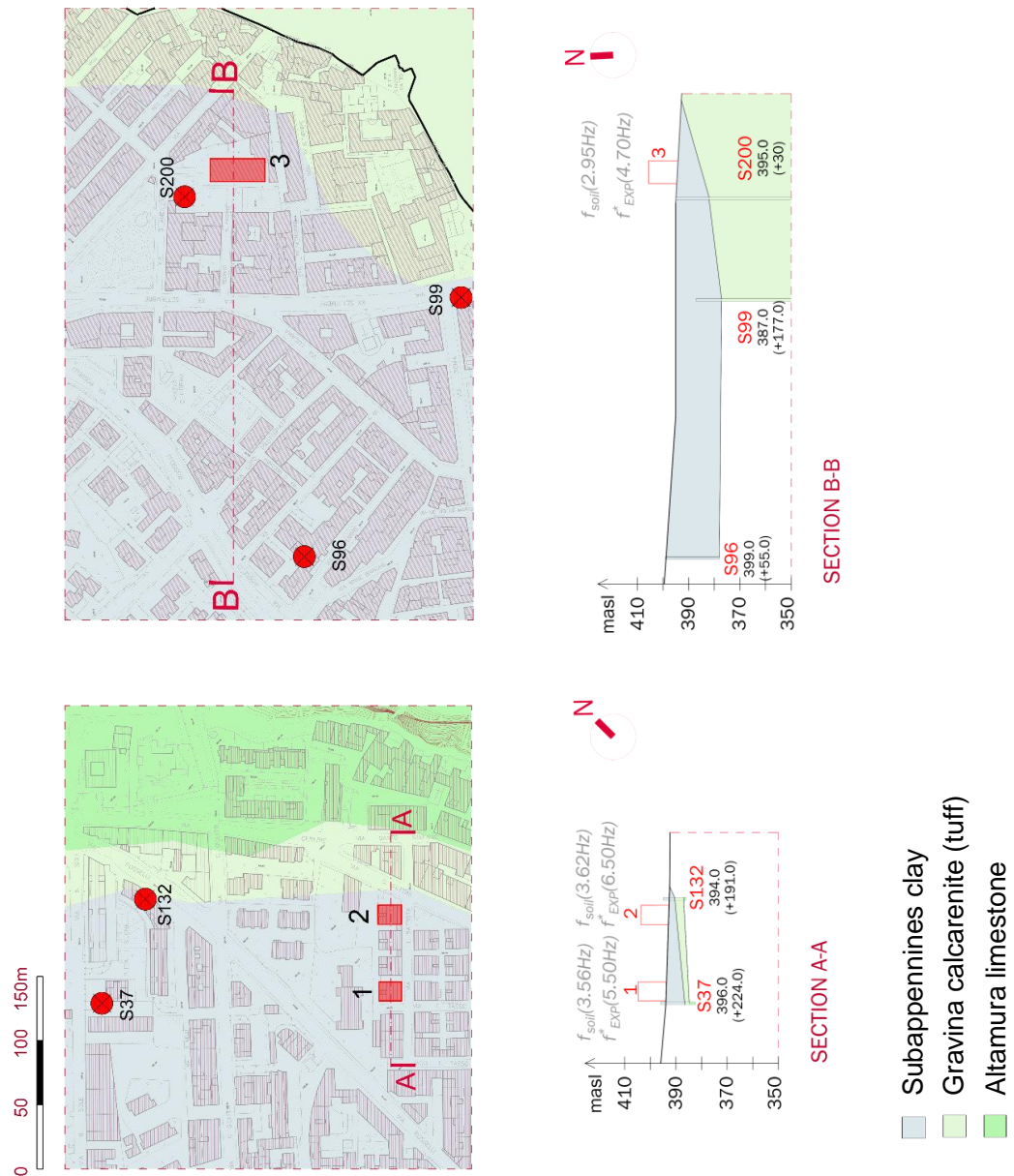
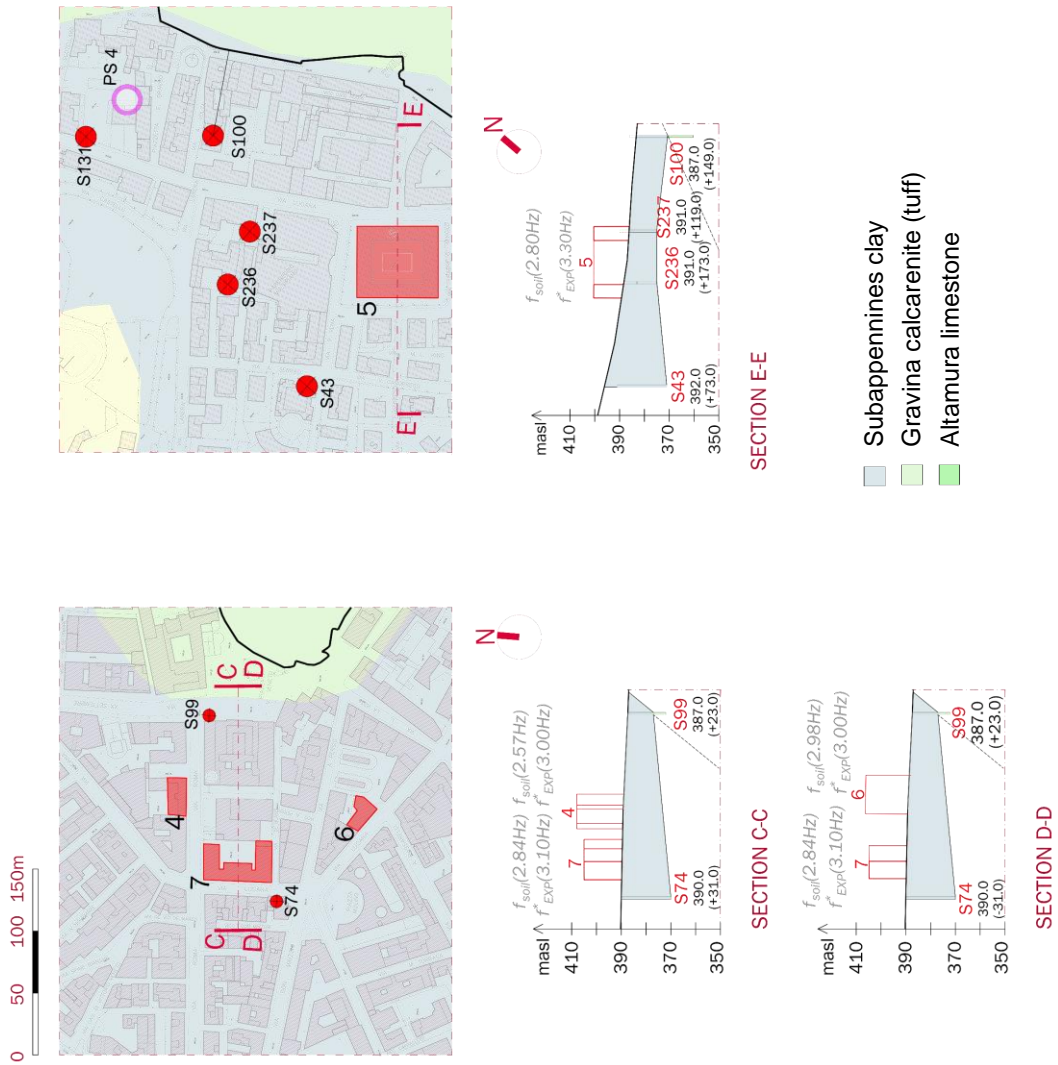


Figure V.4 Geological sections relevant to the seven buildings analysed



FigureV.2 Continued

Table V.1 Buildings characteristics

ID	N° storeys	h (m)	b (m)	f_{EXP}^* (m)	f_{soil} (Hz)	H_C (m)
1	2	10	16	6.50	3.62	4
2	2	11	16	5.50	3.56	7
3	3	12	18	4.70	2.95	9
4	4	18	17	3.00	2.98	≈31
5	2	11	12	3.30	2.80	≈25
6	3	15	14	3.00	3.93	≈27
7	4	19	10	3.10	2.84	≈28

In the study by Gallipoli et al. (2020), empirical correlations were suggested as linear relationships between the height of the buildings and the experimental periods. The whole data set relevant to the 96 buildings considered was sub-divided into groups based on the structural typology (masonry, reinforced concrete) and the soil cover (Gravina calcarenites, Subappennines clays). In particular, from the experimental data of masonry buildings on Gravina calcarenites (soil type B), a reasonably well-defined correlation between the masonry building height, h , and its fundamental period, T_0 , was obtained as $T_0 = 0.0137h$. This latter value can be assumed as a first rough estimate of the fixed-base fundamental period of the masonry buildings typical of this area of the city of Matera.

Figure V.5 shows the comparison between the experimental period, T_{EXP}^* , measured through the H/V spectral ratio on the seven buildings selected and the fixed-base value, T_0 , estimated considering the above correlation relevant to masonry buildings on calcarenite. It can be noted that the deviation of T_{EXP}^* from T_0 increases with H_C , highlighting a likely SSI effect.

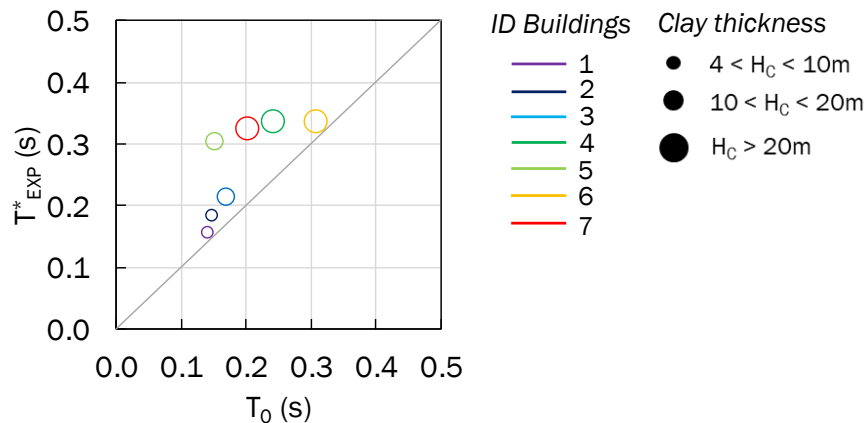

Figure V.5 Comparison between the experimental and fixed-based periods

Table V.2 summarizes the mechanical properties of the different materials, obtained by the down-hole and/or the seismic refraction tests (Gallipoli and Lupo, 2012) nearest to the buildings. The mechanical properties of the masonry were derived from Tab. C.8.5.1 (MIT, 2019), considering a tuff masonry with irregular texture, based on the most recurrent typology in the historical centre near the “Sassi” area.

Table V.2 Mechanical properties of soil and masonry

Material	V_s (m/s)	G (MPa)	ρ (kg/m ³)
Subappennines clays	190	63	1750*
	250	122	
Gravina calcarenites	450	109	1800**
	750	984	
Altamura limestone	914	2297	2750***
Masonry	/	450	1600

*Typical average values for soft clay and loose sand, **soft rock, ***hard rock
(Lanzo and Silvestri, 1999)

Figure V.6 shows the seven SFS cross-sections for each building, considering the soil stratigraphy obtained from the geological sections in Figure V.4. The building height and width were obtained by the Gallipoli et al (2020) surveys, whereas the thickness of the bearing walls was set based on relations with the building height, used in the past (Augenti and Parisi 2019) for the masonry building design (Section II.2). For the two-stories buildings it was assumed $s=0.70\text{m}$, for three-stories buildings $s=0.81\text{m}$, for four stories buildings $s=0.93\text{m}$ and for five stories buildings $s=1.03\text{m}$. An enlargement of 0.15 m at each side of the bearing wall was considered as foundation base width. The value of D was set to 1.5 m for buildings 1, 2, 4, 5, 7, and to 3.50m for the buildings 3, 6, where an underground level is present.

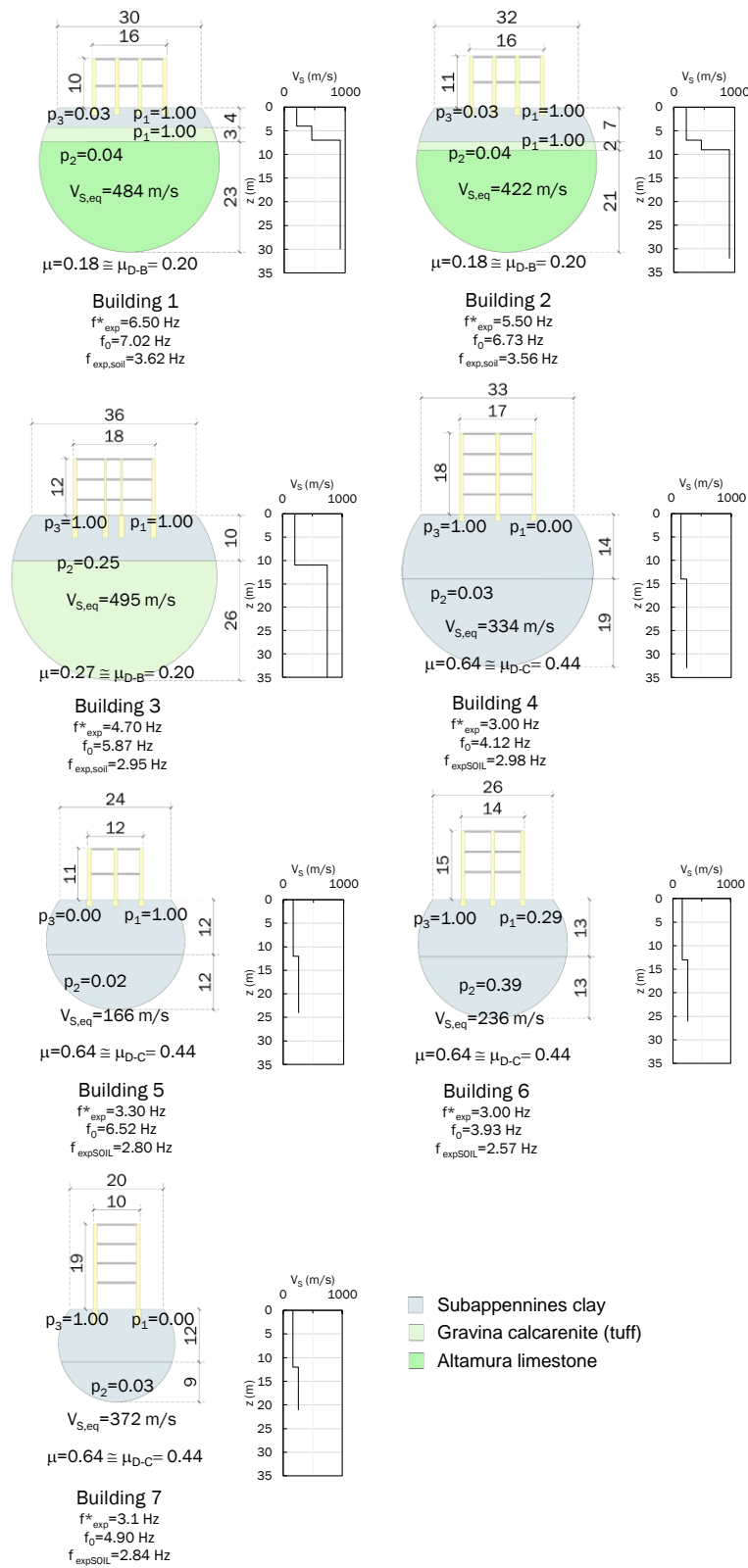


Figure V.6 Soil and foundation volumes, for each building, affected by inertial interaction

The weighting coefficients, p_1 , p_2 and p_3 (Section III.4), were chosen by comparing the seismic impedance ratios between the soil layers, μ (reported in Table V.3) with those of the parametric study, i.e. $\mu_{DD}=1.00$, $\mu_{DB}=0.20$, $\mu_{DC}=0.44$, $\mu_{CB}=0.45$. The seismic impedance ratios between the soil layers were computed as follows:

$$\mu_{12} = \frac{(V\rho)_1}{(V\rho)_2} \quad (V.2)$$

where the subscript 2 and 1 indicated respectively the shallow cover and the in-depth formation.

Table V.3 SSI parameters (σ_{eq} and corresponding f^*/f_0 values)

ID Building	$V_{s,eq}$ (m/s)	μ	σ_{eq}	f^*/f_0
1 (DB)	484	0.18	6.64	0.85
2 (DB)	422	0.18	5.79	0.82
3 (DB)	495	0.27	6.78	0.87
4 (DC)	334	0.64	4.57	0.83
5 (DC)	166	0.64	2.27	0.51
6 (DC)	236	0.64	3.24	0.73
7 (DC)	372	0.64	5.10	0.86

To calculate the equivalent stiffness and density, G_{eq} and ρ_{eq} , of the system consisting of the embedded foundation and the layered subsoil, Eqs. (III.24) and (III.25) were adopted. Thus, the equivalent shear wave velocity for each SFS system was computed through Eq. (III.26), as summarised in Table V.3. The corresponding value of the frequency reduction ratio, f^*/f_0 , was estimated through Eq. (III.17).

Table V.3 also reports the values of σ_{eq} and the corresponding values of f^*/f_0 . As shown, for the same number of stories, i.e. buildings 1-2-5, the fundamental frequency reduces with the decrease of σ_{eq} induced by the increase of thickness of the clay layer, as shown in Figure V.5.

Figure V.7 shows the comparison between the experimental periods versus the values obtained from the application of the simplified method, either in its traditional expression (full symbols), i.e. through σ computed using the shear wave velocity of the soil cover, or by the proposed approach (empty symbols), i.e. through σ_{eq} . It can be observed that the traditional formulation overestimates the actual values, while a significantly better agreement is found between the proposed procedure and the experimental data.

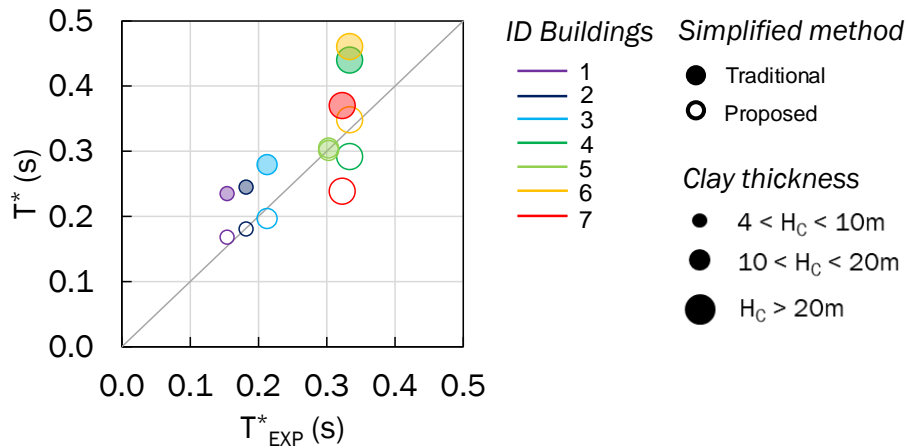


Figure V.7 Comparison between the experimental and analytical periods, the latter calculated with the traditional and the proposed approach

V.3. The case study of a school building at Visso

The procedure was also applied to a well-documented case study of a single building, the “Pietro Capuzi” school located in Visso, a village in Marche region (Figure V.8c). Built around 1930, it was severely damaged by the 1997 Umbria-Marche earthquake sequence; after restoration, it was accurately characterised and monitored by the Civil Protection Department, and finally practically destroyed by the recent Central Italy sequence in 2016 (Brunelli et al 2020).

The structure extended over a 620 m² floor surface, resembling a flipped "T" (Figure V.8c), and consisted of two stories and an attic covered by a pitched wooden roof. The vertical walls were characterized by a two-leaf stone masonry, apart some internal pillars made by a brick masonry. The diaphragms were composed by a concrete-masonry flooring system, except for the attic that was made by iron beams and thin, hollow clay bricks. In the '90s, after the 1997 Umbria-Marche earthquake sequence, some extensive retrofitting interventions were provided, mainly consisting of mortar injections through some internal walls, insertion of some tie-rods, improvement of the walls-to-roof connection and replacement of part of the timber roof structure, deteriorated due to ageing.

The foundation of the building composed of larger bearing walls with a shallow embedment, except for the North-East side, where there was a partially underground additional level.

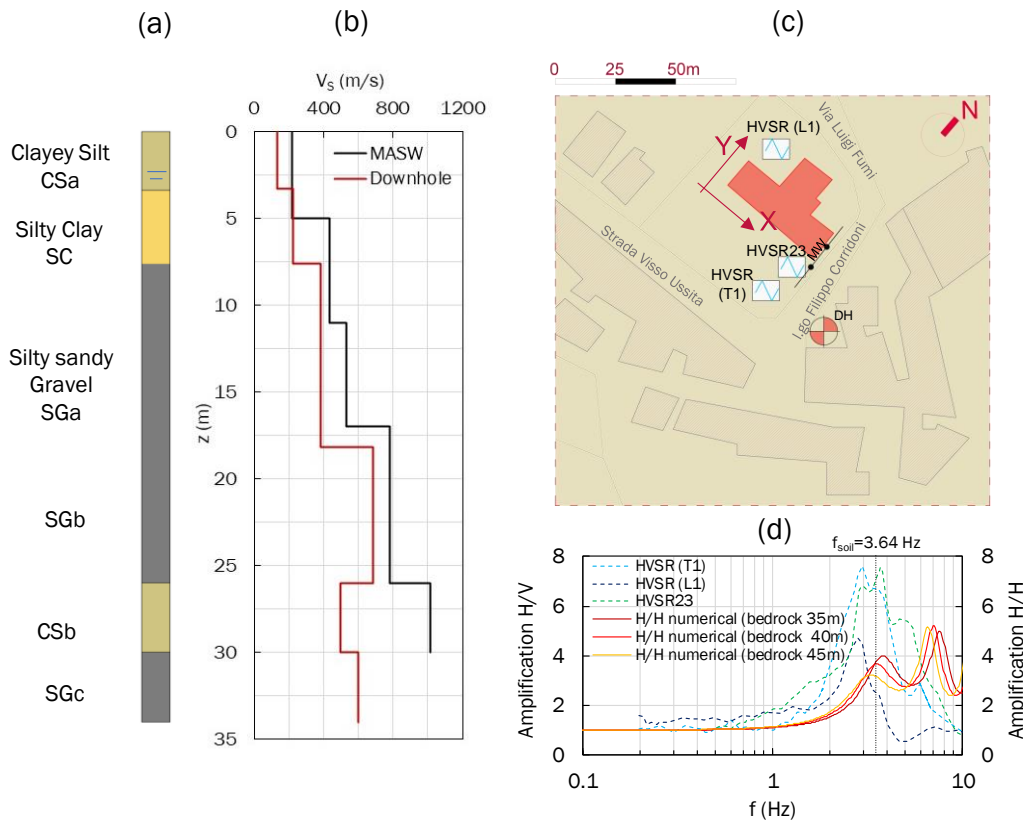


Figure V.8 (a) Soil profile, (b) V_s profiles measured through DH and MASW tests, (c) plan view of school and location of the surveys and (d) HVSRL1 results

V.3.1. Geotechnical characterization

Figure V.8c shows the field tests executed during the seismic microzonation study following the Central Italy earthquake in 2016 (MZS3 2018). A borehole was drilled down to 35m, confirming the presence of a silty-sandy gravel formation (SG), locally interbedded by clayey silt (CSa, CSb) and silty clay (SC) lenses, as shown in Figure V.8a. The water table was intercepted at 2m below the ground level. A down-hole test was performed in the borehole, leading to the measurement of the shear wave velocity profile shown in Figure V.8b. The value of V_s generally increases with depth, showing a significant increase around 18m. An inversion in the V_s profile was measured around 26m in depth, where the silt lenses are thicker and closer to each other. The DH results are almost in accordance with the V_s profile measured through a MASW test (ReLUIS 2018a) close to the borehole, again shown in Figure V.8c. Also, numerous records of

ambient noise to compute the soil resonance frequency through the horizontal to vertical spectral ratio technique (HVSR).

Since no samples were taken from the borehole, the physical and mechanical properties of the soil were adopted on the basis of those collected and adopted in the seismic microzonation of surrounding villages.

Table V.4 summarizes the physical and mechanical properties of the subsoil profile. The unit weight, γ , and the Poisson's ratio, ν , were inferred from data collected in the seismic microzonation. The small-strain parameters and the bedrock depth were validated comparing the experimental predominant frequencies with the resonance value computed through 1D seismic response analyses performed along the same vertical. The comparison is shown in Figure V.8d with reference to three possible bedrock depths (35m, 40m and 45m) compatible with the geological model; being the comparison satisfying for any of the three depths hypothesized, the intermediate value of 40 m was assumed for the analysis.

Table V.4 Soil mechanical properties for soil (*ReLUIS 2018b*)

	Z _{min} (m)	Z _{max} (m)	ρ (kg/m ³)	V _s (m/s)	G (MPa)	ν
CS _a	0	3.2	2000	136	38	0.4
SC	3.2	8	2000	226	104	0.4
SG _a	8	18	2100	383	314	0.3
SG _b	18	26	2100	683	999	0.3
CS _b	26	30	2000	500	510	0.4
SG _c	30	40	2100	602	776	0.3
Bedrock	40	/	2200	1300	3790	/

V.3.2. Calibration and assessment of the simplified model

Since permanent accelerometers were installed by the Italian Seismic Observatory of Structures – OSS (Dolce et al. 2017), different records were made available of the school dynamic behaviour under ambient noise. Those records were processed (ReLUIS 2018a) allowing for the identification of modal parameters (i.e. natural frequencies, damping ratios and mode shapes) of the undamaged structure (Lorenzoni et al. 2019). The dynamic identification highlighted that the 1st mode deformed shape results from a combined effect of torsional and flexural behaviour along the y-direction, while the 2nd mode is purely torsional and the 3rd purely flexural along the x-direction. Cattari et al., (2019), de Silva et al., (2019b) and Brunelli et al., (2020), compare the experimental frequencies with the results of modal analyses performed on a 3D fixed-base model and a 3D compliant-base model, in which the base restraints were

replaced with translational and rotational springs simulating the soil-foundation impedance. The comparison confirmed the expected significant effect of the SFS interaction on the dynamic behaviour of the structure, due to the low stiffness of the foundation soil.

The SSI effects were also investigated through the replacement oscillator (RO) based on the Maravas et al (2014) formulation, by approximating the structure with a single degree of freedom (SDOF) system, characterized by a viscous damping ratio equal to 3% and the dynamic properties associated to the first vibration modes of the fixed-base configuration as resulting from the modal analysis. In order to evaluate the SFS effects on the first mode, the SDOF system was considered to be placed on a compliant foundation characterized by the sum of the impedances of the y-oriented bearing walls; on the other hand, the sum of the impedances of the x-oriented bearing walls was considered in the calculations associated to the third mode (Brunelli et al. 2020). Soil stiffness was assumed equal to the small-strain shear modulus of the shallowest layer, G_0 , in order to predict the fundamental period recorded during the on-site dynamic identification.

The procedure outlined in Chapter III was applied to the sections A-A and B-B drawn across the short sides of the T-shaped building along the x and y direction, respectively (see Figure V.9a). With reference to the geometric layout shown in Figure V.9b, the properties summarized in Table V.4 were considered for the soil, and for the masonry it was assumed $G=858\text{MPa}$ and $\rho=2000\text{kg/m}^3$. The width and the height above ground of the structure are 11 m and 10.15 m, respectively, while for the foundation an enlargement of 0.15 m at each side of the bearing wall ($s=0.60\text{m}$) was considered, leading to a width equal to 0.90 m. The value of the foundation embedment, D , was set to 2.95 m, where the underground level is present (green fill in Figure V.9a) and 0.6 m elsewhere.

Table V.5 Equivalent values of soil compliance for the different embedment

Material	D=0.60 m				D= 2.95m			
	A (m ²)	G_{eq} (MPa)	ρ_{eq} (kg/m ³)	$V_{s,eq}$ (m/s)	A (m ²)	G_{eq} (MPa)	ρ_{eq} (kg/m ³)	$V_{s,eq}$ (m/s)
CS	77.7				71.3			
SC	115.3				115.3			
SGa	249.4	30.6	742.1	203.0	249.4	31.1	736.3	205.4
SGb	66.5				66.5			
Masonry	1.62				8.0			

The fixed base frequencies, f_0 , associated to the 1st (along y) and 3rd (along x) mode were assumed equal to 5.75-6.76 Hz (1st - 3rd modes) from the results of modal

analyses. As for the Matera buildings, the weighting coefficients p_1 ; p_2 and p_3 were chosen by comparing the seismic impedance ratios between the soil layers, μ (Eq.V.1) with those of the parametric study. Since in the significant subsoil volume four soil layers are intercepted, the values of V_s were assumed as the weighted average of the layers CS and SC (shallow cover) and SGa and SGb (in-depth formation), respectively. A value of $\mu=0.37$ was obtained, close to that corresponding to the case of ground type layering D-C, $p_1=1.00$, $p_2=0.00$ and $p_3=0.17$.

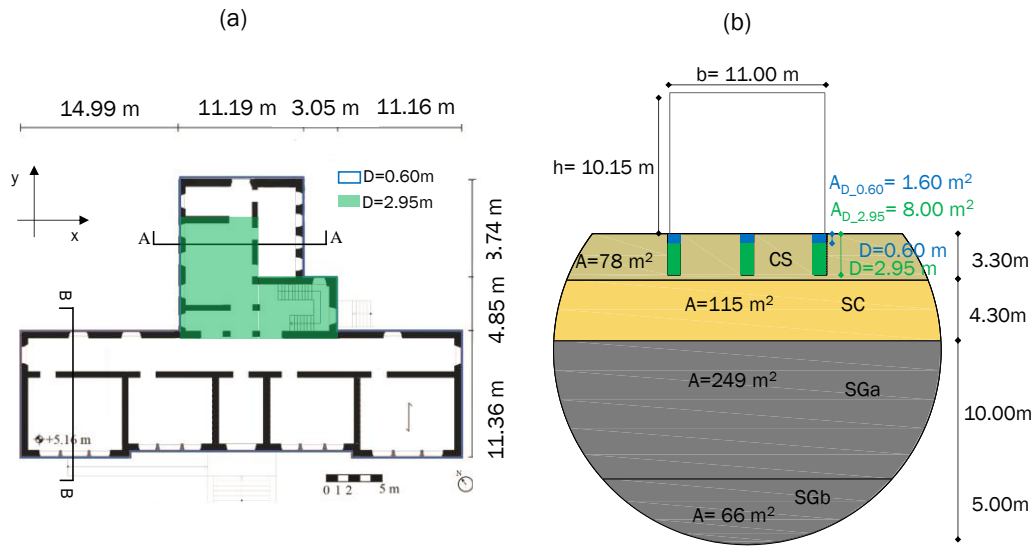


Figure V.9 (a) Plan view of the building (Brunelli et al 2020) and (b) soil and foundation volumes affected by the horizontal motion (section A-A/B-B)

By applying Eqs. (III.24) and (III.25), G_{eq} and ρ_{eq} were computed; thereafter, by applying Eq. (III.26), V_{Seq} was obtained for each embedment D , as summarized in Table V.5. The corresponding value of the frequency reduction ratio, f^*/f_0 , was estimated through Eq. (III.17).

Figure V.10 shows the comparison between the compliant base periods T^*_{EXP} , T^*_{NUM} and T^*_{RO} , as obtained from the experimental measurements (EXP), the modal analysis by 3D compliant base models (NUM), and the replacement oscillator with dynamic impedance (RO), respectively, versus the values T^* obtained from the application of the simplified method. This latter was adopted either according its traditional expression, i.e. through σ computed using the shear wave velocity of the soil cover, $V_{s,CS}$ (Figure V.10a) or by the updated approach proposed in this study, i.e. through σ_{eq} (Figure V.10b). It is apparent that the traditional formulation overestimate the frequency reduction (Figure V.10a), while a significantly better agreement is found between the

updated procedure and the experimental data or numerical results, as shown in Figure V.10b.

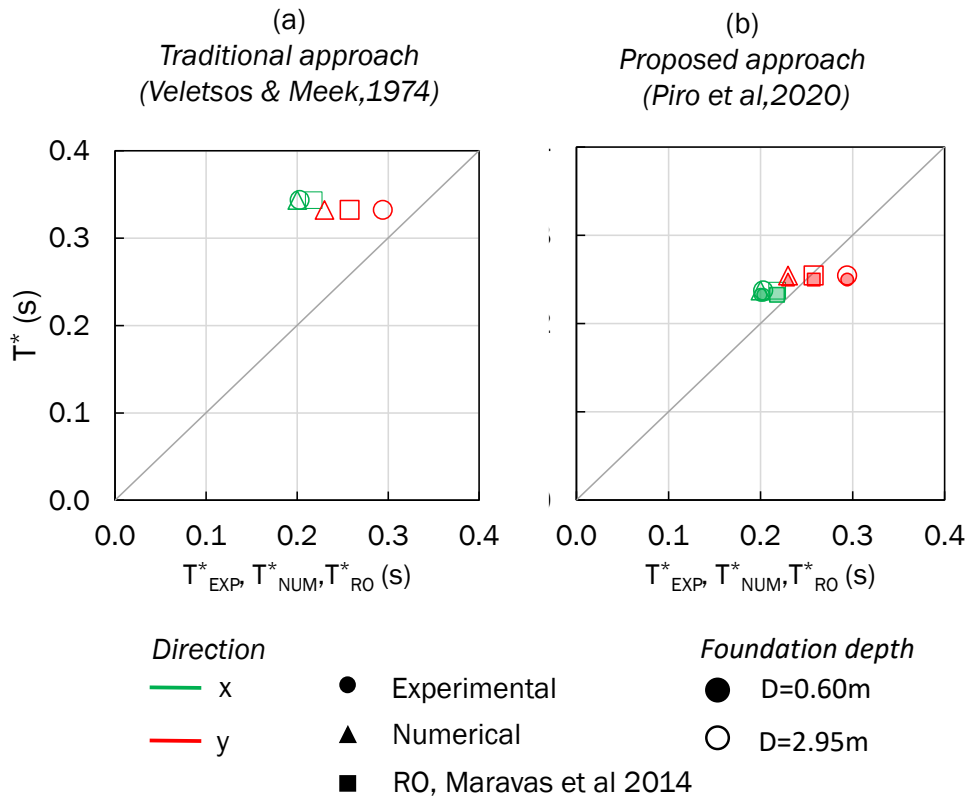


Figure V.10 Comparison between the compliant base periods (T_{EXP}^* , T_{NUM}^* and T_{RO}^*) and the analytical periods calculated with the (a) traditional and (b) updated approach

V.4. The case study of Sant'Agata de' Goti historical centre

Many historical towns which rest on soft rock slabs (Fenelli et al., 1997) are affected by seismic and landslide hazards due to complex geological and morphological conditions, especially in Central-Southern Italy. These causes could entail the evaluation of the seismic site response particularly complex and difficult to verify (Pagliaroli et al. 2020). Among these historical towns, there is Sant'Agata de' Goti, (Figure V.11b) a picturesque medieval village located in Campania region (Italy), edified on a tuff cliff between two creeks, Riello and Martorano (de Silva et al., 2013; Piro et al., 2017; Vuoto et al., 2018; Piro et al., 2019). The characteristic of this site is the articulate system of cavities dug under the whole historical centre to build the above ground structures. Typically, the main walls of the above-ground structure were built

during the quarrying activities on the lateral sides of the pit. As a result, the shape and embedment of foundations are often irregular and the limits between the structure and the surrounding rock are hard to be distinguished.

At urban scale, such complex site condition (morphology and the underground cavities) could lead to ambiguous ground motion amplification. In fact, under low-amplitude input motions, hence for a linear dynamic soil response, the presence of underground cavities is expected to attenuate the surface motion compared to the free-field condition (e.g., Sanò, 2011). This attenuation depends mainly on the cavity geometry (depth from the ground surface, diameter and shape), and on the ratio between the predominant frequency of the input motion and the fundamental soil frequency (Chiaradonna et al. 2014). Evangelista et al., (2016), instead, evidenced an amplification induced by the presence of the cavities under high amplitude motions that was caused by nonlinear effects especially at high and intermediate frequencies. Previous studies on the town of Sant'Agata de' Goti by Scotto di Santolo et al. (2015) showed the relevance of the presence of cavities for the seismic stability of the cliff and a reduction of the acceleration above the cavity axis.

At the building scale, instead, the presence of underground storeys can influence the reparability after an earthquake (i.e. repair time and cost), and hence the seismic resilience of historical buildings (Piro et al., 2017). A correct assessment of the building reparability also requires a realistic simulation of the elasto-plastic stress-strain behaviour of the masonry. To this aim, an advanced strain-softening constitutive model was carefully calibrated by Vuoto et al. (2018) on experimental data and implemented in the SSI model used in this study.

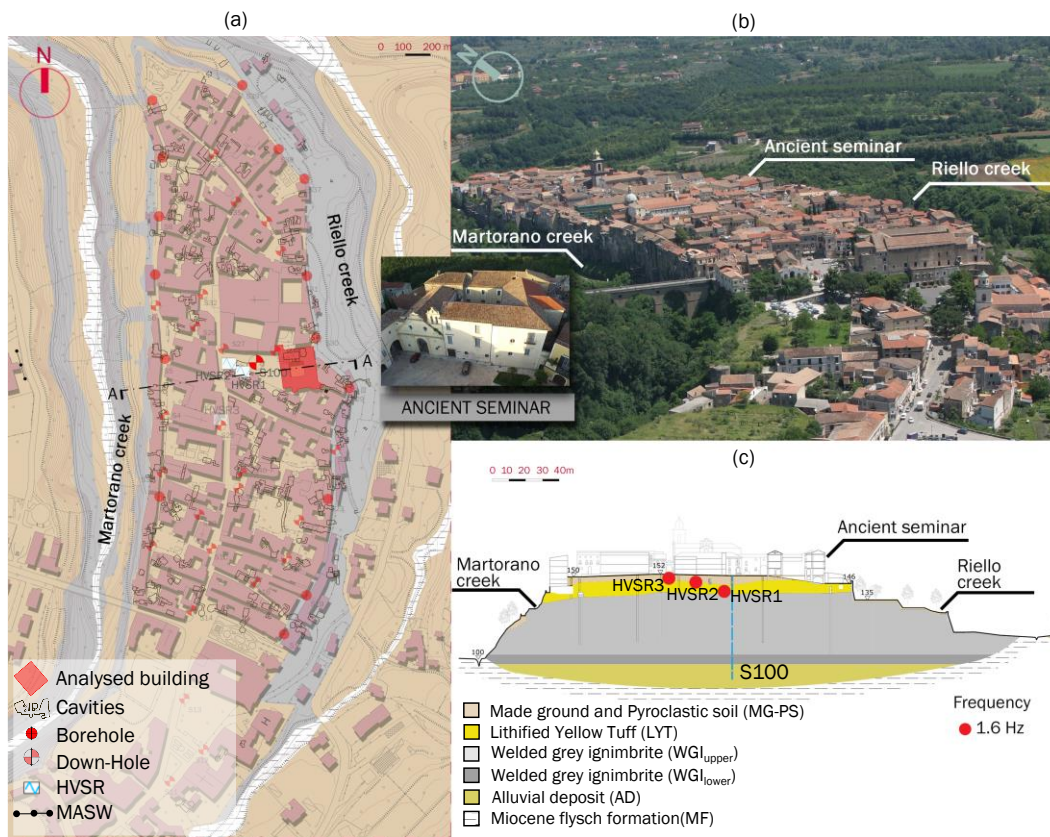


Figure V.11 Sant'Agata de' Goti: (a) map; (b) aerial view; (c) geological section

V.4.1. Subsoil characterization

The historical centre of Sant'Agata de' Goti (Figure V.11) lies on a N-S oriented tuff cliff, about 170 m wide and 600 m long, bordered west and east by two valleys formed by the Martorano and Riello rivers, respectively. The main geological formation (Figure V.11c) characterising the cliff is represented by the volcanoclastic formation of the Campanian Ignimbrite (De Vivo et al. 2001), where three lithofacies can be distinguished from the bottom: low-cemented grey tuff (i.e. 'welded grey ignimbrite') with scoria and pumices (WGI_{lower}), well-cemented grey tuff with dark and grey scoria, pumices and subordinately lithics and crystals (WGI_{upper}), lithified yellowish tuff (LYT). The Campanian Ignimbrite overlies three alluvial layers of silty sand (SS), clayey silt (CS) and sandy gravels (SG), defined as alluvial deposit (AD). This deposit rests on a bedrock of Miocene age (MF), which outcrops along the Martorano and Riello valleys at about 100 and 115m a.s.l., respectively. Since no boreholes reached the Miocene layer, the variation of its depth underneath the alluvial deposit was assumed on the basis of field observations of the inclined outcropping layer in the lateral valleys.

The geological model shown in Figure V.11c was confirmed by the stratigraphy obtained by a trench excavated in 1995 by ENI society (Ermolli et al., 2010) about 2 km from the historical centre of Sant'Agata de Goti. Since the areas are close in terms of geological asset and the alluvial deposit (AD) is not different from the alluvial member recognized in the trench, the correlation can be considered satisfying. Summarising, from the above considerations the maximum depth of Miocene flysch was assumed as located at around 66m below the historical centre (Piro et al., 2019). Measurements of shear wave velocity on outcrops at nearby sites showed that such a formation can be considered as the seismic bedrock for the whole area (Piro et al. 2017).

The LYT layer is crossed by a complex system of cavities (Figure V.11a), resulting from the past quarrying activities aimed to extract building material. Some underground rooms were partially filled over time, but most of them are still used to store food. Their stability under gravity loads was preliminarily investigated by de Silva et al. (2013) through simplified approaches. Their effect on the seismic site response was evaluated by Scotto di Santolo et al. (2015) through numerical analyses performed on a cavity damaged by the Irpinia earthquake in 1980.

The results of field and laboratory tests executed in the framework of the ReLUIS project (ReLUIS, 2018c) were addressed at integrating existing experimental data collected after several stabilization works executed since 1994 to 2012. The numerous boreholes and down-hole tests shown Figure V.11a were performed in 1994 until a depth of 41m, without intercepting the seismic bedrock (de Silva et al., 2013). In addition, a surface geophysical test, MASW, was performed on the opposite side of the hill in 2009 (Piro et al, 2017). At the end of 2017 (ReLUIS, 2018b and ReLUIS, 2018c), a borehole was drilled down to 63m in the town centre, revealing the stratigraphy shown in Figure V.12a: a 6 m thick shallow cover of made ground and pyroclastic soil (MG-PS) overlies a 5 m thick upper deposit of lithified yellow tuff (LYT) and a deeper layer of welded grey ignimbrite (WGI). Below the pyroclastic formations, three alluvial layers of silty sand (SS), clayey silt (CS) and sandy gravel (SG) were intercepted. Thirteen undisturbed, remoulded and partially undisturbed samples were taken from the borehole to measure physical, static and dynamic properties of the different soil types. Four samples were taken at the depths shown in Figure V.12a to perform consolidated-drained triaxial compression test (TX-CID) on CS and WGI, as well as resonant column (RC) and cyclic torsional shear (CTS) tests on WGI and CS soil. No cyclic or dynamic laboratory tests have been yet performed on LYT, since modifications to the torsional shear equipment should be required due to the high stiffness of the rock material.

V.4.1.1. Small strain properties

A down-hole (DH) test was performed in the borehole, leading to the measurement of the compression and shear wave velocities, V_p and V_s , respectively. The values were obtained as mean slopes of the dromochrones. A significant shear and compression impedance contrast was recognized between the shallow cover and the stiffer LYT formation, while an inversion of both velocity profiles was detected in the WGI formation, followed by a further reduction (for V_s only) around 48m in depth, corresponding to a decrease in the degree of welding of the grey ignimbrite. The shear wave velocity appears to slightly increase with depth in the underlying alluvial layers.

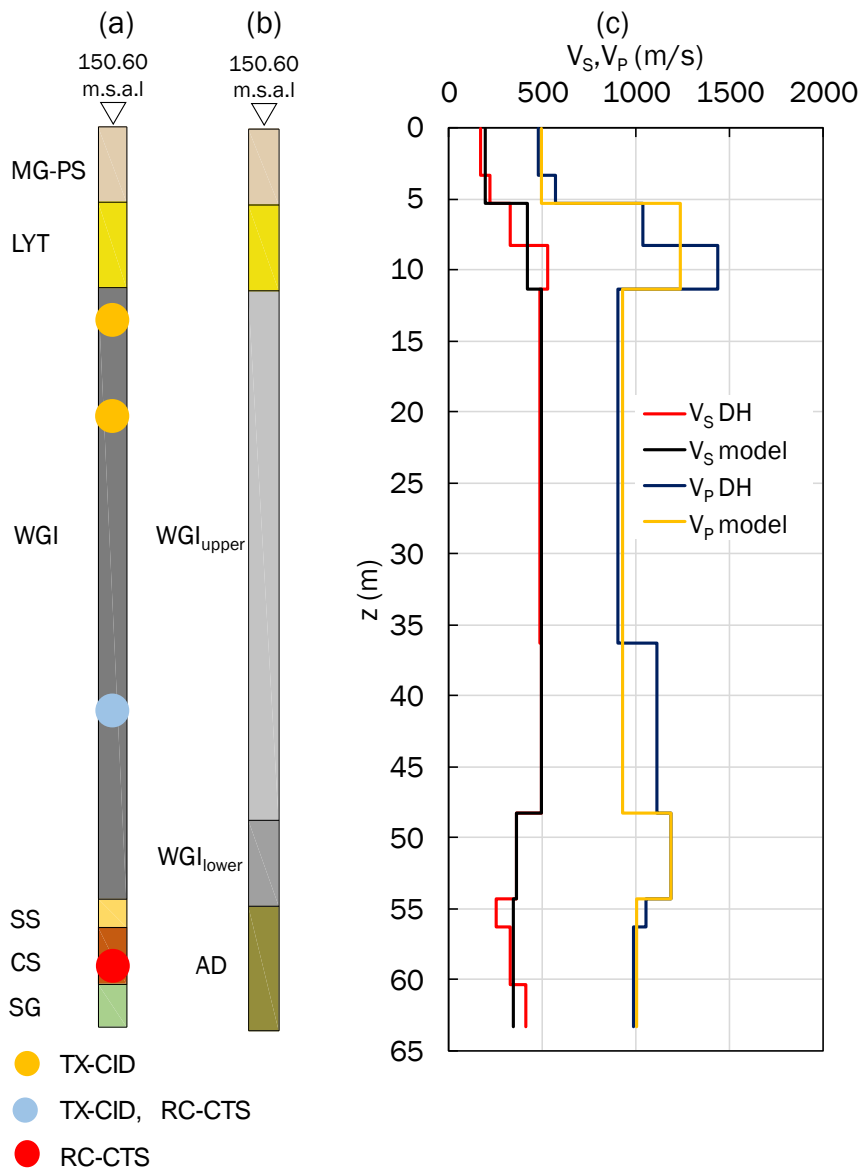


Figure V.12 (a) Borehole layering, (b) V_p and V_s profiles.

Following the most significant variations of mechanical properties, the soil column (Figure V.12a) investigated in the deep borehole was discretized as described in Table V.6, reporting for each range of depths the natural unit weight, γ , compression and shear wave velocities, together with the oedometric, E_{oed} , and shear, G_0 , moduli computed from the measured V_P and V_S . In particular, the mean values measured in MG-PS and LYT were assumed in the calculation, while the values of the alluvial deposit (AD) were calculated from the weighted average of V_P and V_S measured in the SS, CS and SG layers (red and blue lines in Figure V.12b).

The small-strain damping ratio, D_0 , was assumed as the mean value of damping in the strain range between 0.0001%-0.001% on the curves $D-\gamma$ (Figure V.16a), while for MG-PS, LYT and WGI_{lower} on the curves reported by Licata (2015), Vinale (1988) and de Silva et al. (2018), respectively. The $G/G_0-\gamma$ and $D-\gamma$ curves for WGI_{upper} and AD formations were calibrated on the experimental data from resonant column and cyclic torsional shear tests, as shown in Section V.3.1.3.

Table V.6 Small strain properties

	Z_{min} m	Z_{max} m	γ kN/m ³	V_s m/s	V_P m/s	E_{oed} MPa	G_0 MPa	D_0 %
MG-PS	0	5.30	14.97	190	495	374	55	0.54*
LYT	5.30	11.30	15.23	420	1239	2383	274	0.15**
WGI_{upper}	11.30	48.30	13.12	495	925	1144	328	0.54***
WGI_{lower}	48.30	54.30	17.17	362	1191	2483	229	0.63
AD	54.30	66.00	17.27	341	1001	1764	205	1.29
Bedrock	66.00	/	21.00	900	1558	5202	1734	/

* Licata, 2015; ** Vinale, 1988; *** de Silva et al., 2018

V.4.1.2. Back calculation of the bedrock depth

Since the Flysch bedrock was not intercepted by the borehole, 1D bedrock-surface transfer functions were computed on the layered soil model shown in Figure V.12b, using the properties in Table V.6, to evaluate the sensitivity of the frequency response to the increase of the bedrock depth beyond 63 m, i.e. the maximum investigated depth. Those sensitivity analyses were carried out using STRATA code, where equivalent-linear site response analyses were carried out using the hysteretic model described in Section V.4.1.3 and the same input motion used for the 2D linear dynamic analyses (see Section V.4.3).

The resulting functions were compared to the horizontal-to-vertical spectral ratio (HVSr) of the ambient noise recorded on site (Piro et al. 2017). A good agreement of the fundamental frequency ($f_{1soil}=1.60$ Hz) was found by setting the bedrock depth at

66 m, as shown in Figure V.13. The results confirmed the hypothesis on the bedrock depth shown in Figure V.11c.

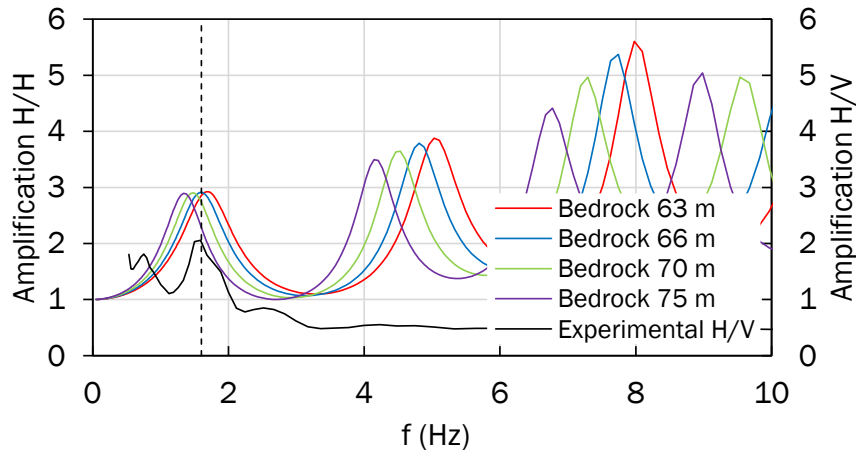


Figure V.13 Comparison HVSR with amplification function at different depth

V.4.1.3. Nonlinear stiffness and damping properties

The resonant column (RC) and cyclic torsional shear (CTS) tests were performed on WGI and CS samples in drained conditions, under an isotropic consolidation stress approximating the estimated mean lithostatic stress. In the resonant column test, the frequency of the input vibration is changed until the resonant condition is determined; as a result, the frequency range applied to both specimens spanned from 30 to 12 Hz. In the cyclic torsional shear tests, a single frequency of 0.5 Hz was used for the CS soil, while both 0.5 and 1 Hz were used for the WGI soft rock. In Figure V.14a-b, the experimental data relevant to WGI and CS samples, respectively, are plotted in terms of normalized shear stiffness, G/G_0 , and damping ratio, D , versus peak shear strain, γ . Both samples exhibit a significant increase of nonlinear and dissipative behaviour beyond a linear threshold strain, γ_l (conventionally defined as that where G/G_0 attains 0.95), of the order of 0.01%. Such a value, typical of fine-grained soils, can be related to the presence of a dominant fine matrix in both materials.

The influence of loading frequency on the nonlinear behaviour is quite ambiguous in the two cases: while the stiffness decays more abruptly for WGI in the RC tests, the opposite occurs for CTS tests, maybe due to some slippage occurring between the driving system and the specimens. The dissipative behaviour appears more significantly affected by the loading rate for the WGI material, showing, rather

surprisingly, a damping decreasing with frequency. On the other hand, the damping of the CS soil is much less influenced by the loading rate.

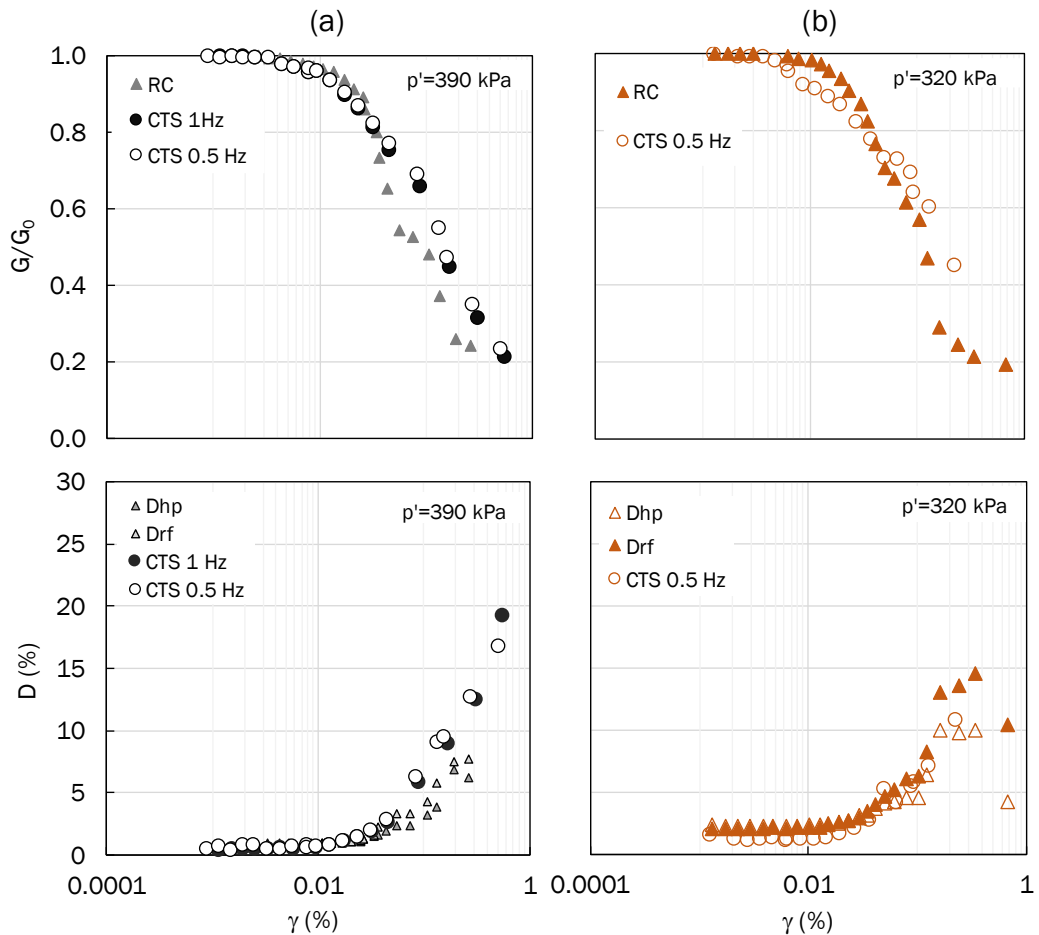


Figure V.14 Resonant column (RC) and cyclic torsional shear (CTS) tests on WGI: (a) G/G_0 - γ , (c) D - γ and on AD (b) G/G_0 - γ (d) D - γ relationships

A hysteretic behaviour was assigned to all materials. The decay of G and the increase of D with shear strain, γ , were introduced in the numerical model through a sigmoidal function, described by Eq. (IV.4) with the parameters a , b and x_0 listed in Table V.7.

The curves relevant to the MG-PS, LYT and WGI_{upper} were calibrated on experimental data from resonant column tests on comparable Neapolitan pyroclastic soils, reported by Licata (2015), Vinale (1988) and de Silva et al. (2018), respectively (Vuoto et al. 2018), and plotted in Figure V.15. The WGI_{lower} and AD curves were calibrated on experimental data resulting from the above-mentioned resonant column and cyclic torsional shear tests. The hysteretic damping was obtained by applying the well-known Masing criteria (Hardin and Drnevich, 1972). As described in Section IV.1.1, the cyclic

response of a cubic soil sample was numerically simulated at different strain levels, from $\gamma=0.0001\%$ to $\gamma=1\%$, and the corresponding $(\tau-\gamma)$ loops were calculated. The comparisons between experimental and numerical trends are shown in Figure V.16a-b for WGI and for CS.

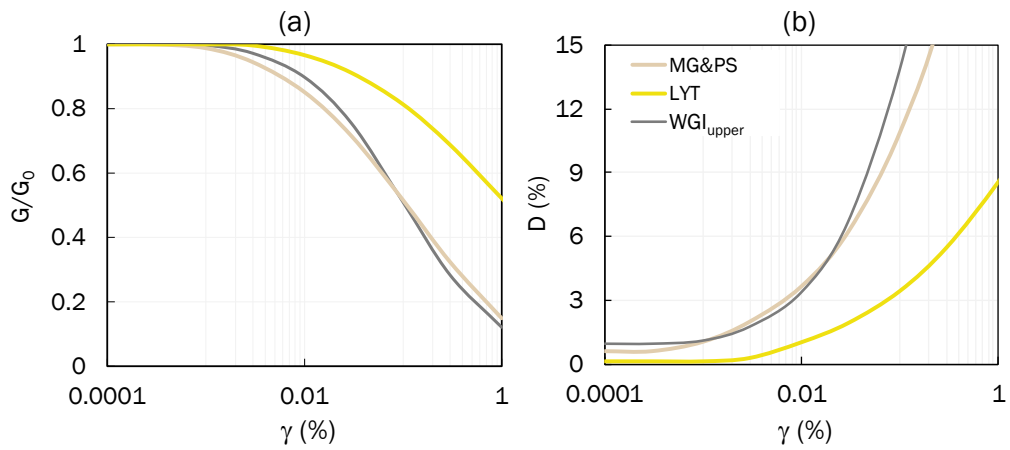


Figure V.15 Variation of normalized shear stiffness (a) and damping (b) with shear strain assumed in the seismic response analyses

Table V.7 Sigmoidal function parameters

Soil-material	Sigmoidal function	a	b	x_0	y_0
MG-PS	Sig4	1.15	-0.65	-0.90	-0.10
LYT	Sig3	1.05	-0.80	-0.01	-
WGI _{upper}	Sig3	1.02	-0.50	-1.00	-
WGI _{lower}	Sig3	1.00	-0.40	-0.50	-
AD	Sig3	1.00	-0.40	-0.30	-

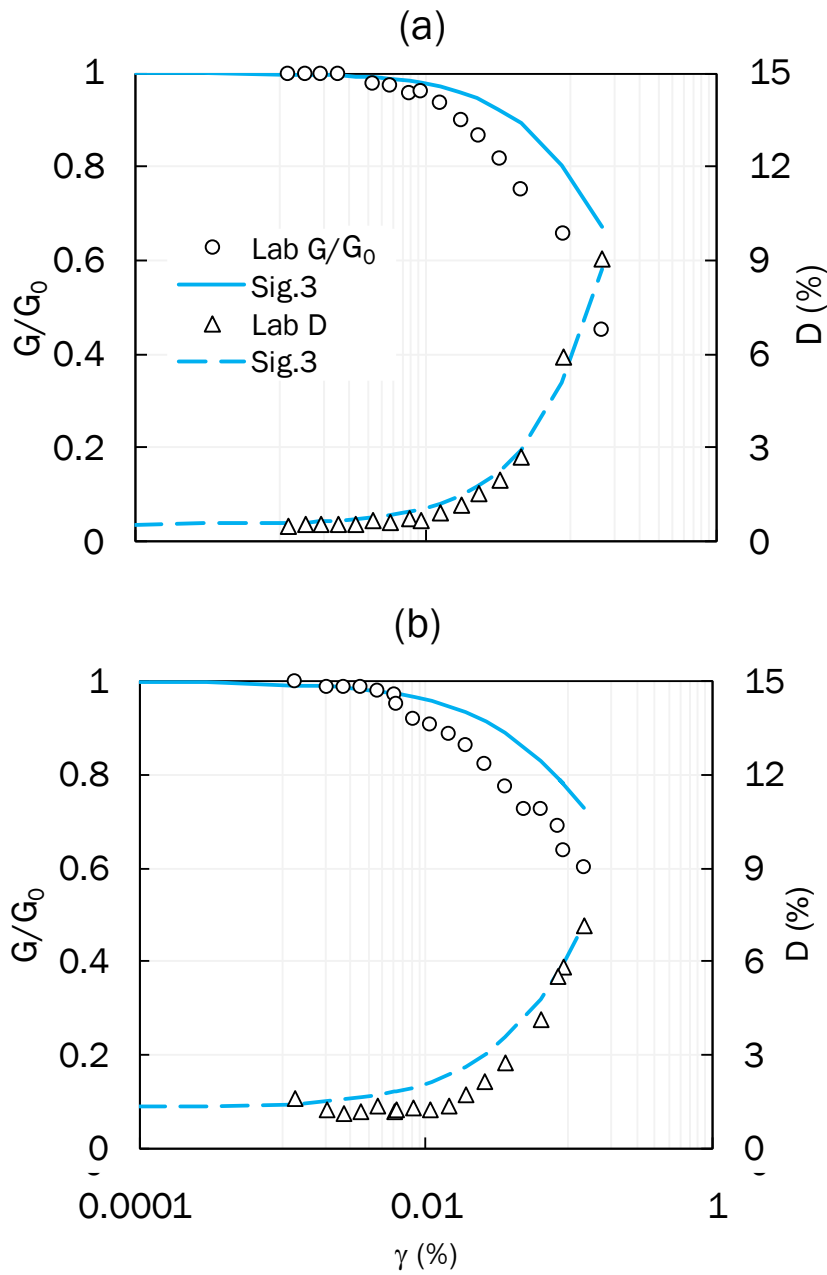


Figure V.16 Comparison between experimental data and hysteretic model: (a) WGI (b) AD

V.4.1.4. Shear strength properties

Five isotropic consolidated-drained (CID) triaxial compression tests were performed on WGI samples taken at three different depths. The specific test conditions involved saturating and then consolidating the specimens under five effective stresses, σ' (15,

100, 200, 400, 600 kPa). The consolidation stage was followed by triaxial compression at a loading rate low enough to ensure drained conditions.

Figure V.17a-b report the q - ε_a and ε_v - ε_a curves measured at different consolidation effective stresses, where q is the deviator stress, ε_a is the axial strain, and ε_v is the volumetric strain. The evolution from a dilatant to an increasingly more contractive behaviour with the increase of consolidation stress is apparent.

The effective strength parameters (friction angle, ϕ' , and cohesion, c') were obtained from the failure envelope in the t - s' plane (Figure V.18b), where s' and t represent the centre and the radius of the failure Mohr-Coulomb circles. From the best-fit line of the failure points, it was possible to calculate a friction angle $\phi'=35^\circ$ and a cohesion $c'=20$ kPa.

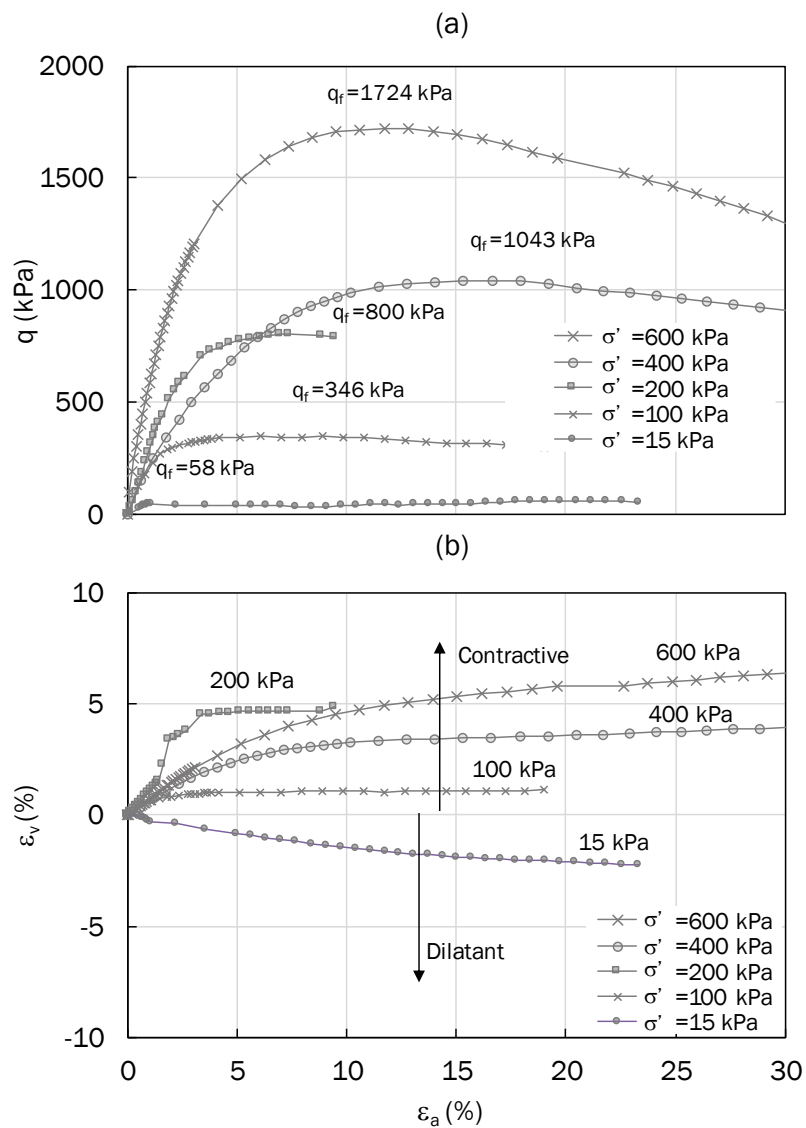


Figure V.17 Triaxial compression test results on WGI: (a) q - ε_a and (b) ε_v - ε_a relationships

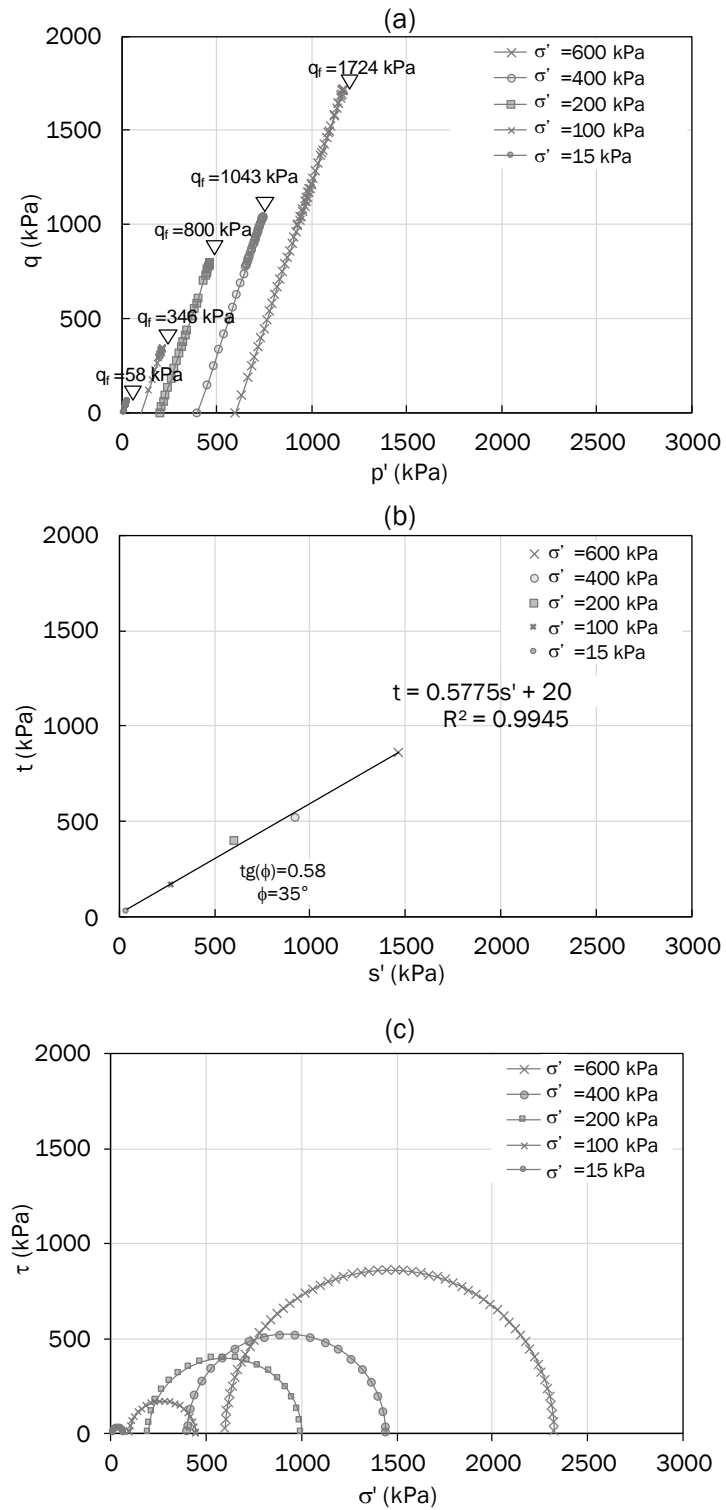


Figure V.18 Triaxial compression test results on WGI: (a) stress paths; (b) failure points, (c) Mohr circles

Only the hysteretic behaviour of the MG-PS, LYT and WGI soil layers was integrated with a Mohr- Coulomb model. Table V.8 reports the strength parameters assigned to the four volcanic materials. For the whole formation LYT, the unit weight, γ , was taken equal to the mean values measured on 21 samples collected after several stabilization works executed in 1994 (as reported in de Silva et al. 2013). The LYT values of ϕ' and c' were obtained from triaxial tests executed in 2015, carried out on specimens (prismatic and cylindrical) collected from a block of LYT fallen in one cavity (Scotto di Santolo et al., 2015). As expected, the uniaxial compression strength $\sigma_c = 2.68\text{MPa}$ associated to the LYT shear strength parameters was found lower than the values measured in 1994 through uniaxial compression tests on samples taken from the intact rock (mean $\sigma_c = 3.95\text{MPa}$). The tensile strength, σ_t , was assumed as 10% of the compression strength. The shear strength of the shallow soil cover (MG-PS) was characterized by the same ϕ' as WGI and null cohesion.

In order to take into account the presence of consolidation works along the Martorano creek, an equivalent material ($\text{WGI}_{\text{reinforced}}$) was assumed in the numerical model (Piro et al. 2019) represented in Figure V.19. The existing retaining walls on the Riello creek were directly modelled assuming the same properties of the LYT.

Table V.8 Strength parameters

	Z_{\min}	Z_{\max}	γ	σ_c	σ_t	ϕ	c'
	m	M	kN/m^3	MPa	MPa	°	MPa
MG-PS	0	5.30	14.97	/	0.002	35	0
LYT	5.30	11.30	15.23	2.68	0.27	23	0.90
$\text{WGI}_{\text{upper}}$	11.30	48.30	13.12	0.16	0.016	35	0.04
$\text{WGI}_{\text{lower}}$	48.30	54.30	17.17	0.02	0.0019	35	0.02
$\text{WGI}_{\text{reinforced}}$	-	-	13.12 ($\text{WGI}_{\text{upper}}$) 17.17 ($\text{WGI}_{\text{lower}}$)	0.46	0.046	35	0.12

V.4.2. Numerical hill model

2D THA were performed through the finite difference software FLAC on the hill model neglecting (Figure V.19a) or including (Figure V.19b) the underground cavities. The size and the location of the cavities were defined considering the most recurrent geometry (i.e. 5m wide and 6m high). The domain reproduces the geological section shown in Figure V.11c, assuming the bedrock coincident with the Miocene flysch formation. The soil domain was assumed to have a width of 518 m and 154m in correspondence of the historical centre. The soil was discretised into a mesh of quadrilateral elements, the size of which was defined by satisfying the criterion by Kuhlemeyer and Lysmer (1973) for accurate modelling of shear wave propagation up to a frequency of 25 Hz.

In proximity of cavities the height of the quadrilateral elements was reduced in order to approximate the cavity shape. Initial conditions of static equilibrium under gravity loads were reproduced for both the models. In presence of cavities was also simulated the excavation of the underground space. As described in Chapters III and IV, the infinite extension in depth of the bedrock is simulated by dashpots attached to the bottom nodes in the normal and shear directions (quiet boundaries). To minimize the domain size, the so-called ‘free-field’ boundary conditions were imposed along the lateral sides.

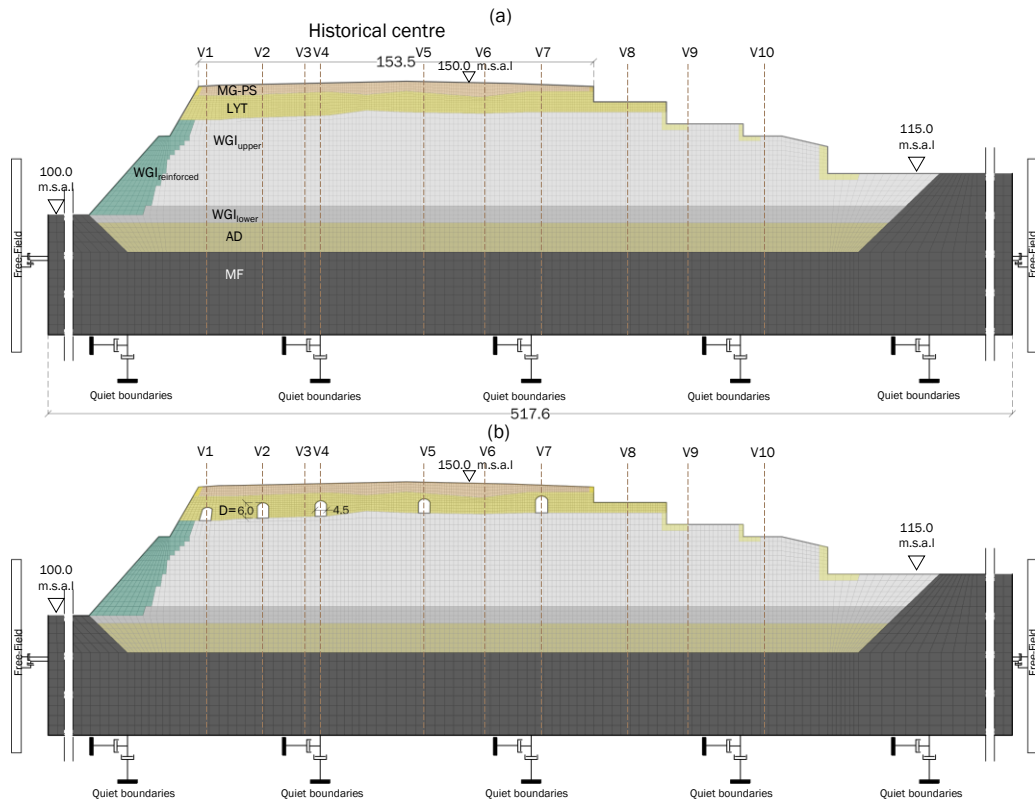


Figure V.19 Numerical model (a) without cavities and (b) with cavities

V.4.3. Dynamic response of the hill

Firstly, LTHA were performed under a low-amplitude random input motion (see Figure V.20) characterised by a frequency range 1-25 Hz and a duration of 30s to evaluate the influence of the site effects and the underground cavities.

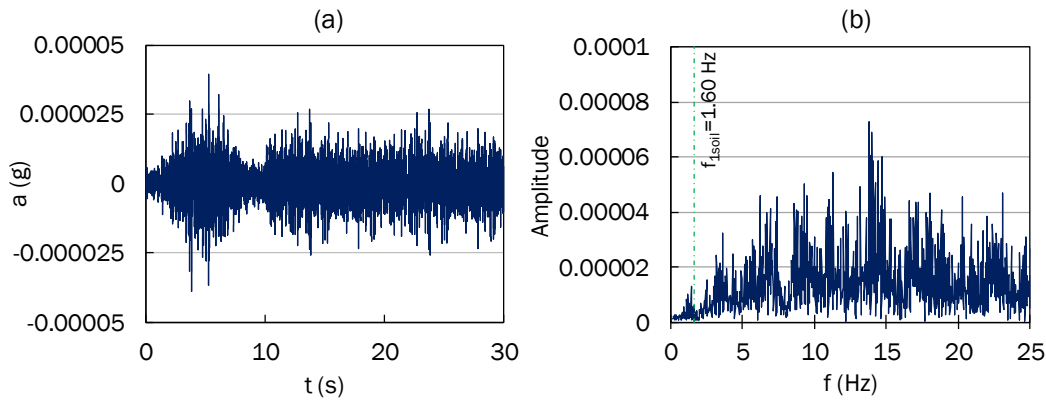


Figure V.20 Input noise for numerical dynamic response of the hill: (a) accelerogram; (b) FFT

The comparison between the whole bedrock-surface transfer functions with and without cavities is shown in Figure V.21 for all the verticals. Only slight modifications of the response can be recognized along the verticals V8, V9 and V10, on the Riello side, introducing the cavities (dotted line). On the other hand, the amplification along the verticals which intercept the cavities is clearly reduced, due to the presence of cavities, from a value of frequency approximately equal to 7 Hz (orange dotted line), see i.e. V2. The latter value corresponds to a ratio $\lambda/D \approx 8$ between the wavelength propagating in the LYT layer, λ , and the cavity height, D . The same comparison along verticals V1, V4, V5 and V7 led to the same result, confirming the dependence of the cut-off frequency on the cavity size (i.e. D) and rock stiffness (proportional to λ), as reported by Sanò (2011).

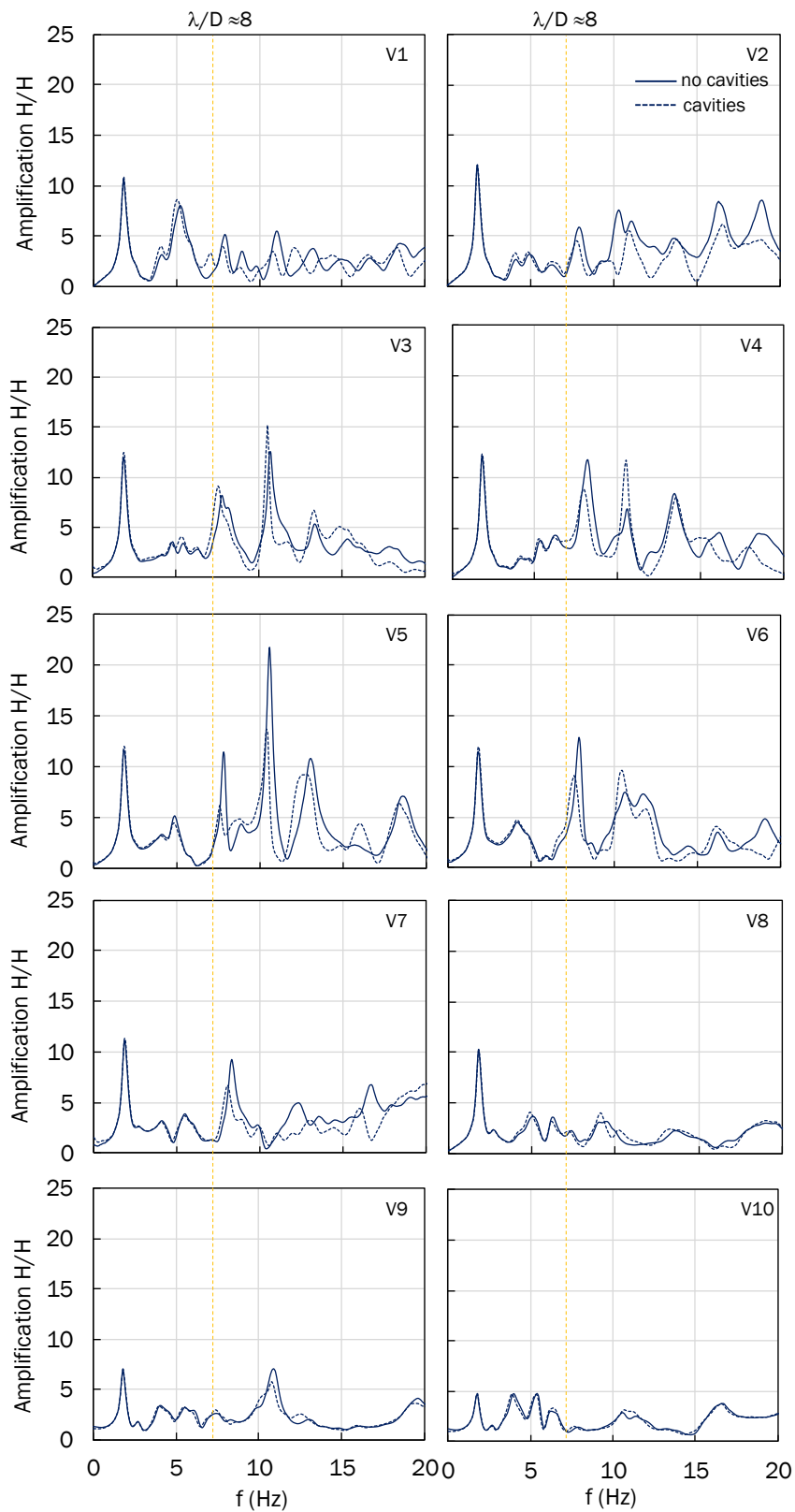


Figure V.21 Bedrock-surface transfer functions with and without cavities along vertical [V1-V10]

Figure V.22b shows the variations along the cross section of the predominant frequency, f_{1soil} (black line), and of the amplification factor of the peak ground acceleration, PGA_s/PGA_b , i.e the ratio between the surface and the bedrock values (red line). Introducing the cavities, the PGA at surface is attenuated close to their axes, whereas only a slight effect is observed on the main frequency. The triangles represent the results of 1D seismic response analyses performed under the same input motion and show lower values than the 2D analysis in terms of both natural frequency and amplification factor, due to topographic effects.

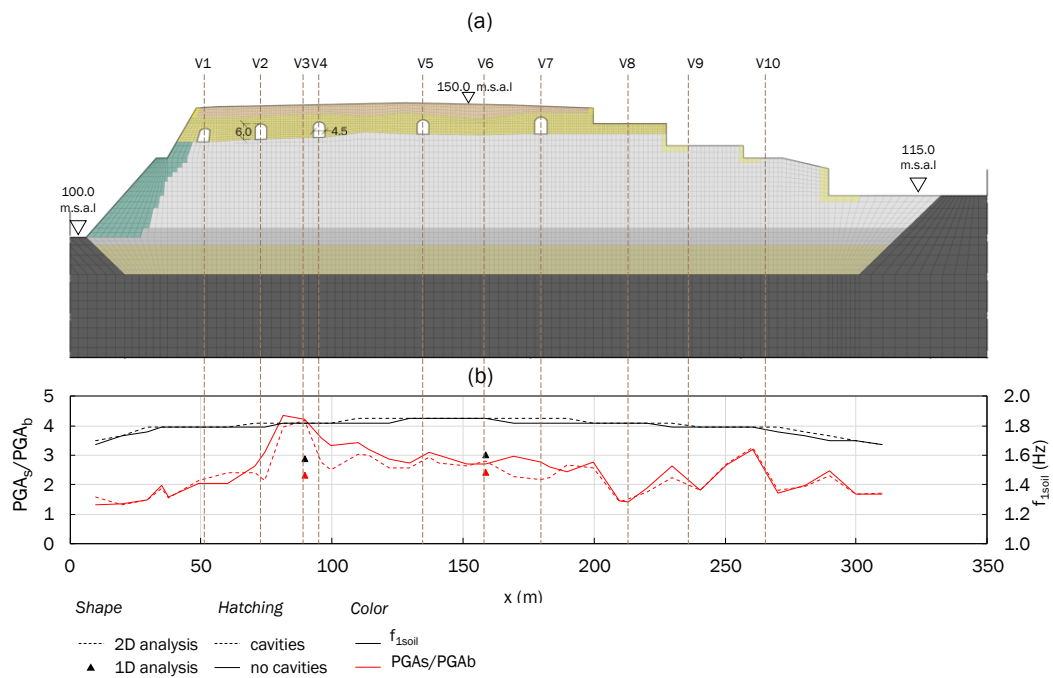


Figure V.22 (a) Numerical model and (b) variability along the cross-section of the ratio PGA_s/PGA_b and f_{1soil} compared to the results of 1D seismic response analyses (V3, V7).

V.4.4. Nonlinear dynamic analysis of the hill

The influence of the site effects and the underground cavities were also investigated through NLTHA. Figure V.23a shows the response spectrum of seven input motions (de Silva et al. 2013) extracted from the ITACA online database (Pacor et al., 2011) as compatible, on the average, with that specified by the Italian Building Code (MIT, 2018) for a flat rock outcrop (denoted as “NTC ‘18” in Figure V.23a) at Sant’Agata de’ Goti. Each input motion was scaled to a peak ground acceleration $PGA = 0.166g$ expected to occur at the reference rock outcrop with a probability of exceedance equal to 10% in 50 years. The signals were relevant to different stations and seismic events occurred in Italy and reported in Table V.9. The NLTHA were performed under the ARQ, ALT and BSC input motions (Figure V.23b), which characterized by significant spectral acceleration amplitude at high, intermediate and low periods, as shown in Figure V.23c.

Table V.9 Properties of the selected records

Earthquake	Mw	Date	Station	Epic. distance km	Comp.	T_M
Irpinia	6.9	23/11/1980	ALT	24	WE	0.52
Gran Sasso	5.4	09/04/2009	ANT	23	NS	0.54
Val Comino	5.9	07/05/1984	PNT	27	WE	0.49
Umbria-Marche	5.6	14/10/1997	CSC	22	NS	0.44
Friuli	5.6	11/09/1976	SRC	26	NS	0.50
Irpinia	6.9	23/11/1980	BSC	28	NS	1.16
Val Nerina	5.8	19/09/1979	ARQ	21	NS	0.25

The results were represented in terms of PGA_s/PGA_b and amplification factor, AF, computed as follows:

$$AF = \frac{\int_{T_1}^{T_2} S_{as}(T) dT}{\int_{T_1}^{T_2} S_{ab}(T) dT} \quad (V.3)$$

where S_{as} is the spectral pseudo-acceleration resulting at surface and S_{ab} is that computed on the input motion. The spectral amplification ratio was computed in the same ranges of periods T_1 - T_2 adopted in Chapter IV, i.e. [0.1s - 0.5s] and [0.5s - 2.0s], representative of squat and slender structures, respectively.

To isolate the stratigraphic amplification, one-dimensional s.r.a were performed considering the same soil properties and input motions as 2D analyses for the verticals V3 and V6. The results are represented in Figure V.24a-b-c as triangles. As expected, at any range of frequency and for every input motion, the 1D results lead to lower

amplification values, highlighting how the seismic response of the hill is influenced by topographic effects.

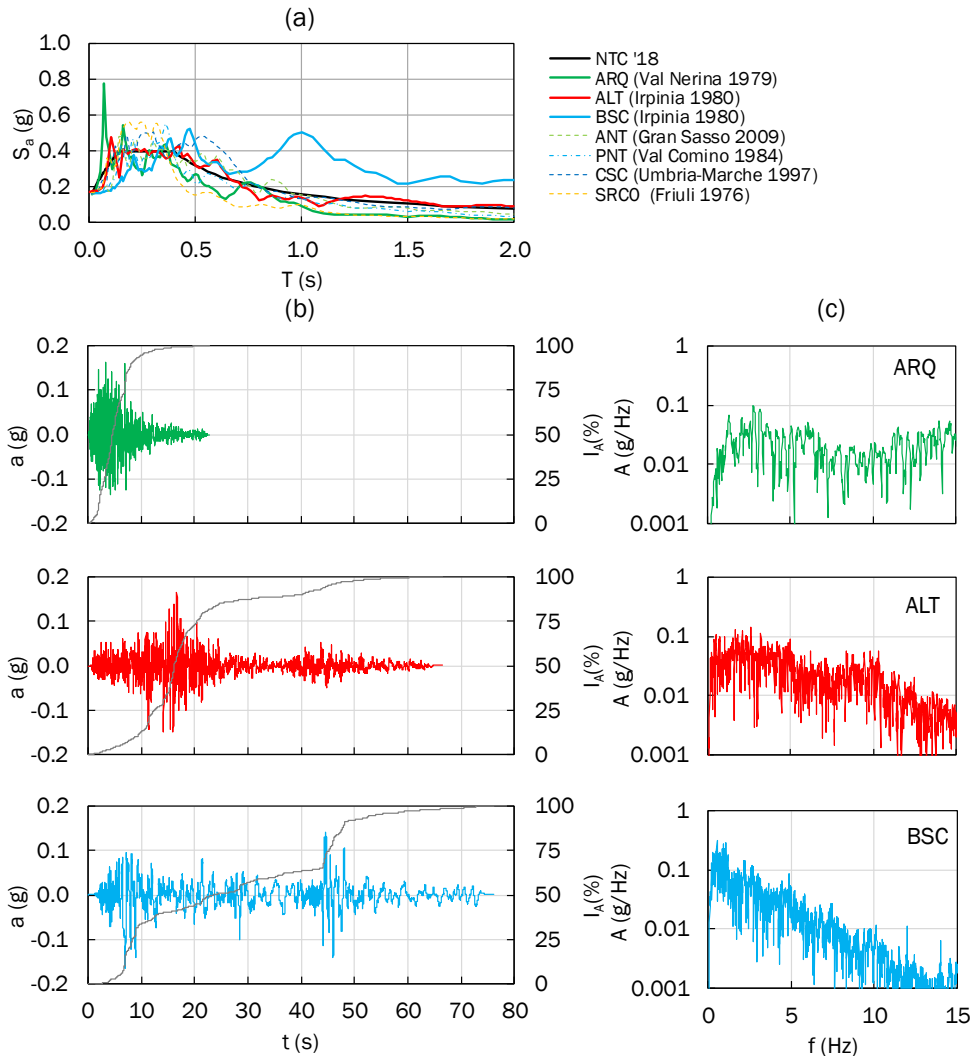


Figure V.23 (a) Comparison between the spectral acceleration of the seven input motions on the average compatible with NTC spectrum for a flat rock outcrop; (b) accelerograms and (c) FFT of the three records used in the analyses

The solid lines in Figure V.24b show how, due to topographic effects, the PGA_s/PGA_b ratios assume higher values in proximity to the slopes, especially under ARQ and ALT input motions, characterized by higher frequency content. A lower variability along the cross section can be recognized at low periods (solid lines in Figure V.24c) which becomes negligible at higher periods (solid lines in Figure V.24d).

The presence of cavities, instead, increases the amplification of PGA compared with the case without cavities, especially in terms of PGA_s/PGA_b (Figure V.24b). In the range of low periods, the effect on AF is less pronounced, becoming negligible at high periods. The cut-off effect, shown under the low amplitude input motion (see Figure V.22b), was not observed under earthquakes at least for frequencies lower than 10 Hz. Under high amplitude input motion, the presence of cavities increases the strain level and, consequently, mobilizes a significant nonlinearity with respect to the case without cavities. Such behaviour could be related to stress concentrations at the edges of openings within a solid medium. As highlighted by the shear strain contour at the end of the analysis shown in Figure V. 25, Figure V.26 and Figure V.27, respectively for ARQ, ALT and BSC motions.

In addition, it can be observed that in correspondence of the Martorano creek (left side) these effects are more apparent with respect to the Riello creek, due to more pronounced topographic amplification.

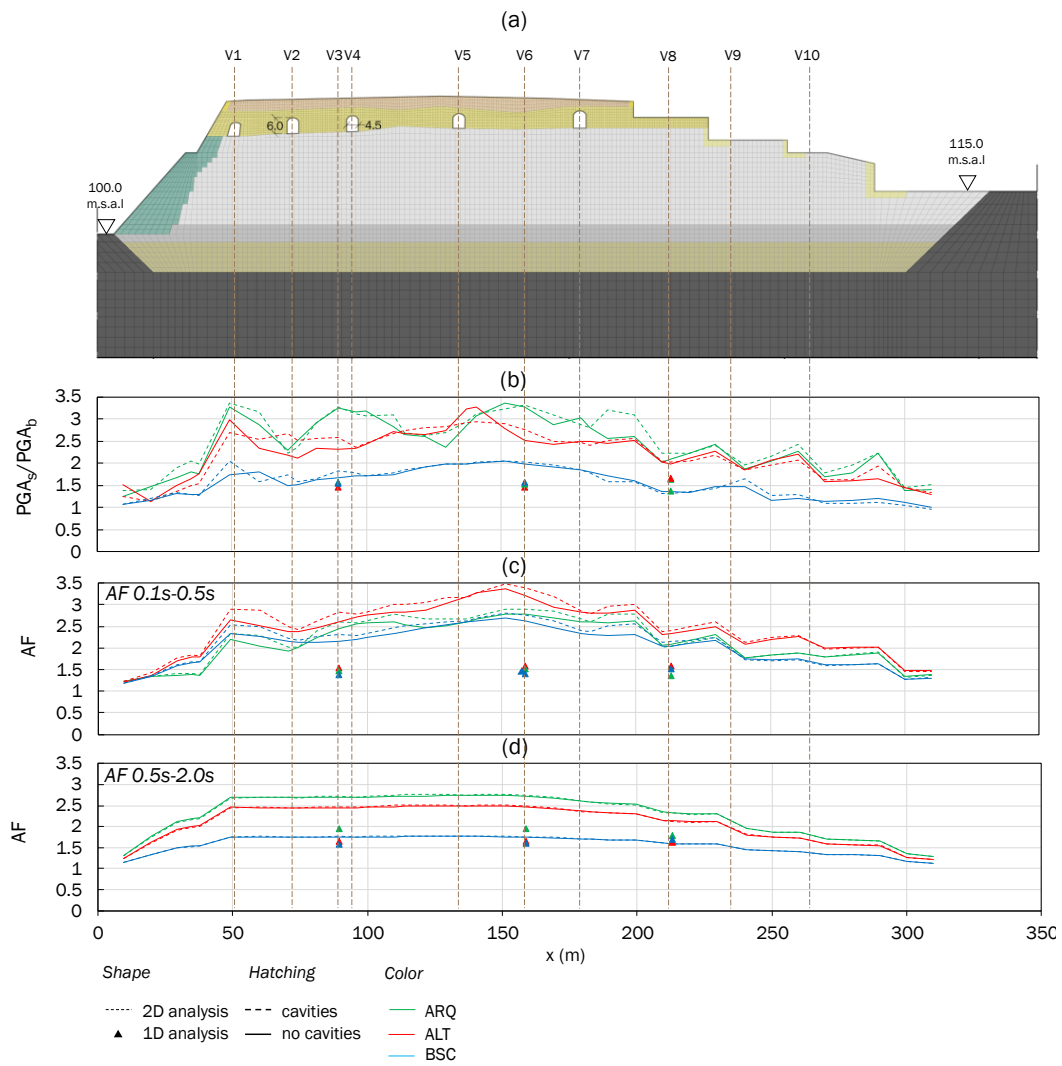


Figure V.24 (a) Numerical model, (b) variability along the cross-section of the ratio PGA_s/PGA_b , (c) of the amplification factor computed in the period range 0.1s-0.5s, (d) 0.5s-2.0s compared to the values computed through 1D analyses along verticals V3, V6.

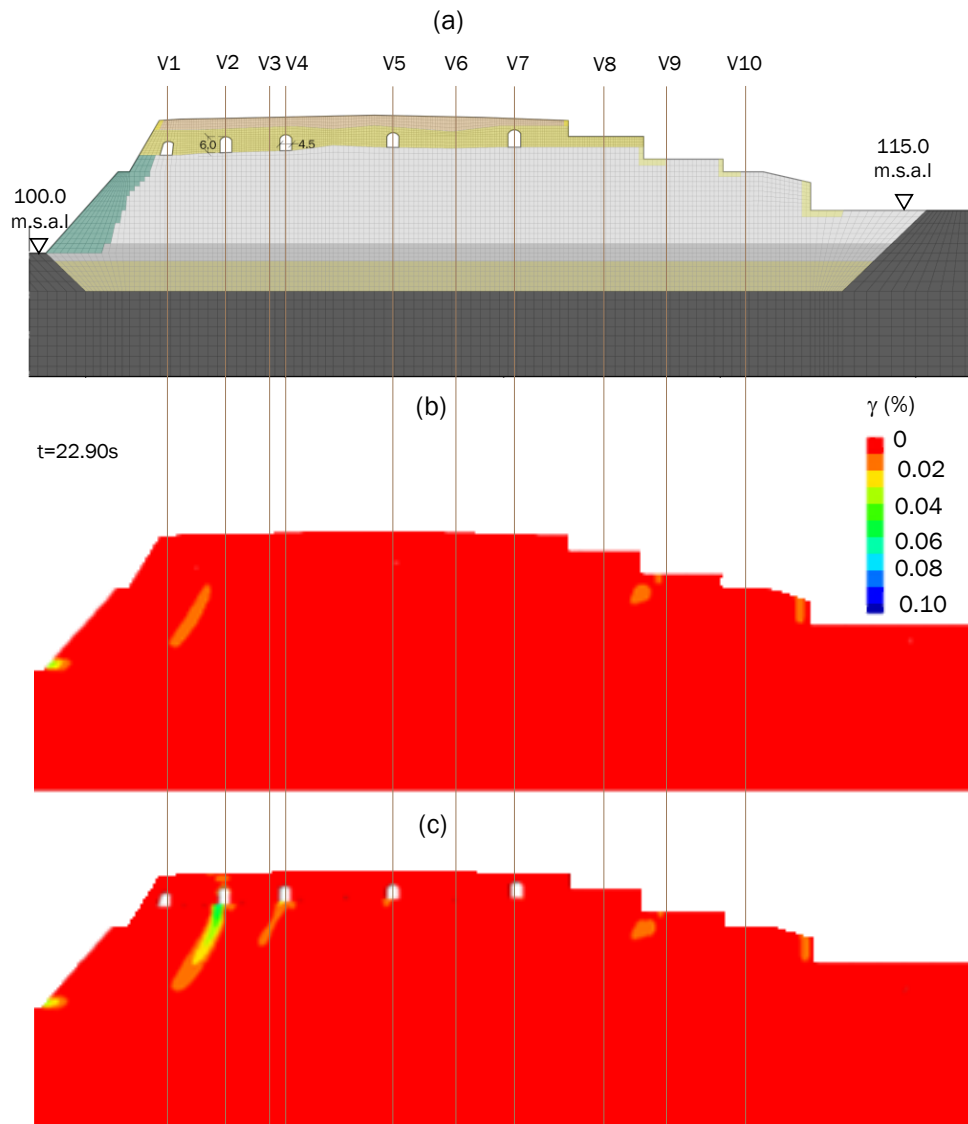


Figure V. 25 (a) Numerical model, shear strain contour at final t (b) no cavities and (c) with cavities (ARQ input motion)

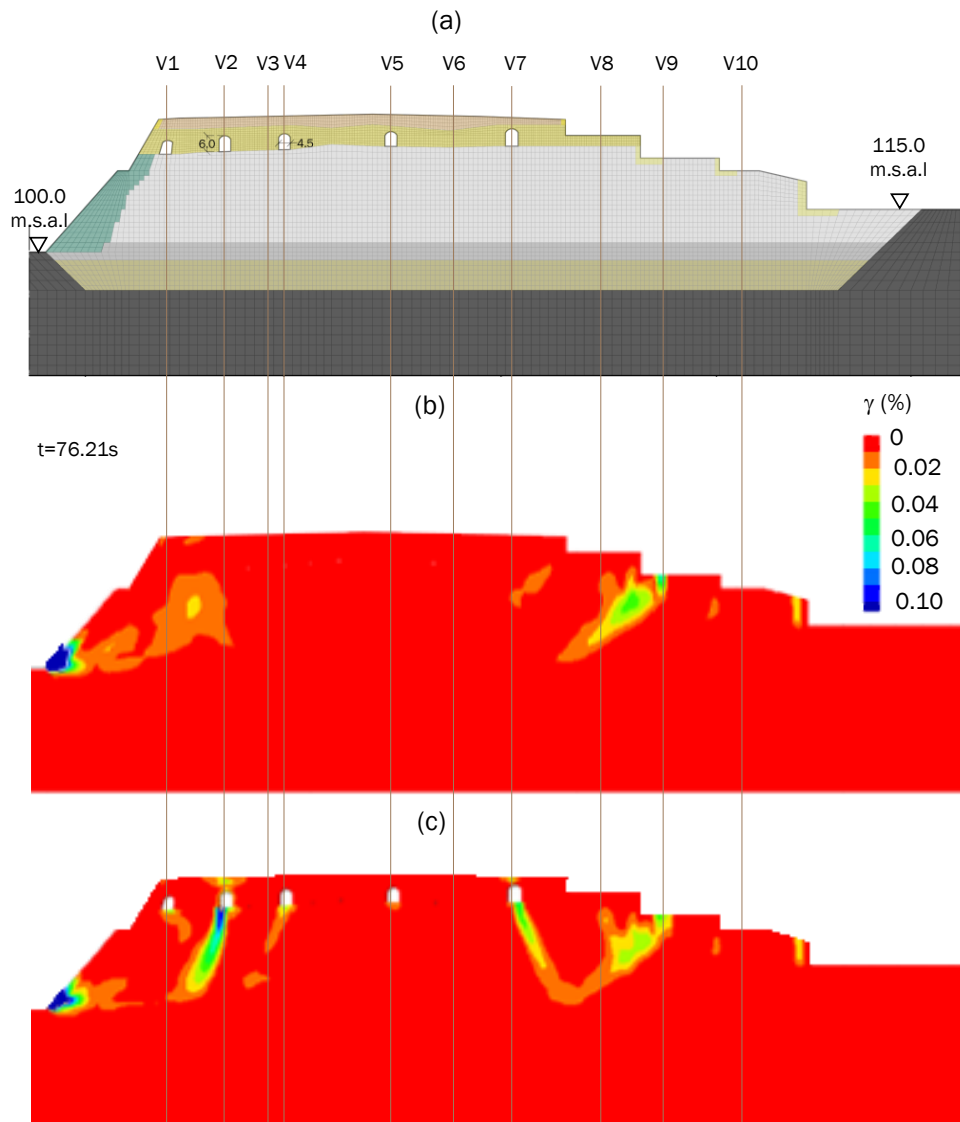


Figure V.26 (a) Numerical model, shear strain contour at final t (b) no cavities and (c) with cavities (ALT input motion)

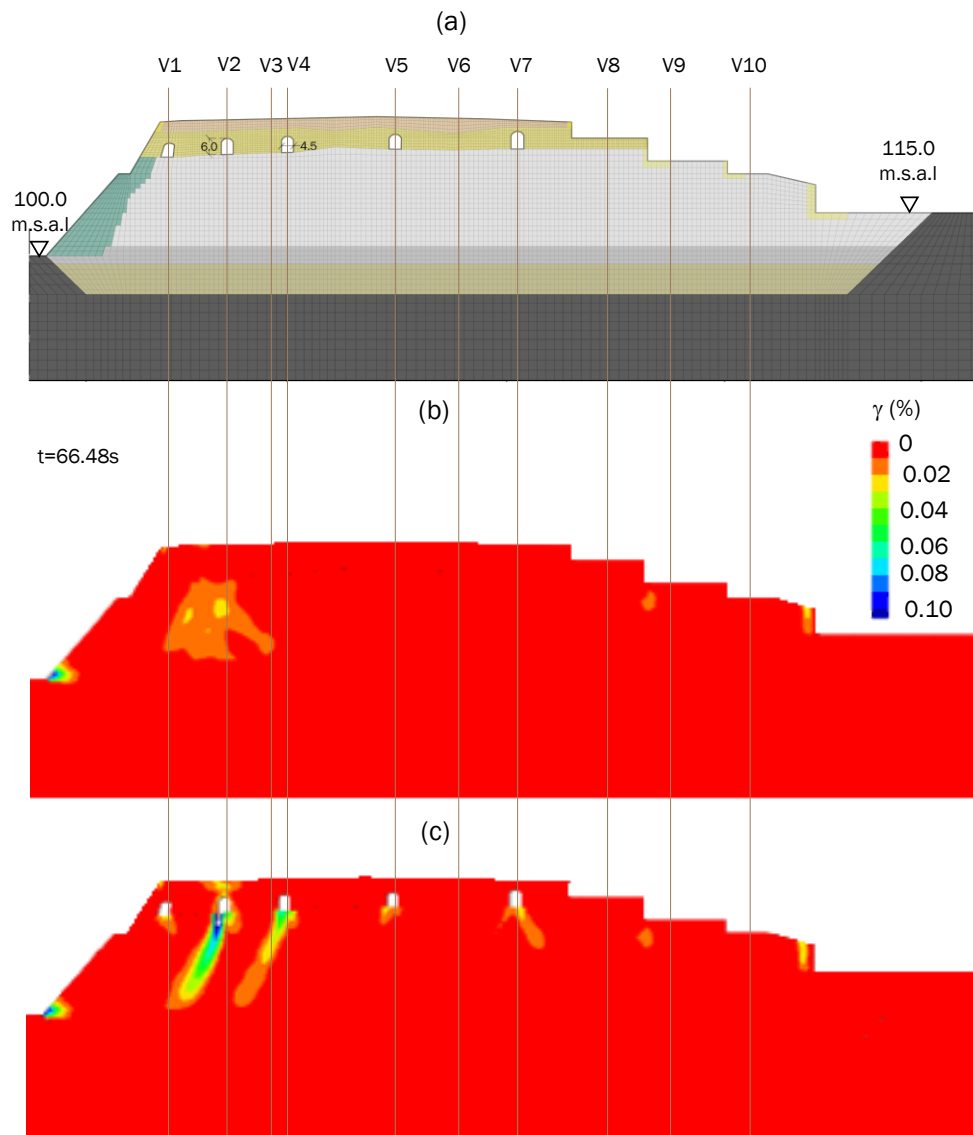


Figure V.27 (a) Numerical model, shear strain contour at final t (b) no cavities and (c) with cavities (BSC input motion)

V.4.5. SFS capacity models

Soil-Foundation-Structure interaction at the building scale was analysed for an ancient seminar (Figure V.28), a historical construction built in 1334 on the eastern border of the historic centre, very close to the ReLUIS investigation site (see Figures V.9-V.10). The first structure was severely damaged by the 1688 historical Sannio earthquake and rebuilt by the Bishop S. Alfonso M. de' Liguori. The loadbearing walls of the masonry building are made up of squared Neapolitan yellow tuff stones, except for the hypogeum, probably older, where the blocks are roughly cut (Figure V.28c). During the 20th century, all floor systems were replaced by one-way joist systems composed of steel I-beams and perforated flat bricks, except for the first floor where the original NYT masonry vaults were left. The original wooden trusses support the pitched tile roof.

Figure V.29 shows the coupled SFS numerical model defined through FLAC2D with reference to the structural sections of the ancient seminar (dotted red rectangle Figure V.28b). The discretization of the model into the mesh represented in Figure V.3 followed the same procedure adopted in Chapter III. To maximize the accuracy, the vaulted underground level was drawn by directly introducing the section obtained from the geometric survey (Figure V.28c).

Since no experimental results on the masonry of the historic centre were available, the compressive stress-strain behaviour was inferred by properly scaling the results of uniaxial compression tests performed by Augenti and Parisi (2010b) on masonry specimens, which were made of NYT stones quarried in Naples, not far from Sant'Agata de' Goti. The elasto-plastic shear strain-softening behaviour was based on a Mohr-Coulomb shear failure criterion (Vuoto et al, 2018). Table V.10 and Table V.11 outline the values assigned to material properties. A cut-off tensile strength σ_t was assumed and set to 1/20 of peak compressive strength.

Table V.10 Physical and mechanical properties of NYT masonry adopted in the analyses (Vuoto et al 2018).

	ρ (kg/m ³)	E (MPa)	G (MPa)	ν (-)	ϕ' (-)	c' (MPa)	σ_c (MPa)	σ_t (MPa)
Peak	1600	1080	360	0.49	22°	0.62	1.90	0.095
Residual						0.16	0.76	

Table V.11 Physical and mechanical properties of the floor beam materials adopted in the analyses.

	ρ (kg/m ³)	A (m ²)	I (m ⁴)	E (MPa)
Steel floor slab	1750	0.35	0.004	30000
Wooden roof truss	303	0.31	0.002	1290

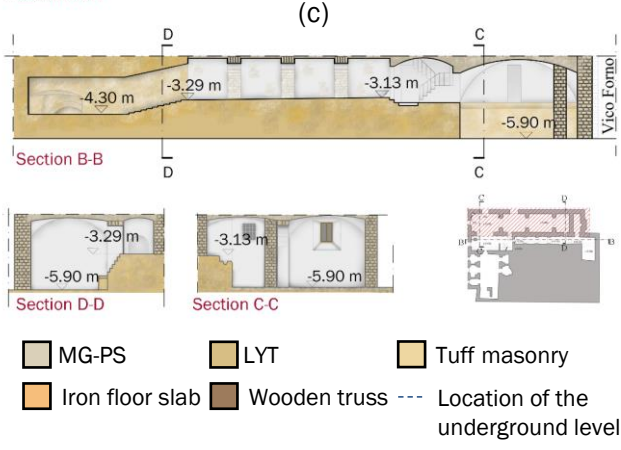
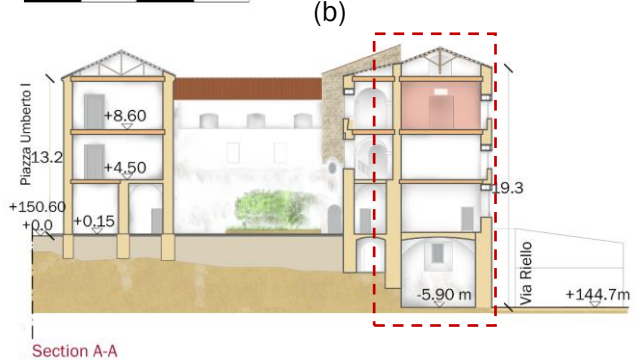
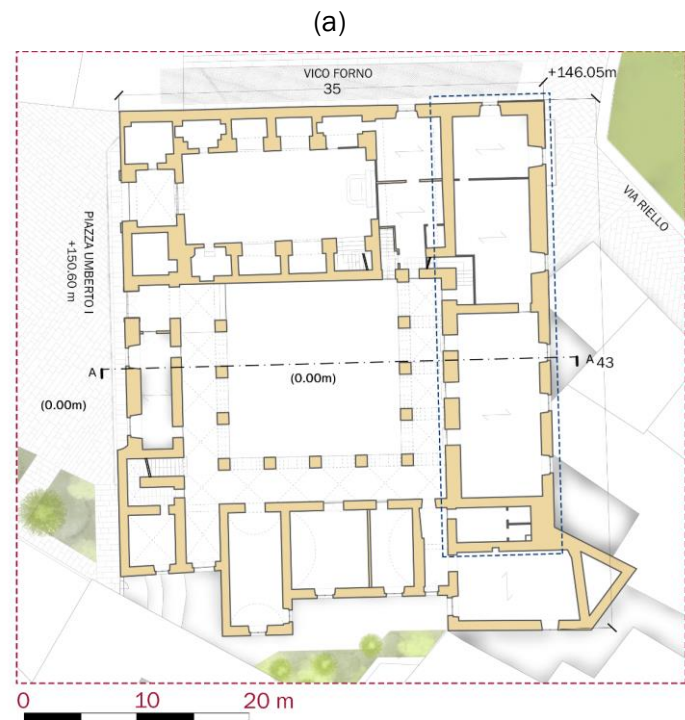


Figure V.28 (a) Plan, (b) section of the ancient seminar and geometric survey of the underground level

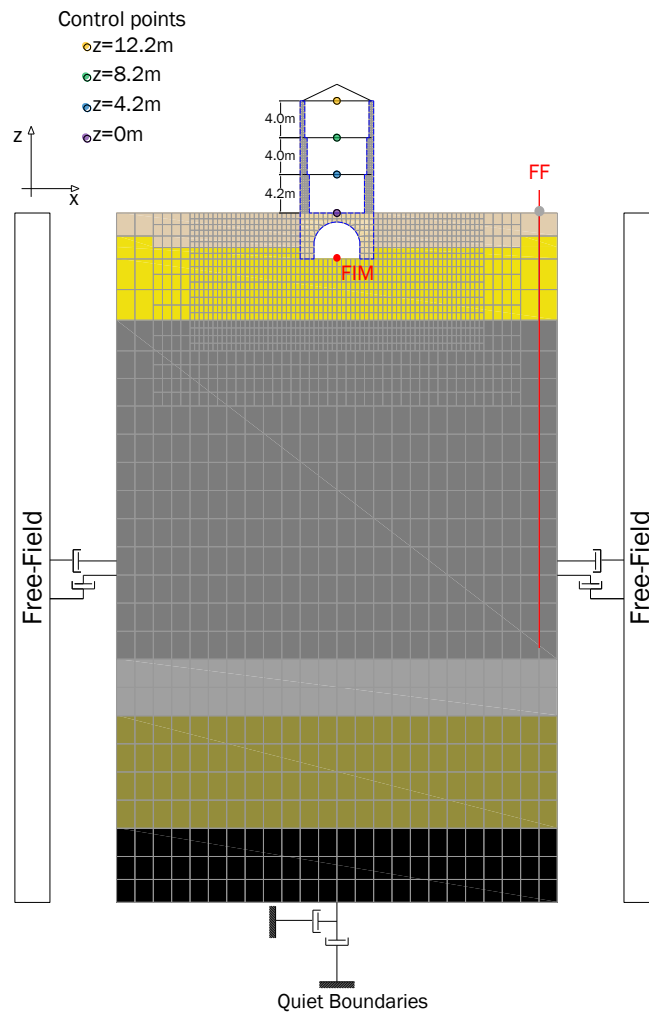


Figure V.29 SFS numerical model of the ancient seminar

Firstly, LTHA were performed under an input noise to evaluate f^* (T^*). The Rayleigh damping was assigned to all the materials (following the procedure in Section IV.1). To the soil materials the values were set equal to the values adopted in the hill NLTHA (Section V.3.2), while for the structure was set equal to 5%.

As described in Sections III.2 and IV.1.2, to compute the fundamental frequency, f^* , the SFS was subjected to a white noise signal (Figure III.4) and the structural response was numerically monitored over 10 s to record the free-vibration behaviour of the SFS system after the end of the forced-vibration stage. To evaluate the variation of f^* , f_0 (FB model) is referred to the three storeys building ($h/b = 1.5$) in Chapter III.

Figure V.30 shows the dynamic response of the structure in terms of displacement time histories at different elevations (see control points in Figure V.29) and FFT computed in the free-vibration stage, respectively. With respect to the fixed-base response, a frequency reduction of approximately 10% is observed between the two

models, from $f_0 = 2.94\text{Hz}$ to $f^* = 2.68\text{Hz}$, probably due to the presence of the underground level which rests on the LYT layer.

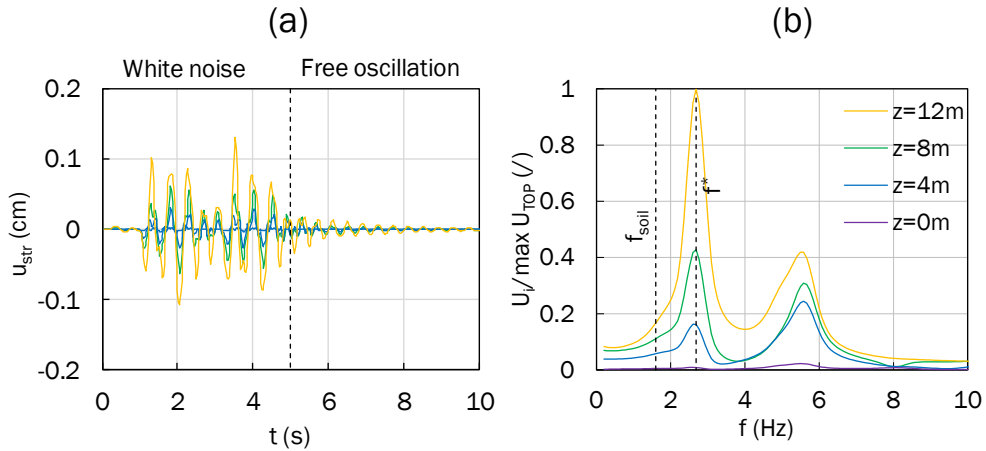


Figure V.30 Dynamic response of the SFS system: (a) time histories and (b) FFTs of horizontal displacements at different structural elevations.

V.4.5.1. SFS nonlinear time history analysis

The seismic safety of the building was assessed by firstly computing, for each input motion, the interstory drift IDR through equation (III.1) and the residual interstory drift (RIDR), using instead of the maximum displacements, u_{max} , the residual displacements, u_{res} , recorded when the seismic acceleration vanishes.

As shown in Figure V.31, both u_{max} (solid lines) and u_{res} (dotted lines) resulted more pronounced at the third floor, highlighting, as in Chapters III and IV, how the reduced thickness of the masonry wall led to higher u and consequently IDR.

To evaluate the structural damage, the residual-to-maximum drift ratio (RMDR) was also computed as follows (see e.g. Parisi et al., 2014):

$$RMDR = \frac{RIDR}{MIDR} \quad (V.4)$$

The higher RMDR, the lower the ability of repairing the masonry structure after an earthquake, even though structural collapse is prevented. The high values obtained from the analyses, reported in Table V.12, are practically indicative of the structural collapse. Table V.12 also reports the values of u_{max} , u_{res} , IDR and RIDR. The occurrence of permanent displacements in the structure are indicated by significant attained strain level, as illustrated in Figure V.32, Figure V.33 and Figure V.34 for ARQ, ALT and BSC motions, respectively; in the plots, the evolution with time at three different instants: t_1 =elastic state, t_2 = $t(\text{PGA})$, t_3 = $t(I_{A95\%})$, of both inelastic compressive

strains/stresses and plastic states are shown. In the plastic state representation, the mesh is deformed and magnified 10 times.

Table V.12 Control points maximum and residual: displacements and drifts; RMDR.

	z	U _{max}	U _{res}	MIDR	RIDR	RMDR
	(m)	(cm)	(cm)	(%)	(%)	(-)
ARQ	0	0.08	0.01	0.02	0.00	0.14
	4	0.42	0.01	0.09	0.00	0.00
	8	0.72	0.18	0.13	0.04	0.32
	12	2.96	-1.08	0.74	-0.32	0.43
ALT	0	0.07	0.00	0.01	1.15	0.04
	4	0.49	0.07	0.12	0.02	0.14
	8	1.42	0.55	0.25	0.12	0.48
	12	6.73	5.19	1.50	1.16	0.77
BSC	0	0.08	0.00	0.02	0.00	0.03
	4	0.49	0.03	0.11	0.01	0.08
	8	1.34	-0.28	0.26	-0.08	0.30
	12	7.21	-5.77	1.64	-1.37	0.84

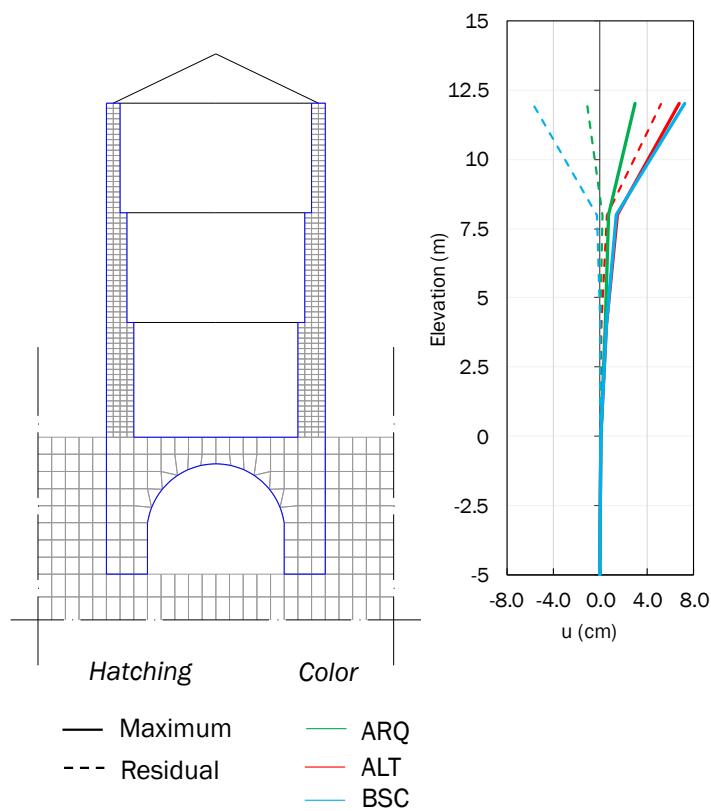


Figure V.31 Profiles of maximum and residual displacements

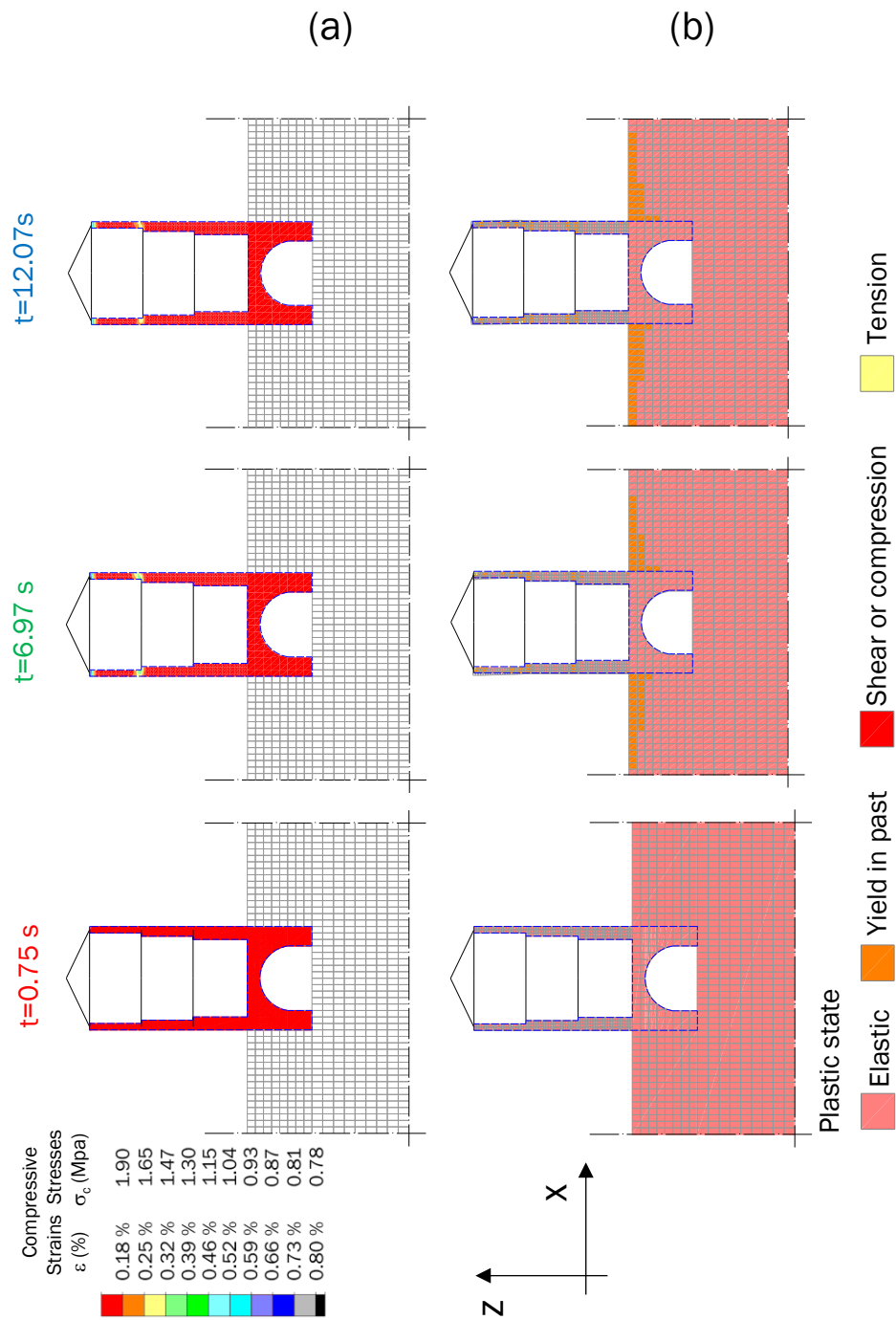


Figure V.32 Evolution with time of (a) inelastic compressive strains and stresses and (b) plastic states (ARQ input motion)

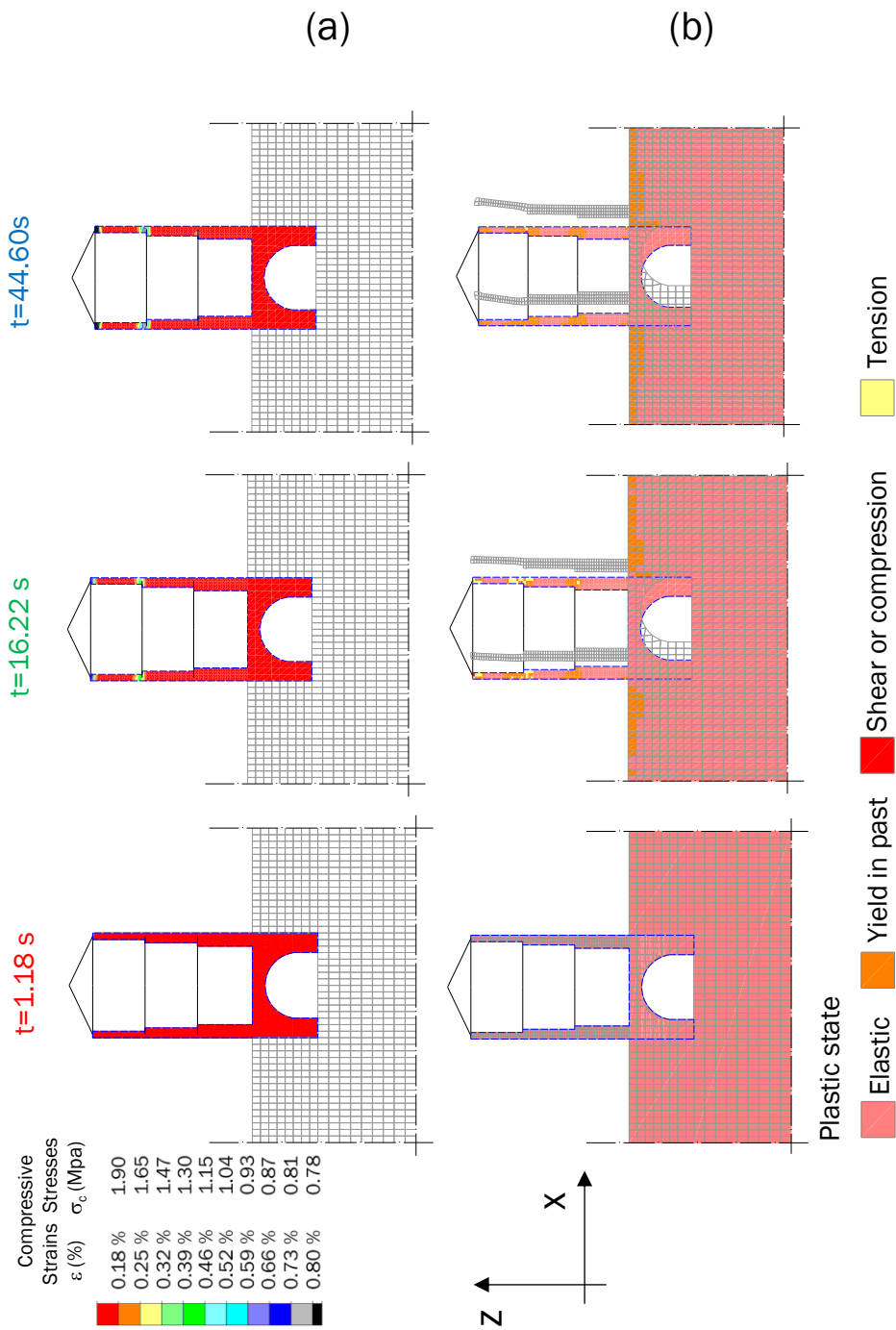


Figure V.33 Evolution with time of (a) inelastic compressive strains and stresses and (b) plastic states (ALT input motion)

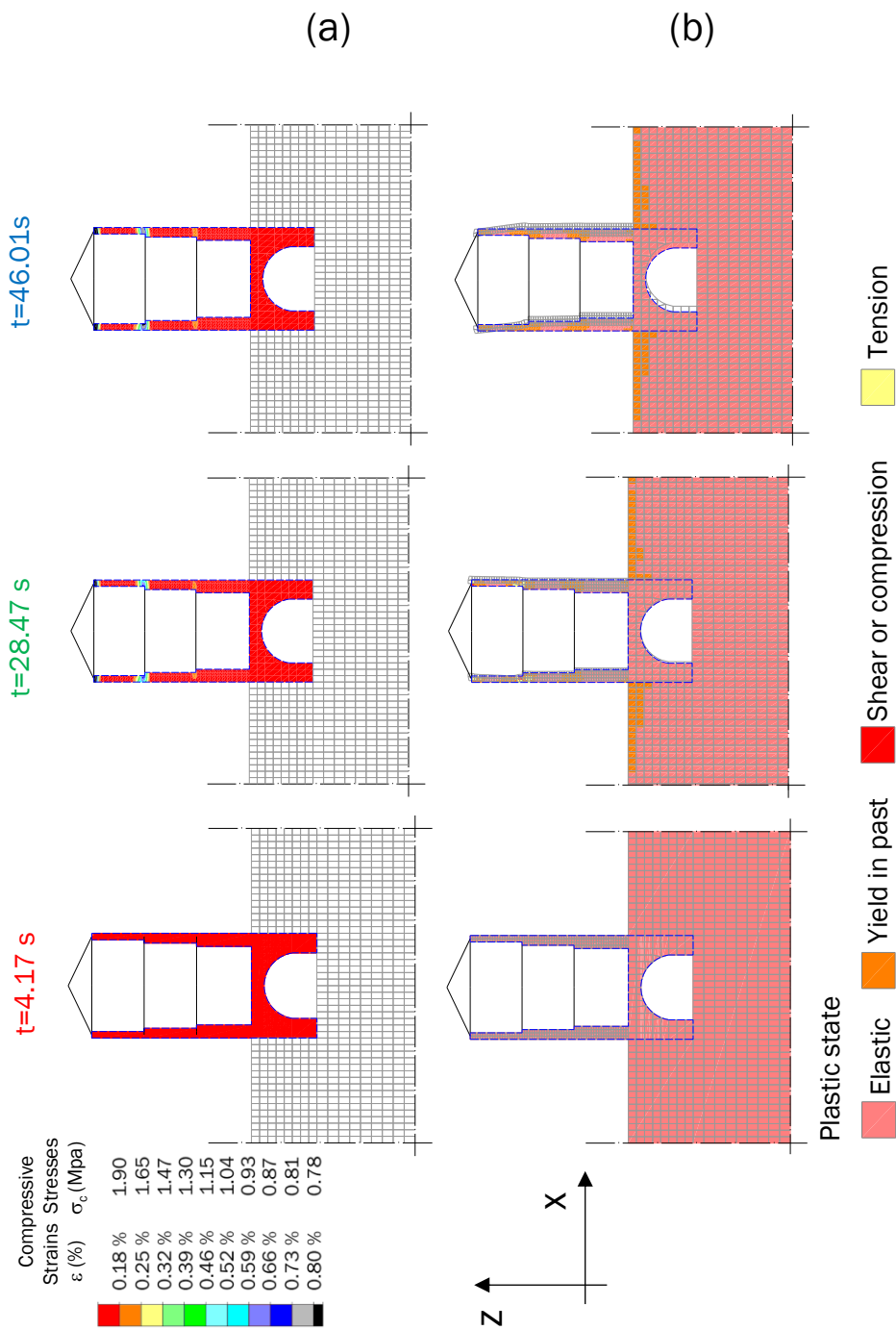


Figure V.34 Evolution with time of (a) inelastic compressive strains and stresses and (b) plastic states (BSC input motion)

For one input motion (ARQ), was also performed a nonlinear dynamic analysis by removing the aboveground elements of the SFS system, in order to compare the FF and FIM. As mentioned in Section II.1 the foundation filters the signal transmitted to

the structure with respect to the free-field counterpart if the foundation is both embedded and stiffer with respect to the soil. In Figure V.35 the comparison between the FIM (red dotted line) and FF (grey solid line) motion is shown, in terms of acceleration time histories at foundation level and *free-field* surface (see Figure V.29) and acceleration spectra. As show the presence of the underground storey reduces the input transmitted to the structure with respect to the *free-field* counterpart.

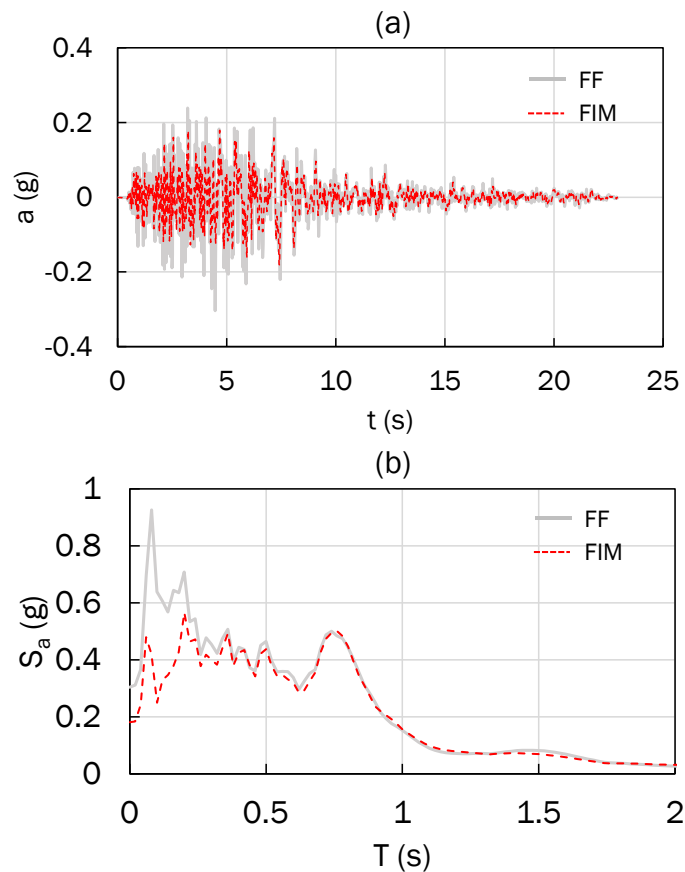


Figure V.35 Comparison between the foundation input motion (FIM) and free-field motion: (a) acceleration time histories and (b) acceleration spectra

V.4.5.2. Seismic fragility

The results of the NLTHA on the building were compared with the predictions obtained in Section IV.3.2. Comparing the materials properties and the thickness of the masonry walls upon which the DL were set, the brick masonry structures with two and four storeys were used as benchmarks, in order to evaluate the probability of failure of both the second and third storey. The selected IMs, PGV and $I_{sa0.1-2.0s}$, show the lowest

standard deviation ($\psi=0.34$ and $\psi=0.38$ respectively) for the four storeys structure, since the highest IDRs are expected at the third storey with the same wall thickness of the four storeys. Firstly, the IMs were computed, for each input motion, on three accelerograms: the input (bedrock) motion itself, the FF motion at foundation level in the SFS model (red line in Figure V.29) and that in the 2D hill model with cavities at vertical V8 (where the Ancient Seminary is located, see Figure V.19). Table V.13 lists the values of PGV and $I_{Sa0.1-2.0s}$ calculated for the three motions in the three different conditions.

Table V.13 IM values

	IM	Input	FF (SFS)	V8 (Hill)
ARQ	PGV (cm/s)	8.83	14.78	15.40
	$I_{Sa0.1-2.0s}$ (m/s)	2.40	4.02	4.20
ALT	PGV (cm/s)	14.84	23.00	21.48
	$I_{Sa0.1-2.0s}$ (m/s)	4.52	6.59	7.08
BSC	PGV (cm/s)	27.60	41.06	38.51
	$I_{Sa0.1-2.0s}$ (m/s)	9.00	12.94	12.57

Figure V.36 shows the FB fragility functions computed for both the IMs. Assuming the structure fixed at the base, and evaluating the seismic soil response through 1D (FF) and 2D (V8) analyses, it is possible to observe that:

- for each of the three seismic motions, the damage level (DL1) corresponding to the formation of the tension cracks at the toe of the wall is always reached;
- for ALT motion, the probability to reach DL2, corresponding to the activation of the rocking mechanism, is almost 50%, considering the effects of site amplification including cavities (square red symbol);
- for BSC motion, instead, the probability to reach DL3, corresponding to the incipient collapse due to overturning, is almost 75%, in 1D conditions, while accounting for site amplification in presence of cavities could lead to a slight reduction in terms of PGV.

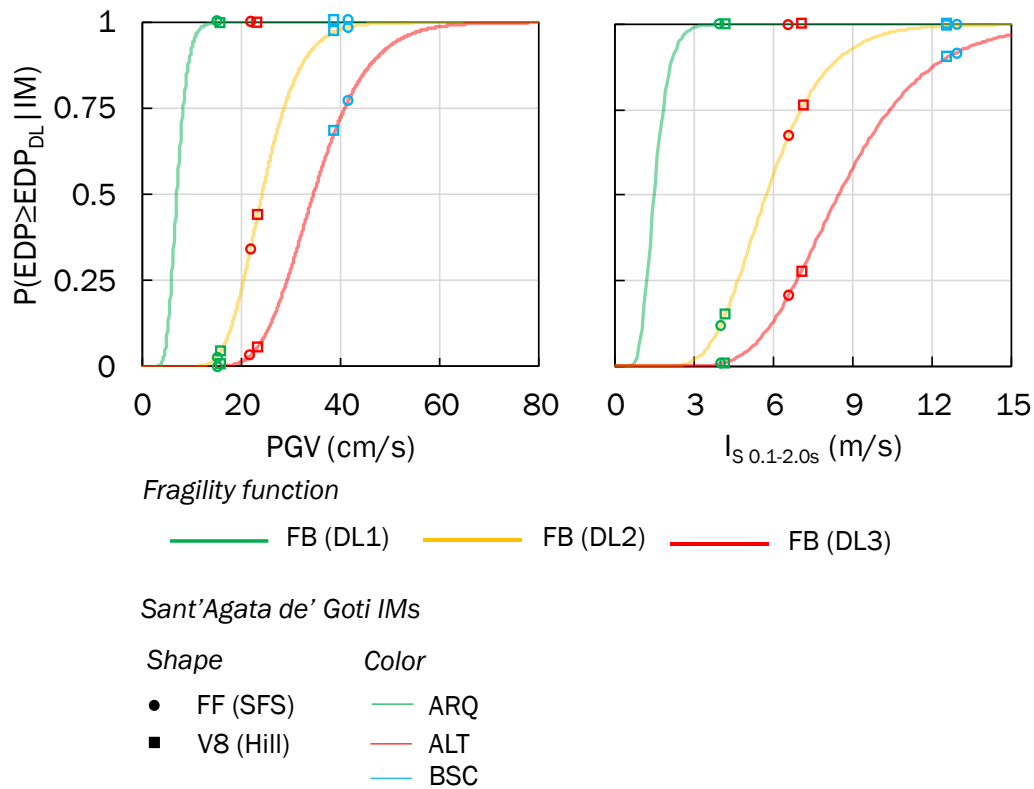


Figure V.36 Fixed-base fragility functions for four-storey masonry buildings

Figure V.37 shows the fragility functions for both FB model and that with homogeneous very soft soil (D_{ho}), computed in Section IV.3, with the values of damage probability (triangle symbols) computed for the same IMs evaluated on the reference input motion. Since the subsoil of Sant'Agata de'Goti in principle might be classified as C ($V_{s,30}=187\text{m/s}$), the comparison between the DL predicted by the numerical simulations and that expected from fragility functions obtained in Section IV.3 can be made considering that the function related to soil C should be expected to fall in the areas between the FB and D_{ho} functions. As expected, neglecting the SSI, the probability of failure is significantly underestimated. Considering ARQ input motion, the damage level DL1 is reached: as a matter of fact, for the seminary, as reported in Table V.12, the value of IDR is 0.47% (Table IV.14 DL1=0.30%). For both ALT and BSC motions, the probabilities of exceeding the three damage levels are greater than 50% considering SSI, while neglecting it they would be 2-5% for DL2 and DL3. Also, in those cases, the IDR reached for the seminar are greater than DL2 thresholds: respectively, IDR is 1.50% and 1.64% against 1.56%, while no collapse due to overturning is observed.

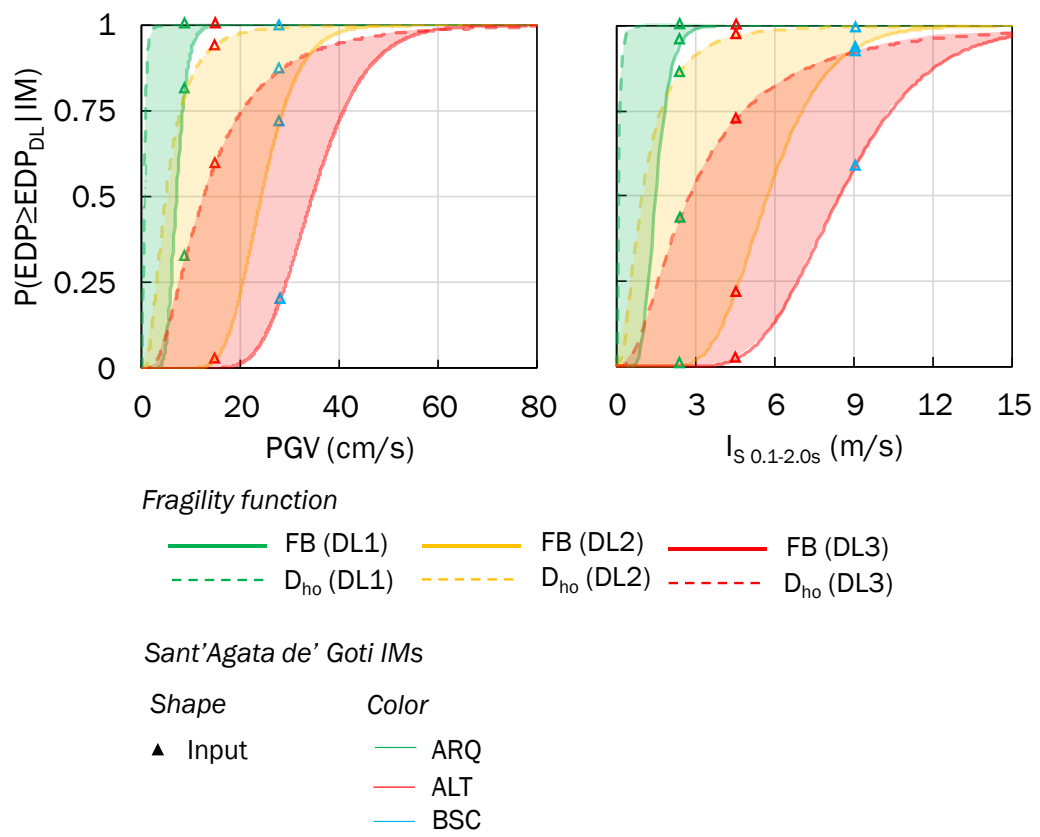


Figure V.37 Fixed base and homogeneous D soil fragility functions for four-storey masonry buildings

VI.CONCLUSIONS AND FUTURE PERSPECTIVES

The parametric analyses and application to case studies previously reported have shown that, with respect to the simplified assumption of fixed-base (FB) conditions, accounting for seismic site response and soil-structure interaction may significantly influence the dynamic response of masonry buildings, which typically exhibit high vulnerability to local failure modes. In particular, it has been confirmed that a reliable prediction of the SSI effects is of critical importance to assess the out-of-plane (OOP) seismic demand.

In Chapter III, the influence of SSI on the variation of the fundamental frequency, f^* , and damping, ξ , was firstly investigated with reference to 2D soil-structure models representing transverse sections of tuff masonry buildings with two, three and four-storeys, i.e. a typical structural configuration rather recurrent in the Italian and European built heritage. A parametric study was carried out through linear finite difference analyses in the time domain on the above building models, subjected to an input noise, by considering homogeneous or layered ground types A, B, C and D (according to EC8 classification by CEN, 2004), as well as two different base configurations (embedded “floating” foundation or underground storey).

The numerical results have highlighted that:

- f^* is reduced due to SSI, especially for squat structures (i.e. those with height-to-width ratio $h/b = 1$) on deformable soil (having width-to-depth ratios $b/D = 3.5$ and $b/D = 1.6$ respectively associated with the presence of an embedded “floating” foundation or underground storey), with a maximum variation as high as 30% with respect to the fixed-base frequency, f_0 ;
- ξ_{rad} (radiation damping) tends to rise up as the soil deformability increases, as well as in presence of the underground storey, because of the larger contact surface between the structure and soil.

The numerical results were first compared to the analytical predictions obtained on a replacement oscillator (RO), in terms of f^*/f_0 variation with the relative soil-structure stiffness, σ . It was observed that the numerical-analytical agreement was not satisfying enough, especially for the layered soil models, because the analytical solutions were adopted by assuming an over-simplified model of rigid footing resting above a homogeneous half-space.

To account for a layered soil nature, as well as for the actual foundation configuration in the definition of σ , an ‘equivalent relative stiffness ratio’, σ_{eq} , was introduced, by properly modifying the shear wave velocity of the soil volume affected by the foundation motion. Weighting coefficients were calibrated on the numerical results by minimising the difference between σ_{eq} and the value of σ , such an assumption allowed for

improving the analytical predictions of fundamental frequency based on the simplified RO approach.

In Chapter V, this updated procedure was applied to two Italian case studies, at both urban scale (on the historical centre of Matera) and at building scale (on the “Pietro Capuzi” school located in Visso). For the case of Matera (Section V.1), a set of seven buildings was chosen with structure and masonry types similar to the SFS models analysed in Chapter III. The soil properties were estimated from existing subsoil investigation (Gallipoli et al., 2020), in order to define the equivalent relative stiffness. For the case of Visso (Section V.2), the structure and soil properties for the school building were based on the studies by Cattari et al. (2019), de Silva et al. (2019) and Brunelli et al. (2020). Comparing the analytical results with the experimental frequencies for both the case studies, a good agreement was found, demonstrating the efficiency of a quick estimation of the frequency variation due to the SSI, if both foundation configuration and layered soil properties are duly taken into account. The proposed procedure was thus validated by both case studies, and it appears promising for being extensively adopted on greater numbers of buildings throughout large areas, in order to identify the situations in which SSI effects should not be overlooked.

In Chapter IV, the effects of site amplification and SSI were also investigated with reference to the nonlinear behaviour of masonry walls, with the objective of analysing the activation of OOP failure mechanisms, as well as of defining on-purpose fragility functions for probabilistic assessment of seismic damage.

To that aim, cloud analyses were carried out on two masonry types (rubble stone and clay brick), with two building height-to-depth ratios ($h/b = 1$ and $h/b = 2$), and either fixed-base or two ground type D profiles (homogeneous and heterogeneous), taking into account both soil and structure nonlinearity. The cloud analysis method was used to identify the most reliable relationship between suitable engineering demand parameters (EDPs), and intensity measures (IMs). In this study, the maximum inter-storey drift ratio was selected as EDP, in order to evaluate the OOP demand. A number of IMs were tested to find the optimal IM that yields the most reliable prediction of the EDP values, providing the lowest dispersion of the EDP-IM correlation.

To describe the structural behaviour until collapse, a set of 15 ground motions was selected from the SIMBAD database, and 180 nonlinear time history analyses (NLTHAs) were carried out.

Firstly, the response of the SFS components was investigated. Comparing the spectral acceleration predicted in free-field conditions between very soft (type D) and very stiff (type A) subsoil, it was observed that:

- in the period range typical of two-storey structures, for weak motions the peak spectral amplitudes, $S_{a,max}$, on ground types D result amplified with respect to rock outcrop A, due to the high soil impedance contrast;

- on the contrary, in the same period range, for strong motions the maximum value of S_a on ground types D is significantly reduced with respect to fixed-base conditions (especially for the heterogeneous soil profile), mainly because of plastic straining and energy dissipation related to soil hysteresis;
- in the period range of four-storey structures, both the weak- and the strong-motion spectral amplitudes on very soft soils are amplified with respect to hard rock outcrop, especially for the heterogeneous soil profile.

With reference to the structure, instead, it was observed that the maximum inter-storey drift (MIDR) predicted by the homogeneous soft soil profile resulted always lower with respect to the heterogeneous profile, since in the former case lower shear strains are reached in the soil volume affected by the foundation motion. In both cases, MIDR is greater with respect to the fixed-base conditions, due to both site and SSI effects.

For each coupling between the building aspect ratio h/b and masonry type, the EDP-IM correlations were computed in order to find the optimal IM. By comparing the values of standard deviation and coefficient of determination, it was found that the best estimate IMs were PGV, Housner Intensity and the integral of spectral accelerations in the period range [0.1 s, 2.0 s]. Once set the parameters of the EDP-IM linear regression model, three IDR thresholds (IDR_{DL}) corresponding to as many DLs were defined to calculate the fragility functions. The IDR_{DL} were defined as suitable fractions of the ultimate limit state value for which the collapse of the wall is caused by overturning (Lagomarsino, 2015).

For each IM and the corresponding soil-structure configuration, the fragility functions were derived. It was found that:

- neglecting site effects and SSI can lead to a significant underestimation of the probability of damage, because the fragility function derived for the FB model is always lower than those relevant to compliant base founded on soft soil, in all the soil-structure configurations;
- for a given h/b ratio, as the masonry deformability decreases from clay brick to rubble stone, the probability of failure at each DL increases due to the higher deformability and lower strength of the construction material.

A reduction factor, R_F , was also defined, in order to quantify the influence of site effects and SSI on OOP seismic fragility of masonry structures. It was observed that:

- for a given IM, for $R_F < 1$ values both site effects and SSI lead to detrimental effects on the OOP behaviour of the structure;
- if R_F is computed in terms of 84th percentile ratio, is observed a beneficial effect, i.e. $R_F > 1$, especially for DL3.

As a preliminary application of the results obtained in the fragility study, NLTHAs were performed on an ancient seminar, a tuff masonry building located in the historical centre of Sant'Agata de'Goti, settled on a ridge made of volcanic deposits (Sect. V.3). Preliminarily, nonlinear 1D and 2D seismic response analyses were performed along

the cross-section of the ridge, since a comprehensive subsoil characterization was carried out through the integration of static and dynamic field and laboratory tests. The above analyses were performed also to evaluate the effects of the underground cavities on the ground motion along the hill surface.

The structure was first assumed as fixed at the base, i.e. the FB model fragility function was used by evaluating IM from the free-field seismic response analyses through either 1D or 2D models. The comparison between the DLs resulting from both ground motion estimates demonstrated that neglecting stratigraphic details and morphological irregularities at the urban scale (such as the topographic profile and the presence of underground cavities) would lead to an underestimation of the probability of damage at the local building scale, especially for DL2 and DL3.

Finally, the DLs predicted by the NLTHA on complete soil-structure models were compared with those estimated through the fragility functions, by assuming that the functions pertaining to ground type C (i.e. that corresponding to the case-study building) are expected to be intermediate between those relevant to FB models and SSI models with a homogeneous ground type D profile. As expected, neglecting SSI the probability of failure is significantly underestimated. As a future perspective, the derivation of specific fragility functions for ground type C will permit to extend those results not only to this particular case study at Sant'Agata de' Goti but also on different urban centres.

More in general, several lines of future research can arise from this study, including:

- (i) optimization in the definition of the weighing coefficients of the proposed approach, to obtain a most reliable tool, taking into account the damping radiation;
- (ii) solving the hazard computability of the selected optimal IMs, and in addition derive specific fragility functions for ground type C;
- (iii) linear and nonlinear time history analyses of SFS models representative of masonry walls loaded in their own plane (2D coupled models) and entire masonry buildings (3D coupled models), in the latter case accounting for the role of floor systems (in terms of in-plane strength and flexibility) and wall-to-wall connections (i.e. flange effects);
- (iv) the derivation of fragility models for other types of OOP failure modes in ancient masonry buildings (e.g. corner failures, horizontal bending failure, and two-way bending failure of walls);
- (v) the derivation of fragility models for in-plane failure modes, namely, associated with the global seismic response of masonry buildings, which can develop if local collapse mechanisms are effectively prevented; and
- (vi) the modelling and propagation of uncertainties associated with materials, geometry, loads and, if possible, capacity models, in addition to the record-to-

record variability considered in this study; such uncertainties also play a key role in seismic risk assessment of existing structures.

REFERENCES

- Augenti N, Parisi F (2010a) Learning from construction failures due to the 2009 L'Aquila, Italy, earthquake. *J Perform Constr Facil.* [https://doi.org/10.1061/\(ASCE\)CF.1943-5509.0000122](https://doi.org/10.1061/(ASCE)CF.1943-5509.0000122)
- Augenti N, Parisi F (2010b) Constitutive Models for Tuff Masonry under Uniaxial Compression. *J Mater Civ Eng* 22:1102–1111. [https://doi.org/10.1061/\(ASCE\)MT.1943-5533.0000119](https://doi.org/10.1061/(ASCE)MT.1943-5533.0000119)
- Augenti N, Parisi F (2019) *Teoria e tecnica delle strutture in muratura*. Hoepli, Milan, Italy
- Augenti N, Parisi F, Prota A, Manfredi G (2011) In-Plane Lateral Response of a Full-Scale Masonry Subassemblage with and without an Inorganic Matrix-Grid Strengthening System. *J Compos Constr.* [https://doi.org/10.1061/\(asce\)cc.1943-5614.0000193](https://doi.org/10.1061/(asce)cc.1943-5614.0000193)
- Avilés J, Pérez-Rocha LE (1996) Evaluation of interaction effects on the system period and the system damping due to foundation embedment and layer depth. *Soil Dyn Earthq Eng.* [https://doi.org/10.1016/0267-7261\(95\)00035-6](https://doi.org/10.1016/0267-7261(95)00035-6)
- Avilés J, Pérez-Rocha LE (1998) Effects of foundation embedment during building-soil interaction. *Earthq Eng Struct Dyn* 27:1523–1540. [https://doi.org/10.1002/\(SICI\)1096-9845\(199812\)27:12<1523:AID-EQE798>3.0.CO;2-5](https://doi.org/10.1002/(SICI)1096-9845(199812)27:12<1523:AID-EQE798>3.0.CO;2-5)
- Baker JW (2007) Probabilistic structural response assessment using vector-valued intensity measures. *Earthq. Eng. Struct. Dyn.*
- Baker JW, Cornell CA (2006) Spectral shape, epsilon and record selection. *Earthq Eng Struct Dyn* 35:1077–1095. <https://doi.org/10.1002/eqe.571>
- Bielak J (1974) Dynamic behaviour of structures with embedded foundations. *Earthq Eng Struct Dyn.* <https://doi.org/10.1002/eqe.4290030305>
- Binda L, Fontana A, Mirabella G (1994) Mechanical behavior and stress distribution in multiple-leaf stone walls. In: *10th International Brick Block Masonry Conference*
- Bruneau M (1994) State-of-the-art report on seismic performance of unreinforced masonry buildings. *J Struct Eng (United States)*. [https://doi.org/10.1061/\(ASCE\)0733-9445\(1994\)120:1\(230\)](https://doi.org/10.1061/(ASCE)0733-9445(1994)120:1(230))
- Brunelli A, de Silva F, Piro A, et al (2021) Numerical simulation of the seismic response and soil–structure interaction for a monitored masonry school building damaged by the 2016 Central Italy earthquake. *Bull Earthq Eng* 19:1181–1211. <https://doi.org/10.1007/s10518-020-00980-3>
- Calabresi G, Manfredini G (1976) Terreni coesivi poco consistenti in Italia. *Riv Ital Geotec*
-

-
- Capatti MC, Tropeano G, Morici M, et al (2017) Implications of non-synchronous excitation induced by nonlinear site amplification and of soil-structure interaction on the seismic response of multi-span bridges founded on piles. *Bull Earthq Eng* 15:4963–4995. <https://doi.org/10.1007/s10518-017-0165-z>
- Cattari S, Sivori D, Brunelli A, et al (2019) Soil-structure interaction effects on the dynamic behaviour of a masonry school damaged by the 2016 – 2017 Central Italy earthquake sequence. *7th Int Conf Earthq Geotech Eng* 1655–1663
- Cavaliere F, Correia AA, Crowley H, Pinho R (2020) Seismic fragility analysis of URM buildings founded on piles: influence of dynamic soil – structure interaction models. *Bull Earthq Eng* 18:4127–4156. <https://doi.org/10.1007/s10518-020-00853-9>
- CEN (2004) Eurocode 8: Design of structures for earthquake resistance – Part 1: General rules, seismic actions and rules for buildings.
- Chiaradonna A, Landolfi L, D’Onofrio A, Silvestri F (2014) Analisi degli effetti di cavità ipogee sulla risposta sismica in superficie. In: XXV Convegno Nazionale AGI: La Geotecnica nella difesa del territorio e delle infrastrutture dalle calamità naturali. Baveno 4-6 giugno 2014.
- Chopra AK (1995) *Dynamics of Structures: theory and applications to earthquake engineering*. Prentice-Hall, Englewood Cliff
- Conti R, Morigi M, Viggiani GMB (2017) Filtering effect induced by rigid massless embedded foundations. *Bull Earthq Eng* 15:1019–1035. <https://doi.org/10.1007/s10518-016-9983-7>
- Conti R, Morigi M, Rovithis E, et al (2018) Filtering action of embedded massive foundations: New analytical expressions and evidence from 2 instrumented buildings. *Earthq Eng Struct Dyn* 47:1229–1249. <https://doi.org/10.1002/eqe.3014>
- Couto R, Bento R, Gomes RC (2020) Seismic performance and fragility curves of historical residential buildings in Lisbon downtown affected by settlements. *Bull Earthq Eng* 18:5281–5307. <https://doi.org/10.1007/s10518-020-00906-z>
- D’Ayala D, Spence R, Oliveira C, Pomonis A (1997) Earthquake Loss Estimation for Europe’s Historic Town Centres. *Earthq Spectra* 13:773–793. <https://doi.org/10.1193/1.1585980>
- D’Ayala D, Speranza E (2003) Definition of Collapse Mechanisms and Seismic Vulnerability of Historic Masonry Buildings. *Earthq Spectra* 19:479–509. <https://doi.org/10.1193/1.1599896>
- D’Ayala DF, Paganoni S (2011) Assessment and analysis of damage in L’Aquila historic city centre after 6th April 2009. *Bull Earthq Eng*. <https://doi.org/10.1007/s10518-010-9224-4>
- D’Onofrio A, Silvestri F (2001) Influence of Micro-Structure on Small-Strain Stiffness and Damping of Fine Grained Soil and Effects on Local Site Response. *International Conferences on Recent Advances in Geotechnical Earthquake*
-

Engineering and Soil Dynamics. 15.

Daniell JE, Khazai B, Wenzel F, Vervaeck A (2011) The CATDAT damaging earthquakes database. *Nat Hazards Earth Syst Sci.* <https://doi.org/10.5194/nhess-11-2235-2011>

De Felice G (2011) Out-of-plane seismic capacity of masonry depending on wall section morphology. *Int J Archit Herit* 5:466–482. <https://doi.org/10.1080/15583058.2010.530339>

de Silva F, Melillo M, Calcaterra D, et al (2013) A study for the requalification and safety against natural hazards of the environmental and building heritage of Sant'Agata de' Goti (Italy). In: *Geotechnical Engineering for the Preservation of Monuments and Historic Sites - Proc. of the 2nd Int. Symp. on Geotechnical Engineering for the Preservation of Monuments and Historic Sites*

de Silva F (2016) Dynamic Soil-Foundation-Structure Interaction for masonry towers: the case study of Carmine bell tower in Napoli. PhD thesis in seismic risk, University of Naples Federico II

de Silva F, Pitilakis D, Ceroni F, et al (2018) Experimental and numerical dynamic identification of a historic masonry bell tower accounting for different types of interaction. *Soil Dyn Earthq Eng.* <https://doi.org/10.1016/j.soildyn.2018.03.012>

de Silva F, Ceroni F, Sica S, Silvestri F (2019a) Fragility curves of slender towers accounting for soil-structure interaction. In: *Proceedings 7th Int Geotech Earthq Eng, Rome, 17–20 June 2019*

de Silva F, Piro A, Brunelli A, et al (2019b) On the soil–structure interaction in the seismic response of a monitored masonry school building struck by the 2016–2017 Central Italy earthquake. In: *7th ECCOMAS thematic conference on computational methods in structural dynamics and earthquake engineering, 24–26 June 2019, Crete, Greece*

de Silva F (2020) Influence of soil-structure interaction on the site-specific seismic demand to masonry towers. *Soil Dyn Earthq Eng.* <https://doi.org/10.1016/j.soildyn.2019.106023>

De Vivo B, Rolandi G, Gans PB, et al (2001) New constraints on the pyroclastic eruptive history of the Campanian volcanic Plain (Italy). *Mineral Petrol.* <https://doi.org/10.1007/s007100170010>

Derakhshan H, Grif MC, Ingham JM, Asce M (2013) Out-of-Plane Behavior of One-Way Spanning Unreinforced Masonry Walls. 409–417. [https://doi.org/10.1061/\(ASCE\)EM.1943-7889.0000347](https://doi.org/10.1061/(ASCE)EM.1943-7889.0000347).

Di Ludovico M, Prota A, Moroni C, et al (2017) Reconstruction process of damaged residential buildings outside historical centres after the L'Aquila earthquake: part II—“heavy damage” reconstruction. *Bull Earthq Eng* 15:693–729. <https://doi.org/10.1007/s10518-016-9979-3>

Doherty K, Gri MC, Lam N, Wilson J (2002) Displacement-based seismic analysis for out-of-plane bending of unreinforced masonry walls. 850:833–850. <https://doi.org/10.1002/eqe.126>

-
- Dolce M, Nicoletti M, De Sortis A, et al (2017) Osservatorio sismico delle strutture: the Italian structural seismic monitoring network. *Bull Earthq Eng.* <https://doi.org/10.1007/s10518-015-9738-x>
- Elsabee F, Murray JP (1977) Dynamic Behavior of Embedded Foundations. R77-33
- Ermolli Russo E, Sardella R, Di Maio G, et al (2010) Pollen and mammals from the late Early Pleistocene site of Saticula (Sant'Agata de' Goti, Benevento, Italy). *Quat Int.* <https://doi.org/10.1016/j.quaint.2009.06.013>
- Evangelista L, Landolfi L, d'Onofrio A, Silvestri F (2016) The influence of the 3D morphology and cavity network on the seismic response of Castelnuovo hill to the 2009 Abruzzo earthquake. *Bull. Earthq. Eng.*
- Faccioli E, Vanini M, Paolucci R (1998) TRISEE: 3D site effects and soil-foundation interaction in earthquake and vibration risk evaluation. Technical report
- Fenelli GB, Pellegrino A, Picarelli L (1997) Stability problems of old towns built on relict plateaux resting on clay deposits. In: *Geotechnical engineering for the preservation of monuments and historic sites: proceedings of the International Symposium on Geotechnical Engineering for the Preservation of Monuments and Historic Sites, Napoli, Italy, 3-4 October 1996*
- Ferreira TM, Costa AA, Costa A (2014) Analysis of the out-of-plane seismic behaviour of unreinforced masonry: A literature review. *Int J Archit Herit* 1558–3058. <https://doi.org/10.1080/15583058.2014.885996>
- Gallipoli MR, Lupo M (2012) Caratterizzazione dei terreni e risposta sismica locale dell'area urbana di Matera. In: ARACNE editrice S.r.l. (ed) *Tecniche speditive per la stima dell'amplificazione sismica e della dinamica degli edifici Studi teorici ed applicazioni professionali a cura di Marco Mucciarelli.* pp 323–342
- Gallipoli MR, Calamita G, Tragni N, et al (2020) Evaluation of soil-building resonance effect in the urban area of the city of Matera (Italy). *Eng Geol.* <https://doi.org/10.1016/j.enggeo.2020.105645>
- Gazetas G (1983) Analysis of machine foundation vibrations: State of the art. *Int J Soil Dyn Earthq Eng* 2:2–42. [https://doi.org/10.1016/0261-7277\(83\)90025-6](https://doi.org/10.1016/0261-7277(83)90025-6)
- Gazetas G (1991a) Formulas and charts for impedances of surface and embedded foundations. *J Geotech Eng.* [https://doi.org/10.1061/\(ASCE\)0733-9410\(1991\)117:9\(1363\)](https://doi.org/10.1061/(ASCE)0733-9410(1991)117:9(1363))
- Gazetas G (1991b) Foundation Vibrations. In: *Foundation Engineering Handbook.* Springer US, Boston, MA, pp 553–593
- Gazetas G (2015) 4th Ishihara lecture: Soil-foundation-structure systems beyond conventional seismic failure thresholds. *Soil Dyn Earthq Eng.* <https://doi.org/10.1016/j.soildyn.2014.09.012>
- GEER (2016) Engineering reconnaissance of the 24 August 2016 Central Italy Earthquake: Ver 2, GEER Report 050, Geotechnical Extreme Events Reconnaissance Association, <https://doi.org/10.18118/G61S3Z>
-

- GEER (2017) Engineering Reconnaissance following the October 2016 Central Italy Earthquakes: Ver 2, GEER Report 050D, Geotechnical Extreme Events Reconnaissance Association Report, <https://doi.org/10.18118/G6HS39>
- Givens MJ, Mylonakis G, Stewart JP (2016) Modular analytical solutions for foundation damping in soil-structure interaction applications. *Earthq Spectra*. <https://doi.org/10.1193/071115EQS112M>
- Hardin BO, Drnevich VP (1972) Shear Modulus and Damping in Soils. *J Soil Mech Found Div*
- Housner GW (1963) The behavior of inverted pendulum structures during earthquakes. *Bull Seismol Soc Am*. <https://doi.org/10.1017/CB09781107415324.004>
- Independent Evaluation Group (IEG) (2007) Development actions and the rising incidence of disasters. The World Bank, Washington, DC
- Itasca (2011) FLAC 7.0 – Fast Lagrangian Analysis of Continua – User’s Guide, Itasca Consulting Group, 3 Minneapolis
- Jalayer F (2003) Direct Probabilistic Seismic Analysis: Implementing Non-linear Dynamic Assessments. PhD thesis at Stanford University, California
- Jalayer F, Cornell CA (2009) Alternative non-linear demand estimation methods for probability-based seismic assessments. 951–972. <https://doi.org/10.1002/eqe>
- Jalayer F, De Risi R, Manfredi G (2015) Bayesian Cloud Analysis: Efficient structural fragility assessment using linear regression. *Bull Earthq Eng* 13:1183–1203. <https://doi.org/10.1007/s10518-014-9692-z>
- Kallioras S, Guerrini G, Tomassetti U, et al (2018) Experimental seismic performance of a full-scale unreinforced clay-masonry building with flexible timber diaphragms. *Eng Struct*. <https://doi.org/10.1016/j.engstruct.2018.02.016>
- Karatzia XA, Mylonakis GE (2019) On the applicability of Veletsos’ wave parameter ($1/\sigma$). *COMPDYN Proc* 1:1924–1932. <https://doi.org/10.7712/120119.7046.19191>
- Kausel E (2010) Early history of soil-structure interaction. *Soil Dyn Earthq Eng* 30:822–832. <https://doi.org/10.1016/j.soildyn.2009.11.001>
- Khosravikia F, Mahsuli M, Ghannad MA (2018) The effect of soil–structure interaction on the seismic risk to buildings. *Bull Earthq Eng* 16:3653–3673. <https://doi.org/10.1007/s10518-018-0314-z>
- Kim S, Stewart JP (2003) Kinematic soil-structure interaction from strong motion recordings. *J Geotech Geoenvironmental Eng*. [https://doi.org/10.1061/\(ASCE\)1090-0241\(2003\)129:4\(323\)](https://doi.org/10.1061/(ASCE)1090-0241(2003)129:4(323))
- Kuhlemeyer R, Lysmer J (1973) Finite Element Method Accuracy for Wave Propagation Problems. *J Soil Mech Found Div*
- Lagomarsino S (2015) Seismic assessment of rocking masonry structures. *Bull Earthq Eng* 13:97–128. <https://doi.org/10.1007/s10518-014-9609-x>

-
- Lam NTK, Griffith M, Wilson J, Doherty K (2003) Time-history analysis of URM walls in out-of-plane flexure. *Eng Struct* 25:743–754. [https://doi.org/10.1016/S0141-0296\(02\)00218-3](https://doi.org/10.1016/S0141-0296(02)00218-3)
- Lanzo G, Silvestri F (1999) *Risposta Sismica Locale, Teoria ed Esperienze*. Hevelius Edizioni
- Licata V (2015) A laboratory and field study on cyclic liquefaction of pyroclastic silty sand. PhD Thesis in Seismic Risk, University of Napoli Federico II.
- Lorenzoni F, Calabria A, De Conto N, da Porto F (2019) Assessment of the dynamic response of monitored masonry buildings after the Central Italy earthquake swarm in 2016. In: 7th ECCOMAS Thematic Conference on Computational Methods in Structural Dynamics and Earthquake Engineering, 24-26 June 2019, Crete, Greece.
- Lourenço PB (1996) *Computational strategies for masonry structures*
- Mackie KR, Stojadinovic B (2005) Comparison of Incremental Dynamic, Cloud, and Stripe Methods for Computing Probabilistic Seismic Demand Models. In: *Structures Congress 2005: Metropolis and Beyond*
- Magenes G, Calvi GM (1997) In-plane seismic response of brick masonry walls. *Earthq Eng Struct Dyn* 26:1091–1112. [https://doi.org/10.1002/\(SICI\)1096-9845\(199711\)26:11<1091:AID-EQE693>3.0.CO;2-6](https://doi.org/10.1002/(SICI)1096-9845(199711)26:11<1091:AID-EQE693>3.0.CO;2-6)
- Mánica M, Ovando E, Botero E (2014) Assessment of damping models in FLAC. *Comput Geotech*. <https://doi.org/10.1016/j.compgeo.2014.02.007>
- Milosevic J, Gago AS, Lopes M, Bento R (2013) Experimental assessment of shear strength parameters on rubble stone masonry specimens. *Constr Build Mater*. <https://doi.org/10.1016/j.conbuildmat.2013.06.036>
- Minas S, Galasso C (2019) Accounting for spectral shape in simplified fragility analysis of case-study reinforced concrete frames. *Soil Dyn Earthq Eng*. <https://doi.org/10.1016/j.soildyn.2018.12.025>
- MIT, Ministero delle infrastrutture e dei trasporti (2019) Circolare 21 gennaio 2019, n. 7 Istruzioni per l'applicazione dell'«Aggiornamento delle “Norme tecniche per le costruzioni”». Gazz Uff della Repubb Ital
- MIT Ministero delle infrastrutture e dei trasporti (2018) *Norme Tecniche per le Costruzioni*. DM 17/1/2018, Italian Mi. Italian Ministry of Infrastructure and Transportation, Rome, Italy
- Mylonakis G, Gazetas G (2000) Seismic soil-structure interaction: Beneficial or detrimental? *J Earthq Eng* 4:277–301. <https://doi.org/10.1080/13632460009350372>
- Mylonakis G, Nikolaou S, Gazetas G (2006) Footings under seismic loading: Analysis and design issues with emphasis on bridge foundations. *Soil Dyn Earthq Eng*. <https://doi.org/10.1016/j.soildyn.2005.12.005>
-

NEHRP Consultants Joint Venture (2012) Soil-Structure Interaction for Building Structures

Pagliaroli A, Pergalani F, Ciancimino A, et al (2020) Site response analyses for complex geological and morphological conditions: relevant case-histories from 3rd level seismic microzonation in Central Italy. *Bull Earthq Eng*. <https://doi.org/10.1007/s10518-019-00610-7>

Parisi F, Augenti N (2013) Earthquake damages to cultural heritage constructions and simplified assessment of artworks. *Eng Fail Anal* 34:735–760. <https://doi.org/10.1016/j.engfailanal.2013.01.005>

Parisi F, Augenti N, Prota A (2014) Implications of the spandrel type on the lateral behavior of unreinforced masonry walls. *Earthq Eng Struct Dyn*. <https://doi.org/10.1002/eqe.2441>

Parisi F, Balestrieri C, Varum H (2019) Nonlinear finite element model for traditional adobe masonry. *Constr Build Mater*. <https://doi.org/10.1016/j.conbuildmat.2019.07.001>

Penna A, Morandi P, Rota M, et al (2014) Performance of masonry buildings during the Emilia 2012 earthquake. *Bull Earthq Eng*. <https://doi.org/10.1007/s10518-013-9496-6>

Petridis C, Pitilakis D (2020) Fragility curve modifiers for reinforced concrete dual buildings, including nonlinear site effects and soil–structure interaction. *Earthq Spectra*. <https://doi.org/10.1177/8755293020919430>

Piro A, De Silva F, Parisi F, et al (2017) Interazione sismica tra terreno, cavità e struttura: un caso di studio nel centro storico di Sant'Agata de' goti. In: XXVI Convegno Nazionale di Geotecnica

Piro A, de Silva F, Martinelli G, et al (2019) Effects of the underground urban development on the seismic response of a historical centre in Italy. In: *Earthquake Geotechnical Engineering for Protection and Development of Environment and Constructions- Proceedings of the 7th International Conference on Earthquake Geotechnical Engineering, 2019*

Piro A, de Silva F, Parisi F, et al (2020) Effects of soil-foundation-structure interaction on fundamental frequency and radiation damping ratio of historical masonry building sub-structures. *Bull Earthq Eng* 18:1187–1212. <https://doi.org/10.1007/s10518-019-00748-4>

Pitilakis D, Karatzetzou A (2015) Dynamic stiffness of monumental flexible masonry foundations. *Bull Earthq Eng*. <https://doi.org/10.1007/s10518-014-9611-3>

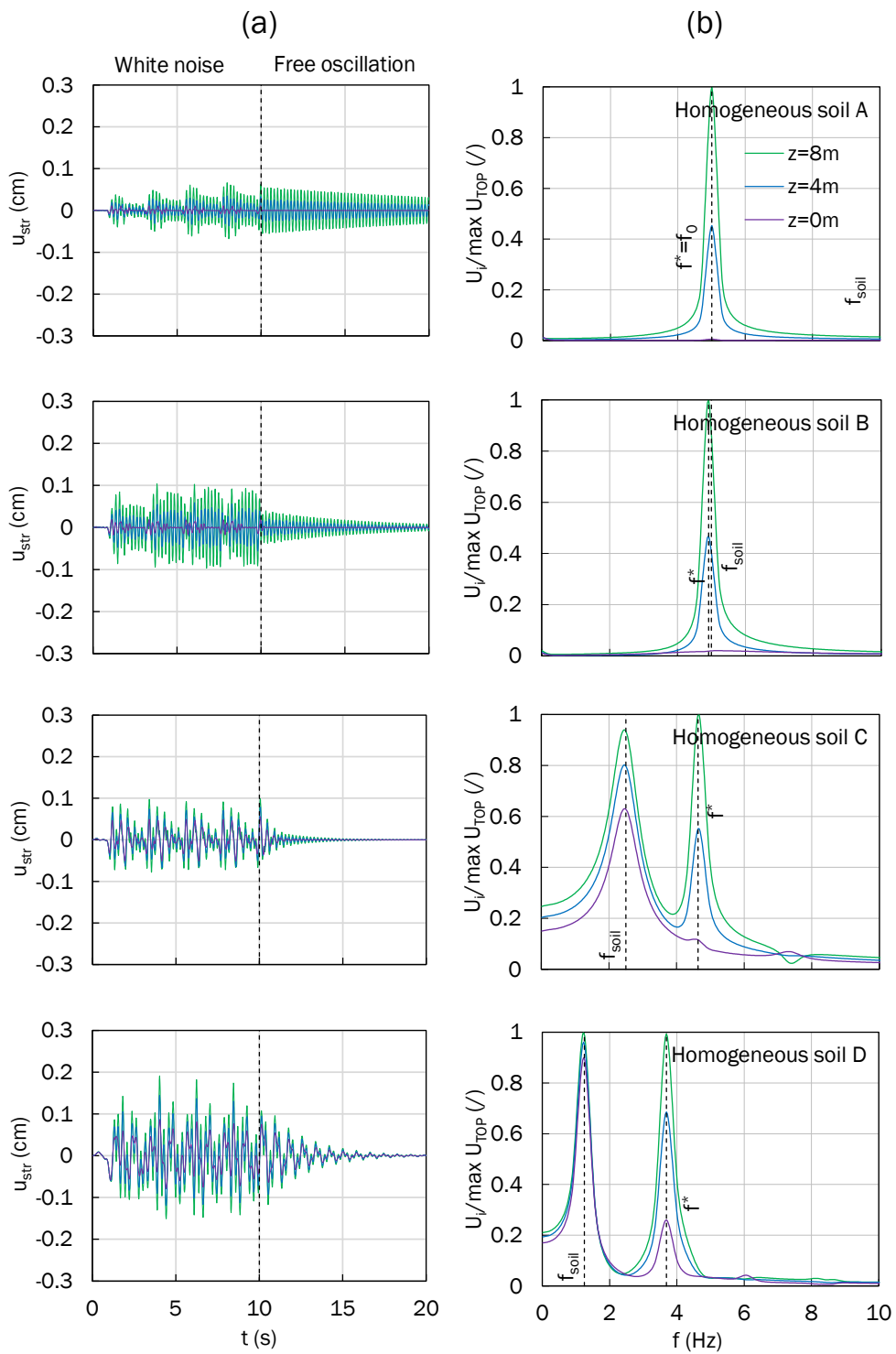
Porter K (2019) *A Beginner's Guide to Fragility, Vulnerability, and Risk*. 2019:

ReLUIIS – Task 4.1 Workgroup report, edited by Cattari S, Degli Abati S, Ottonelli D, Sivori D, et al. (2018a) Report di sintesi sulle attività svolte sugli edifici in muratura monitorati dall'Osservatorio Sismico delle Strutture, Linea Strutture in Muratura, ReLUIIS report, Rete dei Laboratori Universitari di Ingegneria Sismica (in Italian).

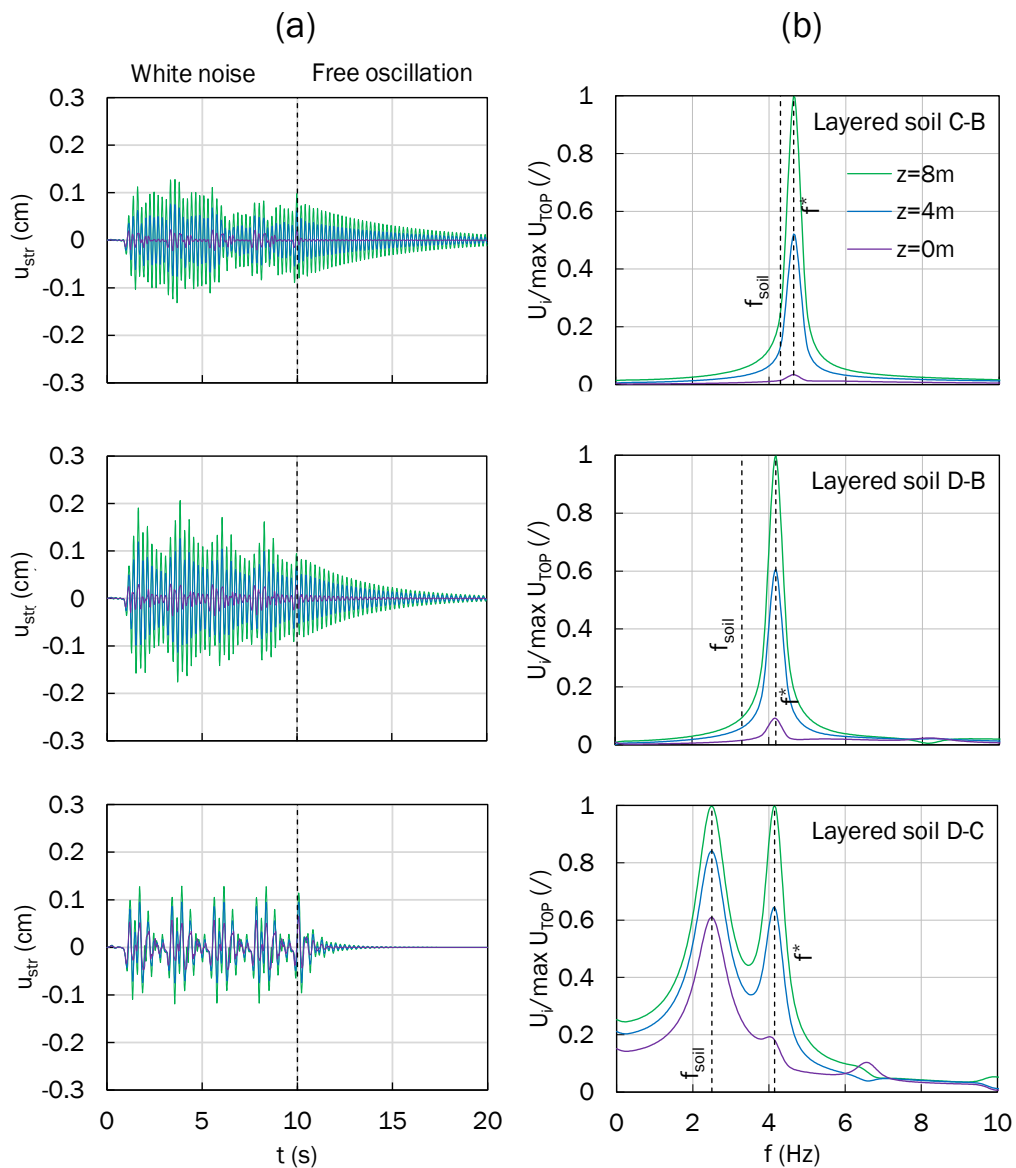
-
- ReLUIS – WorkPackage 3, edited by de Silva F, Piro A, Silvestri F (2018b) Geotechnical characterization of Visso and Sant’Agata de’Goti, ReLUIS report, Rete dei Laboratori Universitari di Ingegneria Sismica.
- ReLUIS – WorkPackage 3, edited by de Silva F, Piro A, Scotto di Santolo A., Silvestri F (2018c) Field and laboratory tests on the subsoil of Sant’Agata de’Goti, ReLUIS report, Rete dei Laboratori Universitari di Ingegneria Sismica.
- Rota M, Penna A, Magenes G (2010) A methodology for deriving analytical fragility curves for masonry buildings based on stochastic nonlinear analyses. *Eng Struct* 32:1312–1323. <https://doi.org/10.1016/j.engstruct.2010.01.009>
- Rovithis E, Kirtas E, Bliziotis D, et al (2017) A LiDAR-aided urban-scale assessment of soil-structure interaction effects: the case of Kalochori residential area (N. Greece). *Bull Earthq Eng* 15:4821–4850. <https://doi.org/10.1007/s10518-017-0155-1>
- Sanò T (2011) Risposta sismica locale in presenza di cavità sotterranee. *Ing Sismica*
- Scotto Di Santolo A, Ciardulli F, Silvestri F (2015a) Triaxial and shear box tests on a pyroclastic soft rock. In: *Volcanic Rocks and Soils - Proceedings of the International Workshop on Volcanic Rocks and Soils, 2015*
- Scotto Di Santolo A, de Silva F, Calcaterra D, Silvestri F (2015b) Preservation of cultural heritage of Sant’Agata De’ Goti (Italy) from natural hazards. In: *Engineering Geology for Society and Territory - Volume 8: Preservation of Cultural Heritage*
- Shirato M, Kouno T, Asai R, et al (2008) Large-scale experiments on nonlinear behavior of shallow foundations subjected to strong earthquakes. *Soils Found.* <https://doi.org/10.3208/sandf.48.673>
- Simões AG, Bento R, Lagomarsino S, et al (2020) Seismic assessment of nineteenth and twentieth centuries URM buildings in Lisbon: structural features and derivation of fragility curves. *Bull Earthq Eng* 18:645–672. <https://doi.org/10.1007/s10518-019-00618-z>
- Simões AG, Bento R, Lagomarsino S, et al (2019) Fragility Functions for Tall URM Buildings around Early 20th Century in Lisbon. Part 1: Methodology and Application at Building Level. *Int J Archit Herit* 0:1–24. <https://doi.org/10.1080/15583058.2019.1618974>
- Smerzini C, Galasso C, Iervolino I, Paolucci R (2014) Ground motion record selection based on broadband spectral compatibility. *Earthq Spectra.* <https://doi.org/10.1193/052312EQS197M>
- Sorrentino L, Liberatore L, Liberatore D, Masiani R (2014) The behaviour of vernacular buildings in the 2012 Emilia earthquakes. *Bull Earthq Eng.* <https://doi.org/10.1007/s10518-013-9455-2>
- Stewart JP, Fenves GL, Seed RB (1999) Seismic soil-structure interaction in buildings. I: Analytical methods. *J Geotech Geoenvironmental Eng* 125:26–37. [https://doi.org/10.1061/\(ASCE\)1090-0241\(1999\)125:1\(26\)](https://doi.org/10.1061/(ASCE)1090-0241(1999)125:1(26))
-

- Stewart JP, Kim S, Bielak J, et al (2003) Revisions to Soil-Structure Interaction Procedures in NEHRP Design Provisions. *Earthq. Spectra*
- Tomažević M, Weiss P (2010) Displacement capacity of masonry buildings as a basis for the assessment of behavior factor: An experimental study. *Bull Earthq Eng.* <https://doi.org/10.1007/s10518-010-9181-y>
- Vamvatsikos D, Allin Cornell C (2002) Incremental dynamic analysis. *Earthq Eng Struct Dyn* 31:491–514. <https://doi.org/10.1002/eqe.141>
- Veletsos AS, Meek JW (1974) Dynamic behaviour of building-foundation systems. *Earthq Eng Struct Dyn.* <https://doi.org/10.1002/eqe.4290030203>
- Vinale F (1988) Microzonazione sismica di un'area campione di Napoli. *Riv Ital di Geotec*
- Vucetic M, Dobry R (1991) Effect of soil plasticity on cyclic response. *J Geotech Eng.* [https://doi.org/10.1061/\(ASCE\)0733-9410\(1991\)117:1\(89\)](https://doi.org/10.1061/(ASCE)0733-9410(1991)117:1(89))
- Vuoto A, Piro A, de Silva F, et al (2018) Seismic soil-structure interaction: two case studies in Sant'Agata de' Goti, Italy. In: XVI European Conference on Earthquake Engineering. Thessaloniki, pp 1–12
- Wolf JP (1985) *Dynamic soil-structure interaction*. Prentice Hall, Englewood Cliff.

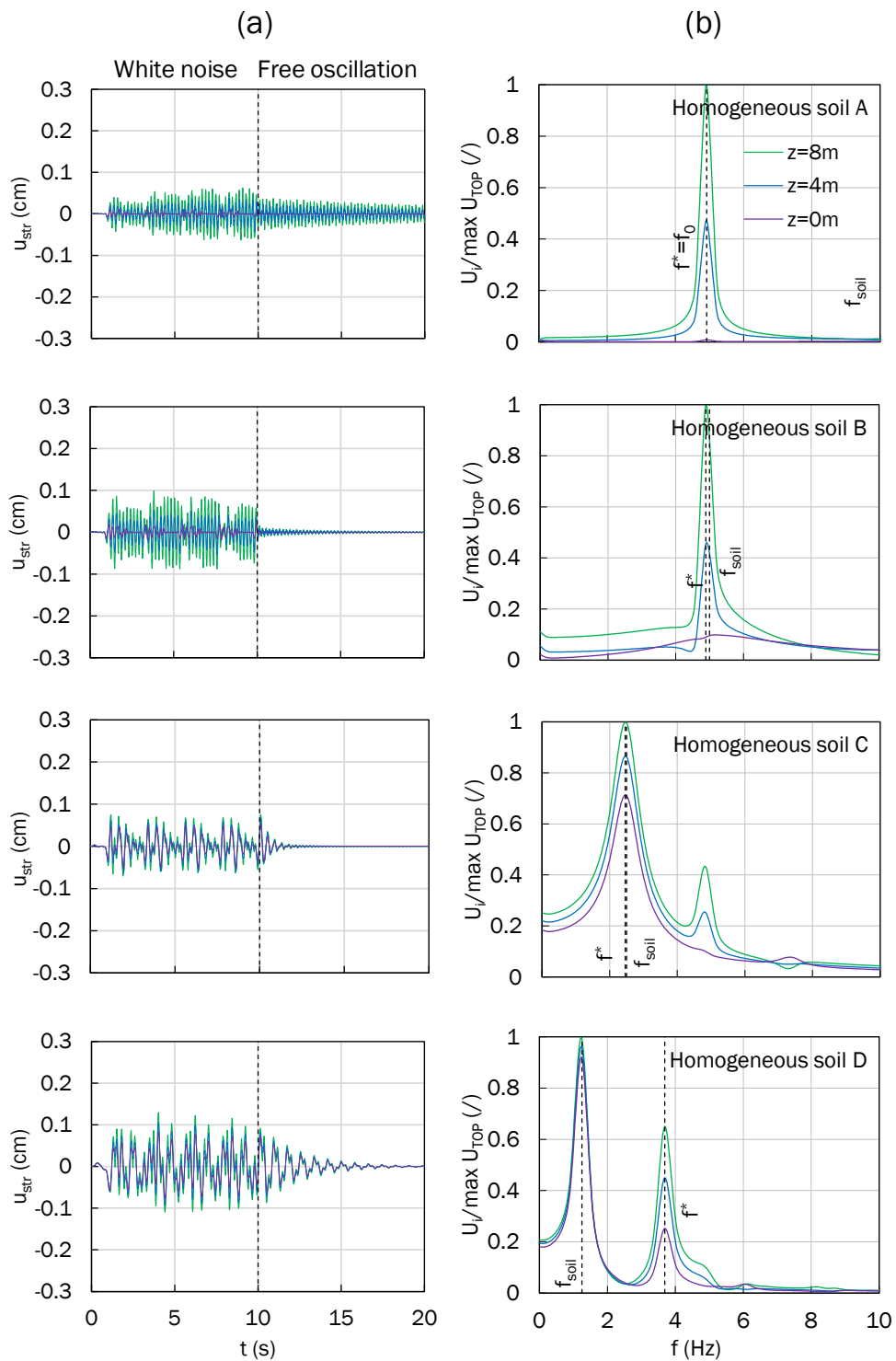
**APPENDIX A
RESULTS OF LINEAR TIME HISTORY ANALYSIS**



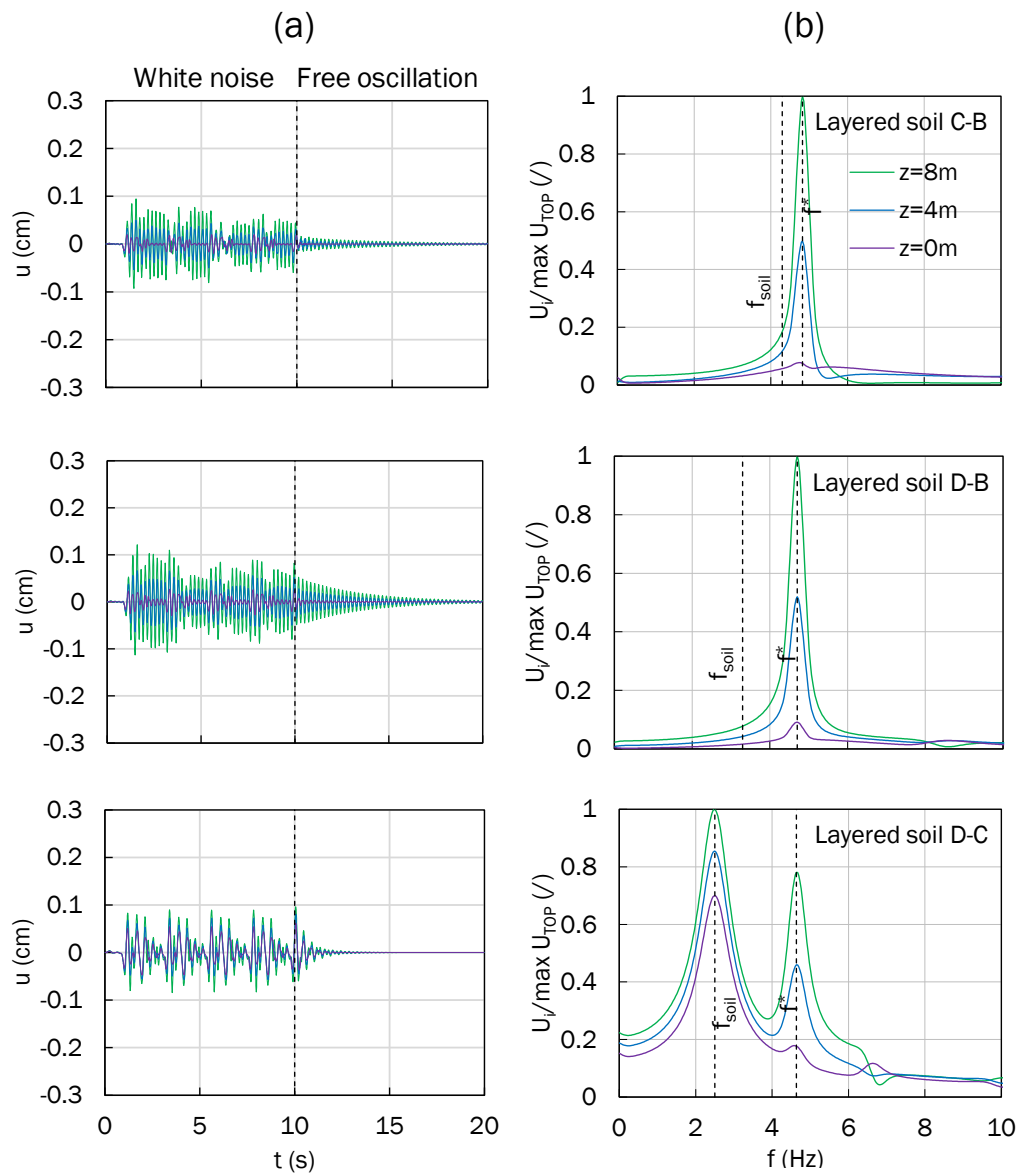
A.A.1 Dynamic response of two-storey SFS system ($h/b = 1$) with embedded floating foundation and homogeneous soil (A, B, C or D): (a) time histories and (b) FFTs of horizontal displacements at different structural elevations.



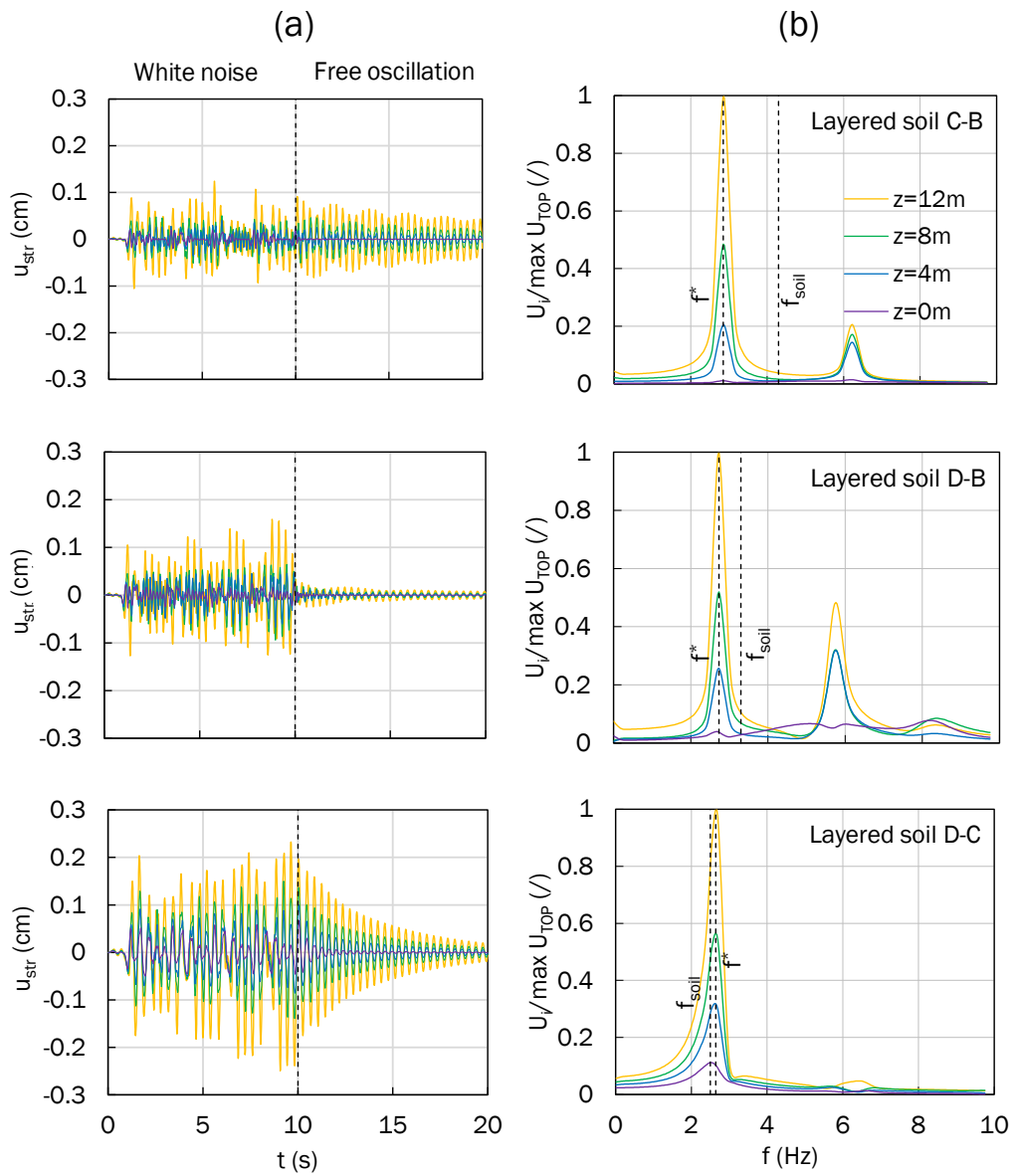
A.A.2 Dynamic response of two-storey SFS system ($h/b = 1$) with embedded floating foundation and layered soil (C-B, D-B, D-C): (a) time histories and (b) FFTs of horizontal displacements at different structural elevations.



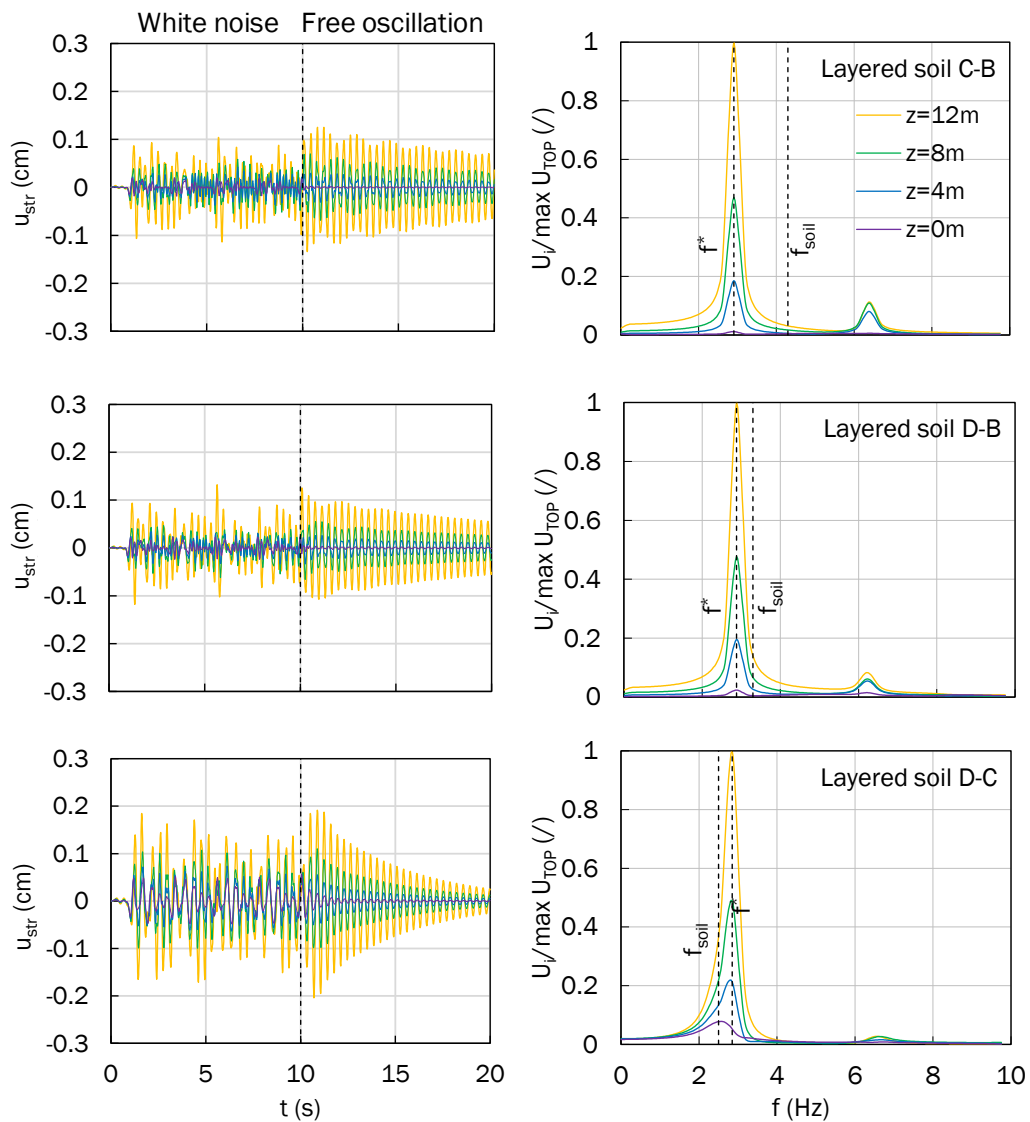
A.A.3 Dynamic response of two-storey SFS system ($h/b = 1$) with underground storey foundation and homogeneous soil (A, B, C or D): (a) time histories and (b) FFTs of horizontal displacements at different structural elevations.



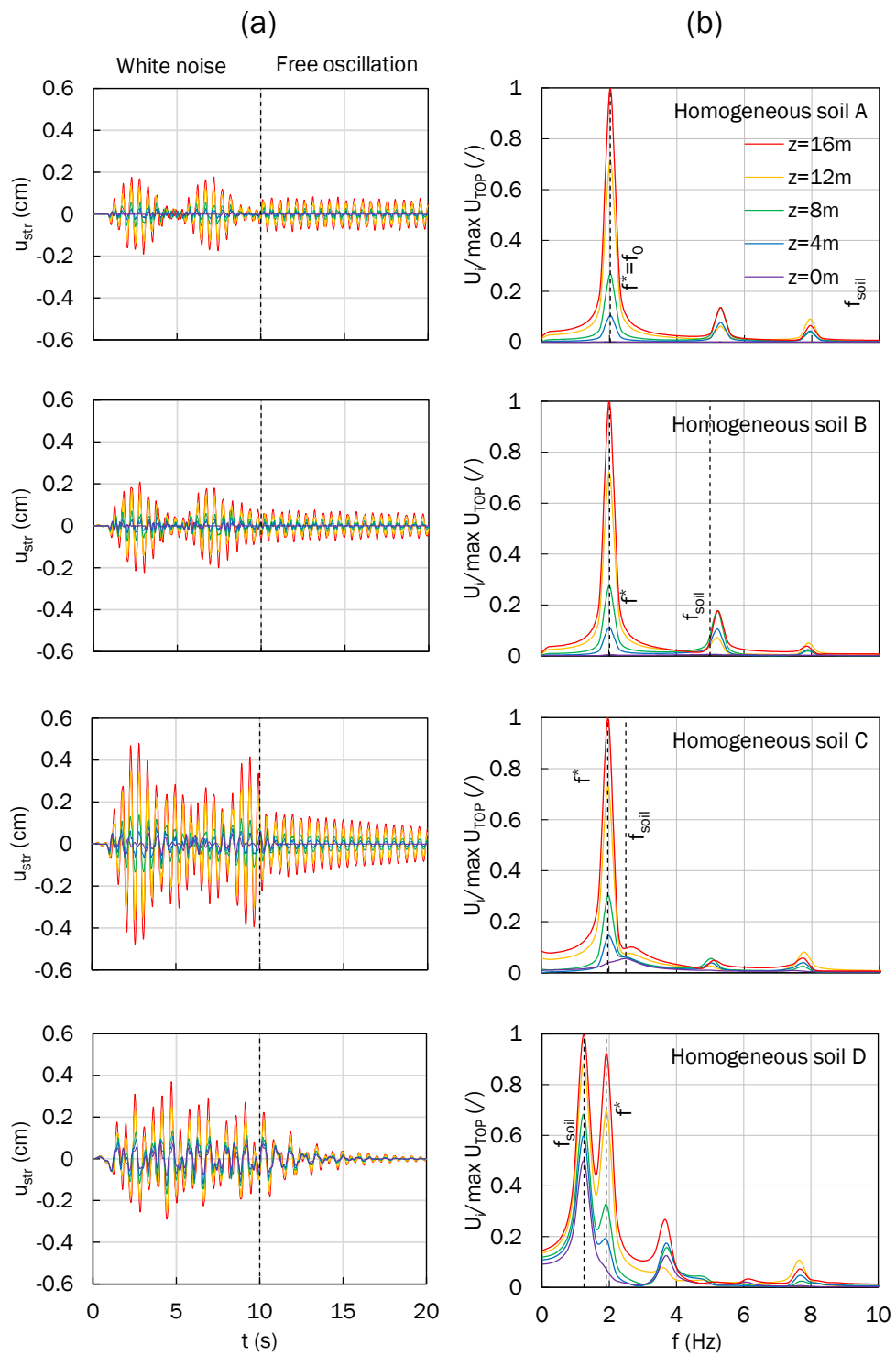
A.A.4 Dynamic response of two-storey SFS system ($h/b = 1$) with underground storey foundation and layered soil (C-B, D-B, D-C): (a) time histories and (b) FFTs of horizontal displacements at different structural elevations.



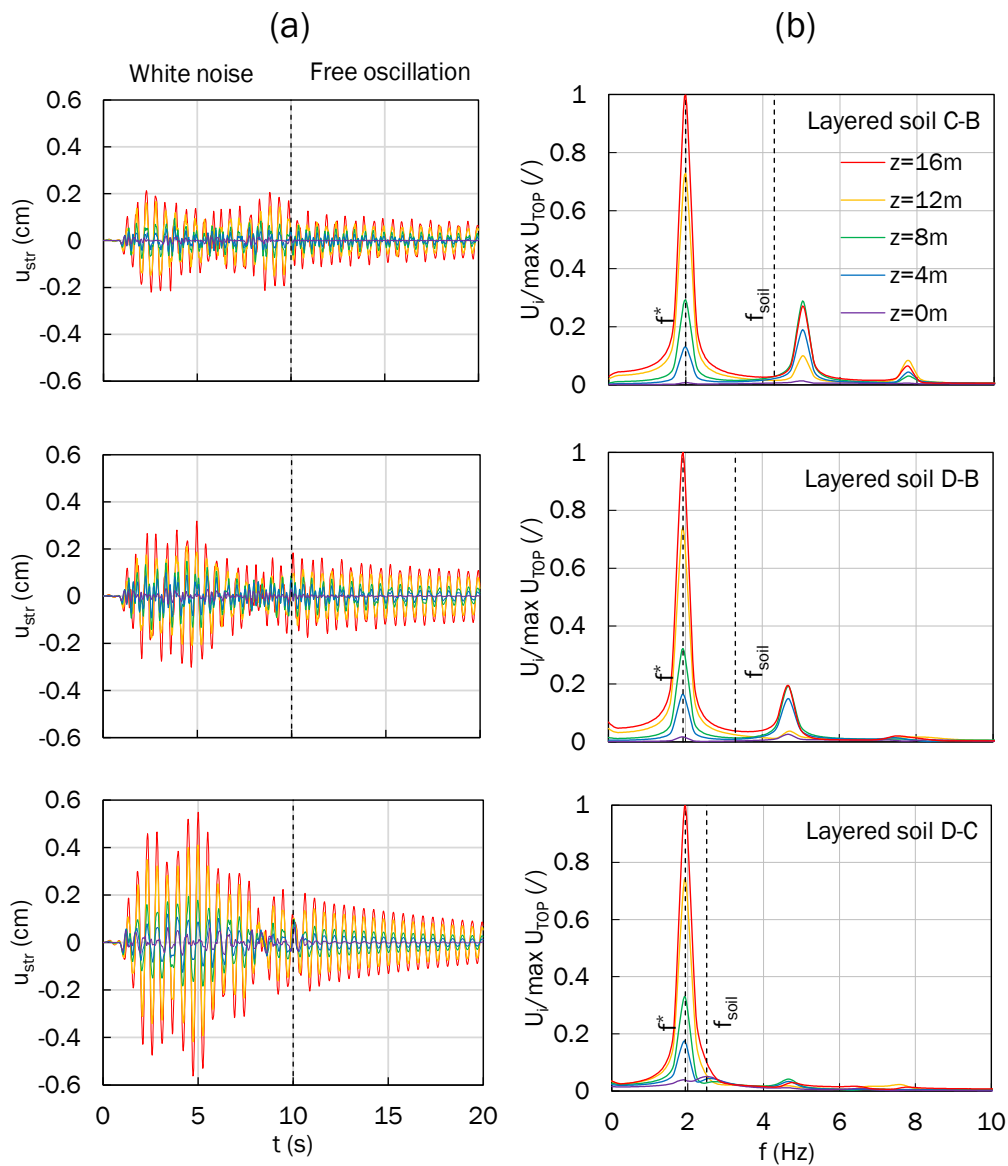
A.A.5 Dynamic response of three-storey SFS system ($h/b = 1.5$) with embedded floating foundation and layered soil (C-B, D-B, D-C): (a) time histories and (b) FFTs of horizontal displacements at different structural elevations.



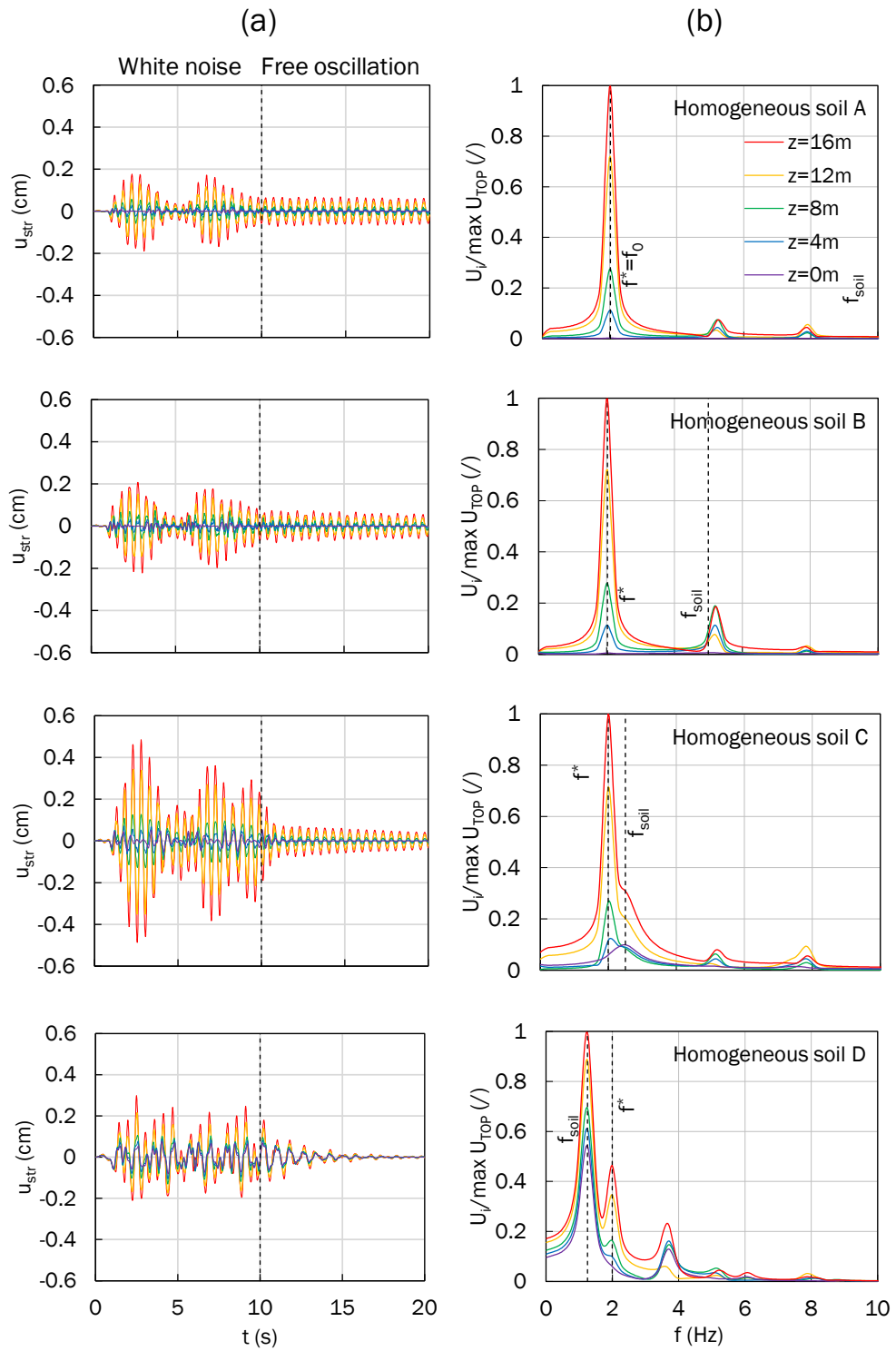
A.A.6 Dynamic response of three-storey SFS system ($h/b = 1.5$) with underground storey foundation and layered soil (C-B, D-B, D-C): (a) time histories and (b) FFTs of horizontal displacements at different structural elevations.



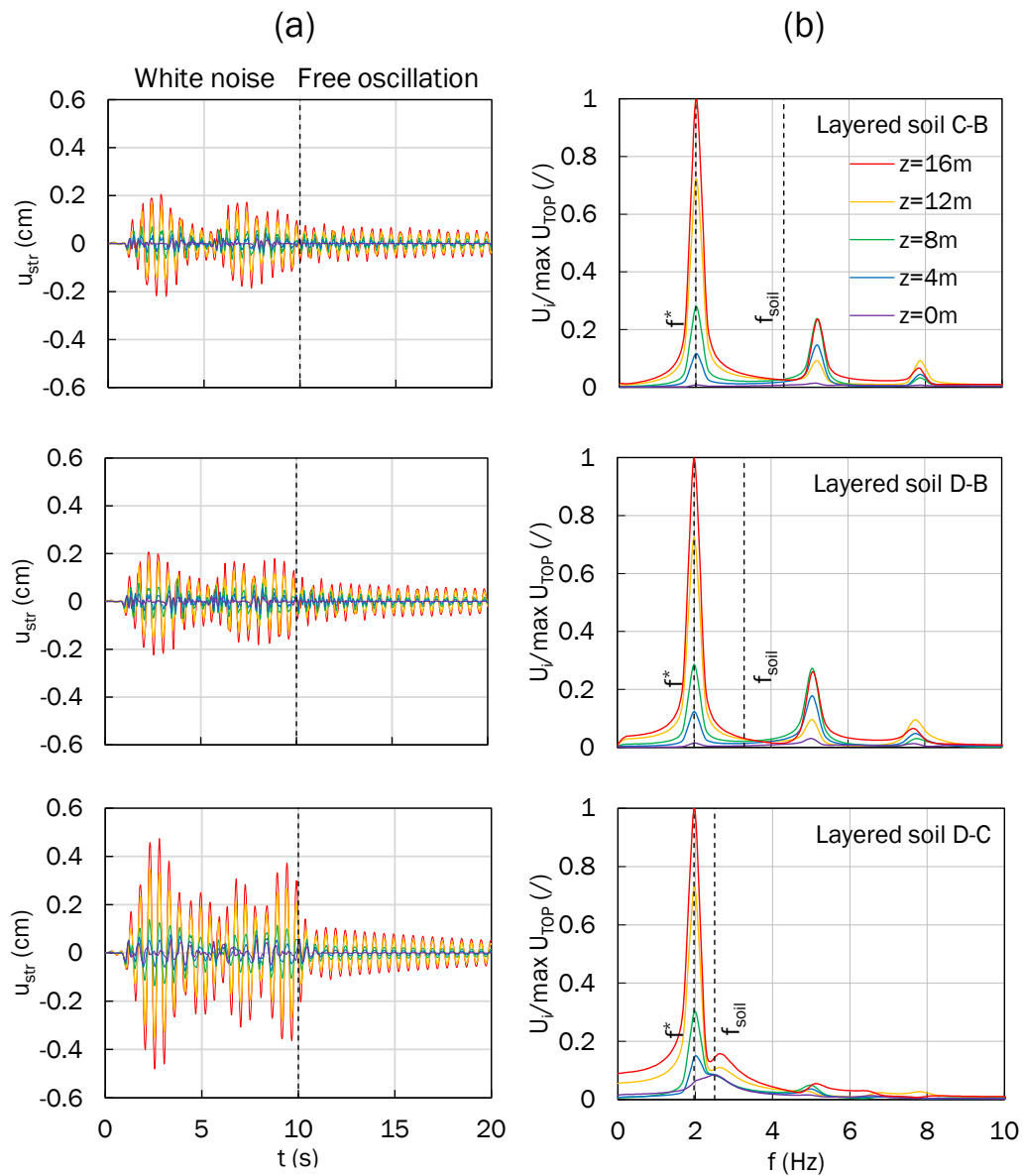
A.A.7 Dynamic response of four-storey SFS system ($h/b = 2$) with embedded floating foundation and homogeneous soil (A, B, C or D): (a) time histories and (b) FFTs of horizontal displacements at different structural elevations.



A.A.8 Dynamic response of four-storey SFS system ($h/b = 2$) with embedded floating foundation and layered soil (C-B, D-B, D-C): (a) time histories and (b) FFTs of horizontal displacements at different structural elevations.

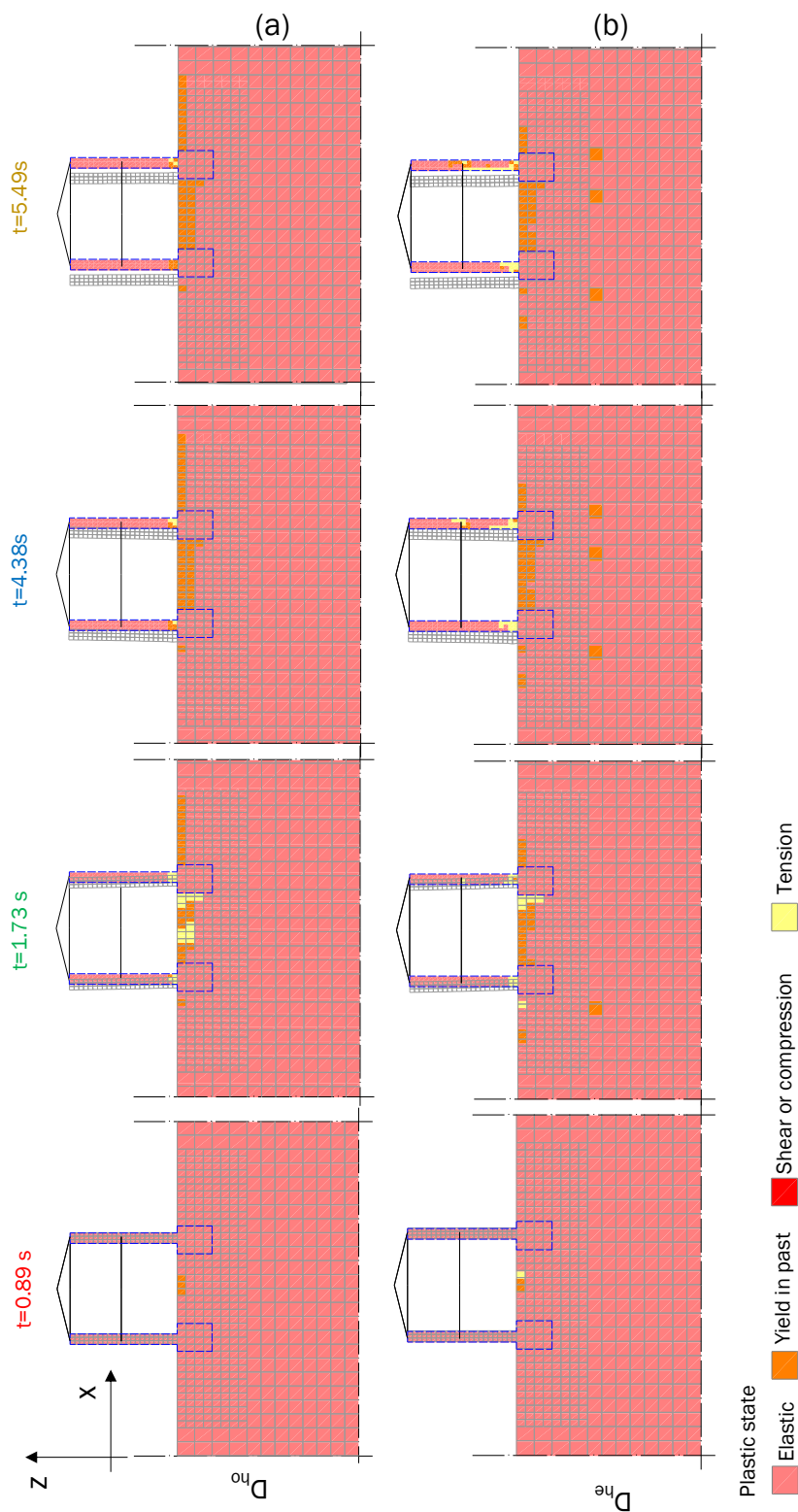


A.A.9 Dynamic response of four-storey SFS system ($h/b = 2$) with underground storey foundation and homogeneous soil (A, B, C or D): (a) time histories and (b) FFTs of horizontal displacements at different structural elevations.

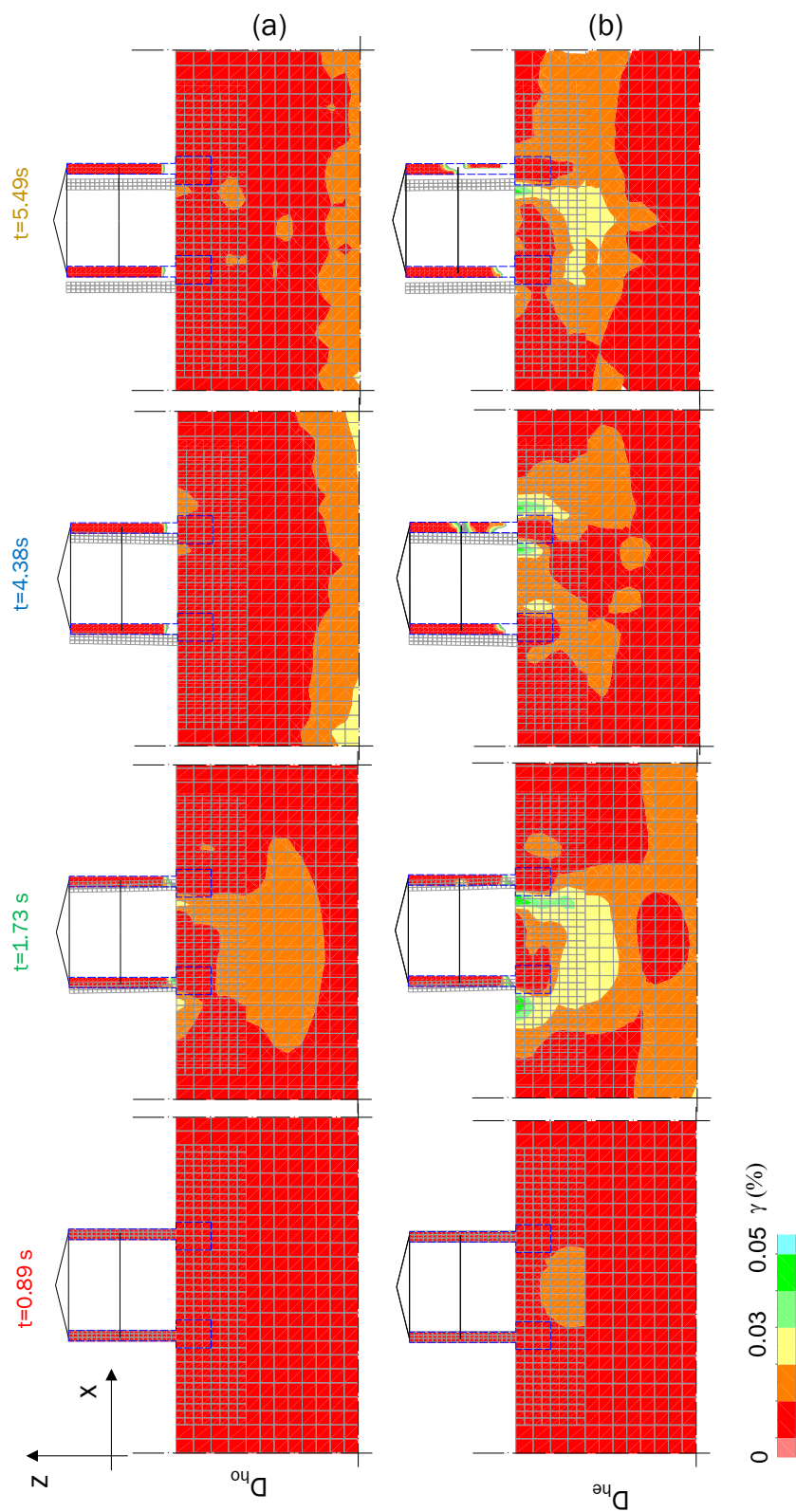


A.A.10 Dynamic response of four-storey SFS system ($h/b = 2$) with underground storey foundation and layered soil (C-B, D-B, D-C): (a) time histories and (b) FFTs of horizontal displacements at different structural elevations.

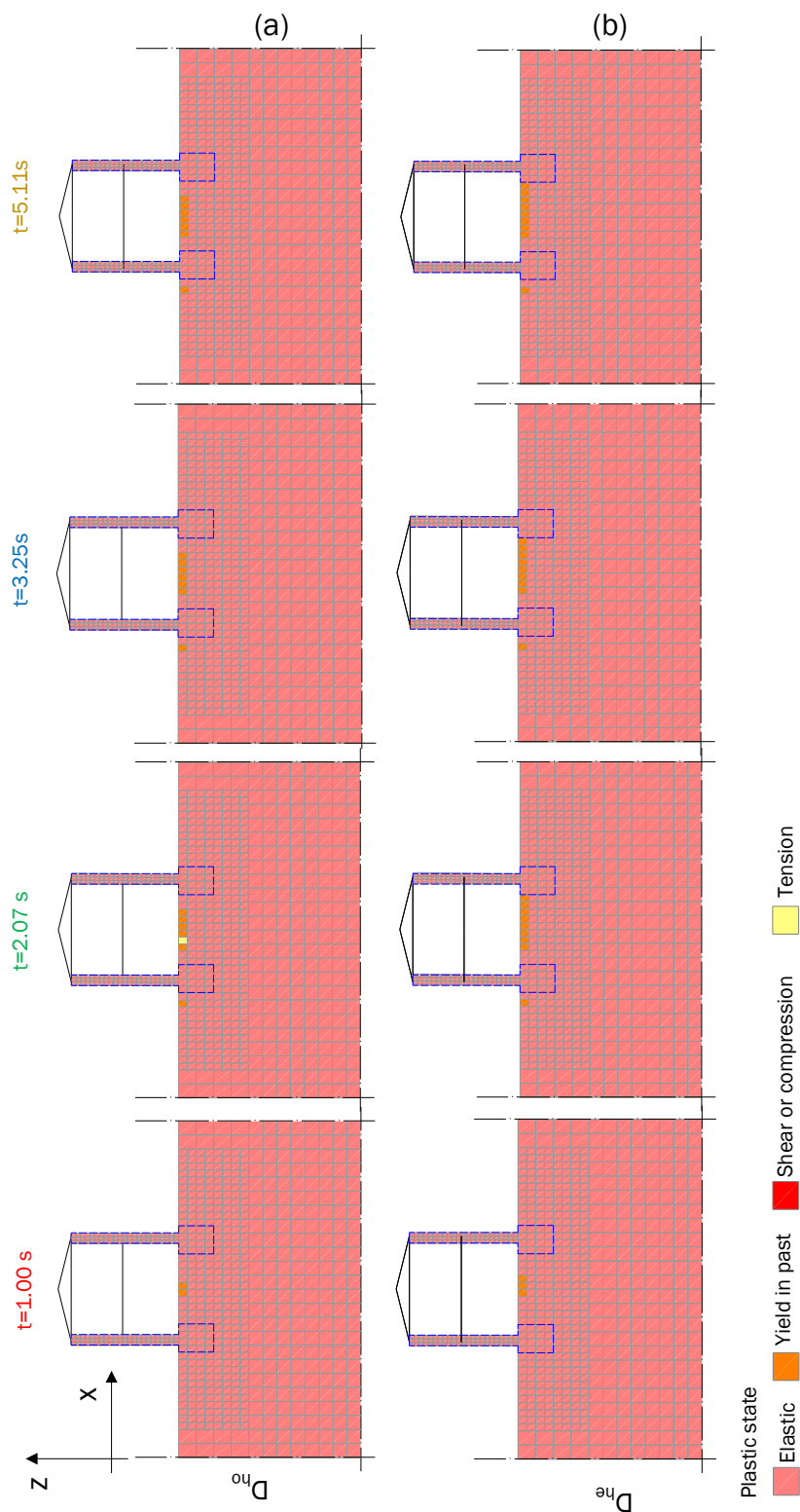
APPENDIX B
RESULTS OF NONLINEAR TIME HISTORY ANALYSIS



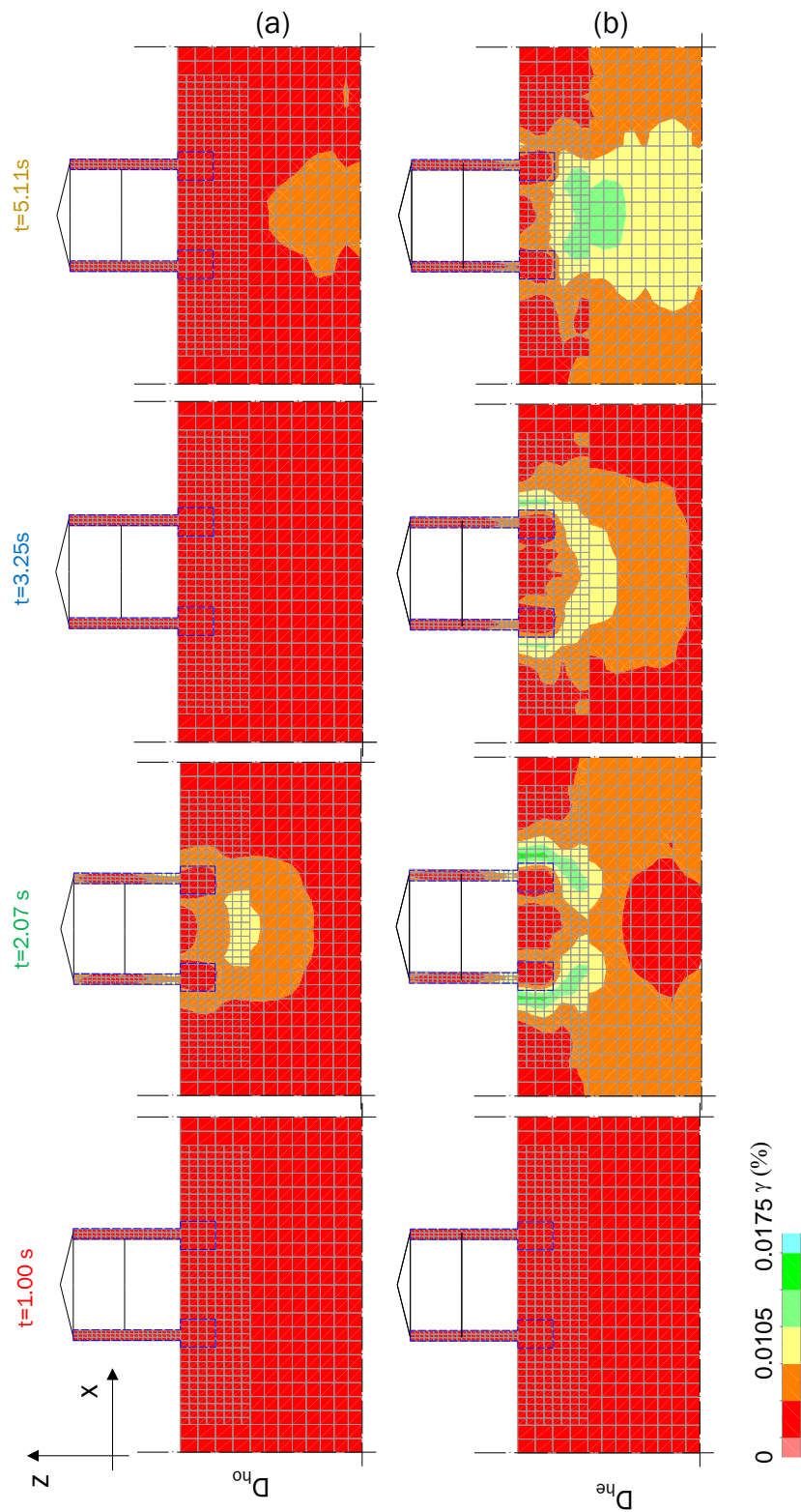
A.B.1 Evolution of deformed shapes and plastic states of the two-storey, clay brick masonry structure, ID 11: (a) homogeneous soil and (b) heterogeneous soil



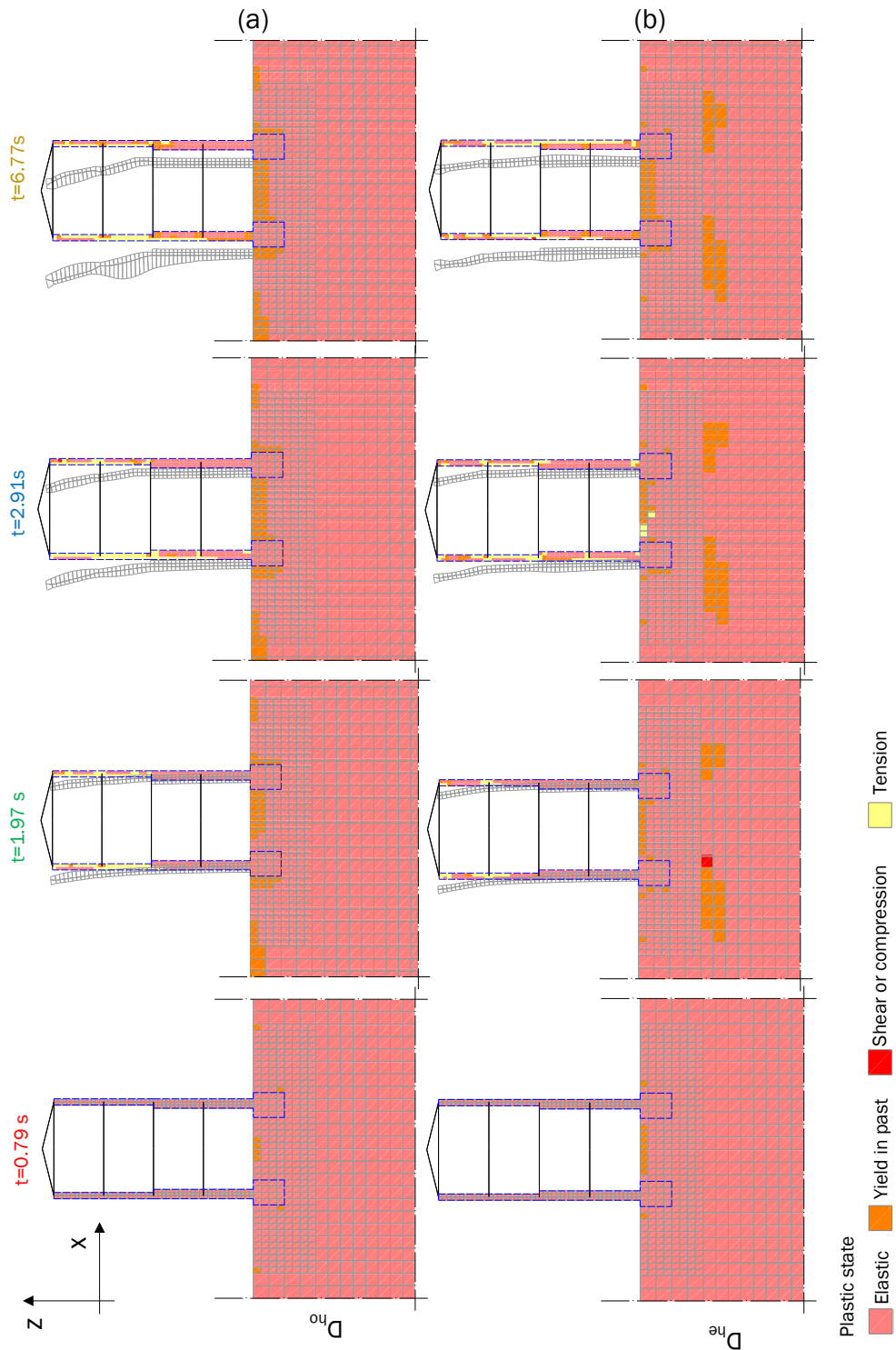
A.B.2 Evolution of deformed shapes and shear strains, ID 11: (a) homogeneous soil and (b) heterogeneous soil



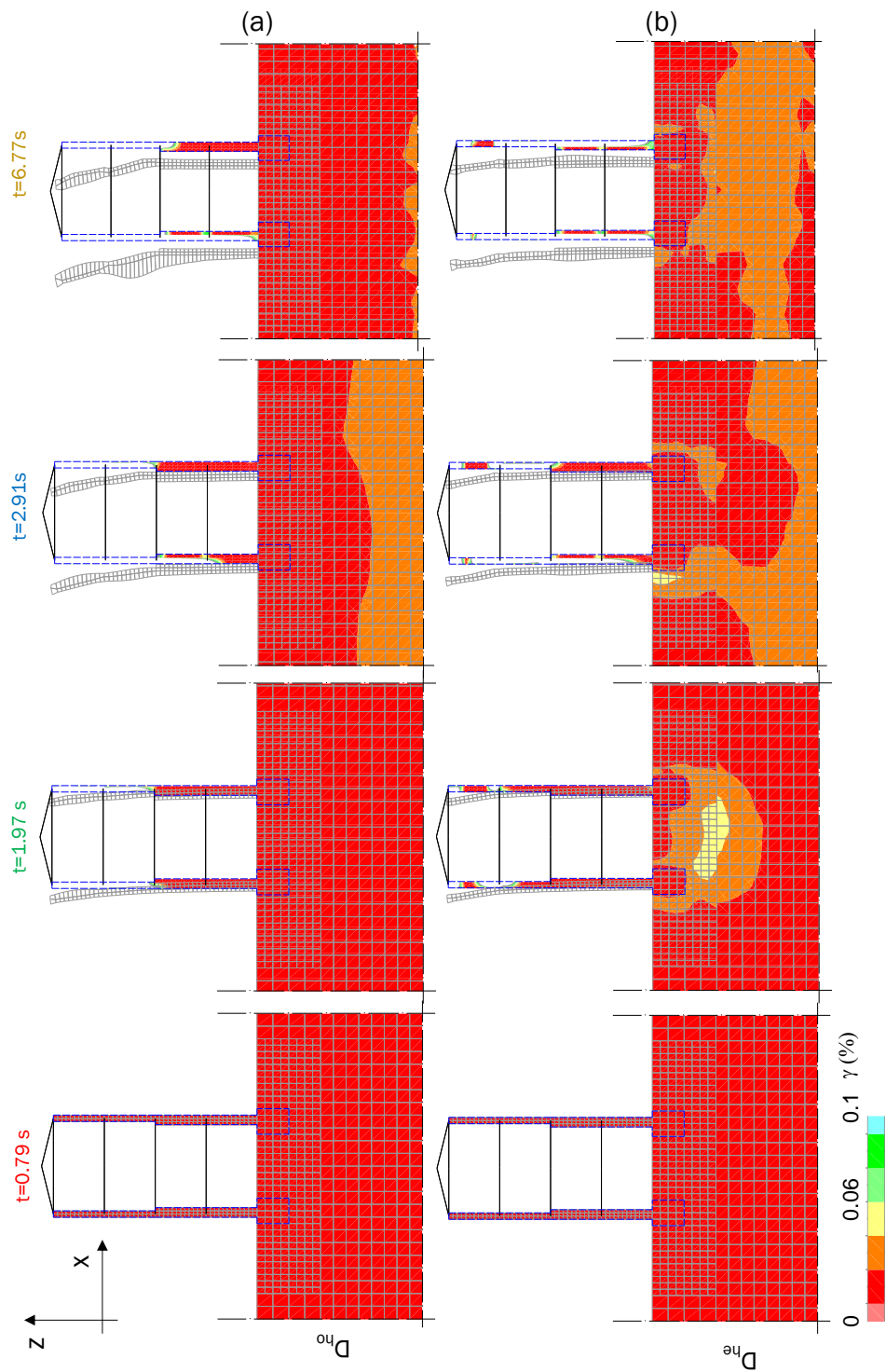
A.B.3 Evolution of deformed shapes and plastic states of the two-storey, clay brick masonry structure, ID 12: (a) homogeneous soil and (b) heterogeneous soil



A.B.4 Evolution of deformed shapes and shear strains, ID 12: (a) homogeneous soil and (b) heterogeneous soil



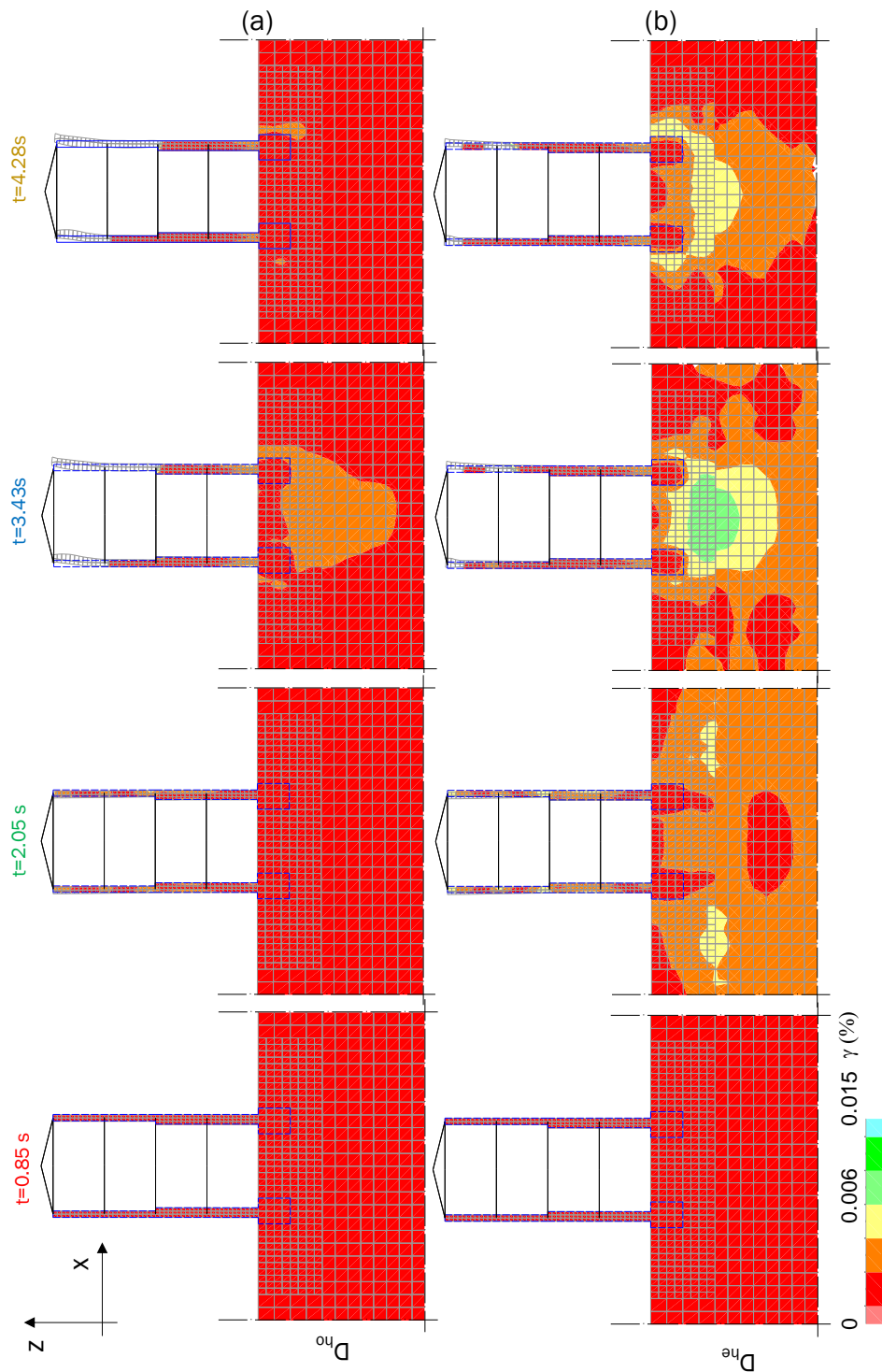
A.B.5 Evolution of deformed shapes and plastic states of the four-storey, clay brick masonry structure, ID 11: (a) homogeneous soil and (b) heterogeneous soil



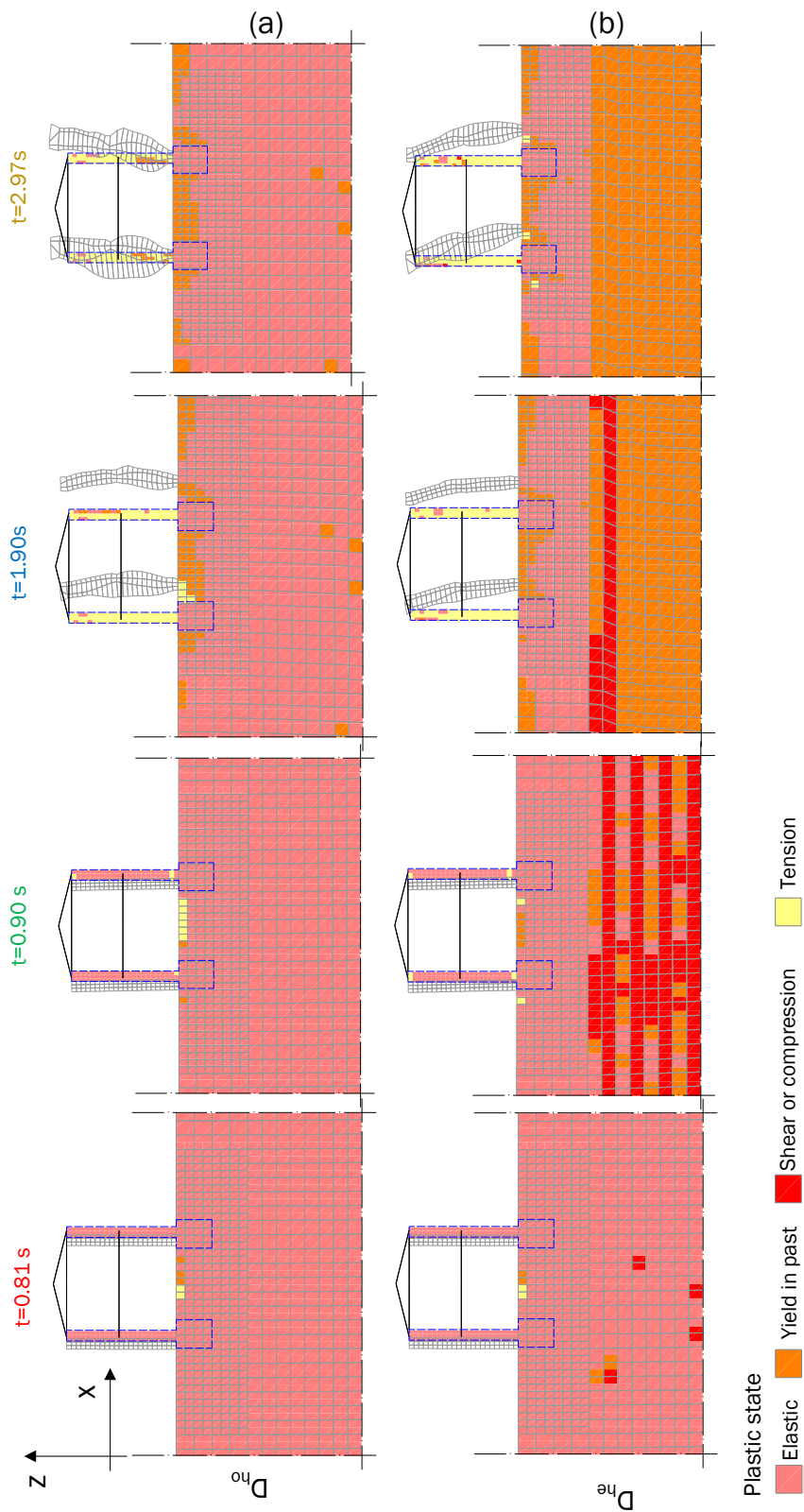
A.B.6 Evolution of deformed shapes and shear strains, ID 11: (a) homogeneous soil and (b) heterogeneous soil



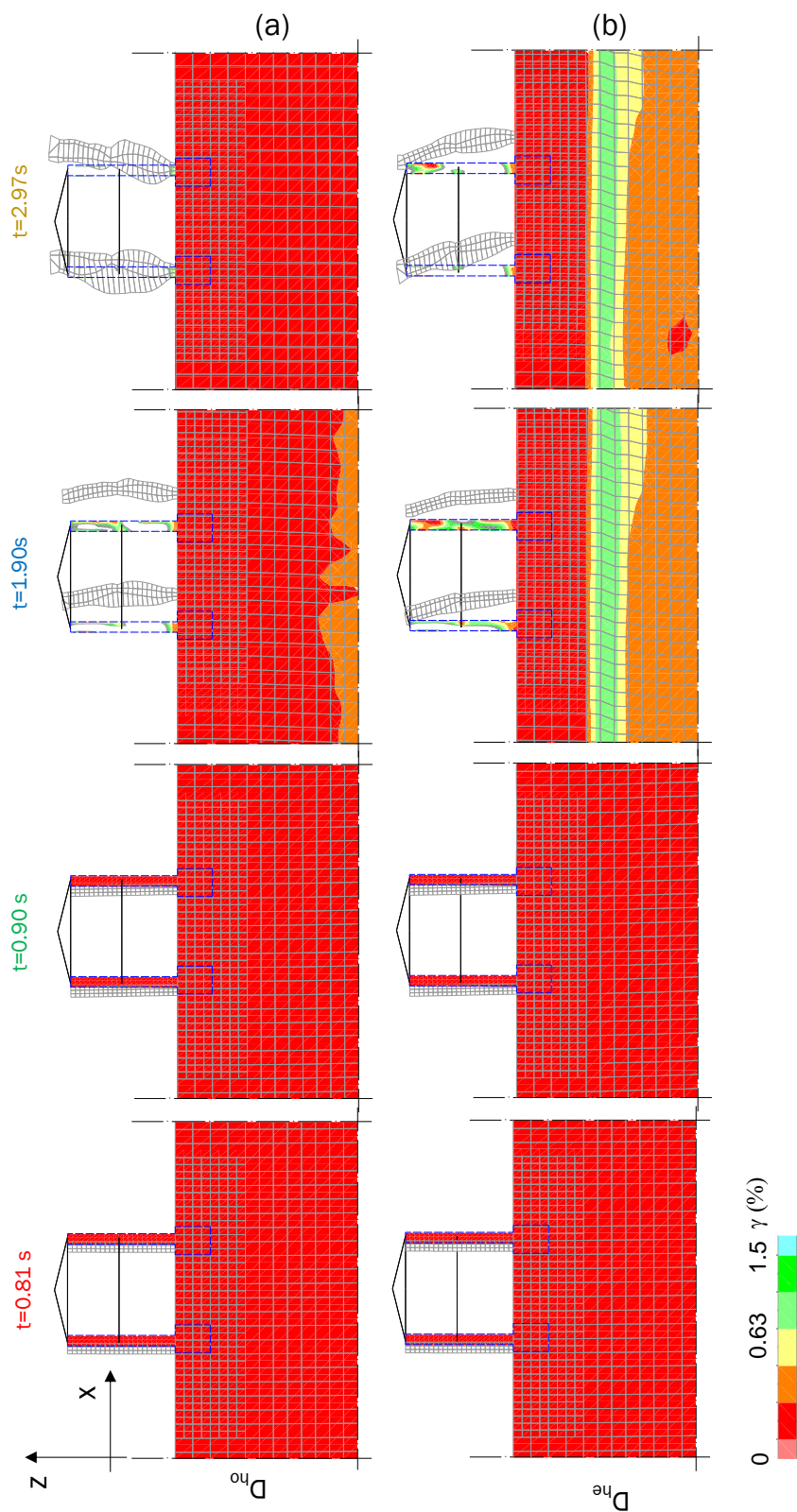
A.B.7 Evolution of deformed shapes and plastic states of the four-storey, clay brick masonry structure, ID 12: (a) homogeneous soil and (b) heterogeneous soil



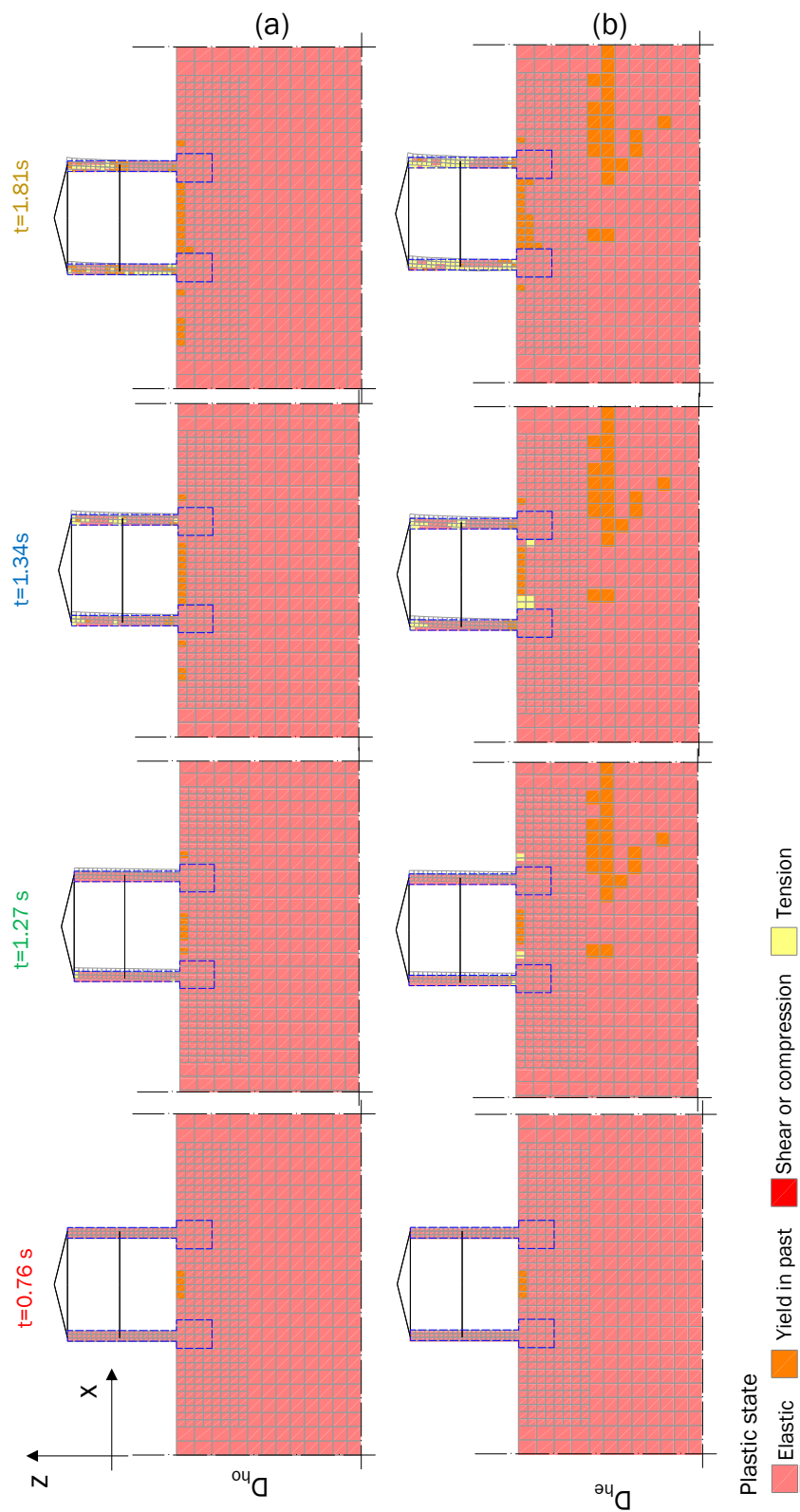
A.B.8 Evolution of deformed shapes and shear strains, ID 12: (a) homogeneous soil and (b) heterogeneous soil



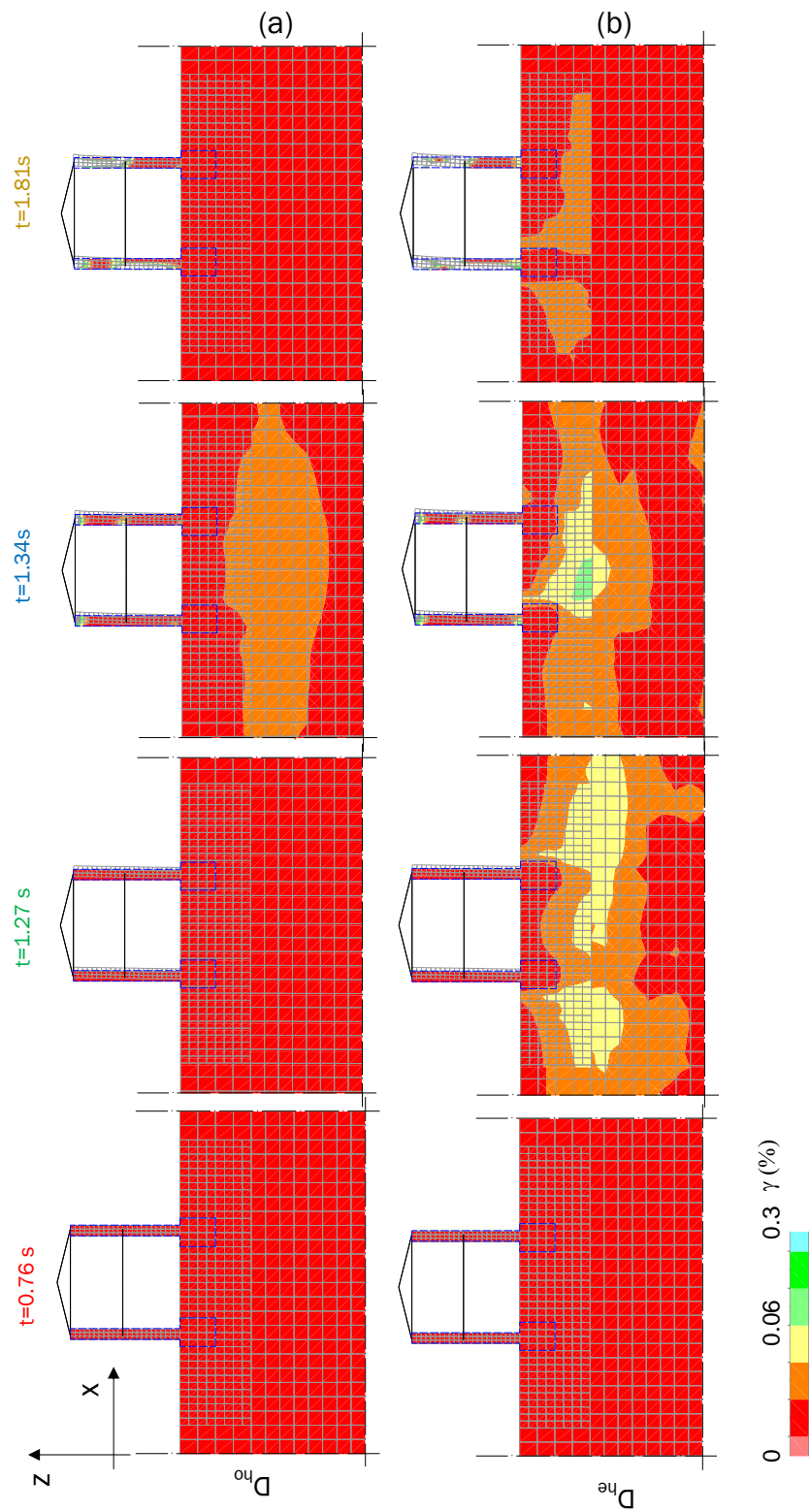
A.B.9 Evolution of deformed shapes and plastic states of the two-storey, rubble stone masonry structure, ID 2: (a) homogeneous soil and (b) heterogeneous soil



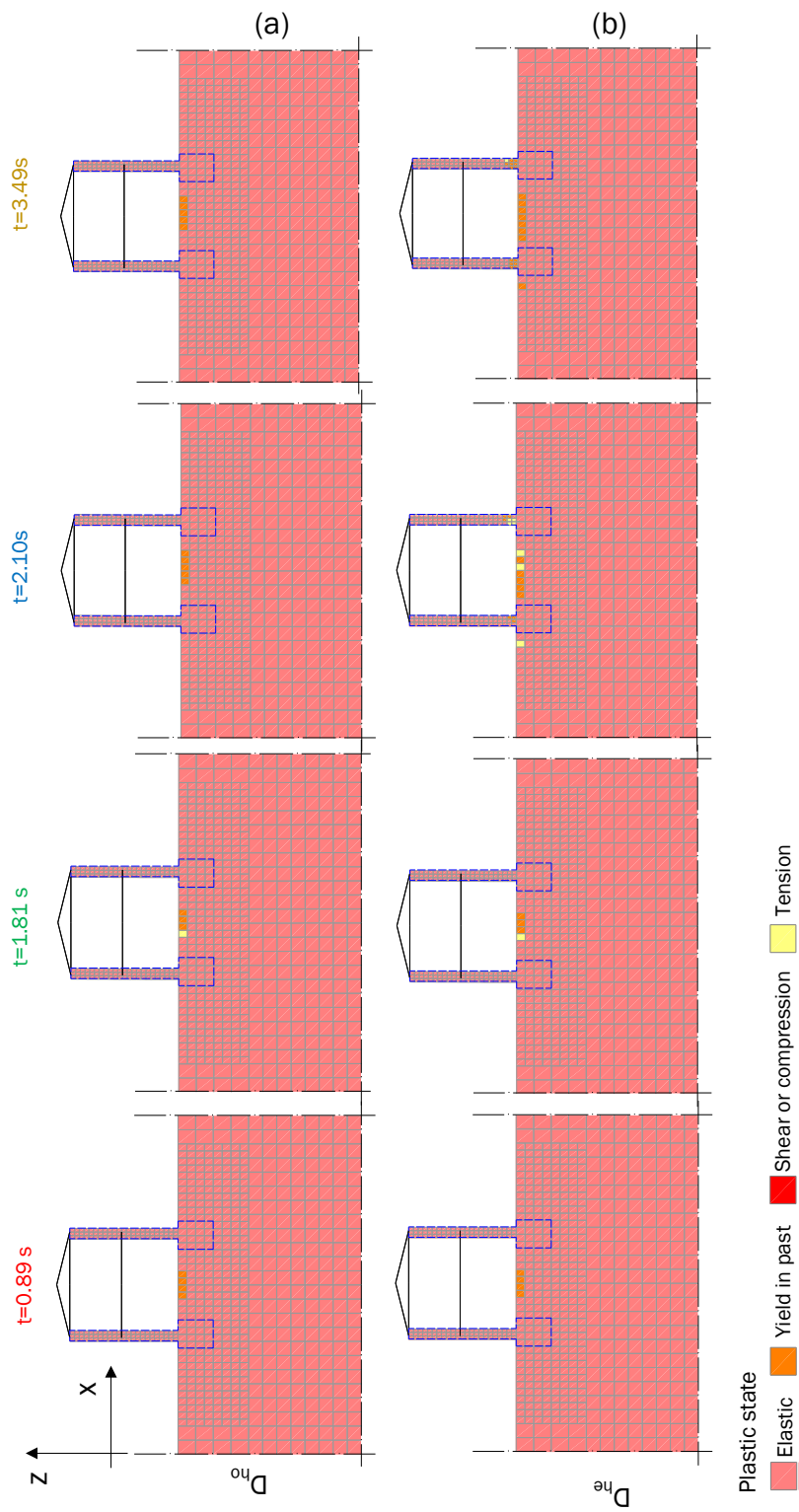
A.B.10 Evolution of deformed shapes and shear strains, ID 2: (a) homogeneous soil and (b) heterogeneous soil



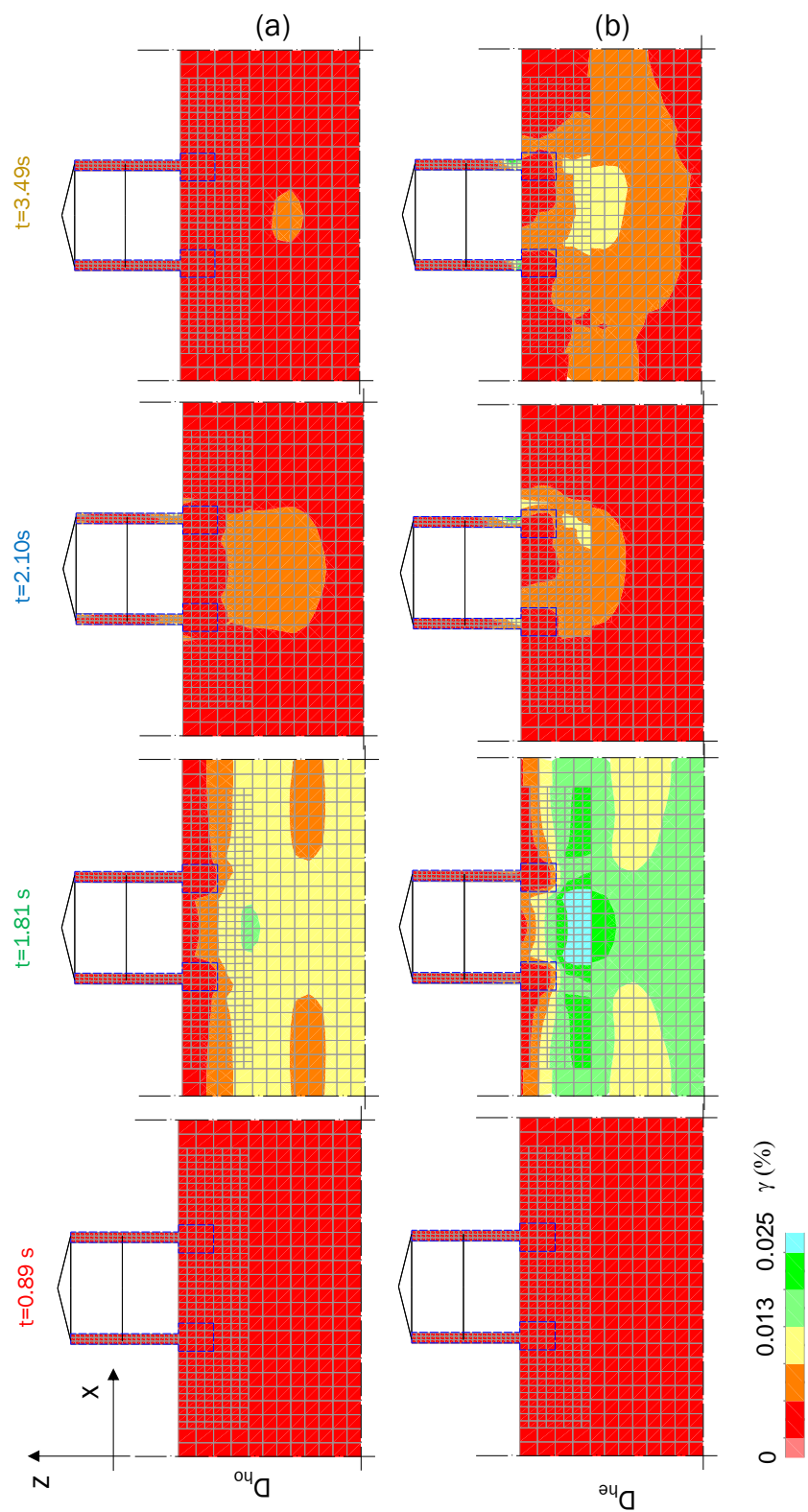
A.B.11 Evolution of deformed shapes and plastic states of the two-storey, rubble stone masonry structure, ID 5: (a) homogeneous soil and (b) heterogeneous soil



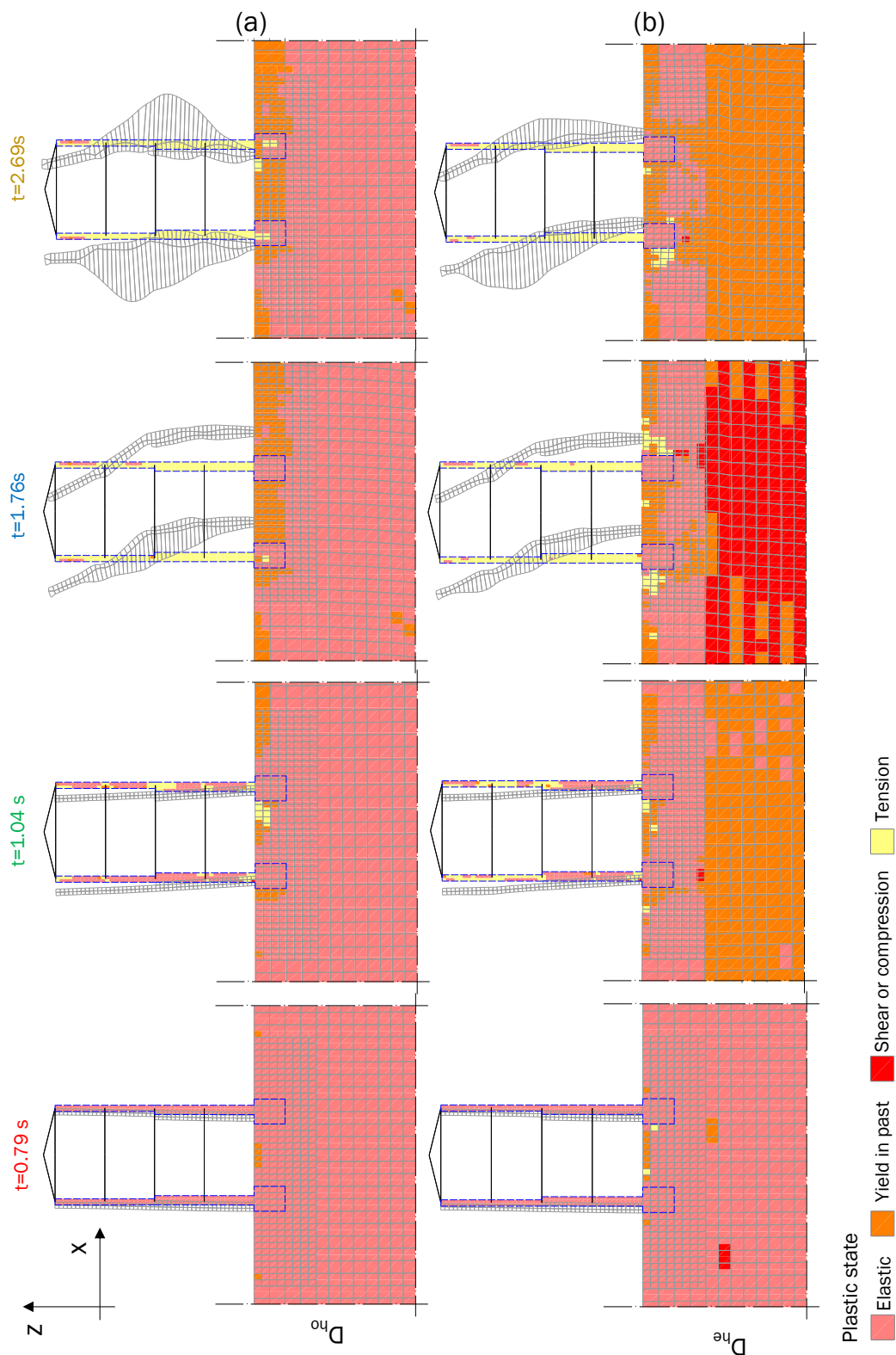
A.B.12 Evolution of deformed shapes and shear strains, ID 5: (a) homogeneous soil and (b) heterogeneous soil



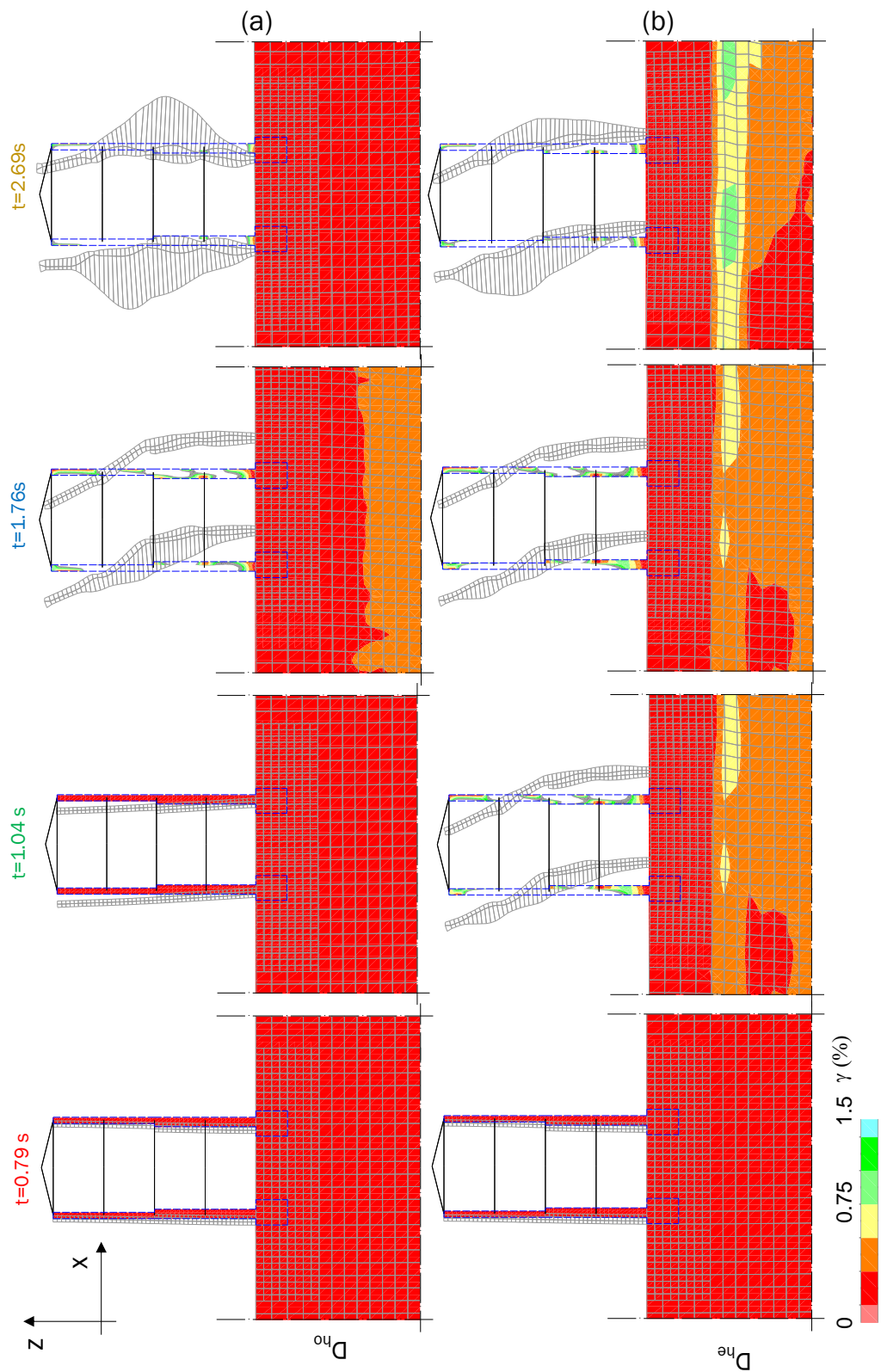
A.B.13 Evolution of deformed shapes and plastic states of the two-storey, rubble stone masonry structure, ID 12: (a) homogeneous soil and (b) heterogeneous soil



A.B.14 Evolution of deformed shapes and shear strains, ID 12: (a) homogeneous soil and (b) heterogeneous soil



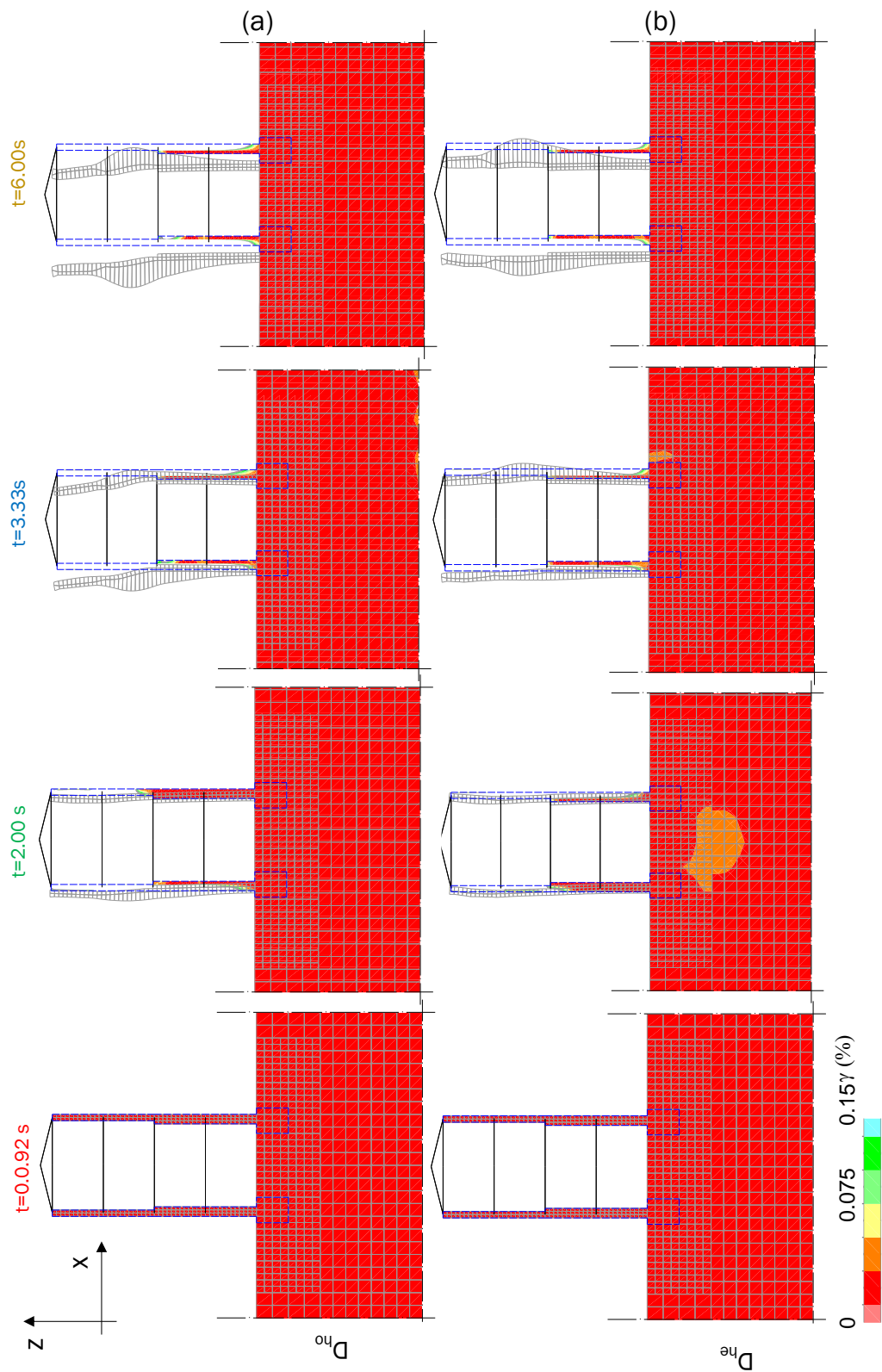
A.B.15 Evolution of deformed shapes and plastic states of the four-storey, rubble stone masonry structure, ID 2: (a) homogeneous soil and (b) heterogeneous soil



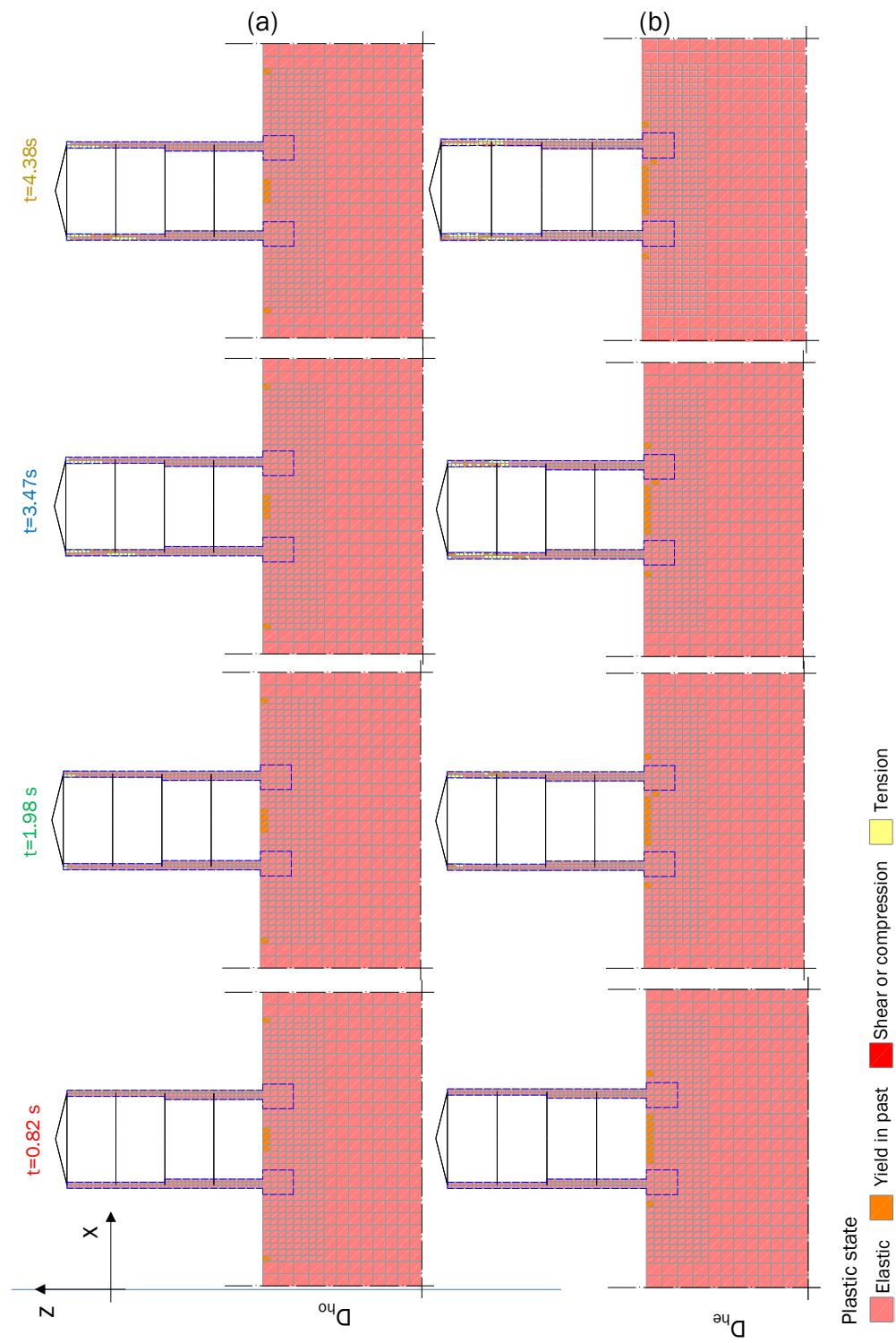
AB.16 Evolution of deformed shapes and shear strains, ID 2: (a) homogeneous soil and (b) heterogeneous soil



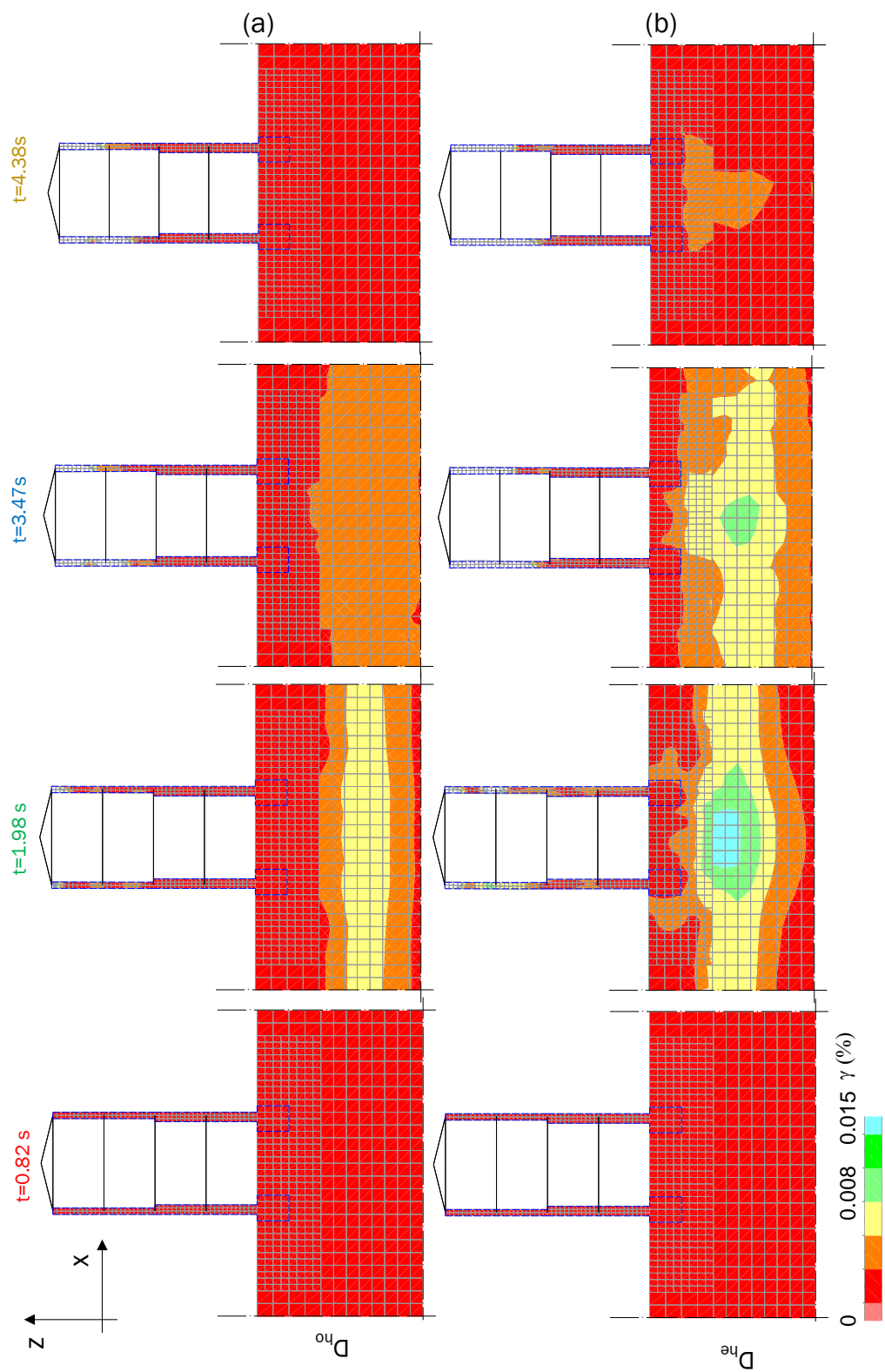
A.B.17 Evolution of deformed shapes and plastic states of the four-storey, rubble stone masonry structure, ID 11: (a) homogeneous soil and (b) heterogeneous soil



A.B.18 Evolution of deformed shapes and shear strains, ID 11: (a) homogeneous soil and (b) heterogeneous soil



A.B.19 Evolution of deformed shapes and plastic states of the four-storey, rubble stone masonry structure, ID 12: (a) homogeneous soil and (b) heterogeneous soil



A.B.20 Evolution of deformed shapes and shear strains, ID 12: (a) homogeneous soil and (b) heterogeneous soil

